Coherent Control of Multi-Qubit Dark States in Waveguide Quantum Electrodynamics

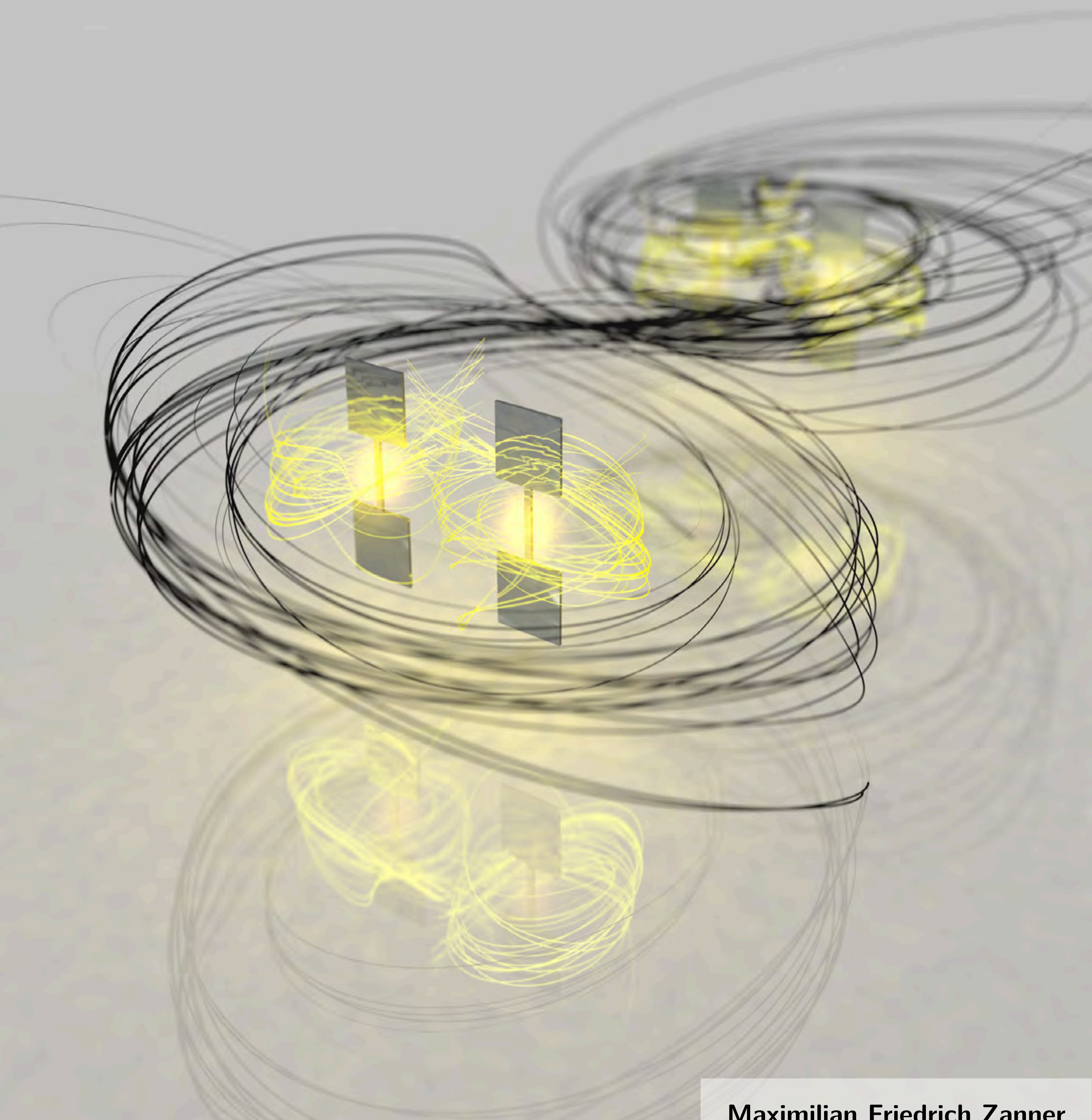

Maximilian Friedrich Zanner

Coherent Control of Multi-Qubit Dark States in Waveguide Quantum Electrodynamics

Dissertation

by

Maximilian Friedrich Zanner

Submitted to the Faculty of Mathematics, Computer Science, and Physics of the University of Innsbruck in Partial Fulfillment of the Requirements for the Degree of Doctor of Philosophy

Carried out at the Institute of Experimental Physics under the Supervision of
Univ.-Prof. Dr. Gerhard Kirchmair

with the Co-Supervisors
Univ.-Prof. Dr. Helmut Ritsch
Dr. Ioan M. Pop

Innsbruck, March 2022

Abstract

Quantum physics has transitioned with great success from research on fundamental effects to harvesting technological applications that influence our everyday life. Stimulated emission in atoms allowed the development of laser systems, quantum mechanical descriptions explain tunneling effects in transistors and other semiconducting devices, and the utilization of the atomic spin enabled the development of novel medical devices via magnetic resonance imaging (MRI). New technologies are trying to improve classical systems with the help of quantum phenomena such as quantum entanglement, quantum superposition or quantum tunneling. These technologies include quantum communication, quantum sensing and quantum computing. In order to realize these new applications it is necessary to achieve coherent control over individual quantum states. This demands the ability to prepare, manipulate and read out the state of the encoded quantum information. Many platforms are trying to realize the interaction between matter and light by interfacing various emitters and electromagnetic environments. These include trapped ions, ultracold atoms or molecules, single spins in silicon, quantum dots, nitrogen-vacancy centers in diamond, photons, and superconducting quantum circuits [1].

Quantum electrodynamics (QED) is the theoretical description of the interaction between matter and light at the level of single excitations and thus the basis for all applications using light-matter interfaces. For a long time it has been proven difficult to observe QED phenomena in fundamental research. The main problem is the weak interaction between the atomic emitter and the three dimensional mode environment of open space. Cavity QED confines light inside a closed volume, which can be used to enhance the interaction between the atom and the light field and enabled the exploration of many QED effects. Circuit QED [2] adapted this approach by using superconducting qubits, serving as artificial atoms and microwave resonators, replacing optical cavities.

One of the key ingredients for new quantum technological applications, like quantum computing and quantum information processing is strong light-matter interaction. Hence, most state of the art superconducting quantum information systems use qubits that are embedded in a resonator or cavity to enhance the interaction. Commonly, the strong-coupling limit is defined as the limit where the desired qubit coupling to a specific channel exceeds the coupling to all dissipative channels [3]. Superconducting qubit-cavity systems protect the quantum information by designing the circuit such that the frequencies of the qubit and cavity are far detuned from each other. In this so-called dispersive regime, the cavity acts as a filter for noise around the qubit frequency that travels through the coaxial lines. At the same time the strong-coupling between the cavity and qubit allows for a quantum non-demolition readout of the qubit state due to the dispersive cavity shift that depends on the state of the qubit. The qubit remains accessible for coherent manipulation by applying pulses through weakly coupled control lines. The combination of these fundamental requirements led to the rapid development of circuit QED as one of the leading platforms for realizing a quantum computer.

Waveguide QED combines open space and enhanced interaction by allowing photon propagation in one dimension and confining the other two dimensions. This allows studying quantum effects in an environment that is closer to the original QED description in free space. Waveguide quantum electrodynamics has become a popular platform to study light-matter interactions by coupling localized quantum emitters to one dimensional photonic channels. There are various platforms, that can be assessed by the ability to deterministically and efficiently couple individual quantum emitters to the waveguide. Due to their small dipole moment, natural atoms can only be coupled very weakly to propagating photons, at best achieving that 50% of the emitted radiation is coupled into the waveguide [4]. Artificial atoms, like quantum dots can be coupled very efficiently, such that over 99% of the emission is guided into the waveguide modes [5]. They have high engineering potential [6] but suffer from inhomogeneous broadening which makes it very difficult to have more than two resonant emitters [7]. Superconducting qubits are usually realized by integrating a nonlinear Josephson junction [8] into an electrical circuit to obtain an anharmonic oscillator that plays the role of an artificial multilevel atom. Superconducting qubits and microwave waveguides can achieve coupling efficiencies of 99.9% [9], the qubits can be reliably fabricated as arrays [10], and they can be designed so that their resonance frequency can be controlled locally by magnetic flux [11]. The engineering capabilities of superconducting qubits led to the observation of a broad range of quantum optical phenomena such as the Mollow triplet [12, 13], ultra strong coupling [14], generation of non-classical photonic states [15, 16], qubit-photon bound states [17], topological physics [18] as well as collective effects [9, 19]. Despite the success of superconducting waveguide quantum electrodynamics, one of many crucial questions remains unanswered: How valid is the two-level approximation, especially for describing collective states beyond the single excitation manifold [1]?

Collective states appear in waveguide QED as a result of waveguide-mediated interactions [20] and interference effects in an ensemble of emitters [4]. The relative phase between individual emitters determines whether the collective state obtains a sub- or superradiant decay rate, i.e. whether it becomes a dark or a bright state. Collective bright states have been measured in various waveguide QED systems [7, 19, 21–23], whereas dark states have only been observed spectroscopically in superconducting waveguide QED [10, 19]. More recently a multi-qubit dark state has been used to build a microwave cavity [9], but full coherent control of the dark state has not been achieved. The difficulty arises from the main property of the dark state - it decouples from the electromagnetic environment of the waveguide. Full control over the dark state provides the possibility to realize a quantum computation and simulation platform using decoherence-free subspaces [24, 25]. For quantum computation purposes the multi-level nature of collective systems requires accurate knowledge of the energy and decay characteristics beyond the single excitation states to avoid detrimental leakage errors out from the computational subspace. Coherent control over the dark states enables the usage as a qubit in waveguide QED. Moreover, the long-lived nature offers a starting point for an accurate characterization of the spectrum and the decay properties of such collective systems, especially for the higher excitation manifolds.

In the scope of this thesis, we investigated the interaction between four superconducting transmon qubits that are coupled to a common waveguide mode environment. The hybridization of the transmon yields collective states that strongly depend on the coupling parameters and transmon anharmonicities. The pairwise arrangement gives rise to a direct coupling that is caused by the capacitance between the metallic transmon pads. Each pair obtains a local dark state in the first excitation manifold, that is long-lived and can serve as a resource for coherence in an open quantum system, such as the waveguide environment. The waveguide-mediated interaction depends on the effective separation and causes coherent exchange coupling or collective dissipation. In this setting we focus on the collective behavior, thus tune the qubits to a frequency that corresponds to a distance of half a wavelength [20]. The emerging dark state is non-local and shared between the distant qubits. Then, the phase of a collective drive must match the phase of the hybridized transitions in order to drive them. We show that two local ports at the qubit pairs can be used to match the drive phase to the symmetry of the bright and dark states, and show that the dark state serves as a starting point for studying the multi-level spectrum of the coupled transmons.

The doctoral thesis is organized as follows: The introductory chapter contains the basic concepts of circuit QED and a description of cavity and waveguide QED. The second chapter summarizes the waveguide QED theory, which is necessary to understand the experimental results. Many results can already be reproduced by QuTiP [26] simulations. But an accurate prediction of the energy spectrum, the decay rates of the states, and the symmetries with respect to a given mode environment are obtained by numerical simulations of the pairwise transmon setup. In the third chapter, a practical approach to the design and development of a waveguide QED setup is presented and the measurement procedure is briefly discussed. In the fourth chapter, the results of the conducted experiments are presented and discussed, while in the conclusion, the significance of the results in a broader sense is explained to conclude the thesis.

Kurzfassung

Die Quantenphysik ist mit großem Erfolg von der Erforschung grundlegender Effekte zu technologischen Anwendungen übergegangen, die unser tägliches Leben beeinflussen. Die stimulierte Emission in Atomen ermöglichte die Entwicklung von Lasersystemen, Quantentheorien werden zur Beschreibung von Transistoren und anderen Halbleiterbauelementen verwendet, und die Nutzung des atomaren Spins ermöglichte die Beobachtung des Inneren von Festkörpern mittels Magnetresonanztomographie (MRT). Neue Technologien versuchen, klassische Systeme mit Hilfe von Quantenphänomenen wie Quantenverschränkung, Quantenüberlagerung oder Quantentunnelung zu verbessern. Zu diesen Technologien gehören Quantenkommunikation, Quantensensorik und Quantencomputing. Um diese neuen Anwendungen zu realisieren, ist es notwendig kohärente Kontrolle über einzelne Quantenzustände zu erreichen. Dies bedeutet, dass es möglich sein muss, den Zustand der kodierten Quanteninformation in den Qubits zu initalisieren, zu manipulieren und auszulesen. Viele Plattformen versuchen, die Quantenkontrolle über die Wechselwirkung zwischen Materie und Licht zu realisieren. Dazu gehören Ionenfallen, ultrakalte Atome oder Moleküle, einzelne Spins in Silizium, Quantenpunkte, Stickstoff-Vakanzzentren in Diamant oder einzelne Photonen sowie auch supraleitende Quantenschaltkreise [1].

Die Quantenelektrodynamik (QED) ist die theoretische Beschreibung der Wechselwirkung zwischen Materie und Licht auf der Ebene einzelner Anregungen und damit die Grundlage

für alle Anwendungen an der Schnittstelle zwischen Licht und Materie. Lange Zeit hat es sich als schwierig erwiesen, QED-Phänomene in der Grundlagenforschung zu beobachten. Das Hauptproblem dabei ist die schwache Wechselwirkung zwischen dem atomaren Emitter und der dreidimensionalen Modenumgebung des offenen Raums. Bei der Hohlraum-QED wird das Licht in einem geschlossenen Volumen eingeschlossen, wodurch die Wechselwirkung zwischen dem Atom und dem Lichtfeld verstärkt werden kann und die Erforschung vieler QED-Effekte ermöglicht wird. Hohlraum-QED mit elektrischen Schaltkreisen [2] adaptierte diesen Ansatz, indem supraleitende Qubits als künstliche Atome verwendet werden, sowie Mikrowellenresonatoren, die die optischen Spiegel ersetzen.

Eine der wichtigsten Voraussetzungen für neue Anwendungen der Quantentechnologie, wie Quantencomputer und Quanteninformationsverarbeitung, ist eine starke Licht-Materie Wechselwirkung. Daher werden in den meisten modernen supraleitenden Quanteninformationssystemen Qubits verwendet, die in einen Resonator oder Hohlraum eingebettet sind, um die Wechselwirkung zu verstärken. Im Allgemeinen wird die Grenze der starken Kopplung definiert, bei der die gewünschte Qubit-Kopplung an einen bestimmten Kanal die Kopplung an alle Verlust-Kanäle übersteigt [3]. Supraleitende Qubit-Resonator-Systeme schützen die Quanteninformation, indem sie die Resonanzfrequenzen von Qubit und Resonator weit voneinander trennen. In diesem so genannten dispersiven Bereich wirkt der Resonator als Filter für Rauschsignale in der Nähe der Qubit-Frequenz, das durch die Koaxialleitungen übertragen wird. Gleichzeitig ermöglicht die starke Kopplung zwischen dem Resonator und dem Qubit ein Auslesen des Qubit-Zustands ohne das dieser zerstört wird mit Hilfe der Frequenzänderung des Resonators, die vom Zustand des Qubits abhängt. Das Qubit bleibt für kohärente Manipulationen zugänglich, indem Impulse über schwach gekoppelte Steuerleitungen gesendet werden. Die Kombination dieser grundlegenden Möglichkeiten der Isolation und Kontrolle führte zur raschen Entwicklung der Schaltkreis-QED als eine der führenden Plattformen für die Realisierung eines Quantencomputers.

Die Wellenleiter-QED kombiniert den offenen Raum mit der verstärkten Kopplung, indem sie die Ausbreitung von Photonen in einer Dimension erlaubt und die beiden anderen einschränkt. Dies ermöglicht die Untersuchung von Quanteneffekten in einer Umgebung, die der ursprünglichen QED-Beschreibung näher kommt. Die Wellenleiter-Quantenelektrodynamik ist zu einer beliebten Plattform für die Untersuchung von Licht-Materie Wechselwirkungen geworden, indem lokalisierte Quantenemitter an eindimensionale photonische Kanäle gekoppelt werden. Es gibt verschiedene Plattformen, die nach ihrer Fähigkeit bewertet werden können, einzelne Quantenemitter deterministisch und effizient an den Wellenleiter zu koppeln. Natürliche Atome können aufgrund ihres geringen Dipolmoments nur sehr schwach an sich ausbreitende Photonen gekoppelt werden und erreichen bestenfalls, dass 50% der emittierten Strahlung in den Wellenleiter eingekoppelt wird [4]. Künstliche Atome, wie z.B. Quantenpunkte, können sehr effizient gekoppelt werden, so dass über 99% der Emission in den Wellenleiter eingekoppelt werden [5] und haben eine hohe technische Variabilität [6], leiden aber unter inhomogenen spektralen Linienverbreiterungen, was es sehr schwierig macht, mehr als zwei resonante Emitter zu haben [7]. Supraleitende Qubits werden in der Regel durch einen nichtlinearen Josephson-Kontakt in einem elektrischen Schaltkreis realisiert, um einen anharmonischen Oszillator zu erhalten, der die Rolle eines künstlichen Atoms übernimmt. Supraleitende Qubits können Kopplungseffizienzen von 99,9% erreichen [9], sie können zuverlässig als Kollektiv von Qubits hergestellt werden [10], und sie können so konstruiert werden, dass ihre Resonanzfrequenz lokal durch magnetischen Fluss gesteuert werden kann [11].

Die technischen Möglichkeiten supraleitender Qubits führten zur Beobachtung eines breiten Spektrums quantenoptischer Phänomene wie dem Mollow-Triplett [12, 13], ultrastarker Kopplung [14], Erzeugung von nicht-klassischen photonischen Zuständen [15, 16], Qubit-Photon gebundene Zustände [17], topologische Physik [18] sowie kollektive Effekte [9, 19]. Trotz des Erfolgs der Quantenelektrodynamik mit supraleitenden Wellenleitern bleibt eine von vielen wichtigen Fragen unbeantwortet: Wie gültig ist die Zwei-Niveau-Näherung, insbesondere für die Beschreibung kollektiver Zustände jenseits der Betrachtung einzelner Anregungen [1]?

Kollektive Zustände treten in der Wellenleiter-QED auf Grunde von Wechselwirkungen und Interferenzeffekten in einem Ensemble von Emittern auf [4]. Die relative Phase zwischen den einzelnen Emittern bestimmt, ob der kollektive Zustand eine sub- oder superradiante Zerfallsrate erhält, d.h. ob er zu einem dunklen oder hellen Zustand wird. Kollektive helle Zustände wurden in verschiedenen Wellenleiter-QED Systemen gemessen [7, 19, 21–23], während dunkle Zustände nur in supraleitenden Wellenleiter-QED spektroskopisch beobachtet wurden [10, 19]. Vor kurzem wurde ein dunkler Multi-Qubit-Zustand zum Erzeugen eines Mikrowellenresonators verwendet [9], aber eine vollständige kohärente Kontrolle des dunklen Zustands wurde nicht erreicht. Die Schwierigkeit ergibt sich aus der Haupteigenschaft des dunklen Zustands - er entkoppelt von der elektromagnetischen Umgebung des Wellenleiters. Die vollständige Kontrolle bietet die Möglichkeit, eine Quantencomputing- und Quantensimulations-Plattform zu realisieren, die dekohärenzfreie Unterräume verwendet [24, 25]. Quantencomputing erfordert die genaue Kenntnis der Energie- und Zerfallscharakteristiken der kollektiven Vielzustandssysteme jenseits der einzelnen Anregungen, um versehentliches Verlassen des Berechnungsunterraumes zu vermeiden. Die kohärente Kontrolle über den dunklen Zustand ermöglicht die Erforschung dieser höheren Anregungszustände und die Charakterisierung der Eigenschaften von Vielkörperzuständen.

Im Rahmen dieser Arbeit untersuche ich die Wechselwirkung zwischen vier supraleitenden Transmon-Qubits, die an eine gemeinsame Wellenleiter-Modenumgebung gekoppelt sind. Die Hybridisierung der Transmons führt zu kollektiven Zuständen, die stark von den Kopplungsparametern und Transmon-Anharmonizitäten abhängen. Die paarweise Anordnung führt zu einer direkten Kopplung, die durch die Kapazität zwischen den metallischen Transmon-Pads verursacht wird. Jedes Paar erhält einen lokalen dunklen Zustand im Zustandsraum der mittels einer Anregung erreicht werden kann. Der Dunkelzustand ist langlebig und kann als Ressource für die Kohärenz in einem offenen Quantensystem, wie der Wellenleiterumgebung, dienen. Die Wechselwirkung, die vom Wellenleiter vermittelt wird, hängt von der effektiven Distanz ab und verursacht kohärente Austauschkopplung oder kollektive Dissipation. In dieser Konfiguration konzentrieren wir uns auf das kollektive Verhalten und stimmen die Qubits auf eine Frequenz ab, die einem Abstand von einer halben Wellenlänge entspricht. Der entstehende dunkle Zustand ist nichtlokal und wird von den entfernten Qubits geteilt. Die Phase eines Antriebs muss mit der Phase der Übergänge übereinstimmen, die er ansteuern soll. Wir zeigen, dass zwei lokale Ports an den Qubit-Paaren verwendet werden können, um die Antriebsphase an die Symmetrie der hellen und dunklen Zustände anzupassen, und zeigen, dass der dunkle Zustand als Ausgangspunkt für die Erforschung der höheren Energieniveaus des gekoppelten Transmon-Systems dient.

Die Dissertation ist wie folgt gegliedert: Die Einleitung enthält die grundlegenden Konzepte der Schaltkreis-Quantenelektrodynamik und eine Beschreibung der Hohlraum- und Wellenleiter-Quantenelektrodynamik. Das zweite Kapitel fasst die Theorie für Wellenleiter zusammen, die notwendig ist, um die experimentellen Ergebnisse zu verstehen. Viele Ergebnisse können bereits durch QuTiP [26]-Simulationen reproduziert werden. Eine genaue Vorhersage des Energiespektrums, der Zerfallsraten der Zustände und der Symmetrien in Bezug auf eine gegebene Modenumgebung wird jedoch durch numerische Simulationen des paarweisen Transmon-Aufbaus erreicht. Im dritten Kapitel wird ein praktischer Ansatz für den Entwurf und die Entwicklung eines Wellenleiter-QED-Aufbaus vorgestellt und das Messverfahren kurz diskutiert. Im vierten Kapitel werden die Ergebnisse der durchgeführten Experimente vorgestellt und diskutiert, während im Schlusswort die Bedeutung der Ergebnisse im weiteren Sinne erläutert wird, um die Arbeit abzuschließen.

Contents

CHAPTER 1

Superconducting Quantum Circuits

More than a hundred years after the discovery of superconductivity in 1911 by Heike Kamerlingh Onnes [27], superconducting circuits have evolved into a tool to study the interactions between microwaves and electrical circuit elements. More recently, superconducting circuits have been developed into one of the most promising technologies for building a quantum computer. One of the building blocks in circuit quantum electrodynamics is the LC harmonic oscillator, which is realized by arranging an inductor and a capacitor in a parallel configuration. There are many physical realizations of such a resonant circuit, which has become one of the workhorses in quantum information technology with superconducting devices. Therefore, we quantize the circuit in the first section in order to describe the electrical circuit in the quantum regime. However, the harmonic nature prevents the addressing of individual transitions, which is necessary to define a qubit. The Josephson junction makes it possible to transform a harmonic oscillator into an anharmonic system, allowing to selectively address individual transitions. One of the most common superconducting qubits and the heart of our experiments is the transmon qubit [11]. In the field of circuit quantum electrodynamics (QED) the transmon is then usually coupled to a harmonic oscillator to properly isolate it from the environment but keeping an access channel for coherent control. The last two sections focus on the main differences between coupling a qubit to a resonant circuit or an environment that has a continuous mode spectrum like a waveguide.

1.1 The Quantum Harmonic Oscillator

An inductor L and a capacitor C form a harmonic oscillator where the stored energy is alternating between the magnetic field of the inductive element and the electrical field of the capacitor. The lumped-element representation of the harmonic oscillator circuit model, realized by a parallel configuration of an inductance and a capacitance is shown in Fig. 1.1a. They are most commonly realized by the physical implementations shown in Fig. 1.1b and c, where the resonant circuit can either be integrated on-chip or realized by a metallic box. On resonance, the electric and the magnetic field oscillate at the natural resonance frequency $\omega_r = 1/\sqrt{LC}$. The discrete resonant modes of the harmonic oscillator simplify the description of the electromagnetic environment, such that it often serves as an example how to quantize an electrical circuit. The LC circuit model can be used to describe electrical circuits with quantum operators by deriving the Hamiltonian according to Ref. [29]. In the node represen-

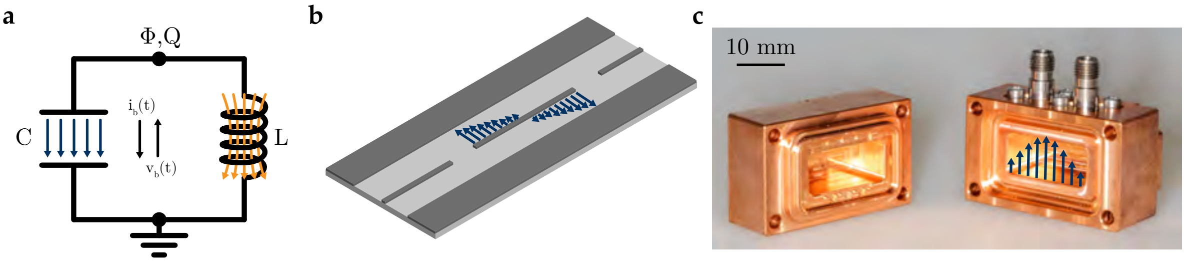

Figure 1.1: Microwave harmonic oscillator. **a** The schematic shows a parallel arrangement of a capacitor C and an inductor L. Drawing the circuit diagram of a harmonic oscillator unifies the descriptions of the physical implementations. **b** A planar $\lambda/2$ resonator is realized by interrupting the transmission line at two points. The sudden impedance change causes the signal to reflect at the ends and provides the boundary conditions for a standing wave. The length of the middle strip determines the resonance frequency. **c** Another way to create an harmonic oscillator is to use the resonant mode of a 3D cavity. The fields in 3D cavities are in the enclosed volume of a conductive material where the inner dimensions determine the resonance frequencies. Superconducting materials and geometric optimizations led to single photon lifetimes up to 10 ms [28].

tation, the generalized node flux Φ and node charge Q are given by the branch voltage v_b and branch current i_b through a circuit element

$$\begin{aligned} \Phi_b(t) &= \int_{-\infty}^{t} v_b\left(t'\right) dt', \\ Q_b(t) &= \int_{-\infty}^{t} i_b\left(t'\right) dt'. \end{aligned} \tag{1.1}$$

The energy of the linear capacitive and inductive elements is given by

$$\begin{aligned} E_C &= \frac{1}{2C}(Q - Q_{\text{offset}})^2 \\ E_L &= \frac{1}{2L}(\Phi - \Phi_{\text{offset}})^2. \end{aligned} \tag{1.2}$$

Setting Q_{offset} and Φ_{offset} to zero at the ground node and promoting the classical variables to quantum operators $\Phi \longrightarrow \hat{\Phi}$, $Q \longrightarrow \hat{Q}$ and $H \longrightarrow \hat{H}$ allows us to write down the Hamiltonian of the LC harmonic oscillator

$$H = \frac{\hat{Q}^2}{2C} + \frac{\hat{\Phi}^2}{2L}. \tag{1.3}$$

The node charge becomes the conjugate variable of the node flux, similar to the momentum and position coordinate of the mechanical analogue. This means that we can relate them by a Fourier transformation and they have to obey the Heisenberg uncertainty principle. Therefore, the two operators also obey the canonical commutation relation

$$\left[\hat{\Phi}, \hat{Q}\right] = i\hbar \tag{1.4}$$

To find the energy eigenstates of the circuit the conjugate variables are expressed with the creation $\hat{a}^\dagger$ and annihilation operators $\hat{a}$

$$\hat{\Phi} = \Phi_{\text{ZPF}}\left(\hat{a} + \hat{a}^\dagger\right), \quad \hat{Q} = -iQ_{\text{ZPF}}\left(\hat{a} - \hat{a}^\dagger\right), \tag{1.5}$$

with the zero-point fluctuations of the flux and charge at the node

$$\Phi_{\rm ZPF} = \sqrt{\frac{\hbar Z_0}{2}}, \quad Q_{\rm ZPF} = \sqrt{\frac{\hbar}{2Z_0}}, \tag{1.6}$$

where the characteristic impedance of the circuit is $Z_0 = \sqrt{L/C}$. Changing the characteristic impedance of the circuit will decrease the vacuum fluctuations of one variable, whereas the other has to increase. For quantum circuits, the zero point fluctuation can reach macroscopic values and are a common tuning parameter for designing circuits [29]. The electromagnetic fields are created by the current flowing through the inductor and the charge on the capacitor plates. The creation and annihilation operators are closely related to the field amplitude operator for a single mode and obey the commutation relation

$$\left[\hat{a}, \hat{a}^\dagger\right] = 1. \tag{1.7}$$

Rewriting the Hamiltonian for the LC oscillator in Eq. (1.3), using the field operators yields the quantum harmonic oscillator Hamiltonian

$$\hat{H} = \hbar\omega_r \left(\hat{a}^\dagger \hat{a} + 1/2\right), \tag{1.8}$$

where the number operator $\hat{n} = \hat{a}^\dagger \hat{a}$ has a discrete eigenbasis (Fock basis) counting the number of elementary excitations in the circuit. They correspond to the number of photons in the electromagnetic field that reside in the oscillator. Neighboring energy levels are equidistantly separated by the resonance frequency ω_r of the circuit.

1.2 The Josephson Junction

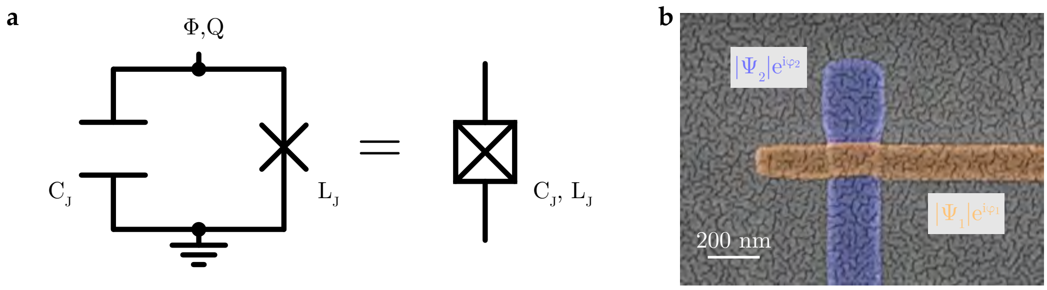

Figure 1.2: Josephson junction. a A capacitance and a non-linear inductive element (cross) represent the Josephson junction in the circuit model. As there is always a capacitance arising from the physical separation of two superconductors the inductance and capacitance are represented by one circuit element. **b** On the scanning electron microscope (SEM) picture, the blue colored superconductor is separated from the orange superconductor by a thin insulating barrier at their intersection. In this case, they are both aluminum wires separated by aluminum-oxide. The rectangular overlap effectively forms a capacitance between both metals and the finite Cooper pair tunneling probability results in a non-linear inductance, both captured in the circuit representation in **a**.

The key element for quantum information processing with microwave circuits is the Josephson junction, a non-linear and non-dissipative circuit element that arguably has been the workhorse for circuit QED experiments over the last two decades [30]. Conventional capacitors and inductors are purely linear and thus cannot provide non-linearity to the circuit, while conventional non-linear elements like CMOS transistors based on semiconducting materials are dissipative. However, there are efforts to utilize transistors in low loss circuits [31].

A realization of a Josephson junction, schematically shown in Fig. 1.2a, is depicted in Fig. 1.2b, where two strips of aluminum (orange and blue) are separated by a thin layer of aluminum-oxide. When cooled down below the critical temperature of aluminum, the superconducting wires and the tunnel barrier form a very low loss anharmonic oscillator with the capacitance arising from the geometry of the metallic wires and the non-linear inductance arising from the tunneling current through the oxide barrier. To form a qubit, the circuit is usually extended with additional linear elements.

The Josephson Equations

The dissipationless current that flows through a superconductor is called supercurrent. It can tunnel between two superconductors that are separated by a weak link, first described by Brian D. Josephson in 1962 [8]. The weak link that is used throughout this thesis consists of a superconductor-insulator-superconductor (S-I-S) junction, similar to the one depicted in Fig. 1.2. As the superconductors are spatially separated, the individual condensates might have different macroscopic wavefunctions with a characteristic complex phase and amplitude [32]. The difference in the phase of the two superconductors $\varphi = \varphi_2 - \varphi_1$ controls the tunneling of cooper pairs through the insulating layer, allowing the apparition of a supercurrent I. The critical current I_c is a parameter that depends on the utilized materials and the geometry of the Josephson junction. The critical current corresponds to the maximum absolute current, up to which Cooper pairs can tunnel from one side of the junction to the other while preserving superconductivity. For stronger currents the Josephson junction abruptly becomes normal conducting and behaves like an ohmic resistor. The relation between the current I and the phase difference φ between the two superconductors is the first Josephson equation

$$I = I_c \sin(\varphi). \tag{1.9}$$

The second Josephson equation describes the time evolution of the phase difference which results in a voltage drop V across the Josephson junction

$$\frac{\partial \varphi}{\partial t} = \frac{2e}{\hbar} V = \frac{2\pi}{\Phi_0} V, \tag{1.10}$$

where we introduced the reduced Planck constant $\hbar$ and the magnetic flux quantum $\Phi_0 = h/2e$ with the Planck constant h and the electron charge e. The inductance L can be calculated by taking the time derivative of the first Josephson equation and combining both Josephson equations

$$\begin{aligned} \frac{\partial I}{\partial \varphi} &= I_c \cos\varphi, \\ \frac{\partial I}{\partial t} &= I_c \cos\varphi \cdot \frac{2\pi}{\Phi_0} V. \end{aligned} \tag{1.11}$$

In analogy to Faraday's law of induction where the change of a current induces a voltage, we can use the relation $V = L\dot{I}$ to rewrite the inductance as

$$L(\varphi) = -\frac{\Phi_0}{2\pi I_c \cos\varphi} = \frac{L_J}{\cos\varphi}. \tag{1.12}$$

The Josephson inductance $L_J = \frac{\Phi_0}{2\pi I_c}$ and energy $E_J = \frac{\Phi_0}{2\pi} I_c$ are characteristic properties that can already be estimated from room temperature measurements by relating the resistance measurement to the critical current, see Sec. 3.3.1. The equation can be rewritten with the definition of the branch flux in Eq. (1.1), such that with $\varphi(t) = \int dt' V(t') 2\pi/\Phi_0 = \frac{2\pi\Phi(t)}{\Phi_0}$ the inductance becomes

$$L(\Phi) = \frac{L_J}{\cos\left(2\pi\Phi/\Phi_0\right)}. \tag{1.13}$$

Hence, the Josephson junction enables the construction of non-linear circuit elements by introducing a cosine dependence in the inductance. To distinguish the Josephson inductance from the linear inductance it is usually represented by a cross in the circuit diagram, shown in Fig. 1.2. In addition to the inductive part, the Hamiltonian of a Josephson junction must also contain the linear capacitive term C_J arising from the physical proximity of the metallic electrodes. The inductive energy that is stored in a Josephson junction can be written as [33]

$$E(\Phi) = -E_J \cos\frac{\Phi 2\pi}{\Phi_0}. \tag{1.14}$$

Using the definition of the charging energy $E_C = \frac{e^2}{2C_J}$ in Eq. (1.2), the normalized charge operator $\hat{N} = \frac{\hat{Q}}{2e}$ and the phase operator $\hat{\varphi} = \hat{\Phi}\frac{2\pi}{\Phi_0}$, the Hamiltonian of the Josephson junction reads

$$\hat{H} = 4E_C\hat{N}^2 - E_J \cos\hat{\varphi}. \tag{1.15}$$

From this Hamiltonian we can see that the energy spectrum of the Josephson junction is not harmonic, but will have corrections when expanding the cosine term. For small phase fluctuations across the junction the quadratic term φ^2 governs the linear behavior whereas the quartic term φ^4 deforms the parabolic shape of the energy potential. The Josephson junction is a dissipationless inductor and provides enough non-linearity, that causes a non-equidistant spacing of the energy levels of an otherwise harmonic oscillator. It enables the design of various qubit realizations by choosing the corresponding inductance and capacitance parameters, as well as the amount of non-linearity.

1.3 The Transmon Qubit

As seen in the last chapter, when the linear inductor of a harmonic LC-oscillator is replaced with a Josephson junction, the energy spectrum is changed. The cosine term of the inductive energy that arises from the tunneling probability of the Cooper pairs through the insulating oxide barrier changes the level spacing such that the transition frequencies between the different states are not equidistantly spaced. If the transitions are resolved, meaning they have sufficiently narrow linewidths, then they are individually distinguishable. The nonlinear engineering capabilities offered by the Josephson element, along with the ability to design low-loss circuits, are being used to develop various types of superconducting artificial atoms [34]. The anharmonic potential allows the addressing of two energy levels from the multi-level system

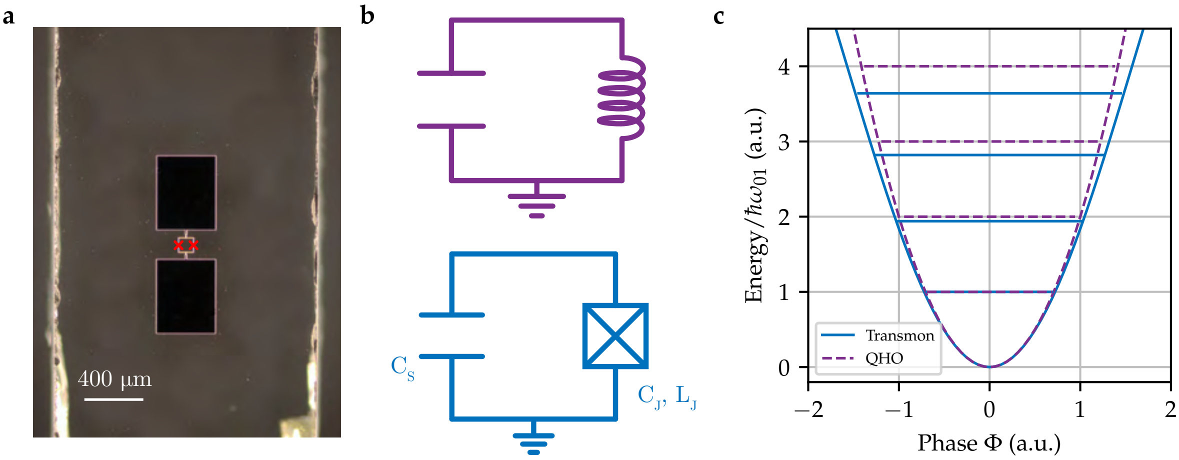

Figure 1.3: The transmon qubit. **a** Optical image of a 3D transmon, used in rectangular cavities and waveguides. The large metallic pads are used to couple strongly to the electromagnetic field of the environment and to provide a shunt capacitance C_S, protecting the transmon against charge noise. Two Josephson junctions, indicated by the red crosses, provide the non-linearity, while the loop geometry realizes a SQUID, enabling a the possibility to tune the resonance frequency of the transmon via an external magnetic field. **b** The circuit diagram of the quantum harmonic oscillator (purple) is slightly modified for the transmon (blue) by replacing the linear inductor with a Josephson junction. **c** The energy potential and level spacing differ because of the non-linear Josephson inductance in the transmon Hamiltonian. Expanding the cosine term for small phase differences results in a quadratic term $\hat{\varphi}^2$ that would give the parabolic shape of the harmonic oscillator. The quartic correction $\hat{\varphi}^4$ widens the quantum harmonic oscillator potential and splits the energy levels to have non-equidistant spacing. For well resolved spectral lines this means that individual levels can independently be populated.

to form a qubit, where usually the ground and first excited state are used as computational basis states. Shunting the Josephson junction with a capacitor C_S, like the metallic pads in Fig. 1.3a, results in a total capacitance $C_\Sigma = C_J + C_S$. By taking into account offset charges $N_g = \frac{Q_g}{2e}$, the quantized Hamiltonian can be written analogously to the Josephson junction as

$$\begin{aligned}\hat{H} =& \frac{(\hat{Q} - Q_g)^2}{2C_\Sigma} - E_J \cos\left(2\pi\hat{\Phi}/\Phi_0\right) \\ =& 4E_C(\hat{N} - N_g)^2 - E_J \cos\hat{\varphi}.\end{aligned} \tag{1.16}$$

The most commonly used superconducting qubit is the transmon [11] where the circuit capacitance is increased such that the Josephson energy dominates over the charging energy $E_J/E_C \gg 1$. This has the effect that offset gate charges n_g have negligible impact on the transition frequency, that can be caused by charge fluctuations in the circuit [11] and ultimately lead to dephasing. The drawback for increasing the coherence properties this way is the reduction of the anharmonicity. The anharmonicity $\alpha = E_{12} - E_{01}$ is defined as the energy difference between the fundamental transition $|0\rangle$-$|1\rangle$ and the next higher transition $|1\rangle$-$|2\rangle$. If the anharmonicity gets too small, leakage into higher states becomes a problem when trying to control the transition from the ground into the first excited state with fast pulses. Usually the transmon is operated in a regime where $E_J/E_C \approx 40 - 100$ and $\alpha/h = -E_C/h \approx 100 - 400\,\text{MHz}$, such that small charge fluctuations do not play a role and control can still be performed reasonably fast compared to the transmon coherence time. Typical pulse lengths for qubit control are on the order of tens of nanoseconds, while the transmon coherence time can reach values exceeding 100 μs. Turning back to the Hamiltonian and considering the fact that the phase fluctuations across the junction are small, as well as neglecting constant offsets, we can write down the expansion of the cosine term and truncate the series at the quartic exponent

$$\hat{H} \approx 4E_C\hat{N}^2 + \frac{E_J}{2!}\hat{\varphi}^2 - \frac{E_J}{4!}\hat{\varphi}^4. \tag{1.17}$$

Following the same procedure as for the harmonic oscillator in Sec. 1.1, introducing bosonic creation and annihilation operators $\hat{b}^\dagger$, $\hat{b}$ allows then to express the phase and charge operators as

$$\begin{aligned} \hat{\varphi} &= \left(\frac{2E_C}{E_J}\right)^{1/4}\left(\hat{b}^\dagger + \hat{b}\right), \\ \hat{N} &= \frac{i}{2}\left(\frac{E_J}{2E_C}\right)^{1/4}\left(\hat{b}^\dagger - \hat{b}\right). \end{aligned} \tag{1.18}$$

This representation illustrates nicely, that fluctuations of the phase $\hat{\varphi}$ are smaller for large ratios E_J/E_C, whereas the charge fluctuations will be large. Thus, the charge degree of freedom is highly delocalized over the large capacitor and renders the transmon insensitive to charge fluctuations, which rapidly led to improved coherence times of superconducting qubits. The creation and annihilation operators can be used to rewrite the Hamiltonian, where the rotating-wave approximation keeps only energy conserving terms

$$\hat{H} \approx \left(\sqrt{8E_JE_C} - E_C\right)\hat{b}^\dagger\hat{b} - \frac{E_C}{2}\hat{b}^\dagger\hat{b}^\dagger\hat{b}\hat{b}. \tag{1.19}$$

The resonance frequency of the fundamental transmon transition $\omega_{01} = \left(\sqrt{8E_JE_C} - E_C\right)/\hbar$ differs to the transition frequency from the first to the second excited state by the anharmonicity $E_C \sim \alpha$.

Flux-Tuning

Two Josephson junction embedded in a loop form the direct current superconducting quantum interference device (DC SQUID). Implemented in a transmon circuit it leads to the ability to tune its resonance frequency. For two identical junctions in a ring that is penetrated by an external magnetic flux Φ the two supercurrents I_a and I_b can interfere to have the total supercurrent

$$I_{\mathrm{tot}} = I_a + I_b = 2I_c \sin\left(\frac{\varphi_a + \varphi_b}{2}\right)\cos\left(\frac{\varphi_a - \varphi_b}{2}\right). \tag{1.20}$$

Here, we already introduced the phase differences φ_a and φ_b between the superconducting electrodes for both Josephson junctions a and b respectively. Integrating the gauge invariant second London equation [33] along a path around the SQUID loop yields the magnetic flux Φ that penetrates the loop

$$\varphi_a - \varphi_b = \frac{2\pi\Phi}{\Phi_0}. \tag{1.21}$$

The total current through the SQUID is then given by

$$I_{\mathrm{tot}} = I_{\mathrm{c,eff}} \sin\left(\varphi_{\mathrm{b}} + \frac{\pi\Phi}{\Phi_0}\right), \tag{1.22}$$

where the effective critical current $I_{\mathrm{c,eff}} = 2I_{\mathrm{c}}\cos\left(\frac{\pi\Phi}{\Phi_0}\right)$ has a strong dependence on external magnetic flux. If both Josephson junctions have different critical currents $I_{c,a}$ and $I_{c,b}$, the total critical current $I_{\mathrm{c,\,eff}}$ is then distributed over the junctions as

$$I_{c,\mathrm{eff}} = (I_{\mathrm{c,a}} + I_{\mathrm{c,b}})\cos\left(\frac{\pi\Phi}{\Phi_0}\right)\sqrt{1 + d^2\tan^2\left(\frac{\pi\Phi}{\Phi_0}\right)}. \tag{1.23}$$

The difference of the junction critical current is given by the ratio $d = \frac{I_{\mathrm{c,a}}-I_{\mathrm{c,b}}}{I_{\mathrm{c,a}}+I_{\mathrm{c,b}}}$ and effectively sets a bound on the lowest achievable critical current. The Josephson energy of the transmon can then be tuned according to

$$E_J(\Phi) = E_{J\Sigma}\cos\left(\frac{\pi\Phi}{\Phi_0}\right)\sqrt{1 + d^2\tan^2\left(\frac{\pi\Phi}{\Phi_0}\right)}, \tag{1.24}$$

in order to change its resonance frequency $\omega_{01}(\Phi) = \left(\sqrt{8E_J(\Phi)E_C} - E_C\right)/\hbar$. More details on designing the transmon parameters can be found in Sec. 3.3.1.

1.4 Bloch-Sphere Representation

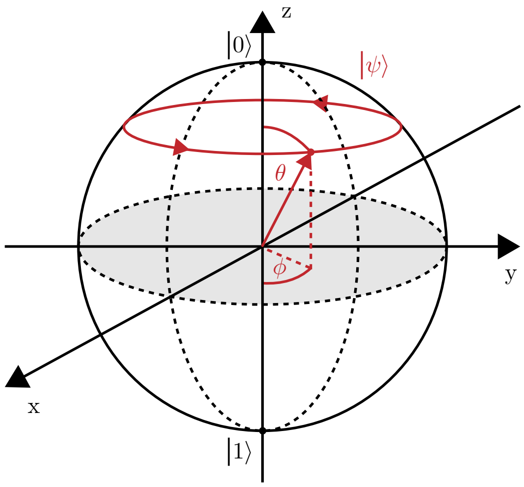

Figure 1.4: Bloch sphere representation of a qubit. A pure qubit state is represented by a point on the surface of the sphere, while a mixed state is located inside the sphere. The vector that points from the center to any point inside or onto the surface of the sphere is called the Bloch vector, which is defined by the angels ϕ and θ. The logical qubit basis states $|0\rangle$ and $|1\rangle$ (also often $|g\rangle$ and $|e\rangle$) are the poles of the Bloch sphere with eigenvectors of the Pauli matrix σ_z. The fact that they are the basis states implies $|\langle\psi|\psi\rangle|^2 = 1$, which gives the radius of the sphere. In the Schroedinger picture the qubit vector precesses around the z-axis with frequency ω_{01}.

Quantum information often uses the Bloch sphere to represent the logical state of a qubit $|0\rangle$ and $|1\rangle$. The Hilbert space of a multi-level system, like a transmon, is then reduced to the ground and first excited state. The Bloch vector describes a quantum state $|\psi\rangle = \alpha|0\rangle + \beta|1\rangle$ of this subsystem. A pure quantum state has unit length, such that $|\alpha|^2 + |\beta|^2 = 1$, which on the Bloch sphere corresponds to a vector connecting the center to any point on the surface. The z-axis connects the north and south poles of the qubit globe and, as the states $|0\rangle$ and $|1\rangle$ of the qubit eigenbasis are located there, is called the longitudinal axis [35]. The x and y axes are called the transverse axes. Using the spherical coordinate system the state vector can be mapped onto the polar $0 < \theta < \pi$ and azimuthal angle $0 < \phi < 2\pi$

$$|\psi\rangle = \cos\frac{\theta}{2}|0\rangle + e^{i\phi}\sin\frac{\theta}{2}|1\rangle\,, \tag{1.25}$$

where θ is now the mixing angle of ground and excited state and ϕ is the phase of the qubit state. The time evolution of a pure state can be described by the time evolution operator $\hat{U}(t) = e^{i\hat{H}t} = e^{i\omega_{01}\hat{\sigma}_z t/2}$, where $\hat{H}$ is the time-independent qubit Hamiltonian, quantized along the z-axis, with basis states $|0\rangle$ and $|1\rangle$. Applying the time transformation to the state $|\psi\rangle$ in (1.25) yields the time-dependent qubit state in the Schroedinger picture

$$\begin{aligned} |\psi(t)\rangle &= e^{-i\omega_{01}\hat{\sigma}_z t/2}|\psi\rangle \\ &= \cos\left(\frac{\theta}{2}\right)|0\rangle + \sin\left(\frac{\theta}{2}\right)e^{i(\phi-\omega_{01}t)}|1\rangle. \end{aligned} \tag{1.26}$$

The ground state $|0\rangle$ and excited state $|0\rangle$ are eigenstates of the Pauli matrix $\hat{\sigma}_\mathrm{z}$, such that $\hat{\sigma}_\mathrm{z}|0\rangle = -|0\rangle$ and $\hat{\sigma}_\mathrm{z}|1\rangle = |1\rangle$. The state $|\psi(t)\rangle$ is precessing around the quantization axis (z-axis) with the transition frequency of the qubit. In particular, the phase is evolving in time with constant angular frequency ω_{01}.

Qubit Driving

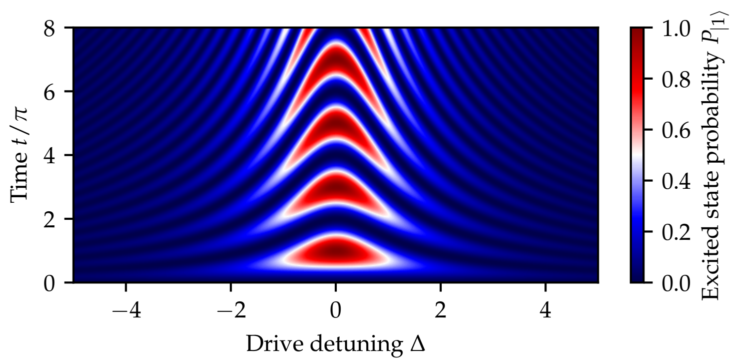

Figure 1.5: Rabi oscillations. The time evolution of a qubit that is driven with amplitude $\Omega = 1$ shows oscillations between the states $|0\rangle$ and $|1\rangle$, see Eq. (1.31). The probability of finding the qubit in the excited state for a resonant drive $\Delta = \omega_{01} - \omega = 0$ oscillates between 0 and 1 while a detuned drive $\Delta \neq 0$ cannot reach 1 anymore. However, for an off-resonant drive the excited state population can be increased when the transition is driven with a larger drive amplitude.

The fundamental transition frequencies of transmon qubits are usually in the GHz regime, thus can be driven by a microwave signal. The time evolution of a qubit state $|\psi(t)\rangle$ in the Schroedinger picture is given by the Hamiltonian $\hat{H}$ acting on the initial state $|\psi_0\rangle$

$$|\psi(t)\rangle = e^{i\hat{H}(t-t_0)}|\psi_0\rangle \tag{1.27}$$

A drive with amplitude Ω couples transversally and induces transitions between the ground and the excited state. In the driven qubit Hamiltonian this drive is modeled by a $\hat{\sigma}_x$ Pauli operator

$$H = \frac{\hbar\omega_{01}}{2}\sigma_{\mathrm{z}} + \hbar\Omega\cos(\omega t + \varphi)\sigma_{\mathrm{x}}, \tag{1.28}$$

with a possible phase offset φ, now omitting the operator hat notation for simplicity. The first term describes the precession around the z-axis of the Bloch sphere at the qubit frequency ω_{01} for an initial state $|\psi_0\rangle$. The transformation $\widetilde{H} = U(t)HU^\dagger(t) - i\hbar U(t)\partial_t U^\dagger(t)$ with $U(t) = e^{i\omega\sigma_{\mathrm{z}}t/2}$ takes the Hamiltonian into the rotating frame of the drive, such that it reads

$$\widetilde{H} \approx h\frac{\Delta}{2}\sigma_{\mathrm{z}} + h\frac{\Omega}{2}\left(\cos(\varphi)\sigma_{\mathrm{x}} + \sin(\varphi)\sigma_{\mathrm{y}}\right), \tag{1.29}$$

where $\Delta = \omega_{01} - \omega$ is the detuning between the qubit frequency ω_{01} and the drive frequency ω. We also applied the rotating wave approximation, that neglects fast rotating terms of the form $e^{2i\omega t}$, such that we can see that the microwave drive induces a rotation around an axis in the xy-plane of the Bloch sphere. By switching to the Schroedinger picture we remove the time dependence of the operators such that we can simplify the Hamiltonian for $\varphi = 0$, yielding

$$\widetilde{H} = h\frac{\Delta}{2}\sigma_{\mathrm{z}} + h\frac{\Omega}{2}\sigma_{\mathrm{x}}. \tag{1.30}$$

The probability of finding the qubit in the excited state is given by $P_1(t) = |\langle 1 \mid \psi(t)\rangle|^2$. Solving the Schroedinger equation with the simplified driven qubit Hamiltonian $\widetilde{H}$, we obtain [36]

$$P_{|1\rangle} = |\langle 1 \mid \psi(t)\rangle|^2 = \frac{\Omega^2}{\Omega^2 + \Delta^2}\sin^2\left(\frac{\sqrt{\Omega^2 + \Delta^2}}{2}t\right). \tag{1.31}$$

A resonant microwave drive $\Delta = \omega_{01} - \omega = 0$ will periodically swap the probability to find the qubit in the excited state between zero and one, which can be observed in Fig. 1.5. This periodic oscillation is called Rabi cycle. It is usually one of the first experiments that is carried out with the time-resolved measurement setup as it allows us to verify that the qubit can be coherently flipped. We can see that a detuned pulse is not able to reach 100% excited state population.

We can also re-write the drive Hamiltonian in the rotating frame by taking into account the experimental pulse generation. For this we define the input signals of an IQ-mixer as $I = \cos(\phi)$ the in-phase component and $Q = \sin(\phi)$ the out-of-phase component. By using a similar procedure we can write down the Hamiltonian for a drive that is resonant with the qubit [35]

$$\widetilde{H} = -\frac{\Omega}{2}(I\sigma_x + Q\sigma_y). \tag{1.32}$$

This shows that if we create a pulse through the I component of the mixer such that we consider it an in-phase drive we rotate the Bloch vector around the x-axis, while a signal through Q creates an out-of-phase signal and therefore rotations around the y-axis.

1.5 Open Quantum Systems

For superconducting qubits the various decoherence mechanisms play an important role for the goal of building a quantum computer. Thus, there are many research areas that try to address the problem from different angles, summarized in Ref. [35]. These areas include the fabrication process that always introduces unwanted contamination and material defects [37, 38], new qubit designs that aim to reduce the susceptibility to certain noise sources, as well as improving cryogenic wiring [39] and instrument control.

In a closed quantum system we can fully predict the state evolution of the qubit. Similar to the last section we only need to know the initial state and the Hamiltonian that describes the system dynamics. In open systems the quantum states are constantly exposed to noise sources that lead to decoherence and destroy the fragile quantum information. Hence, the ideal quantum state as the representation and only considering unitary evolution is not sufficient. The density matrix ρ allows for statistical mixtures and can therefore describe a quantum state that is affected by noise, thus does not lie on the surface of the Bloch sphere

$$\rho = \sum_i p_i \left|\psi_i\right\rangle \left\langle\psi_i\right| \quad \text{with} \quad \sum_i p_i = 1 \tag{1.33}$$

For low temperatures $k_B T << \omega_{01}\hbar$, we can neglect thermal excitation σ_+. With the free qubit Hamiltonian $\hat{H} = \hbar\omega_{01}\hat{\sigma}_z/2$, the time evolution of a quantum state ρ coupled to a dissipative bath can be modeled by a Lindblad master equation [34, 40, 41]

$$\dot{\rho} = -i\left[\hat{H}, \rho\right] + \kappa\mathcal{D}[\hat{\sigma}_-]\rho + 2\gamma_\phi\mathcal{D}\left[(\hat{\sigma}_z + 1)/2\right]\rho. \tag{1.34}$$

In the master equation we used the dissipators $\mathcal{D}$ for operator $\hat{A}$ that are defined as

$$\mathcal{D}[\hat{A}]\rho = \hat{A}\rho\hat{A}^\dagger - \frac{1}{2}\left\{\hat{A}^\dagger\hat{A}, \rho\right\}. \tag{1.35}$$

Each dissipator accounts for a decoherence channel described by the collapse operators $\hat{A}$ and corresponding decoherence rates. The collapse operators for transversal noise are $\sigma_+ = \frac{1}{2}\left(\sigma_x - i\sigma_y\right)$ and $\sigma_- = \frac{1}{2}\left(\sigma_x + i\sigma_y\right)$ and for longitudinal noise σ_z. We also introduced the longitudinal relaxation rate κ of the qubit, which is caused by energy exchange with the environment. In the absence of thermal driving, the relaxation rate κ describes the energy decay from the excited state of the qubit $|1\rangle$ to the ground state $|0\rangle$ [42]. The characteristic time scale for the energy relaxation is the T_1 time

$$T_1 = \frac{1}{\Gamma_1} \simeq \frac{1}{\gamma_\downarrow} \simeq \frac{1}{\kappa}. \tag{1.36}$$

The transverse relaxation rate Γ is associated with the coherence time T_2 that quantifies the characteristic lifetime of coherent superpositions. It includes contributions from pure dephasing γ_ϕ as well as energy relaxation $\kappa = \Gamma_1$

$$T_2 = \frac{1}{\Gamma} = \left(\frac{\Gamma_1}{2} + \gamma_\phi\right)^{-1} \tag{1.37}$$

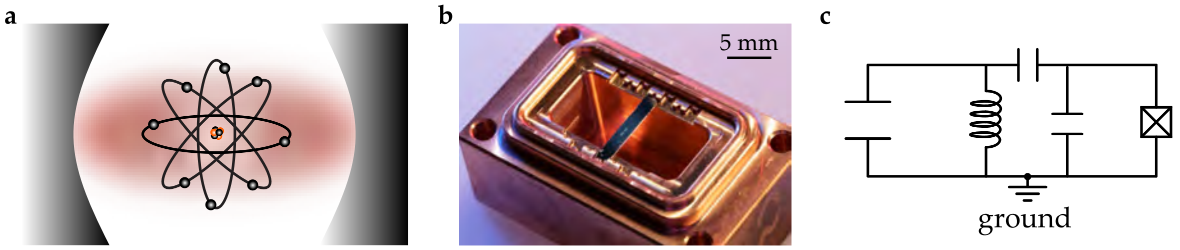

Figure 1.6: Cavity quantum electrodynamics. a Natural atoms interact with the photonic mode of a mirror cavity. The interaction between the atom and the photon is enhanced by each round trip of the photon that is reflected from the cavity walls. **b** The equivalent system in the microwave regime consists of a resonator and a superconducting qubit. **c** The lumped-element representation shows the harmonic oscillator with a linear inductor and capacitor, while the qubit inductance is dominated by the Josephson junction. The coupling is realized by a capacitance between the separate circuits.

1.5.1 Cavity Quantum Electrodynamics

Quantum electrodynamics was introduced by P.A.M Dirac in 1927 [43] and describes the interaction between electromagnetic radiation and matter. Since then the theory was further developed by S-I Tomonaga [44], J. Schwinger [45] and R.P. Feynman[46] for which they were awarded the physics Nobel prize in 1965. However, from an experimental point of view, it seemed difficult to observe QED effects at the level of single excitations because the interaction between individual atoms and photons are too weak. For a field in 3D space, the large mode volume in combination with the small atomic dipole moment imposed an obstacle on the experimental field that took until the late 1980s to be solved by the emergence of cavity quantum electrodynamics [47].

Cavity quantum electrodynamics studies the fundamental interaction of a single light mode and an atom. By placing the atom inside an optical cavity that typically consists of two mirrors, the spontaneous emission can be reduced or enhanced. The setup is schematically shown in Fig. 1.6a. Effectively, the photon is reflected back and forth from the cavity mirrors such that it passes the atom many times and enhances the interaction probability. The circuit analogue to a natural atom trapped between two mirrors is realized by placing a superconducting qubit, such as a transmon into a metallic cavity, shown in Fig. 1.6b or by integrating both constituents into an on-chip circuit. The metallic structures give rise to a capacitive coupling between the transmon and the cavity or on-chip resonator, such that we can absorb both realizations of Fig. 1.6a & b into the circuit representation in Fig. 1.6c. The resonator is described by its frequency ω_r, the root mean square voltage V_{rms} and the bosonic creation and annihilation operators $\hat{b}, \hat{b}^\dagger$, such that the Hamiltonian of the coupled system is given by [11]

$$\hat{H} = 4E_{\mathrm{C}}\left(\hat{N} - N_{\mathrm{g}}\right)^2 - E_{\mathrm{J}}\cos(\hat{\varphi}) + \hbar\omega_{\mathrm{r}}\hat{b}^\dagger\hat{b} + \hat{d}V_{\mathrm{rms}}\left(\hat{b} + \hat{b}^\dagger\right). \tag{1.38}$$

The first two terms describe the transmon, similar to Eq. (1.16) from Sec. 1.3 and the second term the cavity, derived in Sec. 1.1. The last term describes the interaction between the qubit dipole operator $\hat{d} = 2eC_c\hat{N}/C_\Sigma$ and the resonator field. By introducing the matrix elements of the coupling strength $\hbar g_{ij} = d_{ij} V_{\mathrm{rms}}$ with $d_{ij} = 2eC_{\mathrm{c}}/C_{\Sigma}\langle i|\hat{N}|j\rangle$ we can write the Hamiltonian in the basis of the uncoupled transmon eigenstates $|i\rangle$

$$\hat{H}/\hbar = \sum_j \omega_j |j\rangle \langle j| + \omega_{\mathrm{r}} \hat{b}^\dagger \hat{b} + \sum_{i,j} g_{ij} |i\rangle \langle j| \left(\hat{b} + \hat{b}^\dagger\right). \tag{1.39}$$

For large enough ratios of $E_{\mathrm{J}}/E_{\mathrm{C}}$ we find that only nearest neighbor coupling is relevant which allows us to truncate the higher states of the transmon and reduce the description to that of a two-level system. If the qubit-cavity coupling rate is significantly smaller than the transition frequencies of qubit and cavity, i.e. $g_{01} >> \omega_{01}, \omega_r$ the rotating wave approximation can be applied to eliminate the counter-rotating terms $\hat{\sigma}_+\hat{a}^\dagger$, $\hat{\sigma}_-\hat{a}$ describing the simultaneous excitation or deexcitation of both the transmon and the resonator. The result is the effective Jaynes-Cummings Hamiltonian [48, 49]

$$\hat{H}_{JC} = \frac{\hbar\omega_{01}}{2}\hat{\sigma}_{\mathrm{z}} + \hbar\omega_{\mathrm{r}}\hat{b}^\dagger\hat{b} + \hbar g\left(\hat{b}\hat{\sigma}_+ + \hat{b}^\dagger\hat{\sigma}_-\right). \tag{1.40}$$

When the qubit and the resonator are resonant, the last term describes the exchange of individual excitations between the qubit and cavity with rate g. However, the big advantage in superconducting systems is the fact that g can be so large that the system can be operated in the so-called dispersive regime, where the qubit is far detuned from the cavity frequency $\Delta = \omega_{01} - \omega_r \gg g$. State-of-the-art quantum computing approaches make use of the dispersive regime by reverse engineering the Purcell effect [50]. The reduced mode density at the qubit frequency compared to free space decreases the spontaneous emission rate of the superconducting qubit. This enables long qubit coherence times while it still remains accessible for manipulation by applying large amplitude control pulses that compensate for the reduced mode density. Furthermore, the strong coupling between the cavity and the qubit enables a readout of the qubit state only by measuring the cavity. The dispersive Jaynes-Cummings Hamiltonian is obtained by the Schrieffer-Wolf transformation and reads [51]

$$\hat{H}_{\mathrm{disp}} \approx \hbar\omega_r'\hat{b}^\dagger\hat{b} + \frac{\hbar\omega_{01}'}{2}\hat{\sigma}_z + \hbar\chi\hat{b}^\dagger\hat{b}\hat{\sigma}_z, \tag{1.41}$$

where the renormalized resonance frequencies are measured in the experiment for low power [34, 52]

$$\omega_r' = \omega_r - \frac{g^2}{\Delta - E_C/\hbar} \quad \text{and} \quad \omega_{01}' = \omega_{01} + \frac{g^2}{\Delta}, \tag{1.42}$$

with the bare qubit frequency ω_{01} and bare resonator frequency ω_r. The last term of Eq. (1.41) shows that the information about the qubit state is now encoded in the frequency of the resonator that undergoes a qubit state dependent shift $\chi\hat{b}^\dagger\hat{b}\hat{\sigma}_z$ with

$$\chi = -\frac{g^2 E_C/\hbar}{\Delta\left(\Delta - E_C/\hbar\right)}. \tag{1.43}$$

When probing the resonator with a microwave drive at the frequency that corresponds to the qubit being in state $|0\rangle$, the transmission or reflection will change when the qubit state changed to $|1\rangle$ because of the shifted resonance frequency of the resonator. This technique is enabled by the dispersive approximation and offers a way to read out the qubit state in a quantum non-demolition measurement, which means that the projected state of the qubit remains preserved.

1.5.2 Waveguide Quantum Electrodynamics

Observing QED effects for single atoms [53] or molecules [54] in three-dimensional (3D) space is usually difficult due to the spatial mode mismatch between incident and scattered waves, leading to imperfect interference [12]. An alternative platform for studying the interaction of light and matter is waveguide quantum electrodynamics (QED). Here, an atom or artificial emitter is coupled to a one-dimensional channel of propagating electromagnetic radiation. In contrast to free space QED the modes are spatially confined into waveguide to enhance the interaction between photon and atom. Compared to cavity QED, on the other hand, the photons can freely propagate along one direction, whereas cavities confine the photon in all spatial directions creating a standing wave. Traveling photons carry quantum information over large distances which makes them especially interesting for building a quantum internet [55] and add to the quantum optics toolbox in order to gain further insights into light-matter interactions. Reviews on waveguide QED can be found in Refs. [1, 56–58].

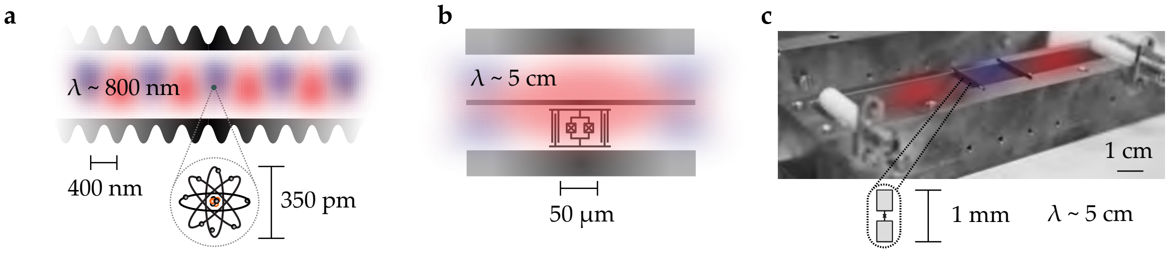

Figure 1.7: Waveguide QED platforms. a A cold atom is coupled to an alligator photonic crystal waveguide. The shaping of the waveguide enables efficient atom trapping and strong photon-atom interactions. **b** Superconducting qubits are capacitvely coupled to an integrated microwave transmission line. **c** Rectangular waveguides are metallic blocks with a milled out inner core that can be used as a waveguide QED platform. The $\sim$ cm wavelength of typical superconducting qubit resonance frequencies sets the dimensions of the inner volume.

While in the 1990s atomic ensembles were coupled to optical fibres [59], one of the first waveguide QED experiment with a single quantum emitter was conducted in 2007 when a Cadmium Selenium (CdSe) quantum dot was coupled to a silver nanowire [60]. When the emitter was optically excited in close vicinity to the waveguide the light was preferentially emitted into the guided modes and could be detected at the ends of the wire. Since then many waveguide QED platforms emerged, realized with various technologies, mostly inspired by cavity QED experiments. To determine their usability for quantum information processing it is important to benchmark their engineering capabilities. They can be assessed by the losses and integratability of the utilized waveguides, as well as the coherence properties and flexibility of the (artificial) atoms. The atom-waveguide interface is typically quantified by the coupling efficiency parameter $\beta = \gamma_\mathrm{r}/\kappa_L$, the ratio of the radiative decay rate γ_r of an individual emitter into the waveguide modes compared to the total emitter linewidth $\kappa_L = 2\Gamma$. Commonly used throughout literature is also the Purcell factor $P = \gamma_r/\gamma_\mathrm{nr}$, where γ_nr includes all parasitic (non-waveguide) energy relaxation rates but not dephasing γ_ϕ [25]. Moreover, the transmitted power ratio through the waveguide for a weak probe signal that is resonant with the qubit is $|S_{21}|^2 = (1 - \gamma_\mathrm{r}/2\Gamma)^2$, which is zero for $\Gamma = \gamma_\mathrm{r}/2$, meaning that intrinsic decay $\gamma_\mathrm{nr} = 0$ and dephasing $\gamma_\phi = 0$ are absent and the decoherence rate $\Gamma = \gamma_r + \gamma_\mathrm{nr} + \gamma_\phi$ is reduced only to the waveguide decay. Thus, we can define the power extinction ratio as $\zeta = 1 - (\gamma'_{\mathrm{nr}}/\Gamma)^2$, where $\gamma'_{\mathrm{nr}} = \gamma_{\mathrm{nr}}/2 + \gamma_\phi$. We will limit the further discussion to the coupling efficiency β.

Optical Waveguide QED

The waveguides for optical frequencies that are used to interface the emitter are usually nanofibers [61], nanowires [62] or nanophotonic crystals [5, 63, 64]. They are manufactured such that their geometries can be modified around the locations of the atom trapping sites. Fig. 1.7a shows an illustration of a cold atom coupled to an alligator crystal waveguide, where the periodic modulation of the waveguide is used to efficiently trap the atoms and engineer strong atom-photon interactions [65]. Optical waveguides can be designed to be almost lossless and photons can be routed over $\sim$ km distances at room temperature while preserving entanglement [66], making them a prime candidate for intracity quantum communication channels [67]. Integrated photonic circuits usually suffer from inefficient chip-to-fiber couplings but recent results show promising solutions [68].

Photonic waveguides are typically interfaced with quantum dots and natural atoms that have transitions in the optical or near infrared frequency range. If a laser-cooled atom like Cesium (Cs) is brought into the vicinity of the tailored waveguide section, it decays into the propagating modes and it is possible to record the emission at the output. The transitions of a given atom are indistinguishable from those of another atom of the same species, i.e. they have no frequency spread and reproducible decay rates. This allows to replicate experiments without worrying about atom parameters, as well as employing large ensembles of identical emitters to study collective behavior. Moreover, natural atoms have multiple transitions, some of which have very long coherence times [69]. The disadvantage is clearly their small dipole moment which results in low coupling efficiencies of around $\beta \sim 50\%$ which is even lower for optical nanofibers $\beta \sim 1\%$ [21]. However the nanofiber trap can capture thousands of atoms that act as an ensemble with enhanced emission properties.

Quantum dots are artificially fabricated regions on a semiconducting chip, that can be included in the photonic circuit. Fabrication is a versatile tool to precisely engineer the properties of the circuit such that strong atom-waveguide interactions were achieved $\beta \sim 99\%$ [70]. The disadvantages of artificial atoms such as quantum dots include imperfections between the design and the actual sample, as well as impurities introduced during the fabrication process. In addition, inhomogeneous broadening limits the use in waveguide QED experiments when more than a single quantum dot is to be used [5].

Other waveguide QED platforms in the optical domain include silicon or germanium vacancies that achieved similar coupling efficiencies like natural atoms. Their main limitations are coming from imperfect spatial and polarization alignment of the vacancy, phonon broadening, finite quantum efficiency which is set by $\gamma_{\mathrm{r}}/2\Gamma$, the branching ratio of the transition and residual spectral diffusion [71, 72]. Organic molecules have been successfully coupled to optical fibres showing a rich transmission spectrum of many transitions [73]. However, the coupling efficiency is relatively low $\beta \sim 0.2$ and the investigation of a larger ensemble of ~ 5000 molecules revealed a large spectral inhomogeneity.

Waveguide QED with Microwave Circuits

The field of microwave waveguide QED experienced a tremendous spark when strong-coupling of a superconducting flux qubit to a coplanar transmission line was realized in 2010 [12]. Even though the qubit was suffering from a large dephasing rate, the elastic scattering measurement revealed a high coupling efficiency $\beta \sim 0.76$. Mitigating charge noise, by switching to transmon qubits further improved the efficiency to $\beta \sim 0.96$ [74]. The simplicity of the initial circuits, shown in Fig. 1.7b, together with the vast engineering capabilities of superconducting qubits and rapidly evolving microwave measurement techniques induced the realization of many superconducting waveguide QED experiments in the following years. The second excited state of a superconducting qubit extended the waveguide QED toolkit by showing that electromagnetically induced transparency can be used to build a quantum switch for propagating microwaves [75] or by realizing a controllable and tunable on-chip quantum amplifier by achieving population inversion in a single qubit [76]. Exploiting the Autler-Townes effect [77] enabled the realization of a single-photon router [74], while measuring the second order correlation function $g^{(2)}(\tau)$ showed strong bunching/antibunching of the transmitted/reflected field, verifying the conversion of a coherent input state to a quantum state by the qubit [15]. It was shown that even the ultrastrong coupling regime can be reached with superconducting qubits, enabling research in new parameter regimes where the coupling cannot be considered a perturbation anymore [14]. Bandgap engineering of the transmission line allowed to observe qubit-photon bound states when the emitter is tuned over a band edge [78]. Very minimalistic circuits containing a single transmon qubit, strongly coupled to the end of a waveguide can be used for sensitive spectroscopy of the thermal occupation of the waveguide [79]. In order to obtain more insights into the different contributions to the total linewidth of a transmon, Ref. [80] performed a systematic study of the involved decoherence mechanisms with a single qubit in a transmission line.

While the last paragraph describes the development of individual qubits that are coupled to a transmission line, the achievement of strong coupling encouraged the realization of multi-qubit experiments. In 2013, strong waveguide-mediated interactions were observed for two emitters that are separated by wavelength distances resulting in frequency-dependent correlated emission and coherent-exchange coupling [19]. Surprisingly, it took 6 years until the next multi-qubit waveguide QED experiments were conceived. By combining the localized interaction of the qubits in the band gap and qubit-photon bound states in the passband, it is possible to realize spin model simulations with both local and long-range interactions [17]. The possibility to create subradiant states that arise from correlated decay inspired the realization of an atomic cavity with two qubits. It was shown that an excitation can be stored in the decoherence-free subspace of two interacting qubits that can coherently swap interactions with with another qubit [9]. Waveguide-mediated interactions between qubits can be used to realize spatially entangled photonic states in the waveguide [16]. Subradiant states also appear when a qubit is coupled at two spatial positions of a transmission line resulting in a giant-atom with tunable linewidth [81]. In the limit when the qubit- or resonator-spacing is much smaller than the wavelength the system can be described as a metamaterial. Effectively the photons travel through the metamaterial which yields new engineering possibilities, especially for realizing waveguides with slow-light [10, 82].

Figure 1.7c shows the conceptual setup for rectangular waveguide QED. Even though rectangular waveguides have been used to realize non-reciprocity [23] and as an interconnect for showing entanglement over two fridges [83] it stays an exotic platform due to its physical dimensions. However, the 3D inner volume offers many possibilities to engineer direct and long-range interactions in multi-qubit systems or even selectively switch off the interactions between individual qubits by properly arranging them [84]. The sharp cutoff-frequency enables the formation of qubit-photon bound states and access to different polarizations of the propagating modes offers versatile coupling schemes. More details on the rectangular waveguide are presented in Sec. 3.1.

Superconducting circuits have proven to be an excellent platform to realize various waveguide QED experiments by realizing strong-coupling and incorporating multiple qubits. However, in a large scale network a superconducting waveguide will not be as practical as an optical fibre, thus it will be necessary to either achieve strong coupling for optical frequencies or build an efficient microwave to optical converter. Another question for multi-qubit experiment is how valid the two-level approximation is, especially for describing collective states beyond the single excitation manifold [1].

System	N	$\omega_{01}/2\pi$	$\Gamma_r/2\pi$	$\beta = \Gamma_r/2\Gamma$
Cs atoms and nanofiber	$\sim 10^3$	340 THz	5 MHz	0.1
Rb atoms and nanofiber	6	390 THz	6 MHz	0.1
Cs atoms and alligator waveguide	3	340 THz	2.5 MHz	0.5
Superconducting qubits	10	10 GHz	5GHz	0.999
Quantum dots	1	340 THz	2 GHz	0.99
Si, N [85] vacancies in diamonds	2	410 THz	100 MHz	0.1
Organic molecules	1	410 THz	100 MHz	0.2

Table 1.1: Waveguide QED platforms. The table is adapted from Ref. [1] with N being the maximal resonant emitters, $\omega_{01}/2\pi$ the typical transition frequency of the emitter, $\Gamma_r/2\pi$ the maximal achieved radiative linewidths and $\beta = \Gamma_r/2\Gamma$ the best coupling efficiency.

CHAPTER 2

Waveguide Quantum Electrodynamics with Superconducting Circuits

Waveguide quantum electrodynamics (QED) describes the interaction of a quantum emitter with a one dimensional propagating mode continuum. For superconducting circuits we start from an electrical engineering perspective that has to be translated into the language of quantum optics, analogously to the derivation of the Jaynes–Cummings model [48] of circuit QED. The waveguide and artificial atom are described by node voltages and fluxes, which are promoted to quantum operators and yield a Hamiltonian that constitutes the typical electrical expressions, inductances and capacitances. The second quantization introduces creation and annihilation operators that are used to rewrite the Hamiltonian that describes the quantum mechanical properties of the system. Losses, decay into the waveguide modes and all dynamics concerning the qubit decoherence are modeled by introducing the master equation formalism for open quantum systems. The ability to obtain analytical expressions for the multi-qubit system lets us calculate or numerically simulate the observables that we want to measure in the experiments. Here, we do not specifically outline the approximations and assumptions, needed for the theoretical derivation but focus on the physical results. For many applications it is sufficient to invoke the two-level approximation to describe the transmon behavior, based on Refs. [20, 86]. However, we will see that it is necessary to go beyond the two-level description of a transmon when considering the higher excitation manifolds in many-body waveguide QED systems. A detailed derivation can be found in Ref.[87]. The chapter closely follows the derivations of Refs. [20, 86, 87]

2.1 Waveguide Circuit Quantization

In order to describe the quantum mechanical properties of the full system we start by quantizing the guided modes along the superconducting waveguide, following the circuit quantization procedure of Ref. [29]. We model the continuous waveguide modes as a set of linear harmonic oscillators with capacitances C and inductances L shown in Fig. 2.1a and consider them to be infinitesimally small unit cells of length dx with characteristic inductances Ldx and capac-

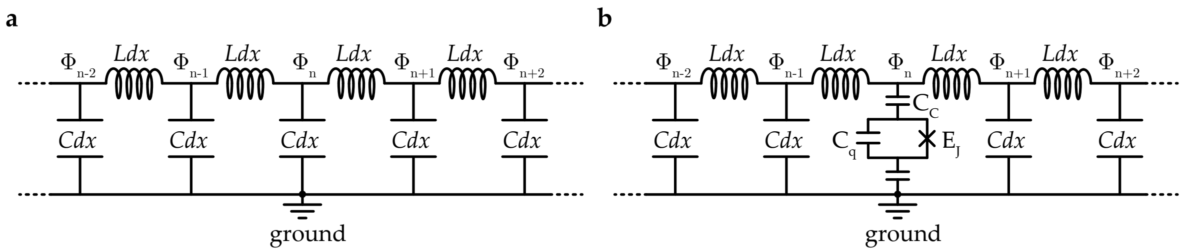

Figure 2.1: Waveguide circuit representation. **a** The waveguide is modeled by a set of inductances and capacitances to ground. We do not account for losses here, but they could be added by a resistive element R. **b** The transmon qubit is coupled capacitively to the waveguide and thus interacts with the propagating modes.

itances Cdx. The telegrapher's equations describe the propagation of the voltage and current through the waveguide [88]

$$\begin{aligned} \frac{\partial V(x,t)}{\partial x} &= -L\frac{\partial I(x,t)}{\partial t} \\ \frac{\partial I(x,t)}{\partial x} &= -C\frac{\partial V(x,t)}{\partial t} \end{aligned} \tag{2.1}$$

The generalized flux variable $\Phi(x,t)$ is expressed in terms of the voltage and the position in the waveguide x

$$\Phi(x,t) = \int_{-\infty}^{t} V(x,t')dt' \quad \text{and} \quad V(x,t) = \dot{\Phi}(x,t). \tag{2.2}$$

The node fluxes are defined as $\Phi_n = \Phi(n\,dx,t)$ such that the capacitive and inductive energies of the waveguide sections can be written analog to a harmonic oscillator

$$E_C = \frac{C}{2}\dot{\Phi}(x,t)^2 \quad \text{and} \quad E_L = \frac{1}{2L}\left(\frac{\partial\Phi}{\partial x}\right)^2. \tag{2.3}$$

The Lagrangian $\mathcal{L} = E_C - E_L$ of the system is

$$\mathcal{L} = \frac{C}{2}\left(\frac{\partial\Phi(x,t)}{\partial t}\right)^2 - \frac{1}{2L}\left(\frac{\partial\Phi(x,t)}{\partial x}\right)^2. \tag{2.4}$$

The non-commuting conjugate momentum of the node flux $\Phi(x,t)$ is the charge density $q(x,t) = \frac{\partial\mathcal{L}}{\partial\dot{\Phi}} = C\dot{\Phi}(x,t) = CV(x,t)$. The Hamiltonian is determined by a Legendre transformation, where we now integrate over the infinite length of the waveguide

$$H = \int_{-\infty}^{\infty} \left[\frac{1}{2C}q^2(x,t) + \frac{1}{2L}\left(\frac{\partial\Phi(x,t)}{\partial x}\right)^2\right] \mathrm{d}x. \tag{2.5}$$

Using the fact that the flux and charge density are canonical conjugates $q(x,t) = C\dot{\Phi}(x,t)$, we quantize the system by promoting the generalized coordinates to quantum operators and introduce creation and annihilation operators $a_k^\dagger, a_k$ for a mode with wave vector k [86]. The operators fulfill the commutation relations

$$\begin{aligned} &\left[\hat{\Phi}(x,t), \hat{q}\left(x',t\right)\right] = i\hbar\delta\left(x-x'\right), \\ &\left[a_k, a_{k'}^\dagger\right] = \delta\left(k-k'\right), \end{aligned} \tag{2.6}$$

thus do not commute for $x = x'$ and $k = k'$. The commutation relation for the same operators but different modes is zero, thus they commute. This allows to write down the Hamiltonian for the waveguide in terms of bosonic creation and annihilation operators

$$H = \sum_k \hbar\omega_k \left(a_k^\dagger a_k + \frac{1}{2} \right). \tag{2.7}$$

The Hamiltonian shows that each mode k is modeled as a linear quantum harmonic oscillator. By replacing the sum over all modes to an integral, we can rewrite the discretized spectrum to the continuous waveguide case.

2.2 Coupling Transmon Qubits to Waveguides

If the physical size of the transmon is much smaller than the wavelength corresponding to its resonance frequency, it can be modeled as a lumped element circuit and added to the circuit of the waveguide. For a transmon that is capacitively coupled to a node of the waveguide in Fig. 2.1b, the discrete Lagrangian can be adapted to [86, 89]

$$\begin{aligned}\mathcal{L} =& \sum_n \frac{Cdx}{2}\dot{\Phi}_n(t)^2 - \frac{\left(\Phi_{n+1}(t) - \Phi_n(t)\right)^2}{2Ldx} + \frac{C_\mathrm{q}}{2}\dot{\Phi}_\mathrm{q}(t)^2 \\ &+ E_\mathrm{J}\cos\left(\frac{2e\Phi_\mathrm{q}}{\hbar}\right) + \frac{C_\mathrm{c}}{2}\left(\dot{\Phi}_0(t) - \dot{\Phi}_\mathrm{q}(t)\right)^2,\end{aligned} \tag{2.8}$$

where we account for all waveguide nodes with the sum over n and the node flux at the transmon Φ_q. We write the Lagrangian as a sum to see that the transmon contribution is just another node term, now described by the characteristic transmon parameters. The capacitance C_c yields the coupling to the waveguide but also additionally contributes to the total transmon capacitance, together with the junction capacitance C_q. In the case of a split junction the Josephson energy E_J is tunable by an external flux, see Eq. (1.24). The conjugate variable of the flux at the transmon position is the charge

$$Q_\mathrm{q} = \frac{\partial\mathcal{L}}{\partial\dot{\Phi}_\mathrm{q}} = C_\mathrm{q}\dot{\Phi}_\mathrm{q}(t) + C_\mathrm{c}\left(\dot{\Phi}_\mathrm{q}(t) - \dot{\Phi}_0(t)\right) \tag{2.9}$$

Assuming that the waveguide capacitance is much larger than the coupling and junction capacitances the qubit capacitances act as a small perturbation [20]. Canonical quantization of the waveguide charge $\hat{q}$ and flux $\hat{\Phi}$, as well as the transmon charge $\hat{Q}_q$ and flux $\hat{\Phi}_q$ results in the Hamiltonian

$$\begin{aligned}\hat{H} =& \int_{-\infty}^{\infty} \frac{\hat{q}(x,t)^2}{2C} + \frac{1}{2L}\left(\frac{\partial\hat{\Phi}(x,t)}{\partial x}\right)^2 dx + \frac{\hat{Q}_\mathrm{q}(t)^2}{2\left(C_\mathrm{c} + C_\mathrm{q}\right)} - E_\mathrm{J}\cos\left(\frac{2e\hat{\Phi}_\mathrm{q}}{\hbar}\right) \\ &+ \frac{C_\mathrm{c}}{C_\Sigma}\hat{q}(0,t)\hat{Q}_\mathrm{q}(t),\end{aligned} \tag{2.10}$$

where the total transmon capacitance is $C_\Sigma = C_\mathrm{q} + C_\mathrm{c}C$. The last term describes the charge-interaction between the waveguide and the transmon. The charge density operator $\hat{q}(x,t) =$

$C\hat{V}(x,t)$ and flux operator $\hat{\Phi}(x,t)$ of the waveguide can also be written in terms of creation and annihilation operators [90]

$$\begin{aligned}\hat{q}(x,t) &= -iC\int\sqrt{\frac{\hbar\omega Z}{\sqrt{4\pi}}}d\omega\left(\hat{a}(\omega)e^{i(kx-\omega t)}-\hat{a}^{\dagger}(\omega)e^{-i(kx-\omega t)}\right),\\ \hat{\Phi}(x,t) &= \int\sqrt{\frac{\hbar\omega Z}{\sqrt{4\pi}}}d\omega\left(\hat{a}(\omega)e^{i(kx-\omega t)}+\hat{a}^{\dagger}(\omega)e^{-i(kx-\omega t)}\right).\end{aligned} \tag{2.11}$$

For the Hamiltonian, we arrived at a description of the energy in the system expressed by inductances and capacitances attributed to either the waveguide or the transmon qubit. Even though the system is fully described by the Hamiltonian in this form, for the quantum mechanical description we introduced the second quantization by expressing the flux and charge operators in terms of the creation and annihilation operators. The same can be done for the transmon term, especially when considering only the two lowest energy states. In general, this is necessary because we want to describe single excitation Fock states and explain quantum many-body systems which is much more complicated in the electrical engineering language.

2.3 Master Equation Formalism

By substituting the expressions for the charge and flux operators of Eq. (2.11) into the waveguide-transmon Hamiltonian Eq. (2.10) in the flux and charge basis we can rewrite it in second quantization, following Refs. [20, 86, 87]. The description can include multiple emitters, thus we sum over j. We will see in Sec. 2.6 that we can describe the transmon as a harmonic oscillator with an on-site interaction term, that will accurately model the higher excitation manifolds. For now, we are only interested in the one-excitation manifold, thus we approximate the transmons as two-level systems, such that it is sufficient to describe the j^{th} transmon charge operator by the σ_j^x Pauli matrix. Furthermore we neglect direct capacitive coupling between the qubits. The bare emitter Hamiltonian for N transmons with fundamental transition frequency ω_j simplifies to the qubit Hamiltonian $\hat{H}_{\text{Q}}$ if we only consider the ground and first excited state

$$\hat{H}_{\text{Q}} = \hbar\sum_{j=1}^{N}\omega_j\hat{\sigma}_j^{+}\hat{\sigma}_j^{-}, \tag{2.12}$$

with the Pauli raising operator $\hat{\sigma}_j^{+}$ and lowering operator $\hat{\sigma}_j^{-}$. The propagating modes of the rectangular waveguide are described by right- and left-moving photons that are created by $a^{\dagger}_{\text{R(L)}}(\omega)$ and annihilated by $a_{\text{R(L)}}(\omega)$ at frequency ω, corresponding to positive and negative wavevectors $k=\pm 2\pi/\lambda$. The continuous Hamiltonian describing the waveguide fields reads

$$\hat{H}_{\text{F}} = \int_0^{\infty} d\omega\hbar\omega\left[a^{\dagger}_{\text{R}}(\omega)a_{\text{R}}(\omega)+a^{\dagger}_{\text{L}}(\omega)a_{\text{L}}(\omega)\right]. \tag{2.13}$$

The equivalent to the charge coupling term of the electrical dipole of the transmons and the waveguide photons is described by the interaction Hamiltonian

$$H_{\text{I}} = \sum_{j=1}^{N} i\hbar g_j\int_0^{\infty} d\omega\sqrt{\omega}\left[a^{\dagger}_{\text{L}}(\omega)e^{i\omega x_j/v}-a_{\text{L}}(\omega)e^{-i\omega x_j/v}+a^{\dagger}_{\text{R}}(\omega)e^{-i\omega x_j/v}-a_{\text{R}}(\omega)e^{i\omega x_j/v}\right]\sigma_j^x, \tag{2.14}$$

where we approximated the qubit charge operator by the Pauli matrix $\sigma_j^x = \sigma_j^+ + \sigma_j^-$ and introduced the speed of light in the waveguide v, as well as the dimensionless coupling strength g_j as defined in Ref. [20]. The system is now described only by qubit and photon operators in second quantization. However, the continuum of the waveguide modes make the calculations complicated. By tracing out the electromagnetic environment, we can insert the Hamiltonian into a master equation for the qubit density operator ρ and model the waveguide as a dissipative bath [9, 20, 56, 91, 92]

$$\frac{d\hat{\rho}}{dt} = -i\left[\frac{\hat{H}_{\mathrm{Q}}}{\hbar} + \sum_j \alpha_j(t)\hat{\sigma}_j^x + \sum_{j,k}\widetilde{J}_{j,k}\hat{\sigma}_k^+\hat{\sigma}_j^-, \hat{\rho}\right] + \sum_{j,k}\gamma_{j,k}\left(\hat{\sigma}_j^-\hat{\rho}\hat{\sigma}_k^+ - \frac{1}{2}\left\{\hat{\sigma}_k^+\hat{\sigma}_j^-, \hat{\rho}\right\}\right) \quad (2.15)$$

The master equation only keeps track of the qubit dynamics and their interaction with each other via the waveguide. Compared to the Hamiltonian description, the explicit waveguide dynamics are not considered. Instead, we assume a coherent time-dependent drive $\alpha(t)$ from the left that acts on the qubits at position $x_j = t_j v$

$$\alpha_j(t) = \frac{\Omega_j}{2}\sin\left(\omega_d(t + t_j)\right), \quad (2.16)$$

where Ω_j is the drive amplitude seen by qubit j and ω_d the drive frequency. The other terms of the master equation describe waveguide-mediated interactions [19, 20] with the coefficients $\widetilde{J}_{j,k}$ and $\gamma_{j,k}$ describing the coherent exchange interaction and correlated decay between sites j and k. With the time $t_{j,k} = |t_j - t_k|$ that it takes a photon to travel between qubit sites j and k for the case of resonant qubits, the coefficients take the simple form

$$\gamma_{j,k} = 4\pi g_j g_k \omega_j \cos\left(\omega_j t_{j,k}\right), \quad (2.17)$$

$$\widetilde{J}_{j,k} = 2\pi g_j g_k \omega_j \sin\left(\omega_j t_{j,k}\right). \quad (2.18)$$

The counter-periodic behavior of those interaction terms implies that the qubit arrangement plays an important role when spacing qubits along the photon propagation of a waveguide QED circuit. Correlated decay is maximized when the qubit spacing is an integer multiple of $\lambda/2$, simultaneously the coherent exchange coupling is switched off. In contrast, when their spacing is an odd multiple integer of $\lambda/4$ the coherent exchange of excitations between the qubits is maximized but the correlated decay is zero.

The assumption that $\alpha(t)$ is the only drive allows to remove the time-dependence of the Hamiltonian by going into the frame that rotates with the frequency of the drive. The rotating wave approximation removes the fast rotating terms, such that $e^{\pm 2i\omega t} \sim 0$, which yields an effective time-independent Hamiltonian

$$\hat{H}_{\mathrm{eff}}/\hbar = \sum_{j=1}^{N}\delta\omega_j\hat{\sigma}_j^+\hat{\sigma}_j^- + \sum_{j=1}^{N}\left(\frac{\Omega_j}{2}\hat{\sigma}_j^+ + h.c.\right) + \sum_{j,k}^{N}\widetilde{J}_{j,k}\hat{\sigma}_j^-\hat{\sigma}_k^+. \quad (2.19)$$

Here, the frequency detuning between the qubit and the drive is $\delta\omega_j = \omega_j - \omega_d$ and we consider the case where thermal driving of the excited state is negligible, i.e. $\hbar\omega >> k_B T$. In order to capture not only the waveguide decay, we extend the effective master equation by replacing the waveguide coupling rate by an effective decay rate $\Gamma_1 = \gamma_r + \gamma_{\mathrm{nr}}$ that not only includes radiative decay into waveguide modes γ_r but also the non-radiative decay rate γ_{nr}. The non-radiative decay rate quantifies all intrinsic relaxation channels. Although these processes are radiative, we use the term "non-radiative" because the emitted photons are not radiated into the waveguide, thus not accessible for our detection setup. The waveguide photons on the other hand are entangled with the emitter and can be measured at the output [93]. Pure dephasing of the qubits is accounted for by the rate γ_ϕ. Thus, we can write down the effective master equation

$$\frac{d\hat{\rho}}{dt} = -\frac{i}{\hbar}\left[\hat{H}_{\text{eff}}, \hat{\rho}\right] + \sum_{j,k}^{N} \gamma'_{j,k}\left(\hat{\sigma}_j^- \hat{\rho}\hat{\sigma}_k^+ - \frac{1}{2}\left\{\hat{\sigma}_k^+\hat{\sigma}_j^-, \hat{\rho}\right\}\right) + \sum_{j=1}^{N}\frac{\gamma_{\phi,j}}{2}\left(\hat{\sigma}_j^z\hat{\rho}\hat{\sigma}_j^z - \hat{\rho}\right). \tag{2.20}$$

This master equation can be solved analytically in the steady state $\dot{\hat{\rho}} = 0$ and the condition $\rho_{00} + \rho_{11} = 1$ to obtain the density matrix. In particular, we are interested in the coherences which are given by the the off diagonal elements $\rho_{01} = \rho_{10}^*$

$$\rho_{01} = -\frac{\Omega}{2\Gamma}\frac{i + \delta\omega/\Gamma}{1 + \dfrac{\Omega^2}{\gamma'\Gamma} + \delta\omega^2/\Gamma^2}, \tag{2.21}$$

where we defined the total qubit decoherence rate $\Gamma = (\gamma_\text{r} + \gamma_\text{nr})/2 + \gamma_\phi = \Gamma_1/2 + \gamma_\phi$. The total energy relaxation rate Γ_1 is usually associated with the characteristic relaxation time $T_1 = 1/\Gamma_1$ of a qubit, while the decoherence rate Γ is associated with the characteristic coherence time $T_2 = 1/\Gamma$, as defined in Sec. 1.5. A typical measurement of the waveguide transmission for different probe frequencies shows a Lorentzian distribution around the qubit resonance frequency. The attributed linewidth is associated with the qubit decoherence rate Γ. For a qubit without any decoherence except the waveguide decay, the transmission of an elastically scattered resonant low power drive is zero, meaning it was perfectly reflected [12]. Decoherence other than the waveguide results in non-zero transmission, such that the ratio between the width and depth of the Lorentzian enables to distinguish between radiative and non-radiative decoherence. Thus we define the non-radiative decoherence rate $\gamma'_\text{nr} = \gamma_\text{nr}/2 + \gamma_\phi$, consisting of non-radiative energy relaxation and pure dephasing to distinguish between information loss and decay into the waveguide. More detailed studies of the incoherently scattered microwaves and time-resolved measurements give further insights into the various decoherence mechanisms [80].

To arrive at a master equation we traced out the photonic degrees of freedom. This allowed us to express the stationary density matrix in terms of qubit decoherence rates and the drive amplitude but prevents the description of the photons, that we usually want to detect. We can retrieve the photonic fields with the help of input-output theory for an input drive coming from the left and only considering right moving photons to find the transmission coefficient. The field operators can be expressed as [20, 87, 94, 95]

$$\hat{a}_\text{out} = \hat{a}_\text{in} - i\sqrt{\frac{\gamma_r}{2}}\hat{\sigma}^-. \tag{2.22}$$

The expectation value of the input field operator $\langle \hat{a}_\text{in} \rangle$ is directly related to the driving amplitude Ω at the qubit position [9]

$$\Omega/2 = -i\langle \hat{a}_\text{in} \rangle \sqrt{\gamma_r/2}. \tag{2.23}$$

This means that the problem reduced to finding the expectation value of the qubit lowering operator, which is related to the density matrix as $\langle \hat{\sigma}_- \rangle = \text{Tr}(\hat{\rho}\hat{\sigma}_-) = \rho_{10}$ with $\rho_{01} = \rho_{10}^*$, which we solved for in Eq. (2.21). This allows us to define the complex transmission parameter S_{21} as the ratio of the output and input fields a_{in} and a_{out} [20]

$$S_{21}(\omega) = \frac{\langle a_{\mathrm{out}} \rangle}{\langle a_{\mathrm{in}} \rangle} = 1 - \frac{\gamma_{\mathrm{r}}}{2\Gamma} \frac{1 - \dfrac{i\delta\omega}{\Gamma}}{1 + \left(\dfrac{\delta\omega}{\Gamma}\right)^2 + \dfrac{\Omega^2}{(\gamma_r + \gamma_{\mathrm{nr}})\,\Gamma}}, \tag{2.24}$$

The complex transmission parameter corresponds to the scattering matrix S, where $S_{11}(\omega)$ is the reflection parameter, while the telegrapher equations imply the conservation of the currents, such that $S_{11}(\omega) + S_{21}(\omega) = 1$ [12]. The scattering matrix is usually obtained by probing the system with a coherent low power drive, such that $\Omega \ll \gamma_r$ and performing a heterodyne detection. Thus the complex values of the scattering matrix have the form $S = I + iQ$ and the absolute transmitted amplitude is $|S_{21}| = \sqrt{I^2 + Q^2}$. Removing all decoherence channels except the waveguide yields that the absolute transmission $|S_{21}|$ is zero for a resonant probe, while the reflected amplitude is $S_{11} = 1 - S_{21} = 1$, indicating that the qubit acts as a perfect mirror for single photons [12]. The absence of transmission can be understood when considering interference effects. The photons that were absorbed by the qubit and re-emitted into the waveguide acquire a π-shift, thus destructively interfere with the incident signal.

Qubit dephasing leads to the loss of phase information during the time that the excitation is absorbed. The re-emitted signal will have a phase that does not match the phase of the transmitted signal, which results in imperfect interference and thus $S_{21} > 1$. Similarly, non-radiative decay results in a smaller amplitude of the scattered signal, also leading to imperfect destructive interference. The same is true if the probe power is too large and saturates the qubit transition, as the drive rate on the qubit depends on the input power and the waveguide coupling [9]. This is due to the fact that the qubit can only absorb one photon at a time and needs to relax to the ground state before being able to absorb another one. If the average number of photons in the input field at the qubit position becomes too high such that the qubit cannot fully relax to the ground state anymore we measure non-zero transmission. In particular, at these high drive strengths, a considerable fraction of the radiation is inelastically scattered and cannot be detected by the heterodyne detection scheme. However, the inelastically scattered radiation can still be observed by a power sensitive measurement of the resonance fluorescence. The appearing sidebands are a signature of the dressed transmon ground and excited states. Together with the bare qubit transition they form the Mollow triplet [96], where the frequency of the inelastically scattered radiation depends on the drive strength. The measurement of the Mollow triplet implies that $|S_{21}|^2 + |S_{11}|^2 < 1$, even for $\gamma_\phi = \gamma_{\mathrm{nr}} = 0$ [12, 97].

2.4 Waveguide-Mediated Coupling

Waveguide-mediated interactions appear for two or more qubits that are coupled to the propagating waveguide modes. For the case of two resonant qubits Q_1 and Q_2 the type of interaction depends on the argument inside the trigonometric functions of Eqns. (2.17) and (2.18). Physically, this means that the amount of correlated decay or coherent exchange depends on the phase that a photon acquires when it travels from Q_1 to Q_2. In order to obtain an experimental tuning parameter that is able to switch between both types of interactions either the distance between the qubits, the photon velocity or the qubit resonance frequency has to be tunable. In the experiment, we simply utilize the flux-tunability of the split junction transmons to change their resonance frequencies, effectively changing the emission wavelength λ. More details on the theoretical studies of waveguide-mediated interactions between two transmons can be found in Refs. [20, 87, 98].

Correlated Decay

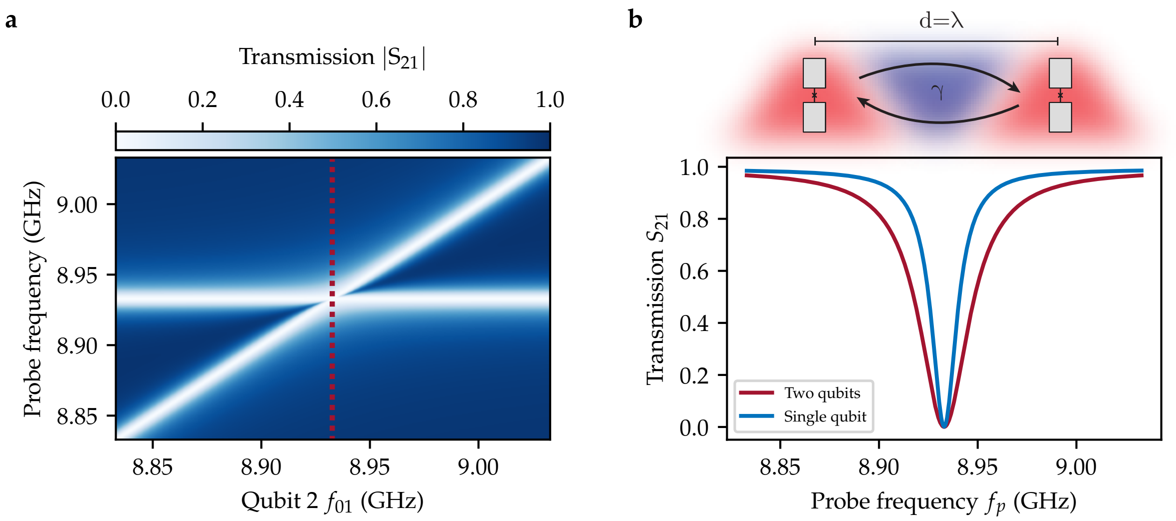

Figure 2.2: QuTiP simulation: Correlated decay. a While Qubit 1 is kept constant at a frequency corresponding to an effective separation of $d = \lambda$, we change the frequency of Qubit 2. By changing the frequency of the probe we can simulate its transmission through the system to observe the characteristic crossing. **b** On resonance we observe the broadening of the linewidth corresponding to the superradiant transition while the subradiant state cannot be driven such that the transition disappears.

For the case of two resonant qubits $\omega_1 = \omega_2 = \omega$ and an effective qubit-qubit separation of $d_x = \lambda$ correlated decay $\gamma_{1,2} \sim \cos(\omega t_{1,2})$ is maximized while coherent exchange coupling $\widetilde{J}_{1,2} \sim \sin(\omega t_{1,2}) = 0$ is absent. If we ignore all decoherence channels except the waveguide we can write the dissipative interaction term of the master equation as [20]

$$\frac{d\hat{\rho}}{dt} = \sum_{\mu=B,D} \Gamma_\mu \mathcal{D}\left[\sigma_\mu^-\right]\hat{\rho}, \tag{2.25}$$

where the collective dissipator is now $\mathcal{D}[\hat{\sigma}_\mu^-]\hat{\rho} = \hat{\sigma}_\mu^- \hat{\rho} \hat{\sigma}_\mu^+ - \left\{\hat{\sigma}_\mu^+ \hat{\sigma}_\mu^-, \hat{\rho}\right\}$ with the indices $\mu = B, D$ accounting for the dark and bright states of the new basis and the dressed lowering operators $\hat{\sigma}_\mu$. The states obtain correlated decay rates

$$\Gamma_B = 2\Gamma \quad \text{and} \quad \Gamma_D = 0, \tag{2.26}$$

meaning that the bright state decays twice as fast as the individual qubits. The dark state is decoupled completely from the waveguide and only limited by its internal decoherence properties. The dark state $|D\rangle = (|ge\rangle - |eg\rangle)/\sqrt{2}$ and bright state $|B\rangle = (|ge\rangle + |eg\rangle)/\sqrt{2}$ are symmetric and antisymmetric superpositions of the single qubit ground and excited state $|g\rangle$ and $|e\rangle$. For a distance of λ, the phase relation of the electromagnetic field in the waveguide is symmetric, meaning the phase between the qubits is an even integer multiple of π: $\varphi = 2\pi$. Thus we can only excite the symmetric bright state. The dark state symmetry is opposite to the field symmetry of the waveguide, eliminating the coupling to the drive field and and also the decay into the waveguide. Note, that for a phase with an odd integer multiple of π, such as for $\lambda/2$ the roles of dark and bright states are reversed, because the individual qubits will sit at positions of opposite drive phase, thus $|D\rangle = (|ge\rangle + |eg\rangle)/\sqrt{2}$ and $|B\rangle = (|ge\rangle - |eg\rangle)/\sqrt{2}$.

In Fig. 2.2 we simulate two qubits around a frequency corresponding to $d = \lambda$ with the Quantum Toolkit in Python (QuTiP) [26]. By solving the effective master equation for the case of two qubits separated by λ in the steady state we obtain the expectation value of the lowering operator, that determines the scattering properties of a drive tone with the corresponding waveguide symmetry resulting in the simulated transmission spectrum. On resonance we see that the bright state obtains twice the single qubit linewidth, while the dark state cannot interact with the waveguide drive and thus does not influence the transmission amplitude.

Coherent Exchange

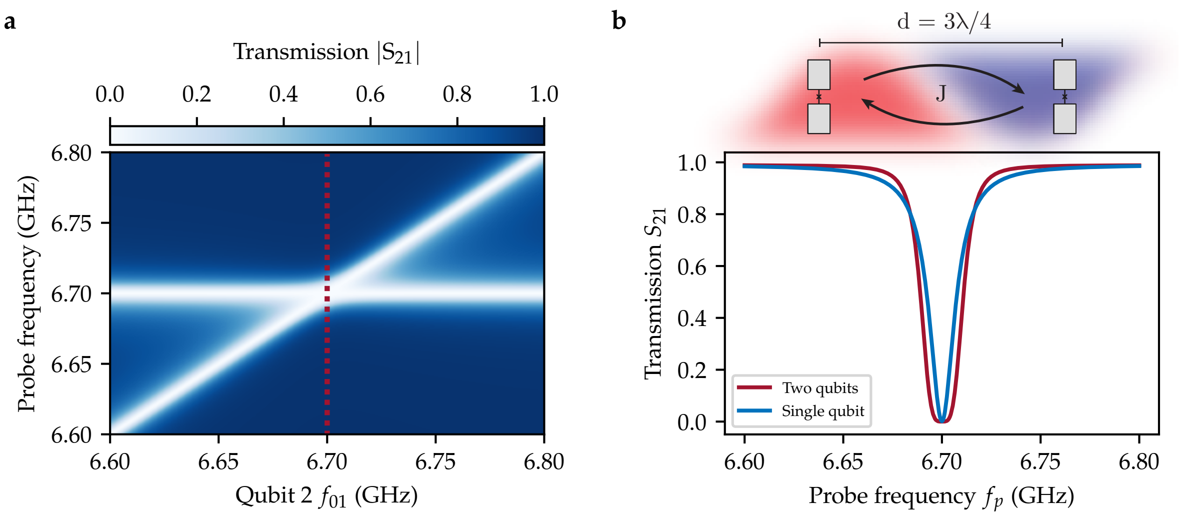

Figure 2.3: QuTiP simulation: Coherent exchange. a While Qubit 1 is kept constant at a frequency corresponding to an effective separation of $d = 3\lambda/4$, we change the frequency of Qubit 2. By changing the frequency of the probe we can simulate its transmission through the system to observe the characteristic crossing. **b** There are no observable signatures of super- and subradiance in the transmission, however the new eigenstates split by $E = 2J$ with $|J| = \gamma_r/2$ resulting in a distorted lineshape.

In contrast to the λ spacing, when two qubits are separated by $d = 3\lambda/4$ correlated decay $\gamma_{1,2} \sim \cos(\omega t_{1,2}) = 0$ is absent but the coherent exchange coupling $\widetilde{J}_{1,2} \sim \sin(\omega t_{1,2}) = \gamma_r/2$ is at its maximal rate. We recall from the effective Hamiltonian the coherent exchange term

$$\hat{H}_I/\hbar = \sum_{j \neq k}^{N} \widetilde{J}_{j,k} \hat{\sigma}_-^j \hat{\sigma}_+^k. \tag{2.27}$$

In contrast to the correlated decay, the individual qubits still emit photons into the waveguide that are then reabsorbed by the other. However, the system will hybridize and the new eigenstates $|+J\rangle$ and $|-J\rangle$ split in energy by $E = 2\widetilde{J}_{j,k}$. Thus, the exchange interaction can be interpreted as a modification of the Lamb shift due to the presence of the qubits coupled to the same electromagnetic environment [20]. The virtual photons emitted and reabsorbed by the same qubit contribute to the Lamb shift. When there is more than one qubit, the virtual photons emitted by one can be reabsorbed by another. This exchange of virtual photons leads to an effective qubit-qubit interaction well known in circuit quantum electrodynamics where qubits interact strongly with a single mode of a resonator. For two resonant transmons that are coupled to a mode of the resonator with coupling strengths g_1 and g_2, we observe an effective interaction strength $\widetilde{J}_{1,2} = g_1 g_2/\delta$ between the transmons, where δ is the frequency detuning between the transmons and the resonator frequency. In the waveguide case the interaction type is the same but the qubits interact with a continuum of modes. The interaction stays the same for any separation $d = (2n+1)\lambda/4$ but the sign of $\widetilde{J}_{j,k}$ will be negative for odd n and positive for even n.

In the transmission simulation in Fig. 2.3, we notice that already the tuning map looks very different from the correlated decay in Fig. 2.2. The sharp features when tuning into resonance disappear and the lines blur together. In the experiment it can be helpful to compare the flux maps in order to identify frequencies corresponding to correlated decay and coherent exchange.

2.5 Direct Coupling

Instead of engineering an effective qubit-qubit interaction via the waveguide where they are separated at least $d = \lambda/4$, we can study the case where they are at the same position with respect to the propagation direction. According to Eq. (2.17) this results in collective decay similar to the λ separated qubit pair. In addition to the collective decay, the vicinity of the metallic transmon pads gives rise to a capacitive coupling that yields a coherent swapping of excitations with rate $J_{j,k}$, similar to the waveguide-mediated coherent exchange coupling strength $\widetilde{J}_{j,k}$. The coupling strength depends on the distance and orientation of the transmon pads [84] and enables $\sqrt{iSWAP}$ two-qubit gates in quantum processors [99]. The state manifold yields a dark state $|D\rangle = (|ge\rangle - |eg\rangle)/\sqrt{2}$ and bright state $|B\rangle = (|ge\rangle + |eg\rangle)/\sqrt{2}$. The individual qubits are exposed to the same phase by sharing a common position with respect to the propagating field. The in-phase superposition of oscillating dipole moments of the qubits interferes constructively, thus the bright state again obtains twice the coupling to the waveguide, while the out-of-phase oscillating superposition destructively interferes to form the decoupled dark state.

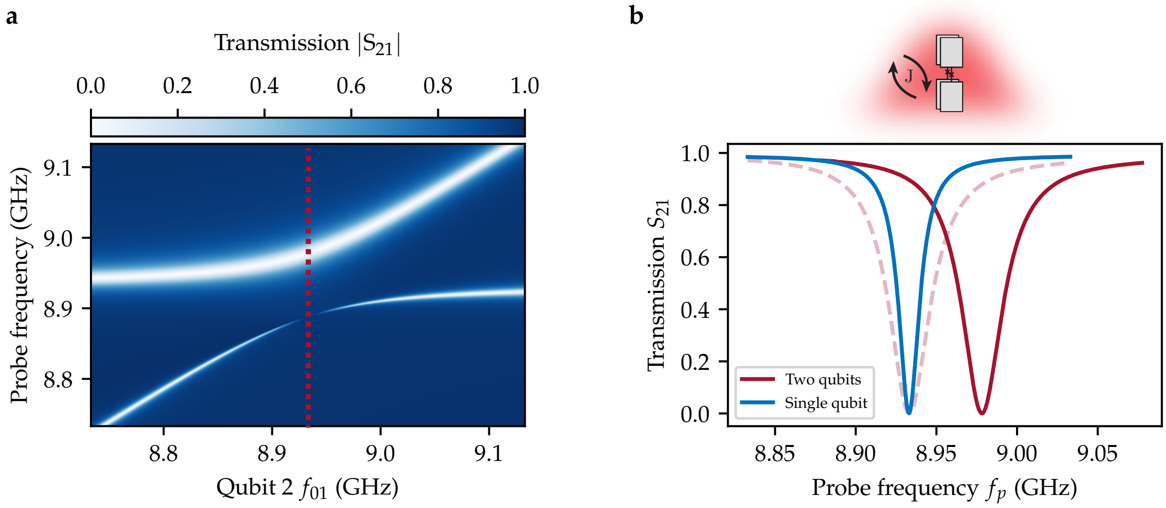

Figure 2.4: QuTiP simulation: Coherent exchange via capacitive coupling. **a** When two adjacent qubits are tuned into resonance they obtain bright and dark states. The capacitive coupling splits the new eigenstates by $2J_{j,k}$, which enables to witness the decoupling process of the dark state if the splitting is large enough. **b** The bright state is visible in transmission and couples stronger to the waveguide than the individual qubits $\gamma_B = 2\gamma_r$. Furthermore, the coherent exchange coupling $J_{1,2}/2\pi = 45\,\text{MHz}$ causes a detuning of the bare qubit frequencies and the bright state (and dark state, not visible in transmission).

In Fig. 2.4 we simulate the transmission for two capacitively coupled qubits that are subjected to the same phase relation by the waveguide. By changing the frequency of Qubit 2 the decoupling and linewidth broadening of the dark and bright state is directly observable. The continuous decoupling can be used as an in-situ tunable waveguide coupling to realize different coupling regimes in the same experimental setup. In the extreme case the dark state decay is only limited by internal dissipation while the bright state decay is orders of magnitude faster. The splitting on resonance is defined by the effective capacitance between the transmons. In the simulation we set the direct coupling strength to $J_{1,2}/2\pi = 45\,\text{MHz}$, thus observe a splitting of 90 MHz. The coupling is highly engineerable by modifying the transmon design and orientation with respect to each other [84], offering a versatile tool to engineer qubit-qubit couplings in waveguide QED in addition to the waveguide-mediated interactions.

2.6 Four Transmons in a Waveguide

In this section we consider the full experimental system, consisting of a capacitively coupled pair of transmons that interacts with a second pair via the waveguide. As depicted in Fig. 2.5, they are tuned into resonance such that the bright transitions of the capacitively coupled pairs match the $\lambda/2$-condition for correlated decay. In this scenario both local two-qubit bright states interact via the waveguide and create the collective four qubit states $|B_4\rangle$ and $|D_3\rangle$. The local two-qubit dark states $|D_1\rangle$ and $|D_2\rangle$ cannot interact via the waveguide. These four states span the first excitation manifold. In the theoretical description we now model the transmons as anharmonic oscillators, instead of two-level systems like in the previous sections.

This is a necessity to accurately model the higher excitation manifolds, already for the two-qubit case and becomes even more important when increasing the size of the many-body system [87]. The section is adapted from Refs. [87, 100].

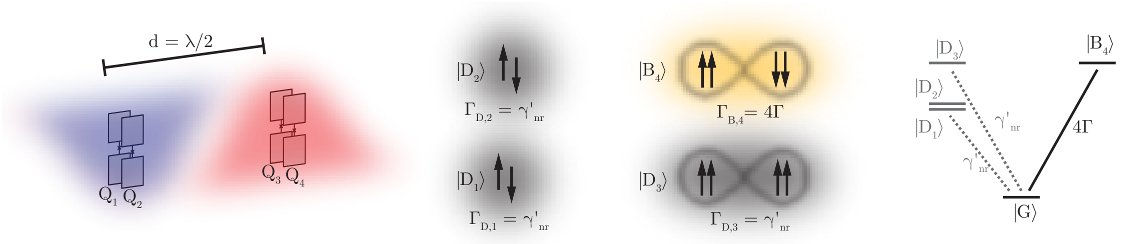

Figure 2.5: Schematic illustration of the full experimental setup. Two pairs of transmon qubits that are separated by an effective distance $d = \lambda/2$ have a maximized correlated decay coupling, mediated by the waveguide, as well as a capacitive coupling within the pair. The interacting transmon system forms the four qubit one-excitation state manifold. It consists of a global delocalized dark state $|D_3\rangle$ and bright state $|B_4\rangle$ with decay rate 4Γ, as well as pairwise dark states $|D_1\rangle, |D_2\rangle$ that are localized at the sites and do not interact with the waveguide or the other pair.

Collective Spectrum of Anharmonic Oscillators

An array of L coupled transmons is modeled by the Bose-Hubbard Hamiltonian [35, 101–104]

$$\frac{\hat{H}_{\mathrm{BH}}}{\hbar} = \sum_{j=1}^{L} \omega_j \hat{n}_j - \sum_{j=1}^{L} \frac{\alpha_j}{2} \hat{n}_j \left(\hat{n}_j - 1\right) + \sum_{j \neq k} J_{jk} \hat{a}_j^\dagger \hat{a}_k, \tag{2.28}$$

where $\hat{a}_j$ and $\hat{a}_j^\dagger$ are the bosonic annihilation and creation operators of the site j. They obey the commutation relation $\left[\hat{a}_j, \hat{a}_k^\dagger\right] = \delta_{jk}$, with the number operator $\hat{n}_j = \hat{a}_j^\dagger \hat{a}_j$. Transmon j has a transition frequency ω_j between the ground state $|g\rangle$ and the first excited state $|e\rangle$ and anharmonicity α_j. Here, the anharmonicity serves as a negative on-site interaction tuning parameter that limits the bosonic nature of the system such that we can describe the transmon as an anharmonic oscillator. For a small anharmonicity, the transmon behaves more like a harmonic oscillator, while for a large anharmonicity the transmon behaves like a two-level system. Capacitive coupling is responsible for the exchange of excitations between sites j and k. For the arrangement in Fig. 2.5 the Bose-Hubbard Hamiltonian reduces to the energy terms of four qubits with two direct coupling terms

$$\begin{aligned} \hat{H}_{\mathrm{T}}/\hbar = & \sum_{j=1}^{4} \left[\omega_j \hat{n}_j - \frac{\alpha_j}{2} \hat{n}_j (\hat{n}_j - 1)\right] \\ & + J_{12} \left(\hat{a}_1^\dagger \hat{a}_2 + \mathrm{h.c.}\right) + J_{34} \left(\hat{a}_3^\dagger \hat{a}_4 + \mathrm{h.c.}\right), \end{aligned} \tag{2.29}$$

In the presence of the waveguide radiation field, the dynamics is governed by a master equation [9, 20]

$$\begin{aligned}\frac{d\hat{\rho}}{dt} &= -\frac{i}{\hbar}\left[\hat{H}_{\mathrm{T}} + \hbar\sum_{j,k}\widetilde{J}_{j,k}\hat{a}_k^\dagger\hat{a}_j, \hat{\rho}\right] + \sum_{j,k}\gamma_{j,k}\left(\hat{a}_j\hat{\rho}\hat{a}_k^\dagger - \frac{1}{2}\hat{a}_k^\dagger\hat{a}_j\hat{\rho} - \frac{1}{2}\hat{\rho}\hat{a}_k^\dagger\hat{a}_j\right)\\ &+ \sum_j\gamma_{\mathrm{nr}}\left(\hat{a}_j\hat{\rho}\hat{a}_j^\dagger - \frac{1}{2}\hat{a}_j^\dagger\hat{a}_j\hat{\rho} - \frac{1}{2}\hat{\rho}\hat{a}_j^\dagger\hat{a}_j\right) + \sum_j\gamma_\phi\left(\hat{n}_j\hat{\rho}\hat{n}_j - \frac{1}{2}\hat{n}_j^2\hat{\rho} - \frac{1}{2}\hat{\rho}\hat{n}_j^2\right)\\ &+ K_\phi\left(\hat{N}\hat{\rho}\hat{N} - \frac{1}{2}\hat{N}^2\hat{\rho} - \frac{1}{2}\hat{\rho}\hat{N}^2\right),\end{aligned} \tag{2.30}$$

where $\hat{H}_{\mathrm{T}}$ is the Hamiltonian of the transmon array given in Eq. (2.29) and the coefficients $\widetilde{J}_{j,k}$ and $\gamma_{j,k}$ are the coherent exchange interaction and correlated decay between sites j and k from Eqns. (2.17) and (2.18). We include non-radiative dissipation γ_{nr} and pure dephasing γ_ϕ of individual transmons. Global dephasing K_ϕ mainly arises from flux noise affecting all transmon where we have denoted the global occupation operator $\hat{N} = \sum_{j=1}^4 \hat{n}_j$. Even though the effect of dephasing is negligible for the qualitative behavior of the simulation, they play an important role in the definition of the lifetime T_1 and coherence time T_2 of the dark state. The properties of the system are then governed by the non-Hermitian effective Hamiltonian,

$$\hat{H}_{\mathrm{eff}}/\hbar = \hat{H}_{\mathrm{T}}/\hbar + \sum_{jk}\left(\widetilde{J}_{j,k} - \frac{i\gamma_{j,k}}{2}\right)\hat{a}_k^\dagger\hat{a}_j - \frac{i}{2}\sum_j\gamma_{\mathrm{nr}}\hat{a}_j^\dagger\hat{a}_j - \frac{i}{2}\sum_j\gamma_\phi\hat{n}_j^2 - \frac{i}{2}K_\phi\hat{N}^2. \tag{2.31}$$

The eigenvalues of the effective Hamiltonian are in general complex valued, $\lambda_\xi = E_\xi - i\hbar\frac{\Gamma_\xi}{2}$, where the real part E_ξ gives the energy and imaginary part Γ_ξ the total decay rate of the state $|\xi\rangle$. The effective Hamiltonian commutes with the total occupation operator, and thus the eigenvalues form manifolds with integer number of quanta [100]. By only using the experimentally extracted single qubit parameters in table 4.1 and capacitive coupling strengths in table 4.3, we can plot the transition frequencies and waveguide decay rates in Fig. 2.6. The eigenstates of the first excitation manifold are either symmetric or antisymmetric with respect to the exchange of transmon pairs. The two-excitation manifold also comprises states that cannot be assigned to a pair-exchange symmetry, but instead they are symmetric or antisymmetric with respect to the exchange of transmons within the pairs. The small differences of $|D_1\rangle$ and $|D_2\rangle$ arise from the unequal direct coupling strengths. This disorder lifts the degeneracy of the dark states $|D_1\rangle$ and $|D_2\rangle$ in the one-excitation manifold, as well as the states $|W_{5(6)}\rangle$, $|F_{7(8)}\rangle$ and $|F_{10(11)}\rangle$ in the two-excitation manifold. In the two excitation manifold is only one dark state $|D_9\rangle = |D_1\rangle \otimes |D_2\rangle$, that corresponds to the trivial case when both local dark states are excited. The imaginary part of the eigenvalue Γ_ξ gives the total decay rate for the state, but we can also calculate the decay rates to individual states, which sum up to Γ_ξ.

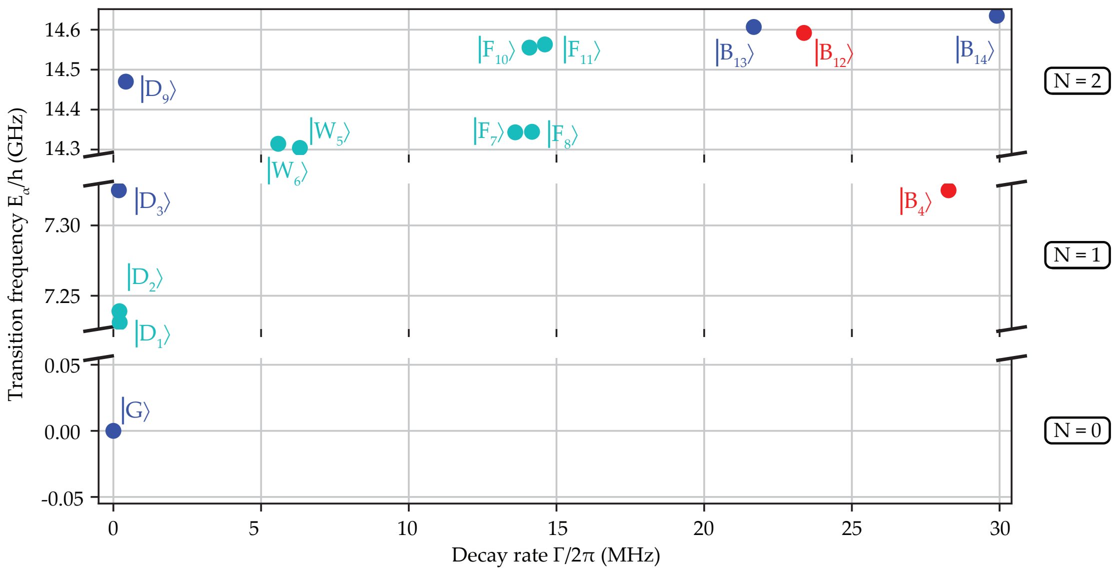

Figure 2.6: Transition frequencies and decay rates. Numerically obtained eigenlevels in zero-, one- and two-excitation manifolds computed with the parameters of Tab. 4.3. The y-axis gives the energy and x-axis the decay rate of the state. Here, the states that are symmetric with respect to the exchange of pairs are colored blue and the antisymmetric ones red. The states with no symmetry under qubit exchange are turquoise. The labeling for the states is $|D\rangle$ - Dark, $|B\rangle$ - Bright, $|W\rangle$ - Weakly radiant, $|F\rangle$ - Faint and the numbering is ascending in energy. F-states mainly contain one excitation in a local state, whereas in the W-states the local states are doubly excited. Note, that it is possible to drive the W-states from $|D_3\rangle$ and $|B_4\rangle$, but not the F-states.

Assuming that all transmons are identical and ignoring dephasing γ_ϕ and K_ϕ, we can analytically solve the eigenstates in zero-, one- and two-excitation manifolds. The one-excitation states are obtained from the ground state with collective operators

$$\hat{D}_1^\dagger = \frac{1}{\sqrt{2}}\Big(\hat{a}_1^\dagger - \hat{a}_2^\dagger\Big), \tag{2.32}$$

$$\hat{D}_2^\dagger = \frac{1}{\sqrt{2}}\Big(\hat{a}_3^\dagger - \hat{a}_4^\dagger\Big), \tag{2.33}$$

$$\hat{D}_3^\dagger = \frac{1}{2}\Big(\hat{a}_1^\dagger + \hat{a}_2^\dagger + \hat{a}_3^\dagger + \hat{a}_4^\dagger\Big), \tag{2.34}$$

$$\hat{B}_4^\dagger = \frac{1}{2}\Big(-\hat{a}_1^\dagger - \hat{a}_2^\dagger + \hat{a}_3^\dagger + \hat{a}_4^\dagger\Big). \tag{2.35}$$

The states in the zero- and one-excitation manifold are then

$$|G\rangle = |00;00\rangle = |0000\rangle\,, \tag{2.36}$$

$$|D_1\rangle = \hat{D}_1^\dagger\,|G\rangle = |00;10\rangle = \frac{1}{\sqrt{2}}\Big(\,|1000\rangle - |0100\rangle\,\Big), \tag{2.37}$$

$$|D_2\rangle = \hat{D}_2^\dagger\,|G\rangle = |00;01\rangle = \frac{1}{\sqrt{2}}\Big(\,|0010\rangle - |0001\rangle\,\Big), \tag{2.38}$$

$$|D_3\rangle = \hat{D}_3^\dagger\,|G\rangle = |01;00\rangle = \frac{1}{2}\Big(\,|1000\rangle + |0100\rangle + |0010\rangle + |0001\rangle\,\Big), \tag{2.39}$$

$$|B_4\rangle = \hat{B}_4^\dagger\,|G\rangle = |10;00\rangle = \frac{1}{2}\Big(-|1000\rangle - |0100\rangle + |0010\rangle + |0001\rangle\,\Big), \tag{2.40}$$

where we have used two different bases. State $|n_1n_2n_3n_4\rangle$ is the Fock basis, where n_j is the number of excitations in the jth transmon. In state $|B_4D_3;D_1D_2\rangle$, on the other hand, B_4, D_3, D_1 and D_2 refer to the number of excitation created by the collective operators $\hat{B}_4$, $\hat{D}_3$, $\hat{D}_1$ and $\hat{D}_2$, respectively.

In the absence of anharmonicity α the eigenstates in the two-excitation manifold are obtained by operating twice with the collective operators. Because of the anharmonicity, the real eigenstates are linear combinations of these states and can be written in the both bases

$$\begin{aligned}
|W_5\rangle =&\frac{1}{Z_5}\left[\frac{2i\gamma-4J+\sqrt{U^2+16\left(J-\frac{i\gamma}{2}\right)^2}}{\sqrt{2}U}\Big(|00;20\rangle-|00;02\rangle\Big)+|11;00\rangle\right]\\
\approx&0.47e^{i\phi_5}\Big(|2000\rangle+|0200\rangle-|0020\rangle-|0002\rangle\Big)+0.24e^{i\psi_5}\Big(|1100\rangle-|0011\rangle\Big), \quad (2.41)\\
|W_6\rangle =&c_1\Big(|00;20\rangle+|00;02\rangle\Big)+c_2\,|02;00\rangle+c_3\,|20;00\rangle\\
\approx&0.47e^{i\phi_6}\Big(|2000\rangle+|0200\rangle+|0020\rangle+|0002\rangle\Big)+0.24e^{i\psi_6}\Big(|1100\rangle+|0011\rangle\Big), \quad (2.42)\\
|F_7\rangle =&\frac{1}{Z_7}\left[\frac{-2i\gamma+\sqrt{U^2-4\gamma^2}}{U}\,|01;10\rangle+|10;10\rangle\right]\\
\approx&0.71e^{i\phi_7}\Big(|2000\rangle-|0200\rangle\Big)+0.32e^{i\psi_7}\Big(|1001\rangle-|0110\rangle\Big), \quad (2.43)\\
|F_8\rangle =&\frac{1}{Z_8}\left[\frac{2i\gamma-\sqrt{U^2-4\gamma^2}}{U}\,|01;01\rangle+|10;01\rangle\right]\\
\approx&0.71e^{i\phi_8}\Big(|0020\rangle-|0002\rangle\Big)+0.31e^{i\psi_7}\Big(|1001\rangle-|0110\rangle\Big), \quad (2.44)\\
|D_9\rangle =&|00;11\rangle=|D_1\rangle\otimes|D_2\rangle\\
=&\frac{1}{2}\Big(|1010\rangle-|1001\rangle-|0110\rangle+|0101\rangle\Big) \quad (2.45)\\
|F_{10}\rangle =&\frac{1}{Z_{10}}\left[\frac{-2i\gamma-\sqrt{U^2-4\gamma^2}}{U}\,|01;10\rangle+|10;10\rangle\right]\\
\approx&0.51e^{i\phi_{10}}\Big(|1010\rangle-|0101\rangle\Big)+0.49e^{i\psi_{10}}\Big(|1001\rangle-|0110\rangle\Big), \quad (2.46)\\
|F_{11}\rangle =&\frac{1}{Z_{11}}\left[\frac{2i\gamma+\sqrt{U^2-4\gamma^2}}{U}\,|01;01\rangle+|10;01\rangle\right]\\
\approx&0.49e^{i\phi_{11}}\Big(|1010\rangle-|0101\rangle\Big)+0.51e^{i\psi_{11}}\Big(|1001\rangle-|0110\rangle\Big), \quad (2.47)\\
|B_{12}\rangle =&\frac{1}{Z_{12}}\left[\frac{2i\gamma-4J-\sqrt{U^2+16\left(J-\frac{i\gamma}{2}\right)^2}}{\sqrt{2}U}\Big(|00;20\rangle-|00;02\rangle\Big)+|11;00\rangle\right]\\
\approx&0.17e^{i\phi_{12}}\Big(|2000\rangle+|0200\rangle-|0020\rangle-|0002\rangle\Big)+0.67e^{i\psi_{12}}\Big(|1100\rangle-|0011\rangle\Big), \quad (2.48)\\
|B_{13}\rangle =&b_1\Big(|00;20\rangle+|00;02\rangle\Big)+b_2\,|02;00\rangle+b_3\,|20;00\rangle\\
\approx&0.22e^{i\phi_{13}}\Big(|2000\rangle+|0200\rangle+|0020\rangle+|0002\rangle\Big)+0.80e^{i\psi_{13}}\Big(|1100\rangle+|0011\rangle\Big)\\
&+0.35e^{i\varphi_{13}}\Big(|1010\rangle+|1001\rangle+|0110\rangle+|0101\rangle\Big), \quad (2.49)
\end{aligned}$$

$$
\begin{aligned}
|B_{14}\rangle =& a_1\Big(\,|00;20\rangle + |00;02\rangle\,\Big) + a_2\,|02;00\rangle + a_3\,|20;00\rangle \\
\approx& 0.14e^{i\phi_{14}}\Big(\,|2000\rangle + |0200\rangle + |0020\rangle + |0002\rangle\,\Big) + 0.46e^{i\psi_{14}}\Big(\,|1100\rangle + |0011\rangle\,\Big) \\
&+ 0.61e^{i\varphi_{14}}\Big(\,|1010\rangle + |1001\rangle + |0110\rangle + |0101\rangle\,\Big).
\end{aligned} \tag{2.50}
$$

Exact forms for states $|W_6\rangle$, $|B_{13}\rangle$ and $|B_{14}\rangle$ in the collective basis $|B_4D_3;D_1D_2\rangle$ are omitted for simplicity. Note that due to non-Hermiticity of the Hamiltonian, the eigenstates are not orthonormal, but instead biorthonormal [105]. The pairwise exchange symmetry can be read from the states written in the Fock-basis: States $|W_6\rangle$, $|D_9\rangle$, $|B_{13}\rangle$ and $|B_{14}\rangle$ are symmetric and states $|W_5\rangle$ and $|B_{12}\rangle$ antisymmetric. Asymmetry of the transmon parameters, such as waveguide and direct coupling removes the symmetry of states $|W_5\rangle$ and $|W_6\rangle$, which explains why both states are visible roughly at the same phase in Fig. 4.25. In the approximated states in the Fock-basis we have neglected the base vectors with amplitude smaller than 0.1. The exact values for the phases ϕ_i, ψ_i and φ_i are omitted for clarity. From these forms it is evident that the states $|W_{5,6}\rangle$ and $|F_{7,8}\rangle$ consist mainly of states with doubly occupied transmons, i.e. these states do not exist for two-level systems. Further, also the highest states $|B_{12}\rangle$,$|B_{13}\rangle$,$|B_{14}\rangle$ contain non-negligible amount of doubly occupied transmons, which is also not possible for qubits.

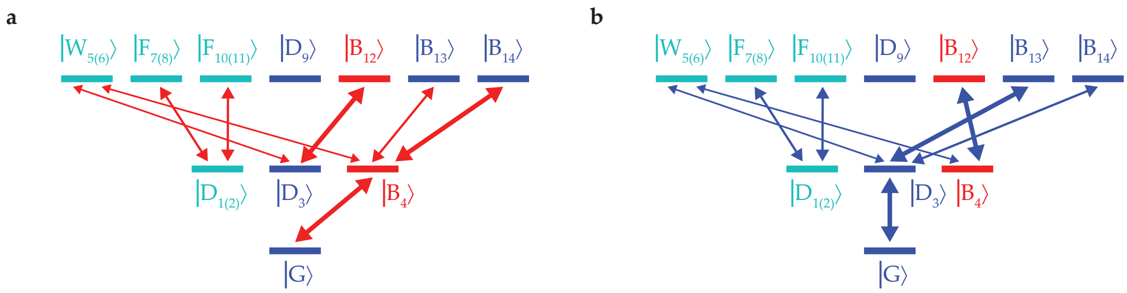

Figure 2.7: Transition symmetries. The state manifolds consist of symmetric (blue) and antisymmetric (red) superposition states, as well as states that have no symmetry with respect to the $\lambda/2$ distance but rather a local symmetry (turquoise) within the pairs. **a** Possible transitions for an antisymmetric drive or decay (red arrows). This resembles the waveguide symmetry, thus the red transitions can be driven by the waveguide field. **b** Possible transitions for a symmetric drive or decay (blue arrows). These transitions cannot be accessed by the waveguide field, meaning they do not radiate into the waveguide but also cannot be controlled by a propagating drive field. The local sideports can drive both red and blue transitions.

The dissipative dynamics cause transitions between the manifolds. We choose to assign a symmetry with respect to the exchange of the pairs which is defined by the operator $\hat{P} = |n_3n_4n_1n_2\rangle\langle n_1n_2n_3n_4|$. The symmetry defines which decay processes occur and which collective drive symmetry is needed to induce transitions between the states. If the pair-exchange operator leaves a state unchanged, i.e. $\hat{P}\,|\zeta\rangle = |\zeta\rangle$ the state is symmetric; if the state obtains a sign change, i.e. $\hat{P}\,|\zeta\rangle = -\,|\zeta\rangle$ it is antisymmetric. We show the symmetry of the superposition states and transitions in Fig. 2.7, where we use the same coloring of the state symmetries as in Fig. 2.6. Here, the symmetric and antisymmetric transitions are depicted as defined for operator $\hat{P}$. A drive that can realize antisymmetrical and symmetrical collective phases allows to drive the scheme depicted in Fig. 2.7a, as well as Fig. 2.7b. In the physical realization of our waveguide QED system the collective system is either driven through the waveguide, which is bound to the antisymmetric drive for a pair-separation of $\lambda/2$ or by two local access points that are located at the sites of the two pairs. The locality allows to manually set a specific phase relation between the sites, that effectively exposes the system to a collective drive phase that can be set by the microwave control electronics. In particular, this means that we are able to drive the dark state $|D_3\rangle$, that cannot be accessed thorough the waveguide but in return promises a long lifetime due to the radiative decay $\gamma_D = 0$.

The width of the arrows in Fig. 2.7 visualizes the relative magnitude of the state decay rate which also indicates how well a drive with matching symmetry induces transitions between them. They are not necessarily related to the decay rate because the available mode environment is set by the antisymmetric waveguide phase. The non-zero decay rates are listed in Tab. 2.1. Thus, we can conclude that we can indeed isolate specific states that do not have a decay rate, such as the dark state $|D_3\rangle$ but are still able to access them by a symmetric drive. In order to not limit the dark state decay time to the losses into the driving channel the ports have to be weakly coupled to the transmons.

Initial state	Final state	Decay rate/$\bar{\gamma}$
$\|B_4\rangle$	$\|G\rangle$	4.0
$\|W_5\rangle$	$\|D_3\rangle$	0.33
$\|W_5\rangle$	$\|B_4\rangle$	0.32
$\|W_6\rangle$	$\|D_3\rangle$	0.34
$\|W_6\rangle$	$\|B_4\rangle$	0.36
$\|F_7\rangle$	$\|D_1\rangle$	1.8
$\|F_8\rangle$	$\|D_2\rangle$	1.9
$\|F_{10}\rangle$	$\|D_1\rangle$	1.9
$\|F_{11}\rangle$	$\|D_2\rangle$	2.0
$\|B_{12}\rangle$	$\|D_3\rangle$	3.2
$\|B_{12}\rangle$	$\|B_4\rangle$	0.61
$\|B_{13}\rangle$	$\|B_4\rangle$	2.9
$\|B_{14}\rangle$	$\|D_3\rangle$	0.02
$\|B_{14}\rangle$	$\|B_4\rangle$	4.2

Table 2.1: Decay channels in the two-excitation manifold. Decay rates between individual states in the units of average individual transmon coupling to the waveguide. We have neglected transitions with a rate smaller than 0.01.

Driving the Dark Qubit

After solving the stationary master equation to obtain the collective spectrum of the one- and two-excitation manifold we investigate the system in the presence of a coherent drive. In particular, we want to find a drive that can excite the dark state $|D_3\rangle$. In the frame rotating with the drive frequency ω, the drive Hamiltonian reads

$$\hat{H}_\mathrm{d}/\hbar = \frac{\Omega}{2}\left[e^{i\phi}\left(\hat{a}_1 + \hat{a}_2\right) + \hat{a}_3 + \hat{a}_4 + \mathrm{h.c.}\right], \tag{2.51}$$

where Ω is the amplitude of the drive and ϕ is the phase difference between pairs. The phase ϕ changes the symmetry with respect to the exchange of the pairs, but its is always symmetric with respect to the exchange of transmons inside the pairs. For the waveguide drive the phase relation is limited to the $\lambda/2$ condition thus $\phi = \pi$. To address the system with arbitrary drive phase relations it is necessary to engineer local control at the sites. This means that the drive is not allowed to excite the waveguide, otherwise the symmetry is always bound to $\phi = \pi$. In the theory, we assume that we can set arbitrary phases ϕ.

Two local sideports, like the ones that we engineered in our setup, allow to control the symmetry of the drive and thus couple different states in the neighboring manifolds by altering the phase between the pairs. For small amplitudes, the drive acts as a perturbation and does not change the eigenstates of the effective Hamiltonian, thus the frequencies and decay rates of Fig. 2.6 are still valid. The assumed drive acts with equal amplitude and phase within the pair, however in the experiment it has an amplitude gradient Ω_δ. This introduces an additional driving term that is always antisymmetric with respect to the exchange of transmons within the pair

$$\hat{H}_{\mathrm{d,asym}}/\hbar = \frac{\Omega_\delta}{4}\left[e^{i\phi}\left(\hat{a}_1 - \hat{a}_2\right) + \hat{a}_3 - \hat{a}_4 + \mathrm{h.c.}\right]. \tag{2.52}$$

The phase and amplitude gradient over the pairs explains why we are able to excite the local dark states $|D_1\rangle$ and $|D_2\rangle$ in Fig. 4.25 and Fig. 4.12.

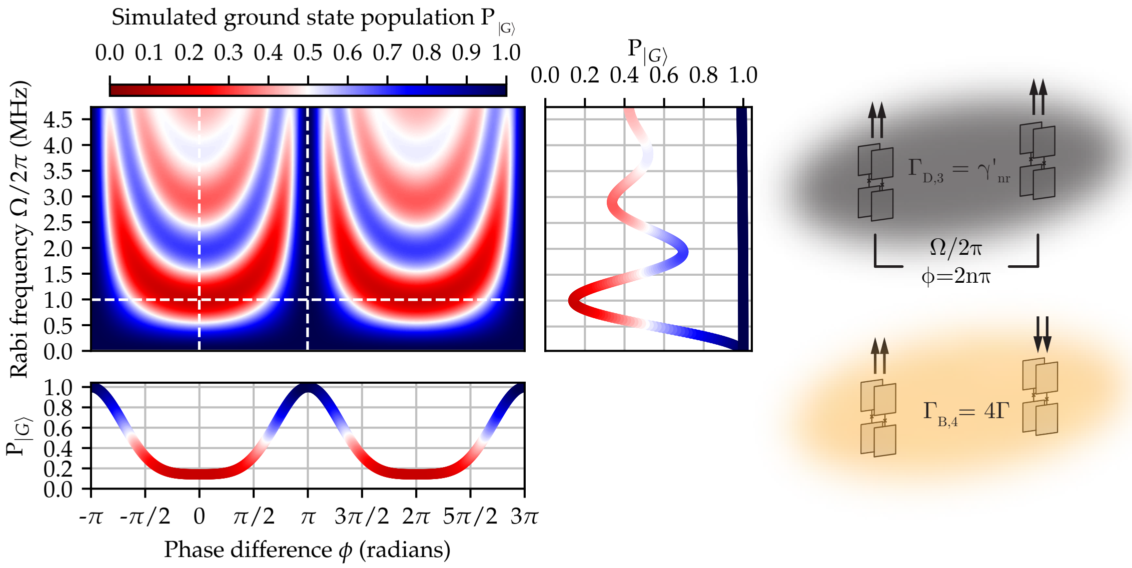

Figure 2.8: Simulated ground state population after the Rabi pulse. The dynamics of the system is solved numerically from the master equation while altering the phase and amplitude of the driving Hamiltonian. After the Rabi pulse, lasting 240 ns, the ground state population is calculated. The Rabi pulse is not perfect, since the ground state population does not go to zero. On the right side we sketch the dark state (top) that is used to store quantum information and controlled by the variable-phase drive. The readout state (bottom) decays to the ground state due to the waveguide environment, such that the scattering properties of the transition can be utilized to read out the ground state population.

A transition amplitudes of the ground state $|G\rangle$ to the non-local dark state $|D_3\rangle$ and bright state $|B_4\rangle$ depend on the phase ϕ of the driving Hamiltonian $\hat{H}_\mathrm{d}$ as [87]

$$|G\rangle \to |D_3\rangle : \quad \frac{\hbar\Omega}{2}\left(1 + e^{i\phi}\right), \tag{2.53}$$

$$|G\rangle \to |B_4\rangle : \quad \frac{\hbar\Omega}{2}\left(1 - e^{i\phi}\right). \tag{2.54}$$

By numerically simulating the effect of the drive on the qubit system we observe periodically Rabi-oscillations between $|G\rangle$ and $|D_3\rangle$ in Fig. 2.8 when the amplitude of the drive field Ω is increased and the phase relation matches $\phi = 2n\pi$ $(n \in \mathbb{Z})$. For an antisymmetric drive with odd integer multiple $\phi = (2n-1)\pi$, we only drive the bright state $|B_4\rangle$ which decays very rapidly to the ground state with the rate $\Gamma_{\mathrm{B},4} = 4\Gamma$, see table 2.1. For phases that are neither fully symmetric nor antisymmetric we drive both states simultaneously, where the respective drive strength is weakened for imperfect antisymmetric phases.

Dark State Coherence

The dark state $|D_3\rangle$ forms a decoherence-free subspace in the Hilbert space of the coupled transmon system by effectively decoupling from the waveguide drive and noise that causes the states to relax back to the ground state $|G\rangle$. They have the ability to be utilized to construct a universal quantum computation platform in waveguide QED [25]. A coupled many-body system is not only subjected to the individual transmon decoherence mechanism but instead the lifetime T_1 and coherence time T_2 of the collective dark state $|D_3\rangle$ are affected by additional noise contributions. The master equation in the zero and one-excitation manifolds can be solved analytically for identical transmon parameters. The correlations between the ground state and dark state evolve in time according to

$$\rho_{03}(t) = \rho_{03}(0)e^{-it(\omega+J)}e^{-t\frac{\gamma_\mathrm{nr}+\gamma_\phi+K_\phi}{2}}, \tag{2.55}$$

from which we identify the characteristic coherence time

$$T_2 = \left(\frac{\gamma_\mathrm{nr}+\gamma_\phi+K_\phi}{2}\right)^{-1}. \tag{2.56}$$

The lifetime T_1 is actually measured using the ground state population. The time evolution is solved from the master equation by assuming that the system is initially in the dark state

$$1 - p_0(t) \approx e^{-t\left(2\gamma+\gamma_\mathrm{nr}+\frac{\gamma_\phi}{2}-\frac{1}{2}\sqrt{16\gamma^2+4\gamma\gamma_\phi+\gamma_\phi^2}\right)}, \tag{2.57}$$

from which we recover the characteristic energy decay time

$$T_1 = \left(2\gamma + \gamma_\mathrm{nr} + \frac{\gamma_\phi}{2} - \frac{1}{2}\sqrt{16\gamma^2 + 4\gamma\gamma_\phi + \gamma_\phi^2}\right)^{-1}. \tag{2.58}$$

Thus, we conclude that the coherence time of the dark state $|D_3\rangle$ depends on the non-radiative decay γ_nr as well as pure local and global dephasings γ_ϕ and K_ϕ. Interestingly also the lifetime depends on the local dephasing. This happens because the local dephasing causes transitions from the dark state $|D_3\rangle$ to the bright state $|B_4\rangle$, which decays through the waveguide.

Even though local dephasing also causes transitions to e.g. the local dark states $|D_1\rangle$ and $|D_2\rangle$, they do not decay into the waveguide thus do not influence T_1. In addition, flux noise that affects the transmons causes unintentional frequency tuning. In the worst case one transmon is detuned to higher frequencies and the other to lower frequencies, which causes symmetry imperfections and a finite waveguide coupling linewidth, similar to the observations in Fig. 2.4.

CHAPTER 3

Experimental Techniques

While many microwave components are commercially available, the key building blocks of superconducting waveguide QED - waveguides and artificial atoms - are individually designed and fabricated such that the parameters can accurately be tailored to the needs of the experiment. The waveguide middle section is fabricated in the mechanical workshop of the Institute of Quantum Optics and Information (IQOQI) where it is milled out of a block of high purity copper. It serves as the sample box, as well as the propagation channel for the microwave photons. After introducing the field characteristics of the waveguide in the first section, we focus on the superconducting qubit design and fabrication. The Quanten-Nano-Zentrum Tirol cleanroom facility was opened in the beginning of 2018 where we started to implement the qubit fabrication by adapting the 3D transmon recipe from the group of Ioan Pop at the Karlsruher Institute of Technology. The last section gives an overview on how the transmon sample is mounted into the waveguide and cooled down to millikelvin temperatures in a dilution refrigerator. The necessary isolation from the environment imposes critical requirements on the wiring that typically starts at room temperature and is routed to the base plate. We then briefly discuss the spectroscopic and pulsed measurement setup to understand the different signal generation and processing schemes. Primarily, the choice of the setup depends on the studied timescales.

3.1 The Rectangular Waveguide

Rectangular waveguides for microwave frequencies are hollow metal tubes with conducting walls. With the development of microwave sources, such as the Barkhausen-Kurz tube and the split-anode magnetron, interest in low-loss transport of microwaves began in the 1930s [106]. The dimensions of the hollow core are on the same order as the largest mode wavelength that can be transmitted, resulting in different cutoff frequencies for different waveguide sizes. Each mode has a specific polarization and can be categorized in TE (transverse electric) and TM (transverse magnetic) modes. TEM (transverse electromagnetic) modes require a second conductor and thus do not propagate in a rectangular waveguide. For practical reasons the most common standardized waveguides range from frequencies between 320 MHz to 330 GHz with corresponding inner dimensions $584\,\mathrm{mm} \times 292\,\mathrm{mm}$ to $0.9\,\mathrm{mm} \times 0.4\,\mathrm{mm}$[1]. The lowest frequencies where current quantum circuits are currently operated are about 100 MHz for fluxonium modes [107] and usually do not go above 16 GHz due to frequency-optimized commercial microwave components. This means that rectangular waveguides are much bigger than their

[1]https://en.wikipedia.org/wiki/Waveguide_(radio_frequency)

integrated transmission line analogue. However there are ideas to combine the advantages of both approaches [108].

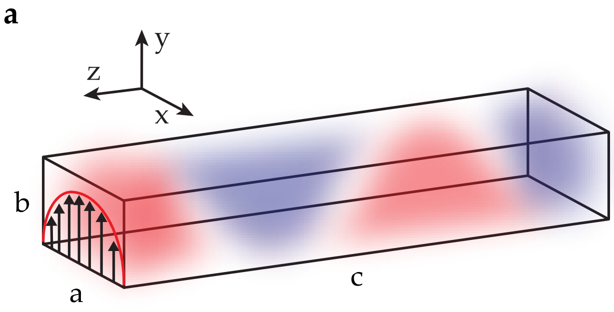

Figure 3.1: Rectangular waveguide. a Schematic of a rectangular waveguide. The electrical field lines of the fundamental mode TE_{10} are parallel to the y-axis and therefore perpendicular to the propagation direction z. Different colors of the propagating field indicate the changing phase through the waveguide. **b** The middle section of the waveguide is milled out of a copper block where the inner dimensions determine the cutoff frequencies. Here only the largest width of $a = 22.9\,\mathrm{mm}$ results in the fundamental mode cutoff frequency f_{10}=6.546 GHz. The clamps on top of the waveguide thermalize the qubits and have two coils attached that can be used to change the emission frequency of the qubits.

The design of the waveguide is defined by two parameters that determine the cutoff of the propagating modes: the width a and height b of the inner hollow volume in Fig. 3.1a. The finite length c of the waveguide middle section, shown in Fig. 3.1b requires the usage of adapters that have to transform the waveguide impedance $Z \sim 500\,\Omega$ to the impedance of the coaxial lines $Z = 50\,\Omega$. Imperfections in the impedance matching cause standing waves inside the waveguide that lead to deviations from the following analytical description. In the rectangular waveguide, we can distinguish modes with no electrical field (TE) and no magnetic field (TM) in propagation direction. Modes with no electromagnetic field (TEM) in propagation direction need a second conductor and can therefore not be excited. TE modes of the rectangular waveguide have no electrical field component in the direction of propagation $E_z = 0$, while the magnetic field $H_z(x, y, z) = h_z(x, y)e^{-i\beta z}$ has to fulfill the reduced wave equation [88]

$$\left(\frac{\partial^2}{\partial x^2} + \frac{\partial^2}{\partial y^2} + k_c^2\right) h_z(x, y) = 0. \tag{3.1}$$

Here we introduced the cutoff wave number $k_c = \sqrt{k^2 - \beta^2}$ with wavevector k and the propagation constant

$$\beta = \sqrt{k^2 - k_c^2} = \sqrt{k^2 - \left(\frac{m\pi}{a}\right)^2 - \left(\frac{n\pi}{b}\right)^2}, \tag{3.2}$$

where $m, n \epsilon \mathbb{N}_0$. The waveguide TE_{mn} modes obtain transverse field components

$$\begin{aligned}
E_x &= \frac{j\omega\mu n\pi}{k_c^2 b} A_{mn} \cos\frac{m\pi x}{a} \sin\frac{n\pi y}{b} e^{-j\beta z}, \\
E_y &= \frac{-j\omega\mu m\pi}{k_c^2 a} A_{mn} \sin\frac{m\pi x}{a} \cos\frac{n\pi y}{b} e^{-j\beta z}, \\
H_x &= \frac{j\beta m\pi}{k_c^2 a} A_{mn} \sin\frac{m\pi x}{a} \cos\frac{n\pi y}{b} e^{-j\beta z}, \\
H_y &= \frac{j\beta n\pi}{k_c^2 b} A_{mn} \cos\frac{m\pi x}{a} \sin\frac{n\pi y}{b} e^{-j\beta z}.
\end{aligned} \tag{3.3}$$

Here where A_{mn} are arbitrary amplitude constants and j is the imaginary unit. For a mode

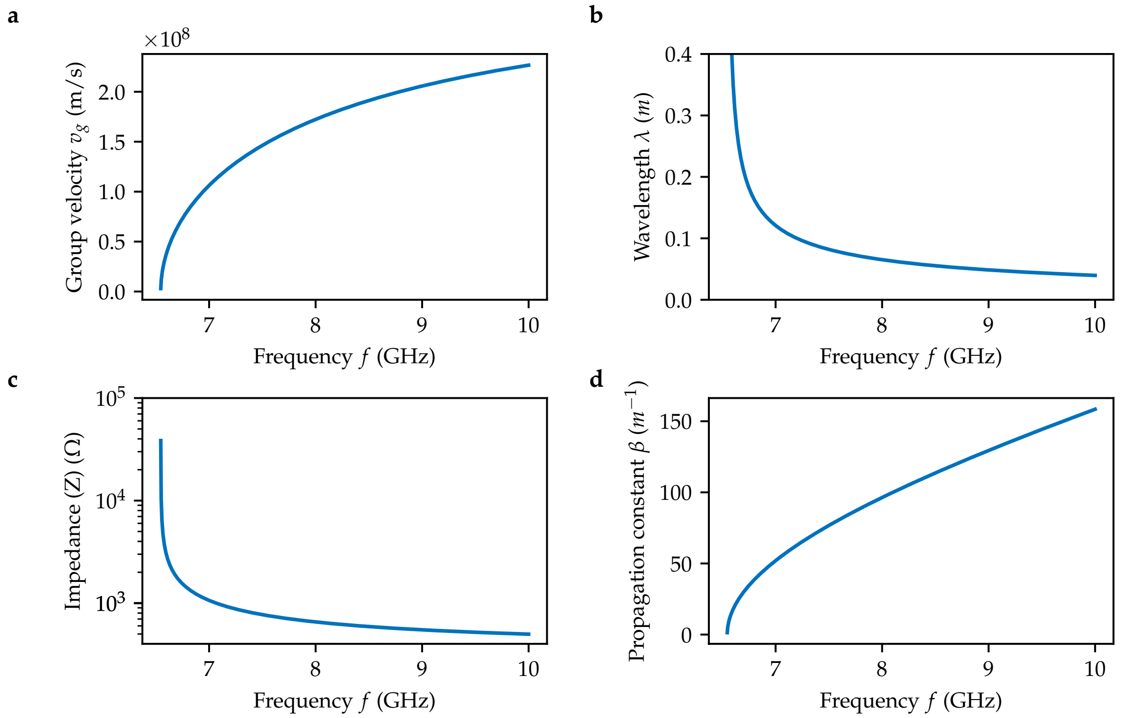

Figure 3.2: Characteristic properties of a WR90 waveguide. **a** The group velocity v of a microwave travelling through the waveguide. For high frequencies it approaches the vacuum speed of light $c = 3 \times 10^8\,\mathrm{m\,s^{-1}}$. **b** The wavelength inside the waveguide changes very rapidly close to the cutoff frequency. **c** The wave impedance slowly approaches the free space impedance $Z_0 = 376\,\Omega$. **d** The propagation constant visualizes the non-linear dispersion of the rectangular waveguide, especially around the cutoff.

to propagate, the wavevector k has to be larger than the cutoff wavevector k_c

$$k > k_c = \sqrt{\left(\frac{m\pi}{a}\right)^2 + \left(\frac{n\pi}{b}\right)^2}. \tag{3.4}$$

For $k < k_c$ the modes correspond to evanescent waves whose fields cannot propagate through the waveguide. Conditioned on the length c of the waveguide and the applied power it is still possible to experimentally measure transmission below the cutoff and investigate bound state physics [78]. The mode with the smallest cutoff frequency is called the dominant or fundamental mode. For $a > b$ the fundamental cutoff frequency only depends on the width a, the permittivity ϵ and the permeability μ.

$$f_{c,10} = \frac{1}{2a\sqrt{\mu\epsilon}}. \tag{3.5}$$

The middle section of the rectangular waveguide (without the coaxial adapters), shown in Fig. 3.1b is fabricated from oxygen-free high purity copper with inner volume dimensions 10.2 mm × 22.9 mm × 100 mm, such that the fundamental cutoff frequency $f_{c,10} = 6.546\,\mathrm{GHz}$ only depends on the longest extension a = 22.9 mm perpendicular to the propagation direction, the vacuum permittivity ϵ and permeability μ. This mode has a polarization of the electric field that is parallel to the y-axis and a sinusoidal field amplitude with the maximum at the center. This is important for the coupling strength between the mode and a dipole antenna, such as the transmon qubit. The next higher mode cutoffs are the TE_{20} mode at $f_{c,20} = 13.091\,\mathrm{GHz}$ and TE_{01} mode at $f_{c,01} = 14.696\,\mathrm{GHz}$. For frequencies above the cutoff, the electromagnetic mode propagates through the hollow core of the waveguide with propagation constant $\beta = \sqrt{k^2 - k_c^2}$, defined by difference of the wavevector $\mathrm{k} = \omega\sqrt{\epsilon\mu}$ and the cutoff wavevector $\mathrm{k_c} = \pi/a$. For real β the wave impedance

$$Z_{TE} = \frac{E_x}{H_y} = \sqrt{\frac{\mu}{\epsilon}}\frac{k}{\beta} \tag{3.6}$$

is also real and relates the transverse electric and magnetic fields. The wavelength in the waveguide is defined as

$$\lambda = \frac{2\pi}{\beta}, \tag{3.7}$$

which is in general larger than the wavelength of a plane wave in vacuum $\lambda = 2\pi/k$. The characteristic properties for such a rectangular waveguide are plotted in Fig. 3.2. Especially, close to the cutoff frequency the dispersion is not linear, enabling the creation of chirped pulses to address individual qubits in the waveguide [109].

3.2 Finite Element Simulation of Linear Circuits

Simulating classical circuits of dielectrics and conducting materials with a finite element simulation software has become a standard tool to investigate the sample behavior before the costly physical construction. The simulation already gives approximate quantities of the defining parameters, even for complicated circuits, where it can be difficult to find analytical solutions. Figure 3.3a shows the Ansys HFSS[2] model of a rectangular waveguide QED setup that consists of a perfect conducting box with a vacuum hollow core of dimensions 10.2 mm × 22.9 mm × 100 mm to achieve the fundamental cutoff frequency $f_{c,10} = 6.546\,\mathrm{GHz}$. The ends of the box are terminated with two waveports that send waves from one side of the waveguide to the other and are used to extract quantities like S parameters, etc.

The qubit substrate is modeled as a sapphire[3] box with dimensions 16 mm × 2 mm × 0.33 mm, where the thickness of 0.33 mm is specifically for the 2" sapphire wafers that were used in

[2] https://www.ansys.com/products/electronics/ansys-hfss
[3] from the HFSS material database

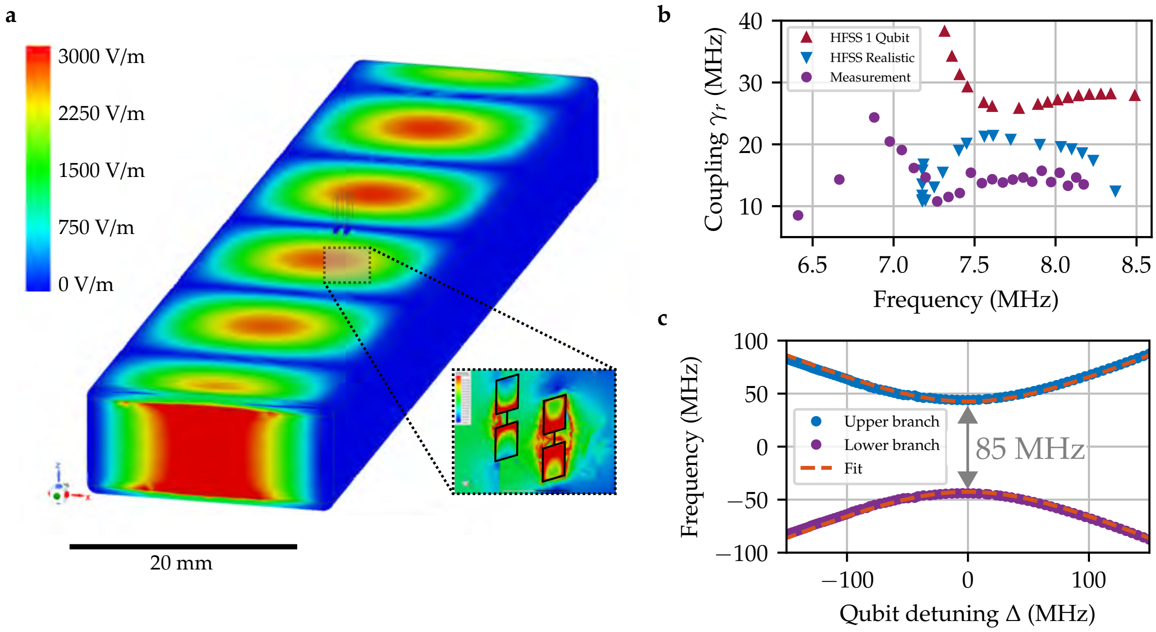

Figure 3.3: Ansys HFSS simulation. a The model consists of a box containing the electromagnetic propagating modes and the transmon qubits (inset). The orientation of the dipole is parallel with the electric field, for which the magnitude is plotted. **b** For a single qubit, we can extract the qubit coupling to the waveguide and compare it to the measured values. We can see that the simulation that also considers the resonances of the other qubits is shifted more towards the measured values. **c** The direct capacitive coupling of two transmons is obtained from an eigenmode simulation, by changing the lumped inductance of one transmon.

the fabrication. Typically we also use 2" and 4" wafers with a thickness of 0.43 mm. The width and height of the substrate can be chosen arbitrarily and depend on the design of the qubit and the anticipated mounting procedure in the sample box. For the transmon model it is helpful to use practical design parameters, e.g. from Refs. [11, 34, 84, 110]. Here, the transmon pads are modeled by perfectly conducting sheets placed on the surface of the substrate with dimensions 0.4 mm $\times$ 0.5 mm (width x height), separated by a 0.2 mm gap, effectively forming a 1.2 mm long dipole antenna parallel to the electrical field component of the propagating waveguide field. The pads are connected by a lumped element inductance L_J that models the Josephson junction which is the dominant contribution of the full transmon inductance. The second transmon is located 1 mm away from the first transmon such that they sit symmetrically around the center of the waveguide.

After simulating the model with the driven modal solution type of HFSS the complex S parameters are extracted. The transmon antenna dipole $\vec{d}$ is designed parallel to the electrical field $\vec{E}$, such that the the product $\vec{d} \cdot \vec{E}$ becomes one dimensional and yields the coupling strength between the waveguide field and the qubit. This dipole-coupling is responsible that the electromagnetic signal of the waveguide interacts with the qubit and changes the transmission around the resonance frequency of the qubit. Changing the antenna design or moving it horizontal to the propagation direction influences the coupling strength [84]. The emerging resonance in the simulated waveguide transmission S_{21} between port 1 and port 2, that are located on opposite faces along the propagation direction, gives direct access to the coupling strength between the qubit and the waveguide mode. The initial unit transmission decreases due to scattering with the fundamental transmon transition. Note, that the transmon qubit is modeled as a harmonic oscillator in HFSS and does not capture typical transmon characteristics like the anharmonicity or power saturation. The resonance is treated similar to the experimental data, such that we can extract the resonance frequency f_{01} and coupling quality factor Q_c from the circle-fit routine [111, 112], that we use to calculate the radiative linewidth $\gamma_r = 2\pi f_{01}/Q_c$. The transmon frequency $f_{01} = \frac{1}{2\pi\sqrt{LC}}$ is changed by varying the value of the lumped inductance $L_J \approx L$. The coupling for a fixed transmon geometry is extracted at different frequencies and plotted against the resonance frequency in Fig. 3.3b. Compared to the measured radiative linewidths the simulated values are overestimated. This can be corrected when we model a scenario that is closer to the measured sample by including the other transmons in the simulation. In the measurement the resonance frequency of the neighboring qubit was $f_2 = 8.7\,\text{GHz}$, while the distant qubits resoannce frequencies were $f_3 = 6.8\,\text{GHz}$ and $f_4 = 6.5\,\text{GHz}$. By choosing the corresponding inductances in the simulation we see that this brings the values closer to the measured coupling rates. With knowledge of the inductance L_J and the extracted resonance frequency the shunt capacitance of the pads is extracted $C = \frac{1}{(2\pi f)^2 \cdot L_J} = \frac{1}{(2\pi \cdot 8.82\,\text{GHz})^2 \cdot 5\,\text{nH}} = 64\,\text{fF}$.

The eigenmode solver of HFSS offers a fast way to extract the capacitive coupling between two adjacent qubits. By assigning a constant lumped inductance for one qubit and changing the inductance of the other qubit we simulate the same model as depicted in Fig. 3.3a around a frequency where no other modes are present. In this case the waveguide is kept at the same size, the waveports are removed and the constant frequency qubit is set to 7.7 GHz. When tuning the other qubit in resonance by changing its inductance the avoided crossing in Fig. 3.3c is observed. By fitting the two branches we can find the frequency where the qubits are resonant, which is at the minimal distance of the branches. The splitting $2J = 85\,\text{MHz}$ yields the coupling rate J_{ij} for the qubits, that we also simulated with the quantum optics simulation software QuTiP [26] in Fig. 2.4.

3.3 Transmon Qubits

The finite element simulation in Sec. 3.2 already provides transmon parameters by modeling the qubits as harmonic oscillators. However, the key element of the transmon is a nonlinear Josephson junction that makes the circuit anharmonic. When designing transmon qubits for 3D waveguide QED experiments, there are multiple parameters to optimize for: the resonance frequency f_0, the anharmonicity α, the transmon ratio E_J/E_C, as well as the range of tunability for double junction transmons with minimal frequency f_{min} and maximal frequency f_{max}. Before describing the fabrication process of the transmons in Sec. 3.3.2 we calculate and summarize the parameters for the fabrication in Sec. 3.3.1.

3.3.1 Design Parameters

The transmon parameters are mainly defined by the shunt and junction capacitances and the inductance of the Josephson junction. From HFSS simulation, where the transmon antenna consists of two aluminum pads of size $400\,\mu\text{m} \times 500\,\mu\text{m}$, we extract the shunt capacitance

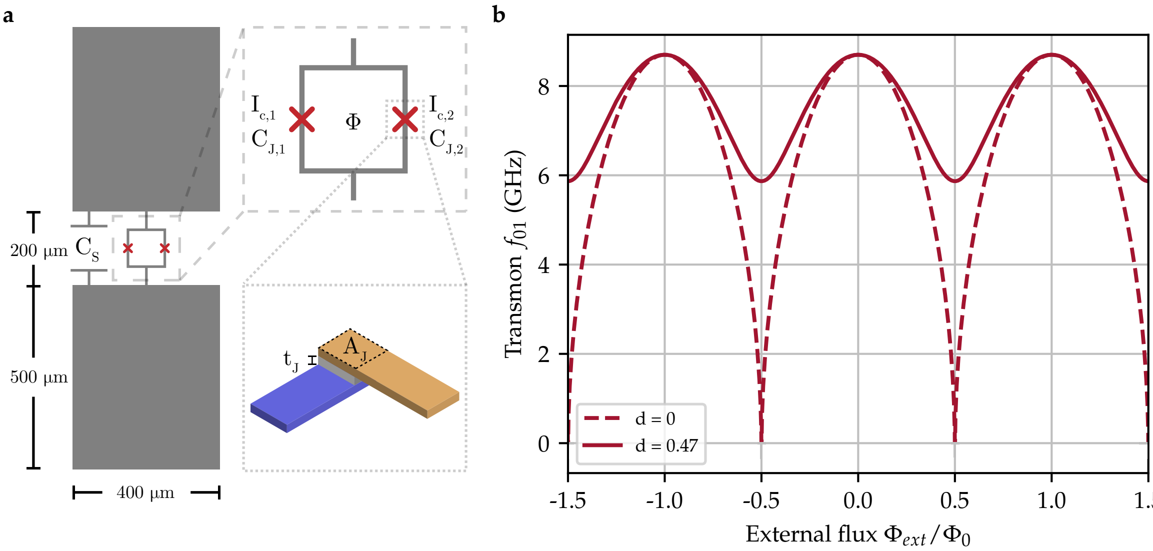

Figure 3.4: Transmon qubit. a The physical qubit consists of a shunt capacitance of two large metallic pads and two Josephson junction, in order to enable flux tunability. The Josephson junction is created by two metallic electrodes (blue and orange) that are separated by an insulating oxide barrier (grey). **b** Transmons with two junctions in parallel are flux tunable. The minimum frequency of identical critical currents, i.e. $d = \dfrac{I_{c,1} - I_{c,2}}{I_{c,1} + I_{c,2}} = 0$ goes to zero, while different critical currents cause a tuning minimum that can be useful to decrease the sensitivity to flux noise. The critical current I_c is defined by the junction area and the oxide barrier.

$C_S = 64\,\mathrm{fF}$. The second main contribution of the transmon capacitance C_Σ is the junction capacitance arising from the metallic electrodes and the insulating oxide barrier, schematically sketched in Fig. 3.4a. The barrier thickness is assumed to be $t = 1.5\,\mathrm{nm}$ [113, 114]. We approximate the junction capacitance as a parallel plate capacitor with area A_J vacuum permittivity ϵ_0 and dielectric constant $\epsilon_{\mathrm{r,AlOx}} \approx 10$ [110, 115] such that

$$C_J = \epsilon_0 \epsilon_{\mathrm{r,AlOx}} \frac{A_J}{t}. \tag{3.8}$$

To make the transmon flux-tunable we incorporate two Josephson junctions that are arranged in a parallel configuration at the center between the transmon pads, see Fig. 3.4a. To decrease the sensitivity to flux noise and obtain a low flux-sweetspot we design them with two different junction areas $A_{J,1} = 200\,\mathrm{nm} \times 1400\,\mathrm{nm}$ and $A_{J,2} = 200\,\mathrm{nm} \times 500\,\mathrm{nm}$. The different electrode areas and the shunt electrodes yield the total transmon capacitance

$$C_\Sigma = C_S + C_{J,1} + C_{J,2} = 64\,\mathrm{fF} + 16.5\,\mathrm{fF} + 6\,\mathrm{fF} = 86.5\,\mathrm{fF}, \tag{3.9}$$

corresponding to a charging energy $E_C = 224\,\mathrm{MHz}/h$. The target frequency of the transmon is set to $f_{01} = 8.7\,\mathrm{GHz}$, such that the resulting target Josephson energy is determined by

$$E_J = \frac{(hf_{01} + E_C)^2}{8E_C} = 44.41\,\mathrm{GHz}/h. \tag{3.10}$$

This means that we have to distribute the total critical current $I_{c,tot} = \frac{2\pi E_J}{\Phi_0}$ according to the area ratio of the split-junction. Here, $\Phi_0 = 2e/h$ is the magnetic flux quantum, e the electron charge and h the Planck constant. The junction asymmetry $d = \dfrac{I_{c,1} - I_{c,2}}{I_{c,1} + I_{c,2}} \neq 0$ causes the extra term in Eq. (1.24), which effectively reduces the tuning range, sensitivity to flux changes and provides a low flux-sweetspot, as shown in Fig. 3.4b. The junction critical currents are then

$$I_{c,tot} = \frac{2\pi E_J}{\Phi_0} = 89.42\,\mathrm{nA} \tag{3.11}$$

$$I_{c,2} = \frac{I_{c,tot}}{A_{J,1}/A_{J,2} + 1} = 23.88\,\mathrm{nA} \tag{3.12}$$

$$I_{c,1} = I_{c,tot} - I_{c,2} = 65.54\,\mathrm{nA} \tag{3.13}$$

Figure 3.4b shows the resulting transition frequency of the transmon $f_{01} = E_{01}/h$ as a function of the normalized external flux Φ_{ext}/Φ_0. The total transmon energy E_{01} is given by the equation

$$E_{01} = \sqrt{8E_C \frac{\Phi_0(I_{c,1} + I_{c,2})}{2\pi} \cos\frac{\pi\Phi_{ext}}{\Phi_0} \sqrt{1 + d^2 \tan^2 \frac{\pi\Phi_{ext}}{\Phi_0}}} - E_C. \tag{3.14}$$

The designed qubit is tunable in the range 5.9-8.7 GHz corresponding to ratios $E_J/E_C = 96 - 198$, well within the transmon regime.

Typically we probe the resistance from one pad to the other at room temperature to determine the critical current I_c of the Josephson junction before cooling down the device. At room temperature, the tunnel barrier behaves like an ohmic resistor that dominates over the resistance of the metal such that the maximal Josephson energy E_J can be estimated by measuring the normal state resistance of the junction R_n, which is related to the critical current $I_{c,tot}$ by the Ambegaokar-Baratoff formula [110, 116]

$$I_c R_n = \frac{\pi}{2e}\Delta(T)\tanh\left(\frac{\Delta(T)}{2k_B T}\right), \tag{3.15}$$

with the Boltzmann constant k_B and the electron charge e. The equation relates the critical current and normal-state resistance only by the material properties and temperature, where $\Delta(T)$ is the superconducting energy gap at temperature T. For $T = 0$ the Ambegaokar-Baratoff Eq. (3.15) simplifies to

$$I_c R_n = \frac{\pi\Delta_\mathrm{c}(0)}{2e}, \tag{3.16}$$

where $\Delta_\mathrm{c}(0) = 180\,\mu eV$ was extracted from the first transmons that were fabricated in the QNZT cleanroom. R_n was measured just before cooling down the samples and compared to the measured resonance frequencies and anharmonicities. $\Delta_\mathrm{c}(0)$ therefore serves as a direct conversion parameter between R_n and the maximal transition frequency f_{01}. Typically we observe an increase of the normal state resistance of up to 10% in the first week after fabrication. Thus, for a target transition frequency of $f_{01} = 8.7\,\mathrm{GHz}$ and charging energy $E_C = 224\,\mathrm{MHz}/h$ the normal state resistance is

$$R_n = \frac{\pi\Delta_\mathrm{c}(0)}{2eI_c} = \frac{\pi \cdot 180\,\mu eV}{2e \cdot 89.42\,\mathrm{nA}} = 3.16\,\mathrm{k\Omega}. \tag{3.17}$$

During the first cooldown of the transmon samples we extracted the maximal frequency presented in table 3.1 and compared to the calculated value by room temperature resistance

	R_n (kΩ)	$f_{01,\max}$ (GHz)	$f_{01}(R_n)$ (GHz)
Q_1	3.11	8.69	8.67
Q_2	3.12	8.66	8.72
Q_3	3.26	8.77	8.58
Q_4	3.12	8.73	8.41

Table 3.1: R_n to f_{01} conversion. The measured room temperature resistance is used to calculate the transition frequency $f_{01}(R_n)$, which can then be compared to the measured value $f_{01,\max}$. To calculate the expected resonance frequencies $f_{01}(R_n)$ we used the extracted charging energies E_C from the anharmonicity measurement in Sec. 4.1.

measurements. We notice a spread in the room temperature resistance, as well as in the maximal resonance frequencies. Qubit 3 shows a higher resistance compared to the others and surprisingly also a higher resonance frequency. We attribute the inaccuracies to the changes in the oxide barriers during the cooldown, that can be different for the individual Josephson junctions. In the course of the experiments the samples were cooled down several times where we additionally observe that the maximal frequency decreases with each cooldown. To avoid any damaging of the samples we only probed the room temperature resistance before the initial cooldown. The flux maps presented in Fig. 4.2 are recorded after several cooldowns and show that the maximal frequency of the transmons is significantly lower compared to the values in table 3.1 corresponding to the first cooldown.

3.3.2 Fabrication of 3D Transmons

a

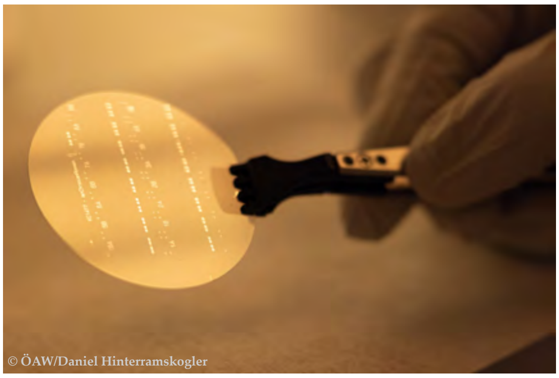

b

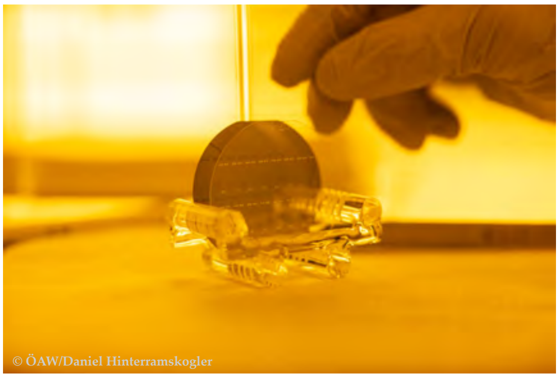

Figure 3.5: Wafer scale fabrication in the QNZT cleanroom facility. a The processed wafer before dicing the qubit chips into pieces (cut-lines indicated by the right angles). **b** Two wafers in a custom-designed wafer boat.

The transmons are fabricated in the facilities of the Quanten-Nano-Zentrum Tirol (QNZT), that was opened in 2018. The transmon qubit design is patterned into a bi-layer resist stack by electron-beam lithography with a Raith eLINE Plus 30 kV. The initial goal was to adapt the 3D transmon design from the Pop group at the Karlsruher Institute of Technology (KIT), which uses sapphire substrates. In hindsight, using a conductive substrate, e.g. high-resistivity silicon that does not require an additional anti-charging layer simplifies the process development and could have saved some time.

Wafer Preparation

The fabrication is done on c-plane sapphire (0001) disks from Crystec (Kyocera) with thickness 330 µm ± 25 µm and diameter 50.8 mm, depicted in Fig. 3.5a (already containing the circuit structures). For our purposes the 2-inch wafers have proven to be a good trade-off between costs and yield, thus we process the full wafer to obtain multiple chips in a single fabrication run and then select the transmons with the best parameters for the cooldown from room-temperature measurements. For better orientation during the fabrication they have a 16 mm standard flat and an engraved serial number (e.g. KC001351). The internal convention to use the backside of the wafer for the circuit structures helps to reduce errors, especially when fabrication steps are done by different people. The wafers are polished on both sides, therefore it is difficult to distinguish between the front and backside. If you can read the serial number you need to turn the wafer upside down to look at the side that is being processed. Alternatively, high-resistivity silicon is a commonly used substrate option due to the low dielectric loss and extensive use in semiconductor integrated circuits.

The initial cleaning step of the sapphire wafers is done in a mixture of sulfuric acid (H_2SO_4) and hydrogen peroxide (H_2O_2), known as piranha solution. The etching removes organic residues from the substrates such that the initial processing conditions depend less on the wafer-handling before arrival in the cleanroom. The mixture is a strong oxidizer, thus will remove most organic matter from the sapphire surface but also adds OH groups, making it very hydrophilic. As we usually do the cleaning for a few (∼10) wafers on a specific day, it is important to consider the time difference between the cleaning and the next processing step. The surface conditions change during storage and the hydrophilicity weakens. In the past, we could only detect the increased hydrophilicity when we added an oxygen plasma before spinning the resist and after piranha cleaning. There, the resist no longer stayed on the wafer surface but immediately crept under it due to the reduced surface tension. The piranha cleaning is done in a large beaker using the quartz wafer boat, depicted in Fig. 3.5b. It was fabricated at the "Center for Chemistry and Biomedicine (CCB)[4]". With this boat it is possible to clean 5 wafers simultaneously. It is important that the wafers are already reasonably clean and completely free of solvents to avoid very heavy reactions and possible explosions or overflowing. Filling the large beaker with 300 ml sulfuric acid allows to almost fully submerge the wafers. Then 100 ml of hydrogen peroxide is added. The reaction is exothermic and the solution gets hot. The wafers are cleaned for 10 min. If the reaction gets weaker, the beaker can be put on a hotplate. The Wikipedia article[5] points out the risks and explains the handling procedure of piranha solutions. After 10 min the wafer boat is transferred into a second beaker that is filled with deionized water to rinse off the piranha solution. One by one, the individual wafers are taken

[4]https://www.uibk.ac.at/aatc/glasblaeserei.html
[5]https://en.wikipedia.org/wiki/Piranha_solution

out of the water, rinsed with deionized water, dry blown and put into wafer boxes for storage.

	Piranha cleaning
Chemical compound	$H_2SO_4 : H_2O_2$ (3:1)
Protocol	Fill beaker with 300 ml H_2SO_4 Submerge wafers using the quartz holder Add 100 ml H_2O_2 Solution gets hot and starts boiling Etch 10 min, stir with wafer holder if reaction gets weaker or use hotplate Transfer holder into second beaker, filled with deionized water, rinse, blow dry with N_2

Resist and Anti-Charging Layer

Coating the surface of the substrate with electron beam sensitive resist allows to imprint patterns with an electron beam lithographic (EBL) machine. Resists, like polymethyl methacrylate (PMMA) can be positive resists, i.e. when they are exposed they undergo a chain scission and become soluble. Negative resists are based on free radicals that cross-link when they are exposed and become insoluble.

For the transmon fabrication we spincoat a bi-layer stack consisting of a 1000 nm thick copolymer bottom layer MMA(8.5)MAA EL13 and a 240 nm thick PMMA top layer 950 PMMA A4 onto the substrate. The top layer is used to define the main structures while the bottom layer has a higher sensitivity, such that it can also be exposed without exposing the top layer. This higher sensitivity is utilized for designing Josephson junctions. When only the bottom layer resist is removed next to a trench, the top layer serves as a shadow for a directional metal evaporation, depicted in Fig. 3.6. The angle of the evaporation then determines if the metal reaches the substrate or not. For a specific resist the thickness is mainly defined by the rotation speed of the spin coater which can be taken from the spin curve, usually provided by the manufacturer but also depends on airflow, applied quantity and solvent evaporation. Thus the thickness has to be calibrated and is always measured and logged. To achieve the desired resist thicknesses with the Suess Microtec LabSpin6, we spin the EL13 copolymer with 1500 rpm and the A4 PMMA with 2000 rpm. Spinning the resist is the most vulnerable step for contamination and requires a cleanroom. Particles or bubbles in the resist cause imperfections in the resist layer. In order to avoid them it is important to clean the substrate before spinning and remove bigger particles by blowing the surface with a N_2 gun. The resist amount should not vary and the pipettes should not be emptied completely to avoid resist bubbles. To reduce the contamination of the large resist bottles we fill the resist into smaller bottles and load the pipette from there. Nevertheless, the bottles should always be inspected visually before applying it to the wafer. An unavoidable problem is non-uniform coating due to the different spinning speed at different radial positions on the wafer and the aggravation of resist at the edge of the wafer due to surface tension that counteracts the centrifugal force of the spinning. Those effects can usually be minimized by constraining the design to the center of the wafer. After each spinning, the wafer is put on the hotplate at 200 °C for 5 min to bake the resist, which evaporates the solvent and hardens it.

The resist and the substrate are made from electrically insulating materials. If we would try and write the structures into the resist using ebeam lithography the sample would accumulate charges and uncontrollably expose the resist. In order to avoid charging of the sample we sputter a thin layer of gold on top of the PMMA A4 resist with the Cressington 108 auto sputter coater. It is also possible to use aluminum as the conductive layer, however the gold sputtering process takes about 5 min and the aluminum evaporation in the Plassys takes about 1 h. This is mainly because the Plassys volume needs to be pumped to high vacuum for an aluminum evaporation in order to prevent the formation of an electrically insulating aluminum oxide layer. The clamps on the ebeam sample holder are later brought in electrical contact with the gold layer, so that it is grounded and the sample does not charge. The gold should be sputtered just before the exposure, as we observed that long storage times lead to changes in the visual appearance of the sample that we did not investigate any further.

MMA(8.5)MAA EL13 resist spinning	
Dynamic dispensing	500 rpm
Spinning speed	1500 rpm
Spinning time	60 s
Hot plate temperature	200 °C
Baking time	5 min
495 PMMA A4 resist spinning	
Static dispensing	0 rpm
Spinning speed	2000 rpm
Spinning time	100 s
Hot plate temperature	200 °C
Baking time	5 min
Gold sputtering	
Table position	All the way down
Ar pressure	0.07 mbar
Current	40 mA
Time	50 s
Remarks	Almost see-through blueish layer of gold

Electron Beam Lithography and Resist Development

The exposure of the bi-layer resist is done in a single step using a Raith eLINE Plus lithography machine employing its maximum acceleration voltage of 30 kV. The utilized resists are positive resists, meaning that the areas that are exposed are removed by the development step. Electron beam lithography is a well established direct write method to pattern design layout files into resists with a focused beam of electrons. The beam is deflected so that it can move over the sample and imprint the design file into the resist. The energy dose of the electron beam that is needed to fully expose the positive resist and make it soluble has to be calibrated in a dose test when exposing a new design or significantly changing the exposed areas around a known design. For negative resists we need the calibration to know the energy for causing crosslinks between the polymer molecules, making them unsoluble. The dose depends on the utilized substrate, previous metallization, resist and gold layer thicknesses, as well as on the

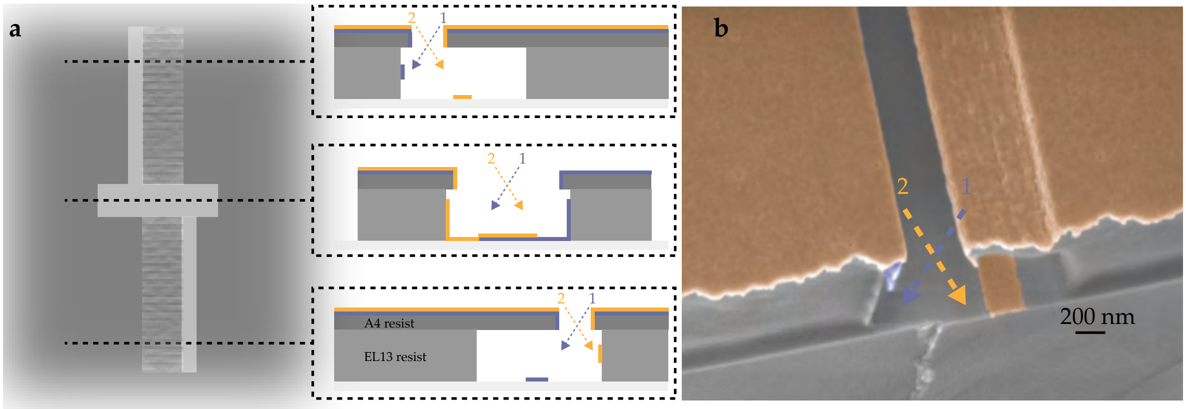

Figure 3.6: Bridge-free junction fabrication. a By using a lower sensitivity bottom resist it is possible to hollow out the top resist and create bridges and overhangs. By using two angles in the evaporation step, the top and bottom electrode can then be separated by making sure that only one wire stays on each side after the lift-off of the resist. **b** SEM picture of a trench that was written to test the ability to create asymmetric undercuts. The wafer was then broken and imaged from the side.

accelerating voltage of the EBL system. The acceleration voltage will influence the amount of forward and backwards scattered electrons. Before the launch of the QNZT cleanroom we fabricated our circuits in the Center for Functional Nanostructures at the Karlsruhe Institute of Technology, where the electron beam lithography system has a maximum acceleration voltage of 50 kV. In theory, the reduction of acceleration voltage decreases the ability to write very narrow structures into the resist due to enhanced scattering processes and leads to more uncontrollable resist exposure. This is especially relevant when the Josephson junction relies on asymmetric undercuts [117]. Nevertheless, for the dimensions and evaporation angles that we implemented the process worked reliably.

The large structures in the transmon design are written with the biggest available aperture (120 µm) in high current mode such that the writing current is about 10 nA and minimizes the writing time. The small structures including the junction are written with the smallest available aperture (10 µm) with a writing current of about 40 pA such that the precision is maximized. It is important to align the apertures with respect to each other to avoid big offsets of the small and large structures. Small offsets coming from misalignment can be accounted for by designing overlapping structures.

Directly after the lithography step, the gold is etched away in a Lugol solution, consisting of potassium iodide with iodine in water and then rinsed in deionized water. Although the gold layer only fulfills a simple task of making the sample conductive we suspect that it is responsible for most of the fabrication issues that we experienced in the beginning. The etching process sometimes left behind some contamination on the wafer that was mainly visible after the metallization step in the Plassys. We compared the process to a similar process but using a silicon substrate. There, the contamination did not appear and we conclude that the contamination is originating from the gold treatment. To minimize the contamination we found that a combination of sputtering a thin gold layer such that the sample looks only very slightly blueish, but thick enough to obtain an uninterrupted gold layer. The etching should be done in a fresh and highly diluted Lugol's solution, meaning that the readily bought bottles should not be exposed to air too long and thinned down with deionized water. We suspect the formation of potassium carbonate could be a reason for the dirt. Mind that the gold etching should not take longer than 30 s to avoid that the resist soaks up too much water. This way we could reduce the contamination to a minimum but the issue should be investigated further.

The resist development in a isopropyl alcohol & water (3:1) solution removes the resist only where it has been exposed. Here it comes into play that the two resists posses different critical doses where they are soluble. When only the lower resist is fully exposed next to a trench, the developer washes out the exposed lower resist from underneath the PMMA, as shown in Fig. 3.6 and enables the fabrication of Josephson junctions via the Niemeyer–Dolan [118] or bridge-free [117] techniques.

Electron beam lithography	
Machine	Raith eLINE Plus
Acc. voltage	30 kV
Base dose	80 μC/cm^2
Dosefactor (large)	5 (approx.)
Dosefactor (small)	7 (approx.)
Dosefactor (undercut)	2 (approx.)
Aperture (large)	120 μm
Aperture (small)	10 μm
Gold etching	
Solution	I_2/KI/H_2O (1:4:40)
Etch time	10 s
Protocol	Put wafer in beaker with Lugol's solution for 10 s
	While taking the wafer out,
	rinse with deionized water
	Shortly put in a beaker filled with
	deionized water and clean the tweezers.
	Rinse wafer with deionized water
	Blow dry using N_2
Resist development	
Solution	IPA/H_2O (3:1)
Temperature	6°C (beaker in chiller)
Time	1 min 45 s
Finish	Rinse with deionized water and N_2 blow dry

Metallization and Lift-Off

After the development the sapphire wafer is covered by a resist mask where only the exposed areas were removed. In the case where the dose was low enough to only expose the bottom layer resist the top layer forms an overhang casting a shadow onto the sapphire surface. An directional aluminum deposition onto the substrate utilizes this PMMA mask to coat the sample at the exposed areas, while it blocks the metal from reaching the substrate in unexposed regions. The deposition is done using a Plassys Bestek MEB 550S electron-beam

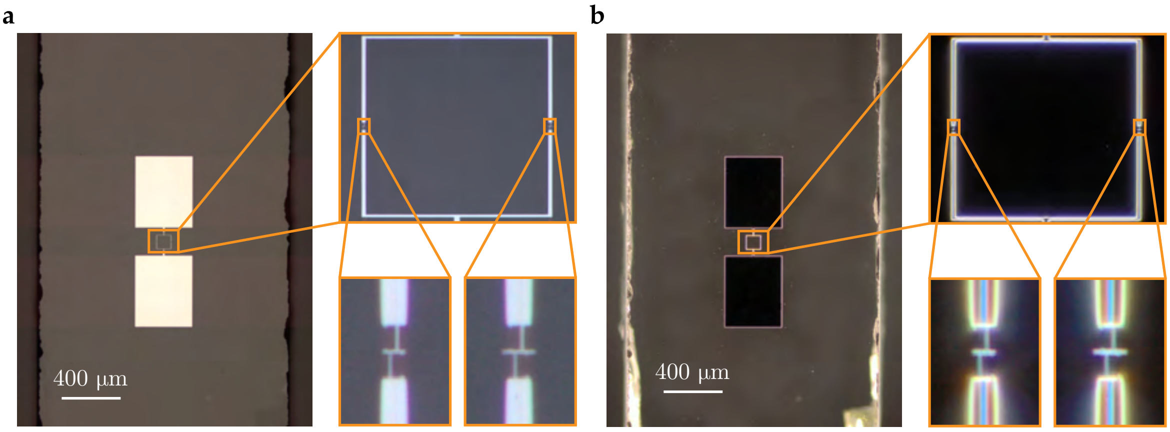

Figure 3.7: Optical micrograph of a 3D transmon. **a** The optical micrograph shows the rough edges of the sapphire chip that was cut into pieces by a mechanical dicing saw. The aluminum transmon pads show up as white rectangles. Zooming in further shows the SQUID loop and the bridge-free junctions. **b** The same pictures but taken with the dark field of the microscope. This is especially useful to inspect the chip for contamination as any grain will show up as a bright spot.

evaporator utilizing a two step shadow evaporation process, shown in Fig. 3.6. The orientation of the sample is critical for the angle evaporation, so the mounting of the sample must be done carefully.

The resist development typically leaves behind unwanted resist residues on the sapphire surface. A soft argon/oxygen descum in the Plassys removes the residues, but also a thin layer of the mask. Thus it should be calibrated properly. Typical advantages of the descum step are a reduction of junction aging and overall cleaner interfaces. In the region where the resist trench is narrow enough, the first aluminum evaporation under an angle[6] of 25° only deposits a wire on the substrate if the designed undercut is on the correct side and forms the lead wire to the junction . Otherwise it is deposited on the resist, see also Fig. 3.6. Then, a controlled oxidation step is used to create a thin aluminum-oxide layer, where the oxidation time and pressure control the barrier thickness, which is usually in the range of a few nanometer. The second aluminum deposition is performed at an angle of −25°, so that a wire is deposited underneath the opposing undercut compared to the first evaporation. This way the Josephson junction is formed by the Al-AlOx-Al sandwich and is connected only via the upper or lower electrode to the rest of the transmon circuit after the resist is removed. Even though we evaporated the metallic layers that form the transmon structure, the resist is still on the sample and is also coated with aluminum that has to be removed. The lift-off is done by leaving the wafer in acetone for a few hours, which dissolves the resist and removes the aluminum that is not in contact with the substrate surface. For a soft ultrasonic treatment the wafer should be transferred into another beaker to avoid too many particles in the beaker. The wafer is then rinsed in isopropyl or ethyl alcohol, followed by deionized water. After the lift-off the wires that lead to the junction are the only single layer aluminum structure such that they effectively separate the upper and lower half of the transmon through the Josephson junction. The transmon structure is shown in the micrograph in Fig. 3.7 taken with an optical microscope.

[6]Tilt angle as defined in the Plassys software.

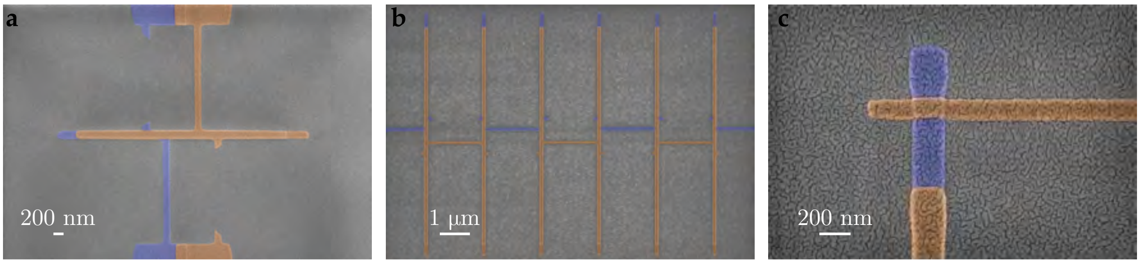

Figure 3.8: Josephson junctions. a The Josephson junction separates the top and bottom part of the circuit. Therefore only the top layer (orange) is connected to the upper circuit and the bottom layer (blue) to the part on the bottom. **b** The Josephson junction in **a** is fabricated in an array with alternating bottom and top layer connection to create a series that can be extended to thousands of junctions. **c** For smaller Josephson junctions the deposited wires are directly used as the Josephson junction, where only the horizontal orange wire was deposited underneath a resist bridge.

The visual inspection with the microscope should be done after every step in the cleanroom and before the cooldown to detect problems in the fabrication process. We show different junction designs in the false colored scanning electron microscope (SEM) pictures in Fig. 3.8. The bridge-free junction is depicted in Fig. 3.8a where the different colors represent the two aluminum layers. The upper part of the circuit is only connected by the top layer (orange), while the bottom part is connected by the bottom layer (blue). The remaining notches show the leftovers of the mirror wires that were removed during the lift-off. In Fig. 3.8b alternating connecting wires are used to form large arrays of Josephson junctions.

Slightly different to the bridge-free junction is the cross-type junction shown in Fig. 3.8c. In our experience it is more reliable to use for small junction areas. It is produced by using only one top resist overhang for the horizontal orange wire in Fig. 3.8c. The fabrication process is outlined in Fig. 3.9, where we do not show the aluminum that is evaporated onto the top layer resist, as it is removed during lift-off and decreases the visibilty of the structures underneath.

Plassys Bestek MEB 550S	
Descum	Ion gun
Ar/O_2 flow	10 sccm/5 sccm
Parameters	$V_{\mathrm{beam}} = 200$ V, $I_{\mathrm{beam}} = 10$ mA, $V_{\mathrm{acc}} = 50$ V
Time	100 s
Gettering	Crucible: Ti
Time, Rate	2 min, 0.2 nm/s
First layer	Crucible: Al
Thickness, Rate, Angle	25 nm, 1 nm/s, 25°
Oxidation	Static
Oxygen pressure	1 mbar
Time	4 min (excl. ramp and pumping)
Second layer	Crucible: Al
Thickness, Rate, Angle	50 nm, 1 nm/s, −25°
Lift-off	
Solution	Acetone on hotplate 60°C
Time	Few hours until resist is fully dissolved
Comments	Prevent evaporation by covering with lid
	After a few hours, spray with acetone while inside beaker
	to detach metal residues from sample
	Rinse with alcohol/acetone and put in new beaker with acetone
	Sonicate gently (135 kHz, 15%)
	Rinse with alcohol and deionized water
	Blow dry with N_2

Initial testing of the fabricated 3D transmon samples showed energy relaxation times in the range of $T_1 = 50 - 100\,\mu s$ and coherence times $T_2 = 5 - 50\,\mu s$, showing that the samples suffer from strong dephasing. Mitigating dephasing mechanism is an ongoing project.

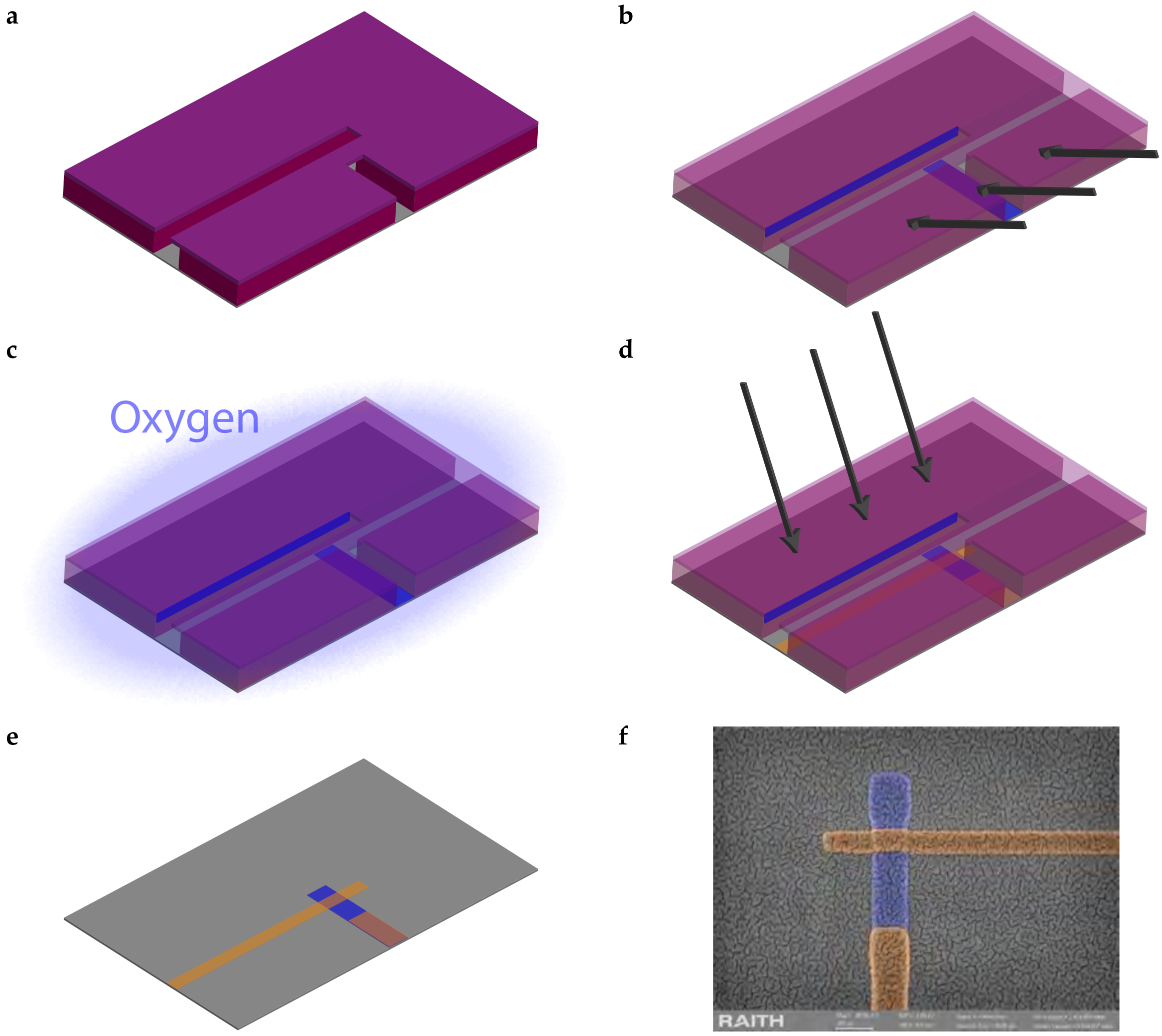

Figure 3.9: Cross junction fabrication. **a** The resist mask consists of a bottom layer resist that is more sensitive to electron-beam radiation than the top resist. **b** The first aluminum layer defines the trench wire that is parallel with the indicated arrows, while the perpendicular wire is deposited on the wall. Of course the aluminum completely covers the top resist but is not shown for better visibility of the important features. **c** Exposing the sample to a controlled oxygen atmosphere creates an oxide layer on top of the aluminum layer. **d** The second aluminum oxidation forms the second junction electrode. The wire is formed underneath the top resist overhang. **e** After lift-off only the wires in direct contact with the substrate remain. **f** SEM picture of a cross-type junction. We see that the wire that is parallel to the evaporation arrows is created twice but has an offset such that the junction only consists of one bottom and one top layer.

Tantalum-Qubit Benchmarks

Recent publications showed promising results with transmons made from tantalum (Ta) thin films [119, 120]. With over 500 µs the tantalum transmons have achieved the best reported lifetimes to date. Instead of the wet-etching process we utilize a dry etching process based on chlorine to define the Ta structures. The utilized wafers are 4" sapphire disks that have

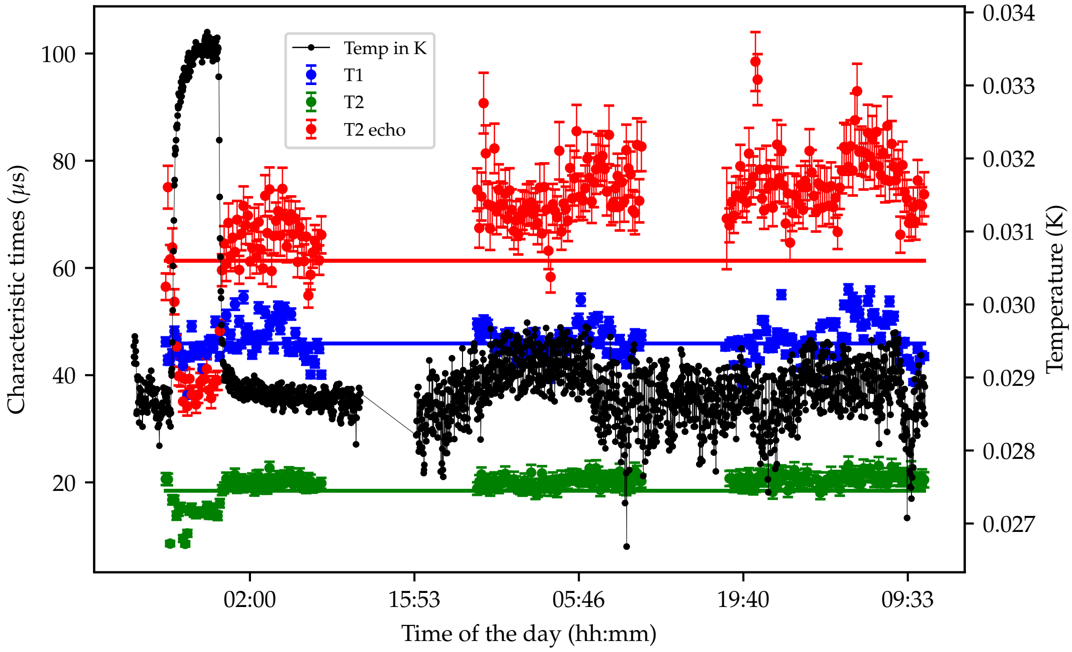

Figure 3.10: Extracted characteristic times. The first good Ta qubit shows promising results with an average lifetime of $T_1 = (45.91 \pm 0.05)\,\mu s$, coherence time $T_2 = (18.44 \pm 0.07)\,\mu s$ and Hahn-echo coherence $T_{2,echo} = (61.3 \pm 0.2)\,\mu s$.

a single side coated with a thin 200 nm layer of tantalum. After we receive the wafers we typically clean them using acetone and rinse them with isopropyl alcohol and DI water. Then we spin a negative resist ma-N 2403 with 2000 rpm for 45 s. In the first lithography we define the large structures such as the transmon pads. The resist is developed with the developer ma-D 525 for 90 s and immediately rinsed with DI water and blow dried. The negative resist leaves the exposed areas unsoluble, such that only the defined structures stay covered by the resist and protects the tantalum during the etching process. We use a plasma with RF power of 50 W, ICP power of 100 W, Cl_2 flow of 4 sccm, Ar flow of 50 sccm and etch for about 260 seconds in the Sentech ICP SI 500. Some samples showed remaining tantalum in parts without resist cover during a visual inspection after the first etching run. In this case, we added at most another 60 seconds in a second etching run without breaking the vacuum to remove the residues. After the etching process the wafer is immediately dipped into water, to avoid that the chlorine residues react with air. Afterwards the wafer is visually inspected and cleaned in a piranha solution. The remaining fabrication is similar to the regular transmon fabrication where we define the Josephson junctions between the Ta pads and evaporate aluminum, according to 3.3.2.

In Fig. 3.10 we show a stability measurement for the first Ta qubit with lifetimes exceeding 40 µs. Similar to the regular aluminum transmons the coherence time T_2 is much lower than the achievable $2T_1$, indicating a large dephasing rate. Compared to Ref. [120] we are still an order of magnitude away from the lifetimes that can be reached with tantalum transmons, thus the Ta fabrication is a vital area of research within our cleanroom facility.

3.4 Setup Specification

The control and measurement of quantum microwave systems have seen rapid development in the past 20 years, while more recently the efforts intensified with the goal to build a commercial fault-tolerant universal quantum computer. The requirement to cool down superconducting qubits to low temperatures not only arises from the critical temperature of the superconductors $T_{\mathrm{Al}} \approx 1\,\mathrm{K}$ but also the typical transition frequencies in the microwave regime $h \times 5\,\mathrm{GHz}/k_{\mathrm{B}} \sim 240\,\mathrm{mK}$, where k_{B} is the Boltzmann constant. Special techniques for mounting and thermalizing the sample, as well as cryogenic wiring techniques from room temperature to millikelvin temperatures have been developed that enable the measurement of quantum circuits [39]. This section is intended to outline the sample mounting and wiring, as well as the utilized measurement setups.

3.4.1 Cryogenic Wiring

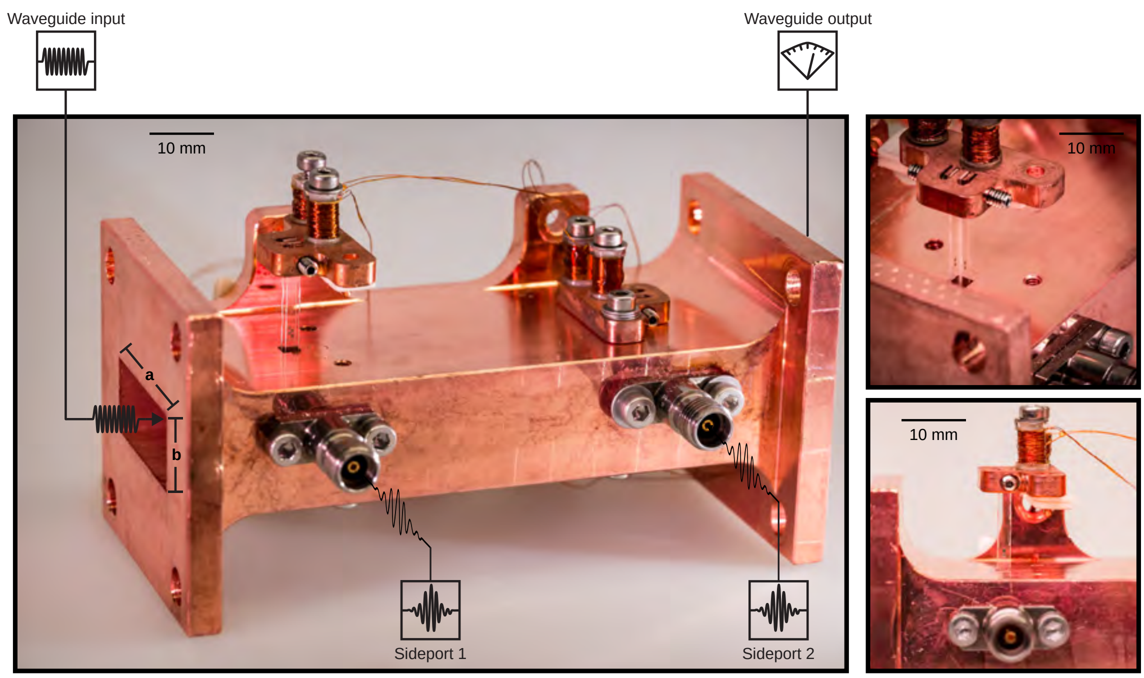

Figure 3.11: Photograph of the waveguide assembly. The waveguide middle section has one set of qubits mounted and the other aligned on the top for better visibility. The coils are mounted such that they have different couplings to the qubits which allows us to individually tune each qubit to a specific frequency. Waveguide-to-coaxial adapters are attached to the open left and right side of the waveguide, such that the transmission can be probed.

The transmons are investigated by scattering microwaves on the transitions. Therefore, we have to route a signal that is generated by a device at room temperature to the base plate of the cryostat and connect it to the waveguide. At the same time the sample has to be thermalized to the temperature of the cryostat in order to not destroy the fragile quantum states or limit their coherence due to quasi-particles and thermal population of excited states.

The rectangular waveguide in Fig. 3.11 serves as both, the thermalized sample box and the connection to the coaxial wiring that guides the signals to the microwave generation and detection system. The qubits are accessed either directly via the signal that travels through the waveguide or the sideports that provide a local microwave field.

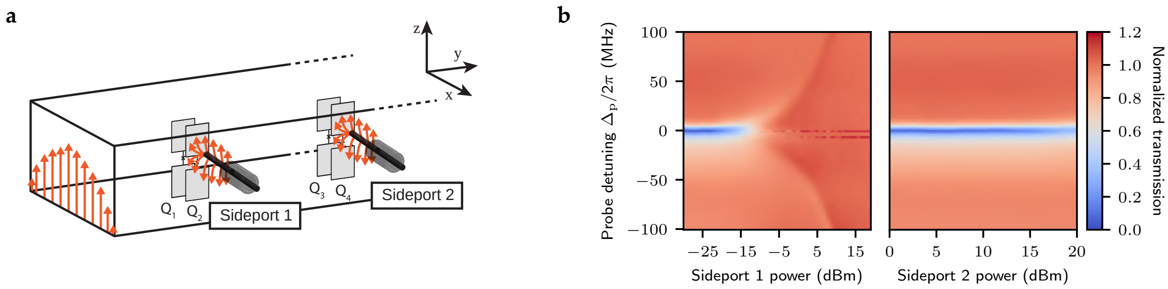

Figure 3.12: Illustrated sideport driving and power calibration. a The electromagnetic field symmetry (red, the electrical field) of the sideports does not coincide with that of the TE_{10} mode (indicated at the left face of the waveguide), the only propagating mode below the cutoff frequency of the second mode (≈ 13 GHz). The field applied through the sideports will be exponentially attenuated and enables us to locally excite pairwise transmons Q_1 and Q_2 or Q_3 and Q_4. The pin is not centered at the middle of the transmons on the z-axis, such that there is a field gradient across the two transmon pads and allows us to also excite local dark states. **b** When we apply a pump tone through the sideports we can calibrate the power arriving at the transmons by observing an Autler-Townes splitting in the coherent scattering measurement through the waveguide which is a direct measurement of the Rabi frequency [77, 121]. In this measurement we tune Q_2 at the decoherence-free frequency $\omega_\pi \approx 7.3$ GHz, while the other transmons are detuned below the cutoff of the TE_{10} mode. We then apply a pump tone through Sideport 1 and Sideport 2. In the left panel we can observe a splitting of the dressed transmon states, while in the right panel we can only observe small saturation effects. We can calibrate all four transmons with this routine to assure a sufficient locality of the driveports.

The sideports sketched in Fig. 3.12a are designed such that the polarization of the electrical field does not coincide with the waveguide field, thus it cannot propagate. The setup has two of those local access channels, that are located at the transmon pairs and enter the waveguide through a hole in the sidewall. Figure 3.12b shows the impact of both sideports on a single qubit, similar to the measurements in Sec. 4.1. Clearly, sideport 1 saturates the qubit at much lower applied power and we can observe an Autler-Townes splitting, while sideport 2 barely saturates the qubit within the shown power range. This locality enables an arbitrary adjustment of the relative phase between the two drive fields applied at sideport 1 and 2. There is also a field gradient within the pair that could potentially be adjusted by inserting a second pin through the opposite wall, however this was not necessary for the experiments.

The clamps, depicted in the detailed view of Fig. 3.11 thermalize the substrate by tightening a small screw on on the side. They also have space for two superconducting coils that are screwed onto the clamp and enable flux-tuning of the transmons. The clamp is then attached to the waveguide middle section that is in direct contact with the sample holder and thermalized to the base plate of the cryostat.

We use a 2016 Triton Cryofree dilution refrigerator system with DU7-300 dilution unit from Oxford Instruments with self built cryogenic microwave wiring. The aluminum circuits have to be cooled down below the critical temperature $T_{Al} = 1.2\,K$ to become superconducting. Furthermore, cooling down the sample to millikelvin temperatures is essential to reach the ground state of the circuit. Only if the thermal energy is much smaller than the energy that is associated with the resonant circuit, i.e. $k_B T \ll \hbar\omega_{01}$, the thermal fluctuations are small enough such that the excited state population is minimized. Additionally, the energy level separation has to overcome the linewidth broadening that originates from dissipation and thermal population of higher excited states [29]. To reach an excited state thermal population of 1% for superconducting qubits with typical transition temperatures of a few gigahertz the circuit has to be cooled down to a few tenths of milikelvin, following a Boltzmann distribution $P_{|e\rangle} \approx \exp\left(-\frac{hf_{01}}{k_B T}\right)$ [122].

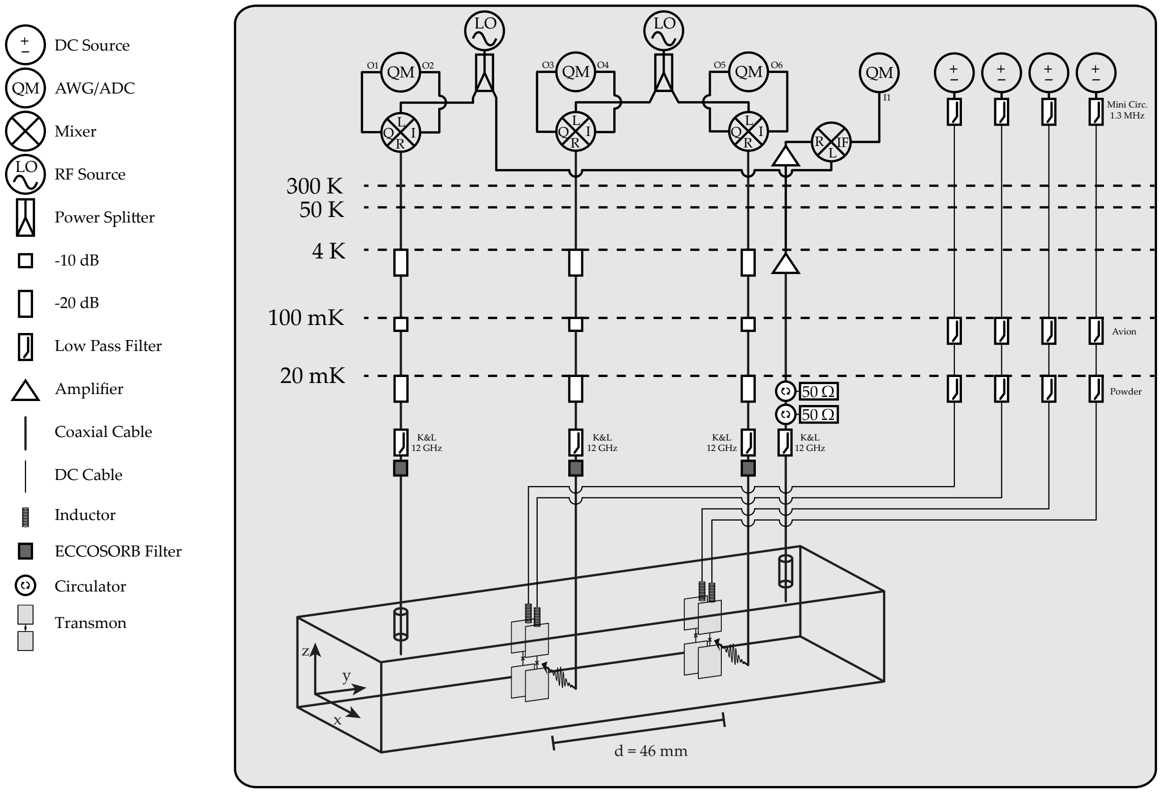

Figure 3.13: Schematic of the experimental wiring with selected components. All microwave cables have to be attenuated at well thermalized anchors at different stages and filtered.

The electronic control is separated into radio frequency (RF) and direct current (DC) components, where the signal generation and detection components are located at room temperature and have to be routed to the base plate of the cryostat. The RF signals are used to drive and probe the circuit, while the DC components are used to apply a flux-bias to frequency-tunable qubits. To effectively suppress Johnson-Nyquist noise, the RF input cables, schematically shown in Fig. 3.13 have to be attenuated at different stages and heavily filtered, otherwise the thermal noise can travel to the sample and dephase the qubit [123]. To suppress thermal conductivity, the inner and outer conductor of the input coaxial cables are made from stainless steel. The rather low electrical conductivity compared to copper means that the signal is attenuated by roughly 10 dB on its way from the top to the base plate. However, to properly thermalize the cables at the cooling stages three attenuators are placed at 4 K, 100 mK and 20 mK.

Only 1% of the signal power passes through a 20 dB attenuator while 99% is absorbed. If it is not thermalized to the actively cooled cryostat plate, the attenuator heats up and emits black body radiation at much higher temperatures. Even though the attenuators are thermalized with copper clamps the question remains how cold especially the inner conductor gets [124]. Concatenating attenuators at different stages in the cryostat is a balance between cooling power and dissipated power. The mean number of thermal photons n_i at stage i with attenuation A_i is given by [39]

$$n_i(\omega) = \frac{n_{i-1}(\omega)}{A_i} + \frac{A_i - 1}{A_i} n_{\mathrm{BE}}\left(T_{i,\mathrm{att}}, \omega\right), \tag{3.18}$$

where the first term represents the attenuated noise photons from the previous stage and the second term from the current stage.

Typical powers of around −130 dBm at the qubit location correspond to detection voltages of a few hundred nanovolt. Even though there is an effort to build single photon detectors for microwave frequencies, the most commonly used strategy is to amplify the signal before detecting it. This has to be done in a way that the effective noise temperature is minimized [125]

$$T_{\mathrm{eff}} = T_1 + \frac{T_2}{G_1} + \frac{T_3}{G_1 G_2} + ..., \tag{3.19}$$

where T_i is the noise temperature and G_i the gain of amplifier i. In the setup, we use a cryogenic high electron mobility transistor (HEMT) from Low Noise Factory and room temperature amplifiers. However, we do not use quantum noise limited amplifiers, which would help to increase the signal to noise ratio and could enable single shot readout. Even though the room temperature amplifiers create the largest noise signal of the output section elements, the cryogenic amplifiers are the dominant noise source for the sample, as seen in Eq. (3.19). We found that replacing the standard switching power supply with linear power supplies results in a dramatic reduction in noise [126]. The waveguide output is connected to a K&L 6L250 lowpass filter and then to two concatenated isolators that shield the sample from thermal photons traveling back from the amplifiers. The output of the second isolator is then connected to the HEMT amplifier, sitting at the 4 K stage by a superconducting coaxial cable to minimize photon loss and reduce thermal conductivity between the stages. Usually, the performance of the setup is restricted to a range between 4 to 12 GHz, which is mostly limited by the utilized filters, circulators and amplifiers.

3.4.2 Microwave Generation and Detection

The waveguide sample is characterized using either a vector network analyzer (VNA) or a pulsed measurement setup in which the Quantum Machines Operator X is the main control instrument. The wiring inside the cryostat is independent of the two options. Figure 3.13 shows only the time-domain setup, which is typically extended with a VNA in the experiment.

The spectroscopic measurements with the VNA are slow, meaning they are only able to investigate the steady state of the system by varying the frequency of the microwave signal. After interacting with the system the signal arriving at the VNA is then compared to the phase and amplitude of the sent signal in a heterodyne detection scheme. Comparing the sent and measured voltages V_1^R and V_1^L at the VNA ports determine the complex S matrix elements [88]

$$\begin{pmatrix} V_1^L \\ V_2^R \end{pmatrix} = \begin{pmatrix} S_{11} & S_{12} \\ S_{21} & S_{22} \end{pmatrix} \begin{pmatrix} V_1^R \\ V_2^L \end{pmatrix}. \tag{3.20}$$

The measurements in the experiment section focus only on transmission S_{21} measurements. In reciprocal systems this is equivalent to S_{12}.

The time-domain setup is able to send and detect microwave pulses on the nanosecond scale and therefore resolve time dynamics of microwave circuits. Pulses are generated by mixing a continuous wave (CW) microwave pump. Here, in the range between $\sim 6\,\mathrm{GHz}$ to $8\,\mathrm{GHz}$ with the I and Q quadrature of a modulated signal between $\sim 50\,\mathrm{MHz}$ to $300\,\mathrm{MHz}$, which is provided by an arbitrary waveform generator (AWG, Operator X - Quantum Machines). The upmixing setup includes various filters, attenuators and switches (not shown in Fig. 3.13) to achieve the desired suppression of noise and unwanted sidebands. The signal is finally filtered at the base plate by a 6L250-12000 low-pass filter from K&L, followed by a custom built Eccosorb filter. The transmitted signal is downconverted to an intermediate frequency using an image-rejection mixer, filtered and finally digitized by the Operator X from Quantum Machines, which serves as the AWG for pulse generation and analog to digital converter (ADC) for signal detection. To cover the range of 400 MHz in the spectroscopy of the two-excitation manifold, we used both the upper and lower sideband to send pulses. The sidebands have a phase difference of 180°, such that the data that was recorded for spectroscopy pulses with the lower sideband is manually shifted by π in the phase-sensitive spectroscopy of Fig. 4.25.

Circle-Fit and Qubit Rates

The low power transmission around the resonance of a qubit coupled to a waveguide is given by the ratio between the the output and input field [9, 12] that resulted in Eq. (2.24)

$$S_{21}(\omega) = \frac{\langle a_{\mathrm{out}} \rangle}{\langle a_{\mathrm{in}} \rangle} = 1 - \frac{\gamma_{\mathrm{r}}}{2\Gamma} \frac{1 - \dfrac{i\delta\omega}{\Gamma}}{1 + \left(\dfrac{\delta\omega}{\Gamma}\right)^2 + \dfrac{\Omega^2}{(\gamma_r + \gamma_{\mathrm{nr}})\,\Gamma}}. \tag{3.21}$$

Here, we defined dissipation rates corresponding to the radiative waveguide coupling γ_r and intrinsic decay γ_{nr}, as well as the total decoherence rate Γ.

The VNA measurement provides the complex scattering matrix defined as the voltage ratio, i.e. we are sensitive to the phase and amplitude. In the case for the transmission $S_{21} = V_{\mathrm{out}}/V_{\mathrm{in}}$ it is defined as the ratio between the output voltage V_{out} of the VNA and the input voltage V_{in} that is detected after interacting with the system. When we plot the transmission in dB scale we usually square the S parameter to get a power ratio, as the power is defined as $P = V \cdot I = V^2/R$, where I is the current and R the resistance. Then we can write the S_{21} parameter as

$$S_{21}(\mathrm{dB}) = 10 \cdot \log_{10}(|V_{\mathrm{out}}/V_{\mathrm{in}}|^2) = 20 \cdot \log_{10}(|V_{\mathrm{out}}/V_{\mathrm{in}}|). \tag{3.22}$$

In the analysis we use a circle-fit routine developed for characterizing linear resonators that are coupled to a transmission line in a notch-type configuration [111, 112]. This way, we take into account the environment and correct for impedance mismatches that are caused by standing waves in the lines, including the waveguide adapters. The notch configuration transmission is given by

$$S_{21}(f) = ae^{i\alpha}e^{-2\pi i f\tau}\left[1 - \frac{(Q_l/\left|Q_c\right|)\,e^{i\phi}}{1 + 2iQ_l\,(f/f_r - 1)}\right], \tag{3.23}$$

where Q_l is the loaded, Q_c the coupling and Q_i the internal resonator quality factor, f is the probe frequency, f_r the resonance frequency of the resonator. The impedance mismatches are absorbed in the parameter ϕ. The environment is considered with the amplitude parameter a, phase shift α and electronic delay τ that arises from the time that a signal travels through the cables and circuit components. As already pointed out in Refs. [127–129] we can compare the definitions of the quality factors and their associated linewidth $\kappa = \omega_{01}/Q$ with the rates obtained from the qubit transmission Eq. (2.24):

$$Q_1 = \frac{\omega_{01}}{2\Gamma} \quad Q_\mathrm{c} = \frac{\omega_{01}}{\gamma_\mathrm{r}} \quad Q_\mathrm{i} = \frac{\omega_{01}}{2\gamma'_\mathrm{nr}} \tag{3.24}$$

In our measurements, the VNA measures S parameters, which are defined as voltage ratios and thus contain the phase information of the signal. However, quality factors are defined by dissipated power in a resonant circuit. To establish a relationship between exponential decay that is either field or power dependent and the quality factors obtained by the circle fit routine, we must include a factor 1/2 for the loaded and internal quality factors to match the definitions in the master equation.

CHAPTER 4

Rectangular Waveguide Quantum Electrodynamics with Transmon Qubits

Most superconducting waveguide QED experiments use transmon qubits coupled to on-chip transmission lines. Integrating both elements into a single chip has the advantage that the required space is minimized, especially when scaling the system to a large number of emitters that are separated by wavelength distances. Nevertheless, rectangular waveguides are very well suited for medium-scale experiments and benefit from the 3D arrangement possibilities of the qubits and superconducting coils. Moreover the chip does not require bonds and can be individually selected after room-temperature characterization. The physics in the waveguide at frequencies above the cutoff is the same compared to the on-chip analogue. The qubits interact with the propagating photons in the waveguide. Thus we characterize the individual constituents by themselves before investigating coupled systems. The waveguide coupling rate of about $\sim 15\,\mathrm{MHz}$ sets the timescale for the individual transmon decay in the range of $\sim 10\,\mathrm{ns}$ such that its parameters are extracted by continuously driving the system into the steady state and measuring the scattered radiation in the frequency-domain. For two qubits the capacitive coupling strength between neighboring qubits is extracted by tuning them into resonance and observing the typical splitting of the hybridized states. The formation of dark states in multi-qubit systems enables the exploration of a regime where the timescales are not dominated by the strong waveguide coupling. This opens up the possibility to perform time-resolved measurements on the two-qubit experiments with direct and waveguide-mediated interactions and the calibration of the decoherence-free subspaces. The four-transmon experiment consists of a pairwise interaction via the waveguide to construct a more complex Hilbert space and shed light on the physics of coupled many-body systems in waveguide QED.

4.1 Single Transmon Waveguide QED

After mounting the transmons into the clamps and sliding them into the waveguide middle section as shown in Fig. 3.11, the open sides are closed by the adapters that connect the waveguide to the coaxial lines. In total we mount four transmon qubits and four superconducting coils that we need to accurately characterize. In this chapter we focus on the single transmon parameters that are extracted by vector network analyzer (VNA) transmission measurements. The VNA measurement provides the complex scattering parameter S_{21} from comparing its output signal to the signal that traveled through the cryostat and interacted with the sample. It only contains information about the elastically and coherently scattered signal. Inelastic scattering processes, such as the observation of resonance fluorescence or the Mollow-triplet [12] can be investigated by using spectrum analyzers or by analyzing the time traces of the pulsed measurement setup. The individual transmon parameters together with the capacitive qubit coupling strengths are sufficient to simulate most of the system dynamics and thus also important to understand the multi-qubit behavior.

Waveguide and Qubits

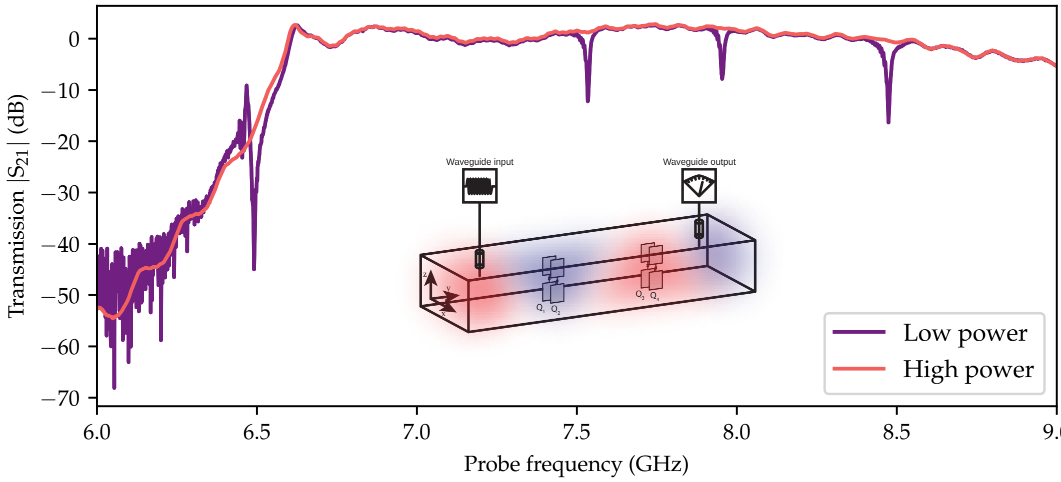

Figure 4.1: Waveguide transmission. The measurement at low power, where low power means about -130 dBm at the qubit positions, shows four resonances that we attribute to the transmon qubits. They disappear when a high power ($\sim$ -60 dBm) is applied due to the non-linearity of the Josephson junction. The qubits effectively act as saturable mirrors [12]. Even when measuring with low power, the qubits are already saturated, which can be seen from the rather low extinction between a resonantly and a non-resonantly transmitted signal $< 20\,\mathrm{dB}$.

Once the sample is cooled down to millikelvin temperatures we conduct a VNA transmission measurement. The signal, emitted by the VNA source port, has to pass through the room temperature coaxial wiring, as well as the cryogenic input wiring, attenuators and filters such that it is attenuated by approx. $70\,\mathrm{dB}$ before interacting with the waveguide sample. Afterwards it has to pass two isolators and a band pass filter before reaching the superconducting coaxial cable. At the $4\,\mathrm{K}$ stage the output cable is connected to a HEMT amplifier where the signal is amplified by $\sim 35\,\mathrm{dB}$ followed by another amplifier at room-temperature that has an additional gain of $\sim 40\,\mathrm{dB}$. Finally, the signal is recorded by the heterodyne detection scheme of the VNA. The high power transmission in Fig. 4.1 shows a measurement through this wiring scheme. Clearly, we can observe that in the low power measurement four resonant features appear at $f_1 = 6.5\,\mathrm{GHz}$, $f_2 = 7.55\,\mathrm{GHz}$, $f_3 = 8.0\,\mathrm{GHz}$ and $f_4 = 8.5\,\mathrm{GHz}$. These resonances are saturable, as they disappear in the transmission when the waveguide is probed with high power (70 dB difference). They correspond to the fundamental transitions of the four frequency-tunable transmon samples with ground state $|g\rangle$ and excited state $|e\rangle$. The initial measurement with no applied flux show resonance frequencies that are randomly spread over the full tuning range of the transmons and depends on the trapped offset-fluxes. The measurement is a quick sanity check in order to verify that all samples survived the mounting and cool-down procedure.

Flux Tunability

In Eq. (1.16) we found that a transmon can be made frequency tunable when it consists of two parallel Josephson junctions. Adding a control parameter yields the necessity to calibrate it, such that we can independently tune the transmon resonance frequencies. The split-junction

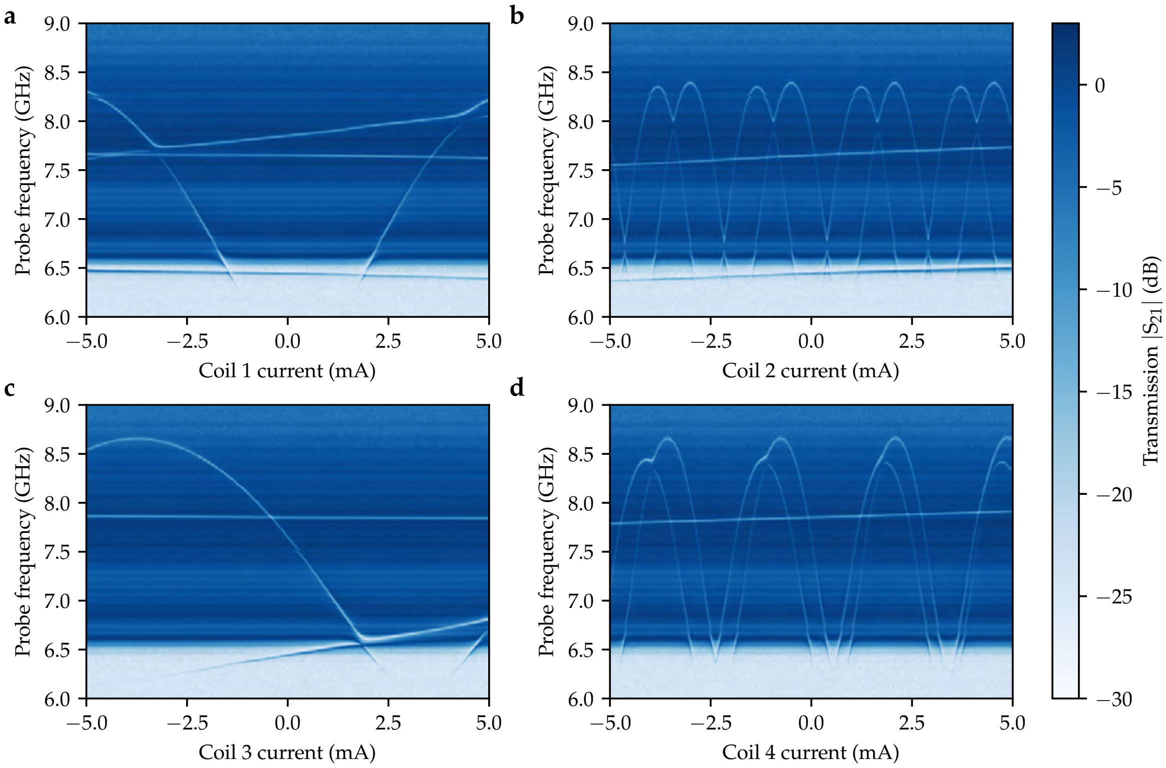

Figure 4.2: Flux maps. **a** By properly placing coil 1 directly on top of Q_1, the magnetic field dominantly couples to transmon Q_2, shifting it by one flux quanta over the whole span of applied current, while Q_1 is only tuned approx. 500 MHz. When the center of the coil axis is placed directly in the plane of the transmon substrate, the magnetic field lines are mainly in-plane with the patterned structures and therefore have only little contribution perpendicular to the SQUID loop. Further away from the center of the coil axis the field will not be as homogeneous and therefore tune qubit Q_2. If the distance gets even larger (4.5 cm) the field is already very weak so that Q_3 and Q_4 are only tuned very weakly. **b** Coil 2 mainly tunes Q_1 and Q_2 with the same strength. **c** Arrangement analogue to **a** but on the other pair, now mainly tuning Q_3. **d** Arrangement analogue to **b** but on the other pair, now simultaneously tuning Q_3 and Q_4.

transmons are tuned via a magnetic field that is generated by superconducting coils on the waveguide housing. Each coil is connected to a DC current source (YOKOGAWA GS210) at room temperature, such that an applied current will change the magnetic field that penetrates the transmon loops. In Fig. 4.2 the generated current is changed from -5 mA to 5 mA while monitoring the transmission through the waveguide. An increasing absolute value of the applied current leads to a stronger magnetic field that changes the resonance frequency of the qubits. Two coils are placed in close vicinity of a transmon pair such that they mainly tune one pair and only marginally affect the other. Here, coils 1 & 2 are placed on top of transmons Q_1 and Q_2 and coils 3 & 4 on top of transmons Q_3 and Q_4. Within the pairs coils 2 and 4 affect both qubits, while the other coils mainly influence the resonance frequency of only one qubit. Although the arrangement helps to reduce flux crosstalk, a proper calibration is needed for independent qubit control. By fitting the analytical expression for the resonance frequency of a transmon with a split junction and maximal Josephson energy $E_{J,max}$

$$\begin{aligned} hf_{01}(\Phi) &= \sqrt{8E_{\mathrm{J}}(\Phi)E_{\mathrm{C}}} - E_{\mathrm{C}} = \\ &= \sqrt{8E_{J,max}\cos\left(\frac{\pi(\Phi+\Phi_{off})}{\Phi_0}\right)\sqrt{1+d^2\tan^2\left(\frac{\pi(\Phi+\Phi_{off})}{\Phi_0}\right)}E_{\mathrm{C}}} - E_{\mathrm{C}}, \end{aligned} \tag{4.1}$$

to the extracted transmon frequencies we obtain the asymmetry parameter d and the flux period Φ. The mutual inductance matrix M converts the current I at the DC source to magnetic flux Φ at the transmon loop

$$\Phi = M \cdot I. \tag{4.2}$$

For our sample, consisting of four qubits and four coils this results in a matrix M of size 4×4. The entries quantify the sensitivity of changes in the current through each coil on the resonance frequency of each qubit. By solving the equations for the desired qubit frequencies, we can find a set of coil currents that satisfies this condition enabling us to independently tune the qubit and calibrate out the crosstalk. The frequency tuning-ranges of the transmons are roughly $f_{Q1} = 5.9\,\mathrm{GHz} - 8.4\,\mathrm{GHz}$, $f_{Q2} = 6.0\,\mathrm{GHz} - 8.35\,\mathrm{GHz}$, $f_{Q1} = 6.1\,\mathrm{GHz} - 8.67\,\mathrm{GHz}$ and $f_{Q4} = 6.0\,\mathrm{GHz} - 8.45\,\mathrm{GHz}$.

Qubit Characterization

When a qubit interacts with the coherent microwave field, interference between the transmitted and the elastically scattered photons lead to a distinct qubit lineshape in the transmission measurement. This lineshape is analyzed to extract the fundamental coupling strengths that define the timescales for the system. In the strong coupling limit they are usually on the order of a few nanoseconds, such that it is convenient to study the system in the steady-state. The anharmonicity of the transmon leads to a power saturable qubit transition we can directly observe with a two-tone spectroscopy. The transmon is a multi-level quantum system where the anharmonicity is a crucial parameter that defines the limit on the excitation pulse length before the drive also substantially induces transitions to the second excited state. By driving the qubit transition beyond qubit saturation, we find that the Autler-Townes splitting is a useful technique for power calibration, particularly because the power arriving at the qubit generally varies for different frequencies. This is particularly important below the waveguide cutoff, where fields cannot propagate and qubit-photon bound states emerge.

The scattering parameter $S_{21}(\omega)$ is a complex quantity with real and imaginary part including information about the amplitude and phase of the microwave signal. The spectral shape of a

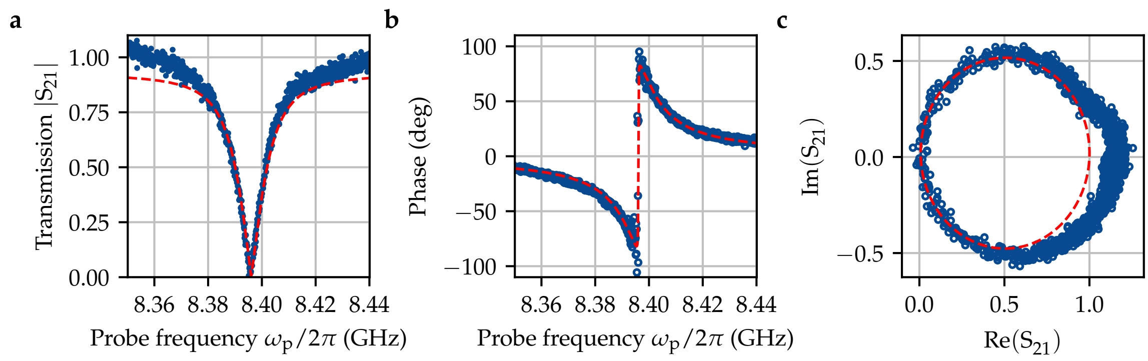

Figure 4.3: Parameter extraction via a circle-fit routine. **a** The transmission magnitude of a low power signal reaches almost zero when the probe signal is resonant with the fundamental transmon transition. **b** The signal experiences a 180 deg phase shift after interacting with the emitter. **c** Performing a circle-fit routine on the complex scattering parameters also accounts for asymmetric lineshapes that are caused by the interference with standing waves in the microwave background. The red dashed line is the result of the circle-fit.

	f_{01} (GHz)	Q_L	Q_c	Q_{int}	$\frac{\Gamma}{2\pi}$ (MHz)	$\frac{\gamma_r}{2\pi}$ (MHz)	$\frac{\gamma'_{\mathrm{nr}}}{2\pi}$ (MHz)	$\frac{\alpha}{2\pi}$ (MHz)
Q_1	7.332	476	493	8878	7.8	14.9	0.4	219
Q_2	7.333	549	576	11651	6.7	12.7	0.3	222
Q_3	7.334	443	468	8238	8.3	15.7	0.5	225
Q_4	7.331	534	564	10079	6.7	13.0	0.4	206

Table 4.1: Transmon parameters. For the extraction of the characteristic single transmon parameters, the fundamental transmon transition f_{01} is tuned to match roughly the decoherence-free frequency f_π. The coupling efficiencies are $\beta_1 = 0.96$, $\beta_2 = 0.95$, $\beta_3 = 0.95$, $\beta_4 = 0.97$.

resonator coupled to a transmission line in a notch configuration is very similar to a qubit in the low power limit $\Omega \ll \gamma_r$. Thus, we use the circle-fit routine [111, 112] to extract qubit Q factors from the transmission data. The benefit of using the circle-fit routine is that an additional term takes into account the environment that gives rise to very asymmetric lineshapes caused by standing waves due to impedance mismatches in the lines [130] as well as the impedance mismatch of the qubit with the waveguide [111]. In Fig. 4.3 the characteristic waveguide QED parameters are extracted by fitting Eq. (3.23) to the transmitted complex scattering parameters around the qubit resonance such that we obtain the resonance frequency f_{01} and the quality factors Q. The other qubits are detuned by a few gigahertz to avoid hybridization and the associated linewidth broadening. For the intended experiments the most interesting region is the frequency that corresponds to a $\lambda/2$ distance between the pairs, thus we list these parameters in table 4.1. By using the relations in Eq. (3.24) we can express the quality factors in terms of waveguide QED decoherence and decay rates according to Eq. (2.24). The measurement has to be done with sufficiently low power to not saturate the qubit. Saturation will lead to an artificial decrease of Q_i. Here, Q_i is a lower bound for the internal qubit losses. For a more accurate characterization of the internal qubit loss rates, the waveguide coupling must be adjusted so that it does not dominate the overall decoherence rate [80].

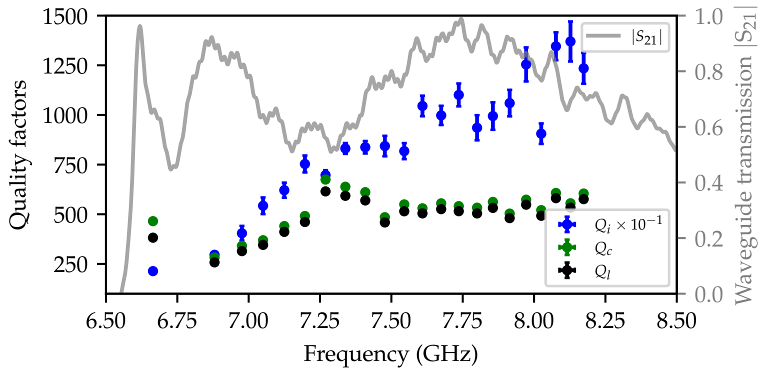

Figure 4.4: Quality factors and waveguide transmission. Close to the cutoff the quality factors increase for increasing frequencies. However, while the loaded and coupling quality factors Q_l and Q_c settle around a constant value, the internal quality factor Q_i begins to settle but eventually keeps increasing as the qubit is tuned towards its flux sweetspot at $\sim 8.2\,\text{GHz}$.

Tuning a single qubit within its frequency range allows to extract its parameters at different regions of the waveguide. In Fig. 4.4 we show the qubit quality factors at different resonance frequencies together with the transmission data for the empty waveguide. When the sample is thermalized to the base temperature of the cryostat we expect that the transmons are limited by flux noise due to their large SQUID area, resulting in a decreasing internal quality Q_i, when tuning the transmon to frequencies away from the upper sweetspot. The decreased speed of light close to the waveguide cutoff frequency $f_{c,10} \sim 6.6\,\text{GHz}$ effectively increases the interaction strength of the photons with the qubits. This causes the quality factors to increase when they are tuned further into the band. At around $\sim 7.2\,\text{GHz}$ they seem to settle to a constant value. For even higher frequencies, the internal quality factor rises until the maximal resonance frequency of the split-junction transmon. The vicinity to the flux sweetspot decreases the transmon susceptibility to flux noise. As shown in Fig. 4.2, around the sweetspot we require a larger applied coil current to change the resonance frequency, thus decreasing the frequency change per flux quantum $df/d\phi$.

In the strong coupling limit, where the decoherence rate is dominated by waveguide decay, the internal quality factor of the transmon Q_i provides only an upper bound for internal decay and dephasing mechanisms as well as for external noise sources. One important noise source is temperature. Effectively, thermal photons saturate the transmon transition which causes a more shallow resonance dip when measuring the absolute transmission. This effect effectively reduces the internal quality factor. Immediately after the cryostat base plate reaches a constant temperature of $T_{base} = 25\,\text{mK}$, we can repeatedly probe the transmission around the resonance frequency and extract the characteristic parameters as done in Fig. 4.3. The excess of thermal population in the first excited state causes the internal quality factor Q_i to increase by a factor of two during 6 h of measuring, due to the further cooling of the sample. Afterwards it settles around $Q_i \approx 8500$, while the resonance frequency keeps fluctuating over a span of 0.5 MHz. Thus, for quality factors $Q_i < 8500$ we seem to be limited by temperature, while for $Q_i \geq 8500$ we are limited by flux noise. Measurements during the following days are consistent with these frequency fluctuations.

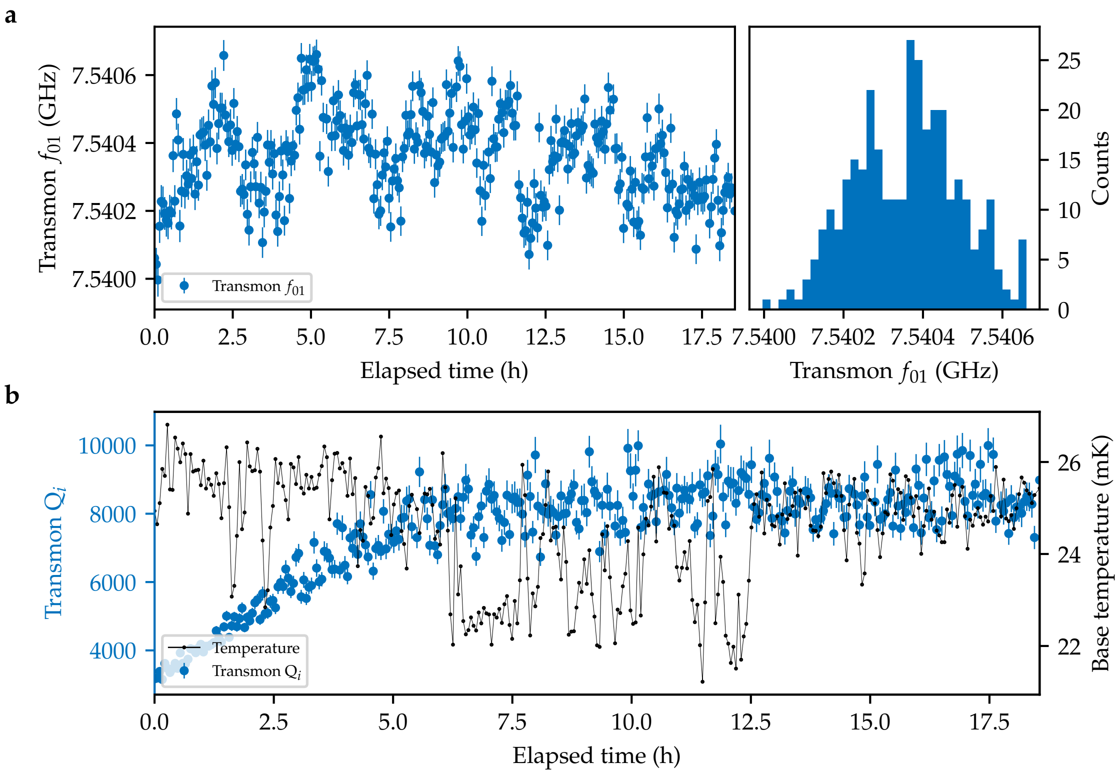

Figure 4.5: Transmon parameters vs. time. After the cryostat reaches a constant temperature we repeatedly measure the transmission around the transmon 0-1 transition f_{01} and perform a circle-fit routine to extract the characteristic parameters. **a** Over the measurement time of 18 h the extracted frequency fluctuates within 600 kHz. **b** The extracted internal quality factor Q_i increases for 6 h, indicating the cooling of a hot sample and environment.

The transmon is often used as a qubit in quantum information processing. In order to suppress leakage, mainly into the second excited state, when trying to populate the first excited state it is important to engineer the anharmonicity of the transmon such that its transition frequencies are sufficiently detuned from each other. The anharmonicity is measured by applying a pump on the fundamental transmon transition, such that we populate the first excited state. With increasing control power, we observe a saturation effect of the transition in Fig. 4.6 when probing the transmission with a tone from the VNA around the resonance frequency. When the first excited state is sufficiently populated, the next higher transition can also be driven, resulting in a resonance dip detuned by the anharmonicity $\alpha/2\pi$. The detuning of those transitions usually sets the lower limit on the pulse length. Once the Rabi frequency of the pulse is comparable to the anharmonicity it causes detrimental leakage into higher excited states, but can be reduced by pulse shaping [131]. For the tuning range of the transmons of $f_{min} \approx 6\,\text{GHz}$ and $f_{max} \approx 8.5\,\text{GHz}$ the measured anharmonicities $\alpha = E_c \sim 220\,\text{MHz}$ gives ratios of $E_J/E_C \approx 85 - 200$.

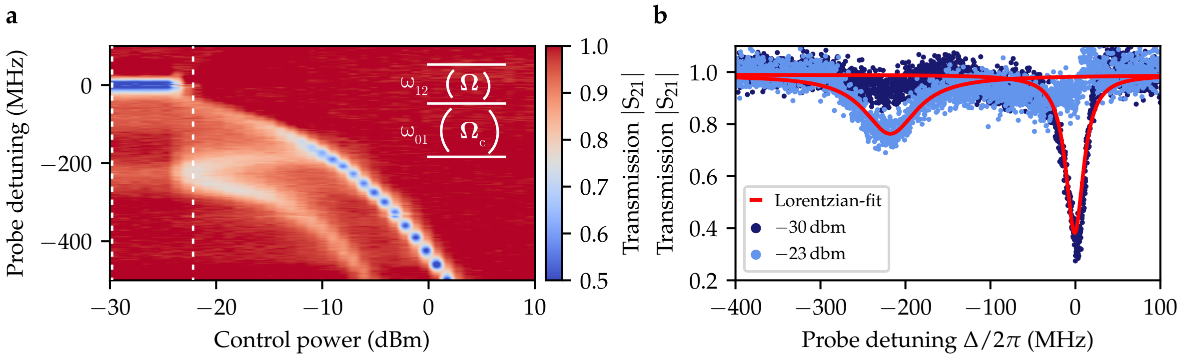

Figure 4.6: Transmon anharmonicity. **a** A control tone with increasing amplitude is resonantly applied through the waveguide to the transmon $|0\rangle$-$|1\rangle$ transition. The transmission is measured at low power such that the qubit is only saturated by the pump. For increasing control power, the fundamental transition starts to saturate while a second transition appears, detuned by roughly $\alpha/2\pi = -220\,\mathrm{MHz}$. This resonance corresponds to the $|1\rangle$-$|2\rangle$ transition of the transmon and enables us to directly measure the characteristic transmon anharmonicity $\alpha = \omega_{12} - \omega_{01}$. For even higher control powers the states are AC Stark shifted due to a dressing with the pump tone. **b** By extracting the dashed linecuts in panel **a**, we can fit two Lorentzians to the transmission to characterize the resonant features, corresponding to the first and second transmon transition.

Saturable Mirror

The non-linear behavior of the transmon can be observed in the transmission measurement in Fig. 4.7 when the probe frequency is swept around the resonance frequency of the qubit and the probe power is increased. If the probe power is below the single photon regime the qubit absorbs the incoming photons and re-emits photons back into the waveguide. In the forward direction the re-emitted photon interferes destructively with the transmitted signal. The apparent reduction of transmission at the resonance frequency of the qubit depends on the ability to interfere with the signal. Imperfect interference happens when the qubit dephases during the time that the photon is stored or if the qubit decays into other parasitic channels such that there is either a phase or an amplitude mismatch between the re-emitted and transmitted photons. From Eq. (2.24) it can be seen that for low power Ω of the incoming photonic field the transmission is perfectly suppressed if it is on resonance with the qubit, acting as a perfect mirror [12]. If the amplitude of the incoming signal becomes so large that the qubit cannot re-emit the photons back into the waveguide before another photon arrives at the qubit we observe saturation effects in the resonant feature. We observe that increasing the power such that more than a single photon arrives per lifetime $\sim 1/\gamma_r$ reduces the interference between the probe signal and re-emitted radiation from the qubit, hence the resonant transmission increases and eventually reaches unity. The low power measurements shown in table 4.1 yield the characteristic qubit rates such that Eq. (2.24) only depends ont the drive strength Ω. This can be used for a power calibration by fitting the analytic transmission to the power dependent data with the fit parameter Ω such that we can relate the applied power at the room temperature electronics to the power that arrives at the qubit. A more accurate way to calibrate the on-chip power can be done by using the Autler-Townes effect.

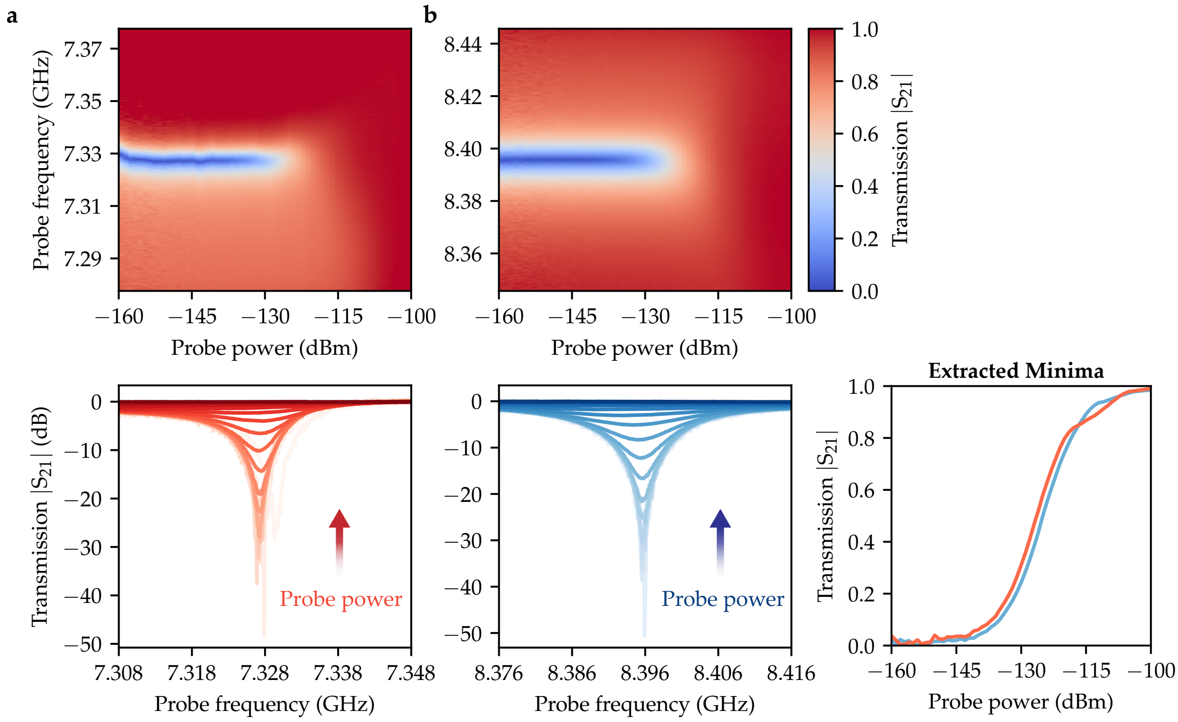

Figure 4.7: Power dependence. The ability to saturate the 0-1 transition reflects the non-linear behavior of a qubit. The probe frequency is varied across the resonance frequency of the qubit while the probe power is increased. **a** If the qubit is flux-tuned to a frequency $f_{01} = 7.33\,\mathrm{GHz}$, where it is very susceptible to magnetic field changes we observe that the resonance minimum fluctuates. For increasing probe power the transition gets less visible. As the qubit can only deal with one arriving photon, it has to emit a photon before it can absorb another one. Therefore the saturation depends on the decay properties of the transmon. **b** When the qubit is tuned to the upper sweetspot where the frequency changes are smaller for equal magnetic field changes, the resonance frequency is more stable. The points of lowest transmission are used to calibrate the probe power, plotted on the right (Extracted Minima). Setting the probe power to $-150\,\mathrm{dBm}$ ensures that the contrast is maximized and the system is not saturated by the probe tone.

Power Calibration

Already when extracting the anharmonicity in Fig. 4.6, it becomes clear that when the pump power is increased beyond the saturation of the $|0\rangle - |1\rangle$ transition, the transmon levels are dressed by the pump field and the Autler-Townes splitting appears for both the $|0\rangle - |1\rangle$ and $|1\rangle - |2\rangle$ transitions [77]. In general, the Autler–Townes effect is a dynamical Stark shift for the case when a resonant oscillating electric field changes the shape of the spectral line. In our case it is the applied oscillating electric field from the microwave pump that alters the emission spectrum of the transmon transitions. The splitting between the dressed transitions is given by the Rabi frequency $\Omega_c = A\sqrt{P}$ where A is a constant that relates the power at the generator P to the drive amplitude at the qubit Ω_c. On its way from the microwave source to the sample, the signal passes filters and attenuators, that are frequency dependent. Moreover, the qubit coupling to the waveguide is not constant in frequency, evident in the

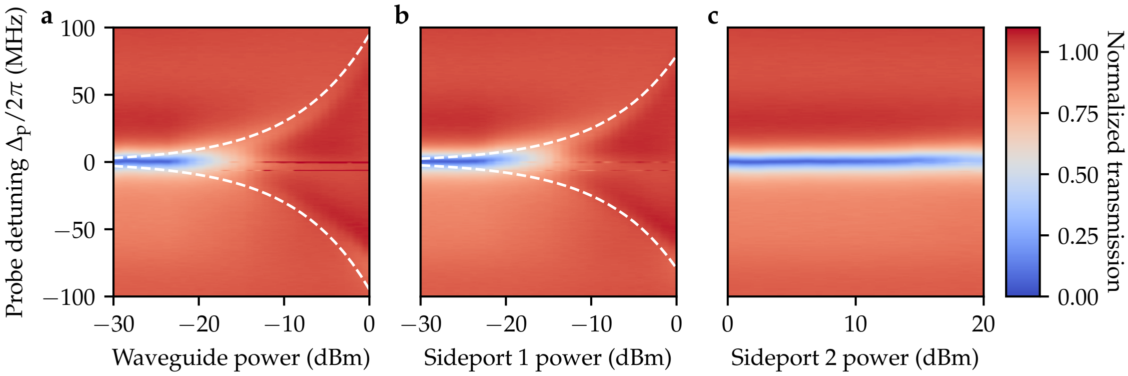

Figure 4.8: Autler-Townes effect. If a pump is applied to the $|0\rangle - |1\rangle$ transition of the transmon the transmission on resonance depends on the pump strength. Depending on the port where the pump is applied the power, that is needed might be very different. **a** Through the waveguide and **b** Sideport 1 (close to the transmon) the Autler-Townes splitting is visible and can be used to calibrate the absolute power at the qubit by fitting the AC Stark shifted transitions. The splitting equals the Rabi frequency and can be used to determine the attenuation from the pump to the qubit location. The white dashed line indicates the splitting, where the distance between the upper and lower branch equals the Rabi-frequency. **c** For a pump tone applied through sideport 2 we cannot observe a splitting within the power range of the signal generator. Sideport 2 is located 45 mm away from the measured qubit, thus couples very weakly, which is important in order to selectively control local qubits.

quality factors shown in Fig. 4.4. Thus, the conversion parameters A in table 4.2 are only valid at the corresponding calibrated frequency.

In Fig. 4.8 we show the transmission around the transition frequency of qubit Q_2 while increasing the pump power of a coherent microwave source. As the power increases, the bare transition saturates and gets dressed by the field of the pump. The AC field splits the two bare transition states into doublets that are separated by the Rabi frequency depending on the amplitude seen by the qubit. For the waveguide port and sideport 1 the qubit sees approximately the same power. Sideport 2 sits 45 mm away and its field does not propagate along the waveguide, therefore the qubit effectively sees a much smaller field for the same applied power. By fitting the dependence of the Rabi frequency on the source power we arrive at table 4.2. The sideports are weakly coupled to the local transmon pairs so that the dark

	A_{WG} (MHz/V)	A_{SP1} (MHz/V)	A_{SP2} (MHz/V)
Q_1	3×10^3	2.5×10^3	< 10
Q_2	3×10^3	1.4×10^3	< 10
Q_3	3×10^3	140	2.3×10^3
Q_4	3×10^3	140	1.6×10^3

Table 4.2: Conversion factors. Fitted conversion factors A from $\Omega_c = A\sqrt{P}$, that converts the signal generator power P into Rabi-frequency Ω_c at the qubits. The calibration is performed roughly at $f = 7.3\,\mathrm{GHz}$ and the indices correspond to the waveguide port, and the sideports 1 & 2.

state decay time is not limited by the losses introduced by the sideports. On-chip circuit QED experiments [132] made use of additional drive lines for over a decade, such that we adapted and implemented them in 3D waveguides. In our experiment, we capitalize on the symmetry between the four qubits and the sideport drives. The side ports provide an amplitude gradient across the local pairs, as verified by the different values for A in table 4.2. The asymmetry will be helpful to access dark states $|D_1\rangle$ and $|D_2\rangle$ that arise from the capacitive coupling, but also the possibility to independently adjust the relative phase ϕ between the pairs. This allows us to apply a symmetric drive which has opposite symmetry of the drive field of the waveguide. The field of the drive port does not coincide with the polarization of the TE_{10} waveguide mode and decays exponentially along the propagation direction of the waveguide, thus the drive is effectively local.

Qubit-Photon Bound States

When the qubit is interacting with itinerant photons in the waveguide the transmission will decrease due to destructive interference. The situation changes when the qubit is tuned below the cutoff-frequency f_c=6.546 GHz of the waveguide. As seen in Fig. 3.2, the waveguide dimensions restrict the propagation of radiation for frequencies that are lower than f_c, thus they are reflected. However, as can be seen in Fig. 4.1 the transmission does not instantaneously drop to zero for frequencies $f < f_c$ but is rather reduced by 50 dB over a range of 500 MHz. This means that for $f \sim 6$ GHz only a fraction of 10^{-5} of the power reaches the output at the other side of the waveguide. If a qubit in the waveguide is tuned to a resonance frequency below cutoff, the evanescent fields of the waveguide can dress the qubit which yields qubit-photon bound states. The bound state obtains an exponentially decaying photonic wavefunction that couples to the input and output ports, enhancing the transmission at the the qubits transition frequency. Measuring the transmission close to the cutoff while tuning a qubit to the lower sweetspot $f_{sp} = 6.2$ GHz in Fig. 4.9a shows that the resonant feature changes from a dip (dark blue) to a peak (white) in transmission. As the excitation pins of the waveguide-to-coaxial adapters on both sides of the waveguide cannot excite a traveling wave at those frequencies, the qubit acts as an additional antenna that increases the coupling between the two pins, effectively increasing the transmission. These qubit-photon bound states have been already observed in circuit QED experiments where a bandgap is engineered on an on-chip transmission line [17, 78, 133] but were also already observed in a rectangular waveguide [134]. We can analyze the bound state peaks by extracting the linewidth for the resonances below the cutoff. Figure 4.9b shows the linewidth against the detuning with respect to the cutoff frequency. By fitting the data we find that the linewidth indeed scales exponentially with the detuning, similar to the suppressed transmission.

Two qubit-photon bound states can interact by tuning them into resonance below the cutoff. For a distant transmon pair this has been shown in [134]. The distant qubit-photon bound state shows an avoided crossing that corresponds to the coupling strength between the bound states. The coupling strength depends on the overlap of the localized photonic wavefunctions. The wavefunctions are more localized when they are tuned further into the stopband, meaning tuned further away from the waveguide cutoff. This again leads to a smaller overlap and thus to a weaker coupling between the two bound states. Here, we investigate the avoided crossing of a directly coupled pair that also results in an avoided crossing, shown in 4.10. Similar to the case where the qubits are tuned in resonance in the waveguide band, we obtain a bright and a dark state when the bound states are resonant. While the transitions in the waveguide

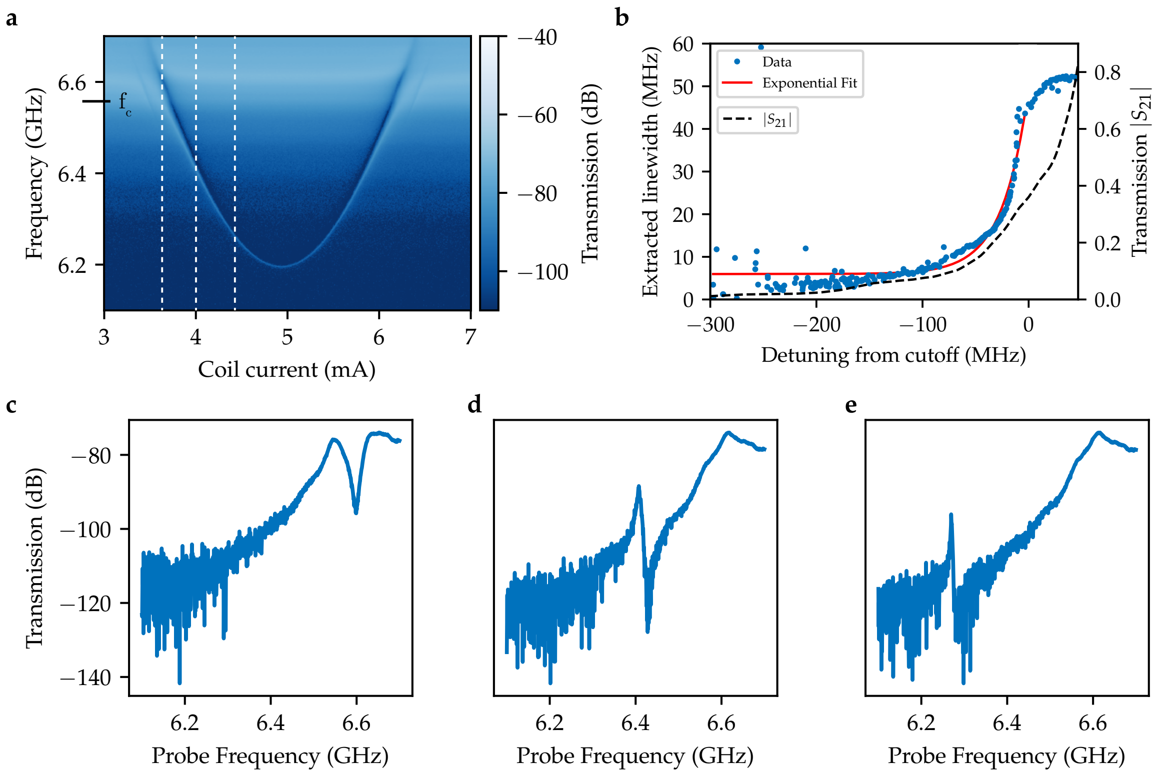

Figure 4.9: Qubit-photon bound states. **a** When a qubit is tuned from the waveguide band below the cutoff-frequency of the waveguide, the resonant feature changes its shape from a dip to a dip-peak and eventually to a peak when measuring the transmission through the waveguide. When the physical distance of the qubit is not too far from the waveguide ports it will directly couple to the excitation pins. **b** As soon as the qubit is tuned below the cutoff-frequency its linewidth decreases exponentially. **d** Extracted linecut from **a** at a coil current of 3.65 mA. **e** Linecut at 4 mA. **f** Linecut at 4.4 mA.

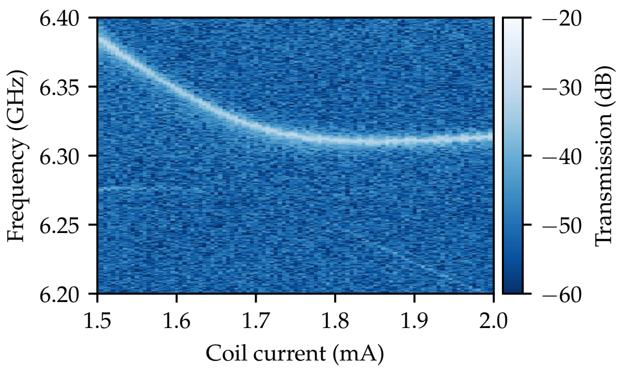

Figure 4.10: Interacting qubit-photon bound states. Two directly coupled transmons are interacting below the cutoff via the capacitive coupling. A detailed measurement of two transmons tuned into resonance below the waveguide cutoff shows that the high frequency peak appears as a bright line while the low frequency peak gets narrower and finally disappears on resonance.

band correspond to frequencies with a decreased transmission due to the scattering processes, the bright transition now corresponds to a frequency where the transmission is significantly increased. As we will see later, we can study the bright and dark states in time-resolved measurements.

4.2 Interacting Qubits

The experiment utilizes two different interaction mechanisms between the qubits. The capacitive coupling between two qubits is engineered by designing the geometry of the transmon antennae and adjusting their physical distance. The observable feature is the avoided crossing of the qubit transitions. When two qubits are separated along the waveguide the interactions oscillate with effective separation distance, swapping from a purely coherent-exchange coupling for distances $(2n-1)\lambda/4$ to a dissipative coupling for distances $n\lambda/2$ with $n\epsilon\mathbb{Z}$. On resonance the qubits form hybridized compounds with new eigenstates that have very different decay properties than the individual transmon.

4.2.1 Capacitive Coupling

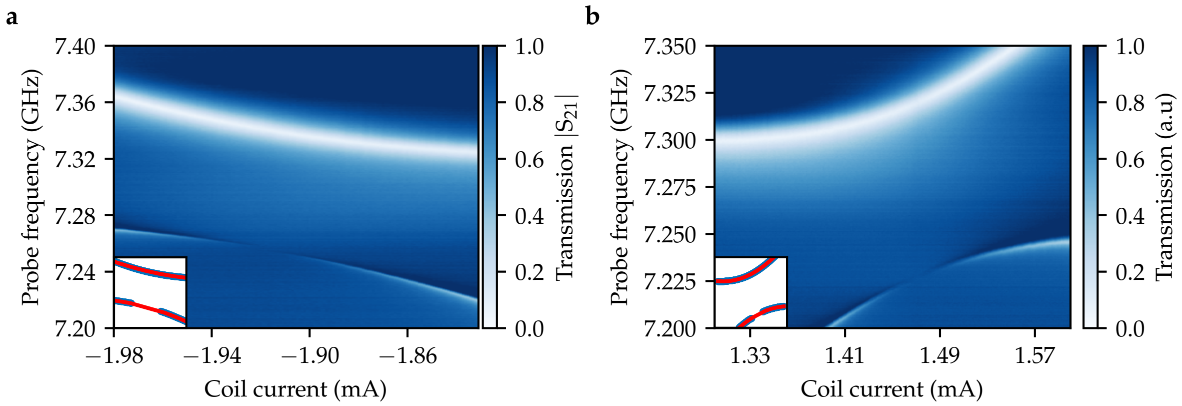

Figure 4.11: Avoided crossing of two qubits. a Tuning two capacitively coupled qubits in and out of resonance results in an avoided crossing. Compared to the individual emitter, the upper branch obtains twice the linewidth, whereas the lower branch disappears from the transmission. The frequency splitting $\frac{2J}{2\pi}$ between the two transitions is used to find the coupling strength J of the qubits. Here between $Q1$ and $Q2$: $J_{12}/2\pi = 43\,\mathrm{MHz}$ **b** For the other qubit pair $Q3$ and $Q4$ we extract $J_{34}/2\pi = 47\,\mathrm{MHz}$.

Tuning two proximal transmons in and out of resonance and measuring the transmission through the waveguide results in an avoided crossing between two transitions, plotted in Fig. 4.11. Fitting the resonances and determining the minimal distance between the branches (see insets) allows to extract the coupling strengths between qubits $Q1$ and $Q2$ as $J_{12}/2\pi = 43\,\mathrm{MHz}$ and qubits $Q3$ and $Q4$ as $J_{34}/2\pi = 47\,\mathrm{MHz}$. In the detuned scenario the branches represent the $|0\rangle$-$|1\rangle$ transitions of the two transmons. In the resonant case the transmons hybridize and form a new set of eigenstates that arise from a direct coupling through the capacitance between the metallic pads of their antennae, sketched in Fig. 4.12a. In this configuration the coupling has an effective $1/r^3$-dependence [84], leading to short range coupling. On resonance, an excitation can swap coherently between the local transmons, resulting in new eigenstates, in particular a symmetric state $|B_{\mathrm{loc}}\rangle = (|ge\rangle + |eg\rangle)/\sqrt{2}$ and an antisymmetric state $|D_{1(2)}\rangle = (|ge\rangle - |eg\rangle)/\sqrt{2}$. In Fig. 4.12a the states are visualized by in- and out-of-phase oscillating arrows. Here, the capacitively coupled transmons are located at the same position with respect to the propagating waveguide field and symmetrically around the center of the waveguide. That means that the phase of the electrical field that propagates through the waveguide is the same for both transmons, thus the antisymmetric state decouples and the waveguide drive can only access the symmetric state. The coherent exchange interaction also lifts the degeneracy of $|B_{\mathrm{loc}}\rangle$ and $|D_{1(2)}\rangle$ and allows us to observe the decoupling of the antisymmetric superposition dark state when we tune the qubits into resonance. At the same time the symmetric superposition bright state in the upper branch obtains twice the linewidth. To characterize the dark states, we measure the ground state population by

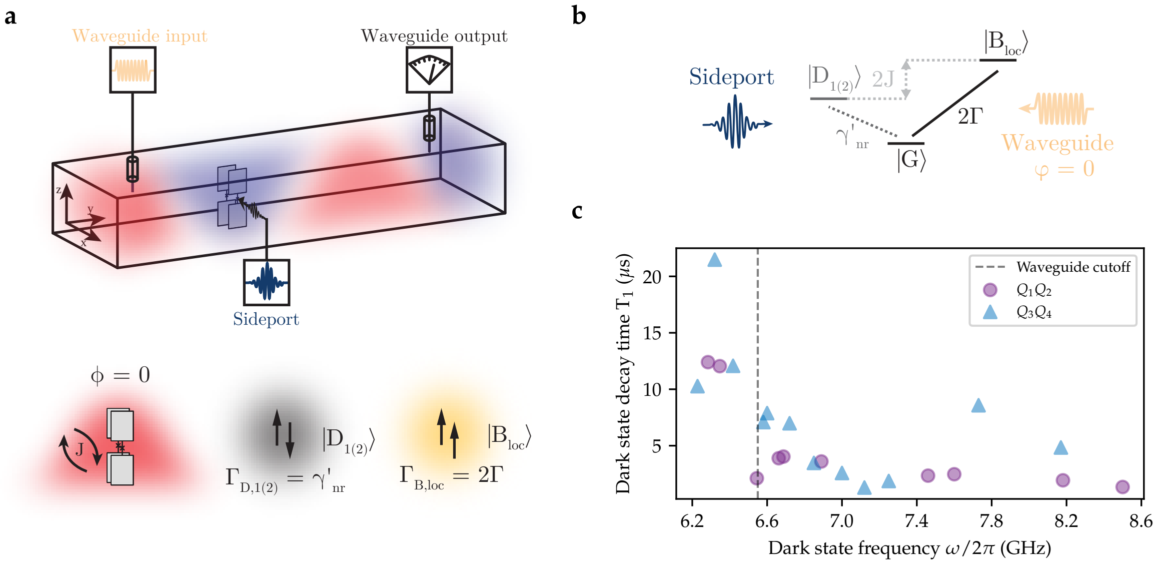

Figure 4.12: Direct qubit-qubit coupling. **a** Schematic of two capacitively coupled transmons in a rectangular waveguide. The metallic plates form the coupling capacitance that is responsible for the coherent exchange coupling. The waveguide ports can only excite the states that match the phase of the waveguide drive field, which is symmetric for the capacitively coupled pair. The sideport has a gradient across the pair and can therefore also excite the antisymmetric states. **b** Measurement protocol of the dark state lifetime. The decoupling of the dark transition from the waveguide and reducing the decay rate to non-radiative losses also imposes the necessity to excite it via the sideports. The readout is done via the bright transition through the waveguide. **c** Dark state decay times plotted against their resonance frequency. Below the waveguide cutoff (dashed vertical line) the decay times increase significantly compared to the times measured in the waveguide band.

employing a state dependent scattering scheme, adapted from quantum non-demolition state detection in trapped ion quantum computing [135]. If the collective system is in the ground state $|G\rangle$ we can coherently scatter photons between the ground state $|G\rangle$ and superradiant state $|B_{\mathrm{loc}}\rangle$ which reduces the transmission through the waveguide for photons that are resonant with the bright transition. This is already evident by the absorption dip in the transmission of Fig. 4.11. If one of the the dark states $|D_{1(2)}\rangle$ is populated, the microwave signal is not scattered, resulting in unit transmission. By tuning the qubits into resonance at different frequencies and selectively exciting the dark state using microwave signals applied through the sideport we can measure dark state relaxation times, shown in Fig. 4.12c. The sideport has a field gradient across the pair, which yields an antisymmetric drive component. This means that the we can access the dark transition and measure the energy relaxation within the range of the transmons tunability. In Fig. 4.12c the extracted dark state decay times are plotted against their resonance frequency. We can even measure the dark state of the interacting bound states below the waveguide cutoff, shown in Fig. 4.10. Here, the transmission is enhanced when there is a resonant transition such that the readout scheme detects a high amplitude signal when the ground state is populated and a low amplitude when the population is in the dark state, already observed in Fig. 4.9.

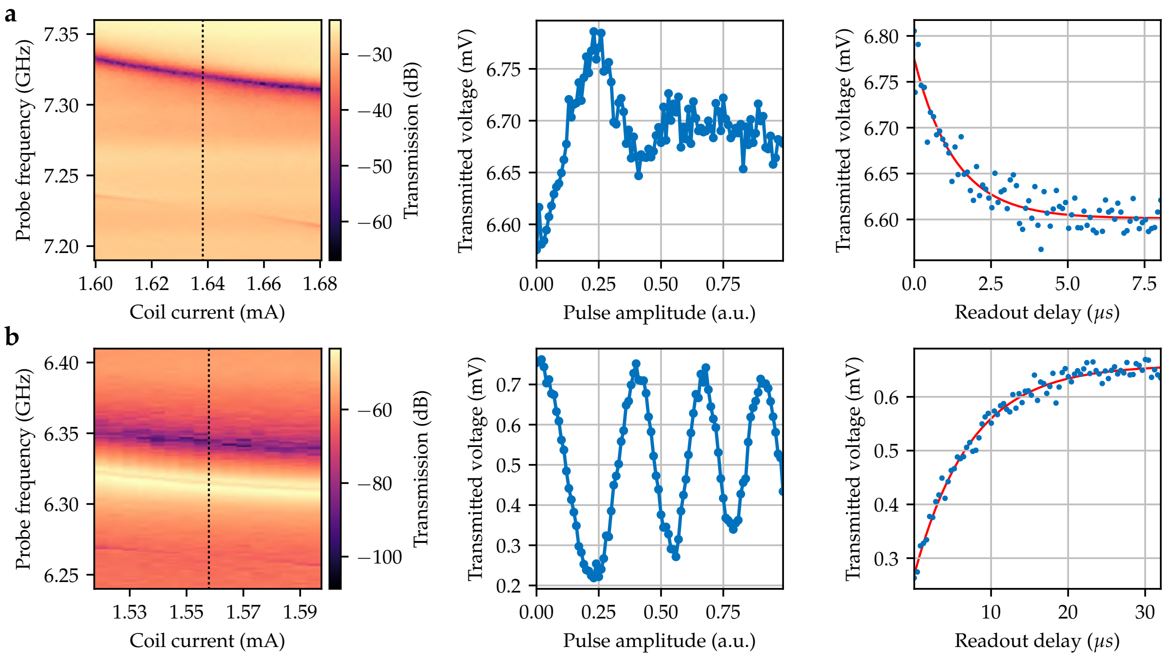

Figure 4.13: Local dark state measurements. a The dark state disappears from the waveguide transmission while the bright state is utilized for the detection. With the antisymmetric component of the sideport one can drive Rabi oscillations while measuring the waveguide transmission through the waveguide ports. This scheme enables to observe the Rabi oscillations for increasing pulse amplitude and to characterize the relaxation time of the dark state qubit. **b** Below the waveguide cutoff frequency the bright feature allows for the same readout scheme. As the unsaturated bound state enhances the transmission we detect a high transmission amplitude when the dark state is not populated and a suppressed transmission for an populated dark state. The optimal frequency is calibrated by performing T_1 measurements for varying frequencies of one transmon, while the other is kept at a constant frequency.

To understand the readout and excitation scheme we compare the situations when the qubits are tuned into resonance in the band of the waveguide and below the cutoff frequency. The interacting transmon characteristics differ when they are in the waveguide band or below the cutoff, as can already be seen in Fig. 4.13. In the tuning maps the bright transition is visible as a peak in transmission when tuning the transmons into resonance outside the band of the waveguide, while in the band it is a dip. The additional dip feature is usually very hard to

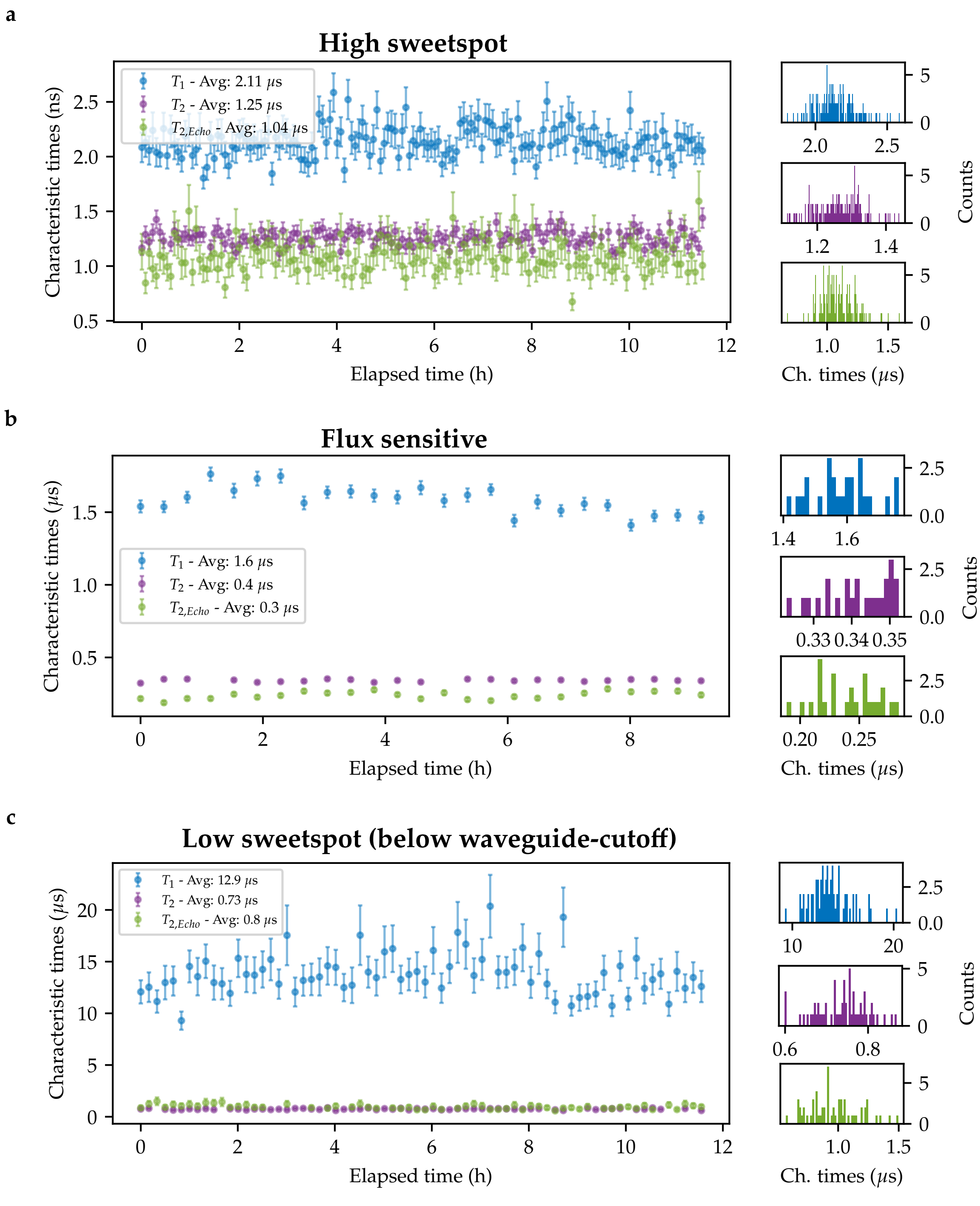

Figure 4.14: Characteristic times. Repeated measurements for a few hours to validate the stability of the coherence in the dark states. **a** The dark state is created close to the upper sweetspot of the two used transmons. **b** On the tuning slope, where the susceptibility to flux noise is maximal. **c** In vicinity to the lower sweetspots well below the waveguide cutoff.

detect as it results in an even lower transmission. The bright feature is then again utilized to read out the dark state qubit for frequencies below the cutoff such that the Rabi measurement shows a high transmission amplitude if we do not excite the system. When the dark state is excited, the bound state cannot enhance the transmission as the transition disappears, thus we measure low transmission amplitudes. Surprisingly, the Rabi measurement for increasing the pulse amplitude shows more oscillations, compared to the in-band Rabi. We attribute this to a weaker driving of off-resonant transitions from the two-excitation manifold. Below the cutoff the waveguide acts as a filter as photons cannot propagate [124, 136], reducing the noise background for the transmons. This is consistent with the improvement of measured T_1 times below the cutoff, but needs further investigation in this context. The resonance condition is calibrated by tuning one transmon in and out of resonance with the other and repeating the T_1 measurement, shown in Fig. D.1. The largest dark state T_1 time corresponds to the optimal tuning of the transmon and thus the optimal symmetry condition.

In addition to the energy decay time T_1 the dark states that are created by the capacitive coupling are also characterized by performing a Ramsey [137] and Hahn-echo [138] experiment to obtain the coherence times T_2 and $T_{2,echo}$. The measurements are then repeated for a 12 hours, while the base-plate temperature is monitored. Figure 4.14 shows the measurements for different dark state frequencies, corresponding to the vicinity of the upper and lower flux sweetspots of the individual transmons, as well as a set of measurements on the slope where they are most susceptible to flux noise. Even in the presence of the four coils with the transmon frequencies tuned to a point with maximal susceptibility the decay times are stable over the time of measurements which enables the usage of the dark states without the need to readjust the magnetic flux between experiments.

4.2.2 Waveguide-Mediated Interactions

Two transmons that are located in the waveguide separated by a distance along the propagation direction of the waveguide field can also be tuned in and out of resonance. Qualitatively, there are already significant differences in the crossings of the qubit transition frequencies in Fig. 4.15, that depend on the frequency where they are tuned into resonance. Effectively, the different frequencies correspond to different qubit-qubit separations and give rise to different waveguide-mediated interactions.

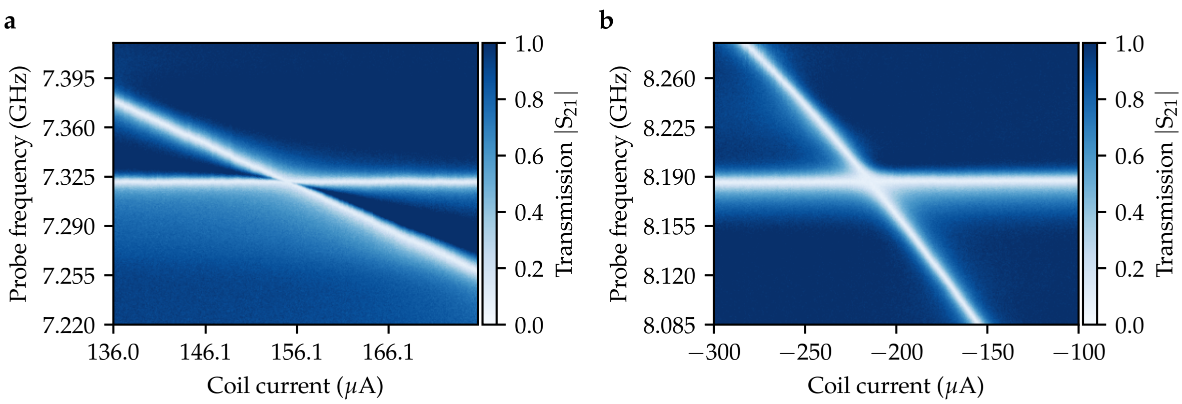

Figure 4.15: Transition frequencies crossings for distant transmons. a At an effective distance $d = \lambda/2$, corresponding to a frequency $f_{\lambda/2} = 7.33\,\text{GHz}$. **b** At an effective distance $d = 3\lambda/4$, corresponding to a frequency $f_{3\lambda/4} = 8.2\,\text{GHz}$.

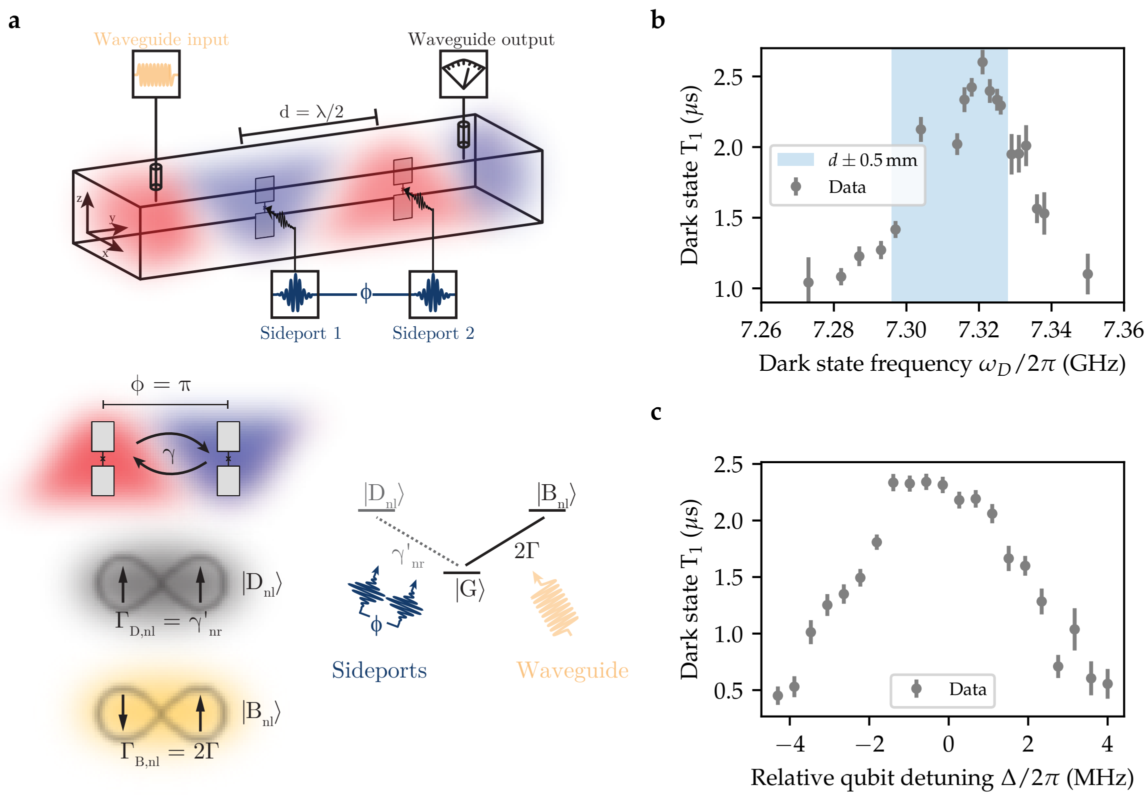

Figure 4.16: Calibrating $\lambda/2$. **a** To calibrate the frequency where correlated decay is maximized we utilize two distant transmon. As the inter-qubit separation is fixed we need to use the flux tuning to set the resonance frequencies. The local drives "Sideport 1" and "Sideport 2" enable us to excite the system with a phase ϕ that is arbitrarily set with the pulse generation electronics. For a distance $\lambda/2$ the correlated decay is maximized resulting in a phase difference between qubits of $\phi = \pi$ for a photon traveling through the waveguide. The hybridized symmetric state $|D_{\mathrm{nl}}\rangle$ thus decouples from the waveguide and the antisymmetric state $|B_{\mathrm{nl}}\rangle$ becomes superradiant. Employing both states we can excite the dark state via the sideports and measure the ground state via the waveguide. **b** Tuning the qubits into resonance at different frequencies and measuring the decay times of the dark state to calibrate the decoherence-free frequency where T_1 is maximized. **c** Detuning one qubit from the decoherence-free frequency breaks the dark state symmetry and results in shorter lifetimes.

A frequency $f_{\lambda/2} = 7.33\,\mathrm{GHz}$ corresponds to a wavelength of $\lambda_{7.33\,\mathrm{GHz}} = 91\,\mathrm{mm}$ in the rectangular waveguide (see Eq. (3.7)). A frequency $f_{3\lambda/4} = 8.2\,\mathrm{GHz}$ corresponds to a wavelength of $\lambda_{8.2\,\mathrm{GHz}} = 61\,\mathrm{mm}$. The crossings are a signature of waveguide-mediated interactions, that depend on the effective separation [97]. When two transmons interact through the waveguide at a separation d_y, schematically shown in Fig. 4.16a, the signal propagating between the transmons acquires a phase $\varphi = 2\pi d_y/\lambda$ that depends on the wavelength $\lambda = 2\pi v/\omega$ and distance d_y, where v is the group velocity in the waveguide and ω the angular frequency of the wave. For the setup with physical separation between the transmons of $d_y = (46.0 \pm 0.5)\,\mathrm{mm}$ a phase difference of $\varphi = \pi$ corresponds to an emission frequency $\omega_\pi/2\pi = (7.312 \pm 0.016)\,\mathrm{GHz}$. There, correlated decay into the waveguide $\gamma_{j,k} = \sqrt{\gamma_j\gamma_k}\cos(\varphi)$ is maximized and coherent waveguide-mediated interaction $\tilde{J}_{j,k} = \sqrt{\gamma_j\gamma_k}\sin(\varphi)/2$ is absent, due to the counter-periodic behavior [20]. Here, the individual waveguide coupling rates are denoted by γ_j and γ_k, for transmons $j \neq k$. The photon-mediated interaction leads to symmetric and antisymmetric states under qubit exchange, i.e. the dark state $|D_{\mathrm{nl}}\rangle = (|ge\rangle + |eg\rangle)/\sqrt{2}$ and bright state $|B_{\mathrm{nl}}\rangle = (|ge\rangle - |eg\rangle)/\sqrt{2}$. For a distance of $\lambda/2$, the phase relation of the electromagnetic field in the waveguide is antisymmetric ($\varphi = \pi$), thus we can only excite the antisymmetric bright state. The dark state symmetry is opposite to the field symmetry of the waveguide, eliminating the coupling to the drive field and decay into the waveguide. In Fig. 4.15a this means that on resonance only the bright state is visible in the waveguide transmission.

To achieve control over the non-local dark state and calibrate the decoherence-free frequency f_π the measurement employs the two additional drives sideport 1 and sideport 2 simultaneously. The locality of the sideport drives that was calibrated in Fig. 4.8 is important as the two-qubit ensemble has to be driven with a symmetric phase to be able to excite the dark state $|D_{\mathrm{nl}}\rangle$. If it would propagate through the waveguide it would obey the phase-relation that is imposed by the waveguide, which is $\phi = \pi$ for $d = \lambda/2$. The locality of the two sideports enables to set arbitrary phases with the signal generation electronics. Similar to the capacitively coupled qubits, the dark state is excited by a pulse on both sideports with a relative phase that matches the dark state symmetry $\phi = 2n\pi$ ($n\epsilon\mathbb{Z}$). The measurement scheme is sketched in Fig. 4.16a. The absence of coherent exchange coupling results in degenerate bright and dark states, such that the pulse is only selective via the phase and not via the frequency. The readout is then performed via the bright state through the waveguide, analogous to Sec. 4.2.1. By tuning the qubits into resonance at different frequencies, selectively exciting the dark state using microwave signals applied through the sideports with $\phi = 0$ and measuring the ground state population via the bright transition we experimentally search for the longest dark state relaxation time around the analytical decoherence-free frequency $f_\pi = (7.312 \pm 0.016)\,\mathrm{GHz}$ and indeed find a maximum at $f_\pi = 7.321\,\mathrm{GHz}$, as shown in Fig. 4.16b.

By keeping one qubit at frequency f_π and detune the other qubit we can measure the dark state resilience against imperfections arising from calibration errors and frequency drifts. In Fig. 4.16c the dark state decay time is constant until the qubit is approximately 1.5 MHz detuned from the second qubit, then starts to decrease to 0.5 ns at a relative detuning of 4 MHz. To confirm that the qubits are not detuned in the search for f_π, this measurement is conducted at each point in Fig. 4.16b.

4.3 Multilevel Waveguide QED with Four Transmons

To build a system that incorporates waveguide-mediated and direct qubit-qubit interactions we include four transmons that are properly arranged inside the waveguide. This enables us to properly characterize a multi-qubit system and benchmark its usability in terms of dark state energy relaxation and coherence times. We show how the dark state is addressed and point out the necessity to further engineer the higher excitation manifold in order to create a useful dark state qubit. The two-excitation manifold has a rich level spectrum that can be turned into a feature by implementing a reset protocol for the dark state. Nevertheless, the manifolds can be engineered to create a better dark state qubit. Realizing the four transmon experiment is a first step towards multi-qubit waveguide QED experiments and opens the door to explore many-body interactions in 3D waveguides. The full waveguide QED system is depicted in Fig. 4.17, which consists of all four transmons and includes the waveguide input and output ports to measure the transmission and the pairwise excitation sideports 1 and

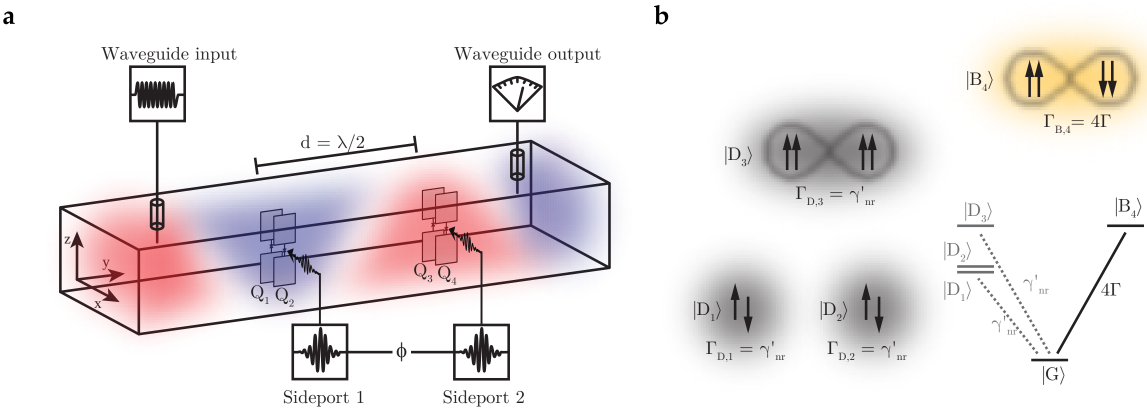

Figure 4.17: Full system with four transmons. **a** Sketch of the waveguide transmon setup with local control lines Sideport 1 and 2 that respectively act on the proximal pair. **b** The combination of capacitive and waveguide-mediated interactions creates a one-excitation manifold with two local dark states and one non-local dark and bright state. Local dark states have a different symmetry compared to the non-local ones, due to the waveguide phase-relation that is imposed on them.

2. The transmons are tuned into resonance by calibrating the mutual inductance matrix between the superconducting coils and the individual qubits, such that the bright transitions of the capacitively coupled pairs match the decoherence-free frequency f_π. Both local two-transmon bright states interact via the waveguide and form the collective four qubit states $|B_4\rangle$ and $|D_3\rangle$, whereas the local two-qubit dark states $|D_1\rangle$ and $|D_2\rangle$ cannot interact via the waveguide. The numbering of the states is according to their energy in ascending order. For degenerate energy levels it is chosen according to their decay rates, where additionally B indicates a bright transition and D a dark transition with respect to the waveguide decay. These four states span the first excitation manifold, depicted in Fig. 4.17b. The local dark states $|D_1\rangle$ and $|D_2\rangle$ have out-of-phase oscillating dipole moments such that they destructively interfere and decouple from the waveguide. They obtain a decay rate that is reduced to the internal decoherence mechanisms γ'_{nr}. The local bright states are oscillating in-phase, such that they couple to the waveguide that mediates the interaction between the pairs. The pairwise out-of-phase oscillating dipole moments create the four transmon bright state $|B_4\rangle$ due to the effective $\lambda/2$ separation between the pairs. The constructive interference results in a four qubit superradiant linewidth 4Γ. The pairwise in-phase oscillating dipoles destructively interfere, such that the subradiant state $|D_3\rangle$ is only reduced to the combined internal loss rates γ'_{nr}.

Only the bright transition $|G\rangle$-$|B_4\rangle$ is visible in the waveguide transmission, the other states of the one-excitation manifold decouple. By measuring the transmission around the resonance frequency of the bright transition we observe a resonance feature. We extract the decoherence rate $\Gamma_{\mathrm{B},4}/2\pi = 30.5\,\mathrm{MHz} \sim 4\Gamma$ resulting from constructive interference of all transmons $\Gamma_{\mathrm{B},4} = \sum_j \Gamma_j$ by fitting complex transmission data. In Fig. 4.18a we show the transmission amplitude of the four-transmon superradiant transition (red data) in comparison with the two-transmon superradiant transition (beige data) with decoherence rate $\Gamma_B \sim 2\Gamma$ and a single transmon (blue data) with decoherence rate Γ. As expected from the constructive interference between the oscillating dipole moments, the coupling to the waveguide increases

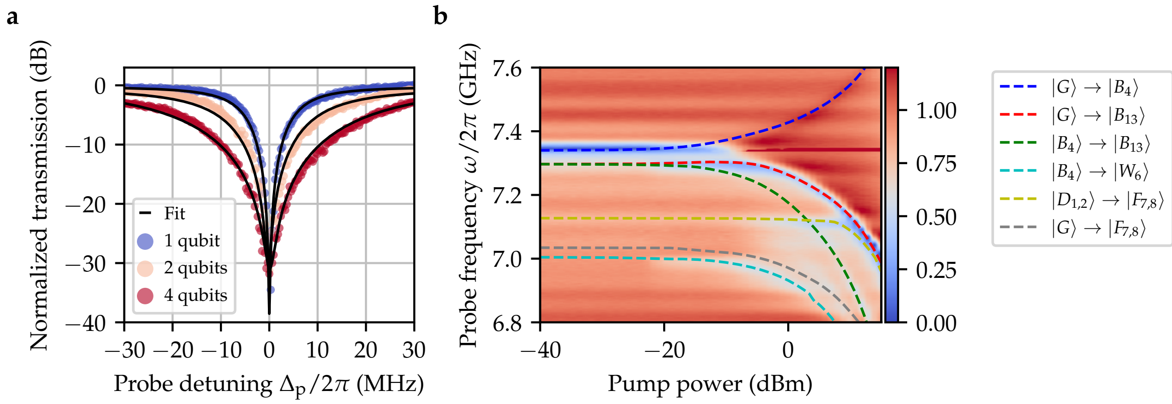

Figure 4.18: Transmission spectroscopy. a Transmission through the waveguide for one, two and four qubits tuned into resonance. The bright states obtain double and fourfold the single qubit linewidth. **b** With a pump tone applied on resonance with the bright transition $|G\rangle$-$|B_4\rangle$ and probing the waveguide transmission the additional states in the two-excitation manifold appear, similar to the measurement of the transmon anharmonicity and the $|1\rangle$-$|2\rangle$ transition. Here, we can observe different transitions corresponding to states in the two-excitation manifold.

linearly with the number of transmons. The dark states $|D_1\rangle$, $|D_2\rangle$ and $|D_3\rangle$ are not visible through the waveguide transmission. However, from the avoided crossings of the transition frequencies of the local transmon pairs we know the frequencies of the local dark transitions $|G\rangle$-$|D_1\rangle$ and $|G\rangle$-$|D_2\rangle$. Furthermore, the frequency of transition $|G\rangle$-$|D_3\rangle$ is the same as for $|G\rangle$-$|B_4\rangle$. Table 4.3 summarizes the measured single transmon and bright state rates, as well as

Transmons	$\Gamma/2\pi$ (MHz)	$\gamma_r/2\pi$ (MHz)	$\gamma'_{nr}/2\pi$ (MHz)	$\alpha/2\pi$ (MHz)	$J_{ij}/2\pi$ (MHz)
Q_1	7.8	14.9	0.4	219	-
Q_2	6.7	12.7	0.3	222	-
Q_3	8.3	15.7	0.5	225	-
Q_4	6.7	13.0	0.4	206	-
Q_1Q_2	14.8 (14.5)	27.6 (27.6)	1.1 (0.7)	-	43
Q_1Q_3	16.8 (16.1)	31.8 (31.6)	0.9 (0.9)	-	-
Q_1Q_4	15.2 (14.5)	28.8 (27.9)	0.8 (0.8)	-	-
Q_2Q_3	15.3 (15.0)	29.0 (28.4)	0.8 (0.8)	-	-
Q_2Q_4	13.7 (13.4)	26.0 (25.7)	0.7 (0.7)	-	-
Q_3Q_4	15.1 (15.0)	27.9 (28.7)	1.1 (0.9)	-	47
$Q_1Q_2Q_3Q_4$	30.5 (29.5)	57.7 (56.3)	1.7 (1.6)	-	-

Table 4.3: Parameter summary. The number in brackets corresponds to the value of the added single qubit linewidths. The numerical simulations need the parameters γ_r, α and J_{ij} and additionally has to distinguish between non-radiative dissipation $\gamma_{nr}/2\pi = 15\,\mathrm{kHz}$, pure dephasing $\kappa_\phi/2\pi = 100\,\mathrm{kHz}$ and collective dephasing $K_\phi/2\pi = 437\,\mathrm{kHz}$.

the direct coupling strengths J_{12}, J_{34} that can be extracted from the waveguide transmission measurements. The bright state linewidths are always approximately the sum of the involved single qubits.

Similar to the Autler-Townes measurement in Fig. 4.8 and the extraction of the anharmonicity α in Fig. 4.6 for the individual transmons we add a coherent pump that is resonant with the $|G\rangle$-$|B_4\rangle$ transition and record the waveguide transmission to spectroscopically observe the multi-level energy spectrum of the four transmon system. In Fig. 4.18b, the pump is applied through the waveguide, thus has a antisymmetric phase relation and saturates the $|G\rangle$-$|B_4\rangle$ with increasing pump power. The dashed lines indicate one and two photon transitions, that match the symmetry and power dependence from a numerical simulation. Where for a single transmon one additional transition appeared, we identify at least 5 transitions in the measured frequency range for the four transmon system. As the pump and readout tone are sent through the waveguide we only observe the transitions that can be driven with an antisymmetric phase $\phi = \pi$. In comparison to a single transmon, where the anharmonicity is given by the difference of the energies $\alpha = E_{01} - E12 \sim 220\,\mathrm{MHz}$, the level spacing decreased already for the one-excitation manifold with the degenerate bright and dark state $|B_4\rangle$ and $|D_3\rangle$ and the local dark states $|D_1\rangle$ and $|D_2\rangle$, that are only detuned by $\sim 90\,\mathrm{MHz}$. Additionally, we see in Fig. 4.18b, that the transitions into the two-excitation manifold, e.g. $|G\rangle$-$|B_{13}\rangle$ are in spectral vicinity of the one photon transitions only being detuned by $\sim 25\,\mathrm{MHz}$ with respect to $|G\rangle$-$|B_4\rangle$ and $|G\rangle$-$|D_3\rangle$. From the numerical simulation in Sec. 2.6 we already know that the linewidth of $|G\rangle$-$|B_{13}\rangle$ is roughly three times the single qubit linewidth 3Γ, meaning that the spectral lines are overlapping and cannot be addressed individually.

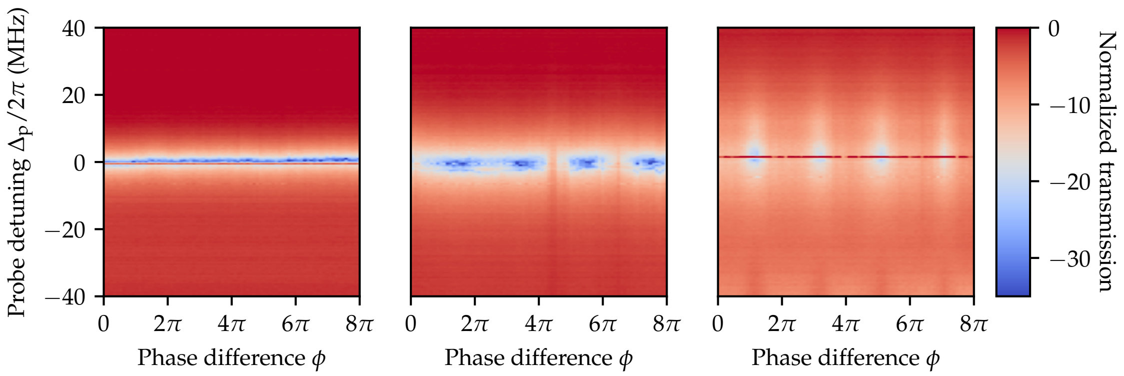

Figure 4.19: Phase-sensitive two-tone spectroscopy. By using the sideports we can change the phase difference between two continuous pumps connected to sideport 1 and 2 and measure the transmission through the waveguide with a weak probe tone. **a** We observe no periodicity for the case of a single transmon. **b** For two transmons we see a periodic change of transmission, depending on the phase difference between the two microwave sources. We attribute the bad quality to the limited phase stability of the coherent microwave sources. **c** For the case of four transmon the features become clearer.

With the sideports we can already investigate the phase dependence with a continuous pump-probe measurement. Each sideport is connected to a coherent microwave source while either one, two distant or all four qubits are tuned to the decoherence-free frequency $f_\pi \sim 7.3\,\mathrm{GHz}$. In Fig. 4.19 we send a coherent tone to sideport 1 and 2. To adjust for power imbalance due to unequal coupling of the excitation ports to the qubits we can use the Autler-Townes power calibration, shown in Fig. 4.8 and table 4.2. By changing the drive phase of one of the microwave sources the effective phase difference between the drives ϕ is varied. We can investigate the symmetries by probing the waveguide transmission around the resonances for one, two and four qubits. For one qubit we do not observe a dependence on the phase while for the case of two distant qubits, as well as the four qubit case we observe a periodicity in the saturation of the transmission dip. The resonance feature appears and disappears depending whether we drive the dark state with a symmetric phase or the bright state with an antisymmetric phase. This is due to the different effective decay rates of the dark and bright state. As the bright state decays much faster it can handle a higher pump power before the transition is saturated. The longer storage time of the dark state leads to saturation at lower pump power.

4.3.1 Rabi Oscillations

The spectroscopic investigation allows to study the energy spectrum of the coupled transmon system over a large measurement bandwidth with narrow spectral resolution. While the transmission only showed one bright state, we were able to reveal multiple transition in the two-tone spectroscopy. In order to utilize the ground state $|G\rangle$ and dark state $|D_3\rangle$ as a waveguide QED qubit we need to achieve coherent control. Due to the symmetry restrictions the waveguide does not have access to this transition, thus we need to use a drive that can match the dark state symmetry. Additionally, access to a long-lived state in the one-excitation manifold also enables a time-resolved measurement of the two-excitation manifold. As we want to explore the four transmon manifold this means that we need to employ the dark state $|D_3\rangle$, because bright state $|B_4\rangle$ decays too fast and leaves us no time to send a second spectroscopy pulse. Moreover, the local dark states $|D_1\rangle$ and $|D_2\rangle$ only give us access to the specific local two transmon subspace. The dark state $|D_3\rangle$ and bright state $|B_4\rangle$ are degenerate energy levels of the four transmon system, thus we cannot use frequency selective driving if we only want to address one or the other. On the other hand, their respective oscillating dipole symmetries are π-shifted, such that a phase selective drive is able to distinguish between them. To characterize the dark state and the sideport drive we study the time-resolved dynamics, when driving the transmon array through the sideports while changing the phase ϕ between sideport 1 and 2. The transition amplitudes from the ground state to non-local dark state and bright state depend on the driving phase ϕ as [100]

$$|G\rangle \rightarrow |D_3\rangle : \quad \frac{\hbar\Omega}{2}\left(1+e^{i\phi}\right), \tag{4.3}$$

$$|G\rangle \rightarrow |B_4\rangle : \quad \frac{\hbar\Omega}{2}\left(1-e^{i\phi}\right). \tag{4.4}$$

The drive of sideports 1 and 2 consists of a 240 ns long Gaussian envelope that is supplied by the Quantum Machines Operator X and mixed with a coherent pump of a microwave generator. Both mixers are connected to the same pump by splitting the signal to eliminate unwanted phase differences between sideport 1 and 2. By selectively exciting the system using microwave signals applied through the sideports with ϕ we can then either induce Rabi oscillations between $|G\rangle$ and $|D_3\rangle$ or drive the bright state. To determine the ground state population, we conduct a reference measurement of the transmitted readout pulse for the case where all transmons are tuned below the waveguide cutoff-frequency and take into accound the dark state decay rate, explained in Sec. 4.3.2. Rabi-oscillations between $|G\rangle$ and $|D_3\rangle$ are observed in Fig. 4.20 when the amplitude of the drive field Ω is increased and the phase difference between the sideports matches $\phi = 2n\pi$ $(n \in \mathbb{Z})$. For an antisymmetric drive with odd integer multiple $\phi = (2n-1)\pi$, we only drive the bright state $|B_4\rangle$ which decays very

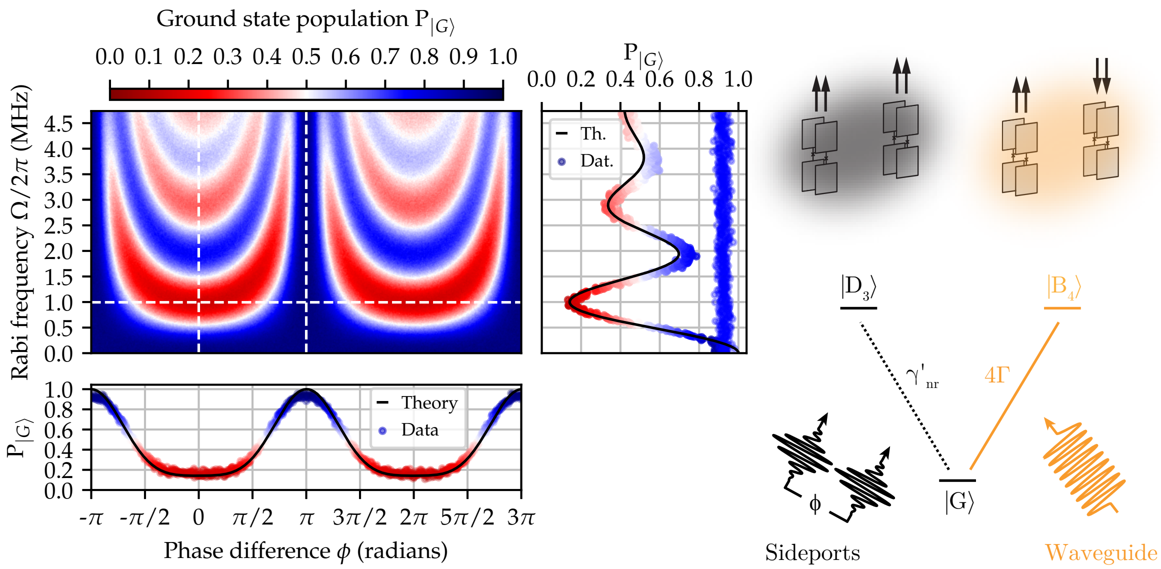

Figure 4.20: Coherent control of the dark state. We apply a gaussian shaped pulse of total length $t = 240\,\text{ns}$ and standard deviation of $\sigma = 40\,\text{ns}$ to observe Rabi oscillations between the ground state $|G\rangle$ and the non-local four qubit dark state $|D_3\rangle$ as a function of the Rabi frequency Ω and the sideport phase difference ϕ. By applying the pulse through the sideports we can set the phase ϕ independently. The ground state population is read out by sending a 5 µs long rectangular pulse through the waveguide, resonant with the transition between states $|G\rangle$ and $|B_4\rangle$. The right panel shows a vertical linecut at the white dashed lines of the colormap for phase-difference $\phi = 0$ and $\phi = \pi$. The lower panel shows a horizontal linecut for a Rabi-frequency of $\Omega/2\pi = 1\,\text{MHz}$. For the theory curve, we simulate the Hamiltonian Eq. (2.29) and master equation Eq. (2.31) with the single transmon parameters and direct coupling strengths J_{12} and J_{34}. The conversion from transmitted amplitude to the ground state population is explained in Sec. 4.3.2.

rapidly to the ground state with the rate $\Gamma_{B,4}$. For phases that are neither fully symmetric nor antisymmetric we drive both states simultaneously, where the respective drive strength depends on the phase. We see that the relative phase of the local drives plays an important role for the system and can be used to distinguish the degenerate bright and dark state.

Again, we measure the ground state population by employing the state dependent scattering scheme, presented for the two transmon cases. Here, we can coherently scatter photons between the ground state and superradiant state $|B_4\rangle$, if the collective system is in the ground state $|G\rangle$. This reduces the transmission through the waveguide, as can be seen from the 4 qubit resonance in Fig. 4.18a. If the dark state $|D_3\rangle$ is populated, the microwave signal is not scattered, resulting in unit transmission. The conversion from transmitted amplitude to the ground state population is explained in Sec. 4.3.2, as we require the knowledge of the T_1 time first.

Instead of changing the excitation pulse amplitude we can also change its length which decreases the pulse width in frequency space. Figure 4.21a shows Rabi oscillations between the ground state $|G\rangle$ and collective dark state $|D_3\rangle$, where we increase the amplitude on the vertical axis and the length on the horizontal axis of a Gaussian excitation pulse with con-

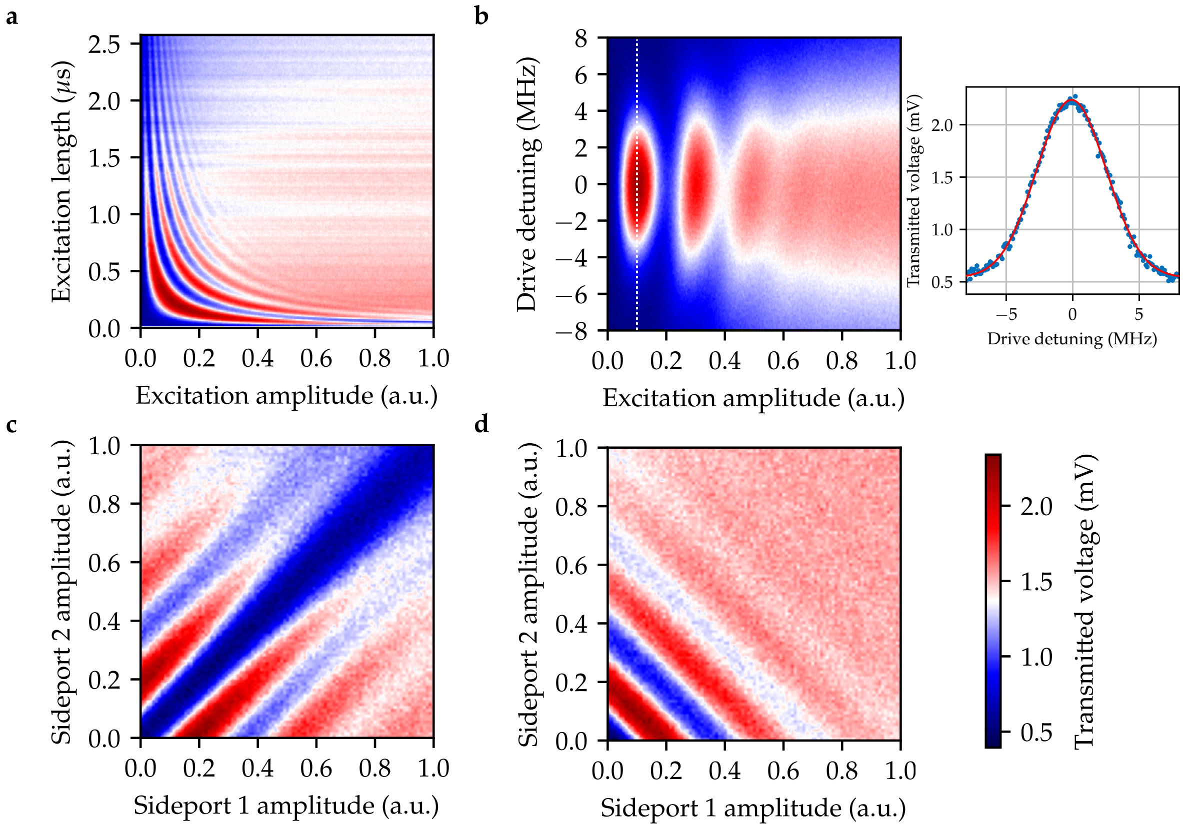

Figure 4.21: Rabi-oscillations between $|G\rangle$ and $|D_3\rangle$ for different parameters. a Varying the pulselength and amplitude we observe more oscillations for longer pulses as the effective width of the pulse in the frequency domain becomes smaller, hence a more frequency-selective driving is possible. Finite decay time T_1 limits to go to very long pulses. **b** When detuning the drive frequency we observe a damped oscillation and a width in frequency that corresponds to the pulse. The inset shows the indicated linecut, now plotted against the frequency of the excitation pulse and fitted with a Gaussian function. **c** Setting the phase to $\phi = \pi$, we cannot observe Rabi-oscillations for equal pulse amplitudes on both sideports. Only when we introduce unequal drive strengths, we recover oscillations. **d** With the phase fixed to $\phi = 0$, we have an optimal symmetrical drive that can drive the dark state $|D_3\rangle$. As long as there is enough symmetrical part in the drive, we can drive oscillations.

stant phase relation between the sideports $\phi = 0$. The amplitude between sideports is equally increased in this measurement. On the one hand, a longer pulse decreases the width in frequency space and therefore leads to less driving of off-resonant transitions, mainly to $|B_{13}\rangle$ and $|B_{14}\rangle$, on the other hand, it longer excitation pulses compete with the finite lifetime of the dark state $|D_3\rangle$. For long pulses a substantial amount of dark state population has decayed back into the ground state and we measure low transmitted voltages when we send a readout pulse corresponding to a large ground state population. For short pulses but large amplitudes the parasitic driving of other transitions is dominant such that the dark state preparation is limited. We find the highest contrast, corresponding to the highest dark state population for a pulse length of 240 ns. Thus, we set this as the length of the π-pulse to excite the dark state qubit.

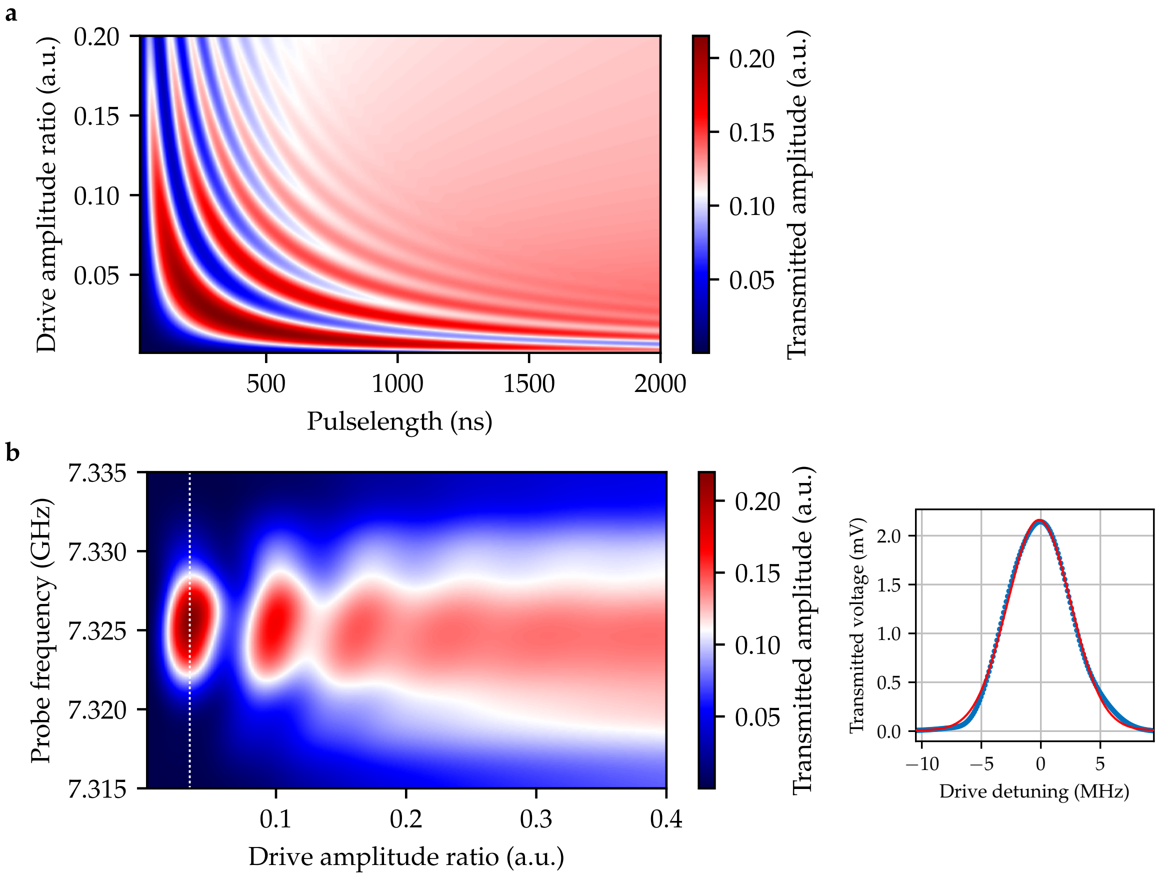

Figure 4.22: Dark state Rabi simulations. **a** Varying the length and amplitude of the dark state excitation pulse in the numerical simulation results in periodic Rabi oscillations. For the amplitude we are limited by driving of higher excited states, while for the increasing pulse length we are limited by the finite dark state lifetime T_1 in good agreement with the measurements in Fig. 4.21a. **b** For a detuned pulse we recover the measurement in Fig. 4.21b.

In Fig. 4.21b the Gaussian pulse with fixed pulse length of 240 ns, $\sigma_{\mathrm{ns}} = 40\,\mathrm{ns}$ and $\phi = 0$ is detuned with respect to the transition frequency of $|G\rangle$-$|D_3\rangle$. As the dark state $|D_3\rangle$ is the only long-lived state within this frequency range, the width on the frequency axis of a π pulse is a convolution between the Gaussian excitation pulse and the natural qubit lineshape. We can extract the width σ by fitting a Gaussian function $y = A\exp\left(-(x-\mu)^2/(2\sigma^2)\right) + y_0$ to the transmission in the inset of Fig. 4.21b, corresponding to the indicated linecut at the π amplitude to obtain $\sigma = 2.62\,\mathrm{MHz}$. The system's sensitivity to the symmetry of the pulse is not only affected by the phase but also the amplitude difference between sideport 1 and 2. If we keep the phase and the length constant and vary the amplitude of sideport 1 and 2 individually, we introduce an amplitude gradient. The transmission amplitude for a phase difference between the sideports 1 and 2 of $\phi = \pi$ in Fig. 4.21c shows that with symmetric increase of power we cannot drive Rabi oscillations as we are mainly driving the collective bright state $|B_4\rangle$. The state immediately decays back into the ground state, thus shows a low transmission amplitude. We can distort the drive symmetry by a power imbalance between the drive ports which shows that amplitude and phase contribute to the resulting pulse symmetry. In Fig. 4.21d the phase is set to $\phi = 0$ corresponding to the dark state phase relation. We find good agreement in the theoretical prediction of the Rabi oscillations for the variable pulse power, length and detuning in Fig. 4.22. By extracting the frequency width of a π-pulse we find $\sigma = 2.66\,\mathrm{MHz}$, similar to the experimental data.

4.3.2 Dark State Characterization

A multi-qubit dark state in a waveguide QED setup presents a valuable resource for the storage of quantum information in a dissipative environment [139]. The long-lived nature of subradiant states opens up the possibility to prepare interesting states in interacting quantum many-body systems and investigate the dynamics [140, 141], to study many-body localization in disordered arrays [142, 143] or even realize a quantum computation and simulation platform within an open quantum system [25]. The ultimate usability for scaling up experiments depends on the achievable control and coherence time of the multi-qubit states. By measuring the energy decay time T_1 and coherence time T_2 of the dark state $|D_3\rangle$ we characterize the hybridized coherence properties of four transmons and obtain a first benchmark on the scaling by comparing them to the characteristic times of the two transmon systems.

Energy Relaxation

The energy relaxation time T_1 is measured by populating the dark state with a π-pulse. The power and relative phase between sideport 1 and 2 that are required to maximally populate the dark state are extracted from the intersection of the dashed horizontal line and the vertical line at $\phi = 0$ of the Rabi measurement in Fig. 4.20. Choosing the amplitude with the highest dark state population increases the contrast in the measurement. After a variable time τ we perform the readout scheme described in Sec. 4.3.1. By fitting an exponential function $y = A\exp(-\tau/T_1) + y_0$ we extract a time constant $T_1 = (1.71 \pm 0.06)\,\mathrm{\mu s}$, which means that we reduced the individual radiative coupling rates from roughly $\gamma_\mathrm{r}/2\pi = 15\,\mathrm{MHz}$ to $\gamma_{D_3} = \frac{1}{2\pi \cdot 1.7\,\mathrm{\mu s}} = 93.6\,\mathrm{kHz}$ corresponding to a Purcell reduction of $\gamma_\mathrm{r}/\gamma_{D_3} = 160$. Compared to the bright state coupling rate $\gamma_{B_4}/2\pi = 57.7\,\mathrm{MHz}$ the decay dynamics of the dark state is $\gamma_{B_4}/\gamma_{D_3} = 616$ times slower. Fig. 4.23a shows a typical exponential decay of the excited state $|D_3\rangle$ into the ground state $|G\rangle$. As seen in the definition of the dark state decay time in Eq. (2.58), the rate of the dark state energy relaxation is also affected by dephasing which usually only affects the coherence of a single transmon qubit [34]. Recalling Eq. (2.58)

$$T_1 = \left(2\gamma_\mathrm{r} + \gamma_\mathrm{nr} + \frac{\gamma_\phi}{2} - \frac{1}{2}\sqrt{16\gamma_\mathrm{r}^2 + 4\gamma_\mathrm{r}\gamma_\phi + \gamma_\phi^2}\right)^{-1}, \tag{4.5}$$

the decay time has contributions of the non-radiative decay rate γ_nr, as well as radiative rate γ_r and dephasing γ_ϕ, where the latter cancel in the case that either of them is zero. If both are non-zero this means that dephasing can increase the radiative decay such that it increases the total energy relaxation rate, even in the absence of an intrinsic decay rate $\gamma_\mathrm{nr} = 0$. In the absence of dephasing, the decay time reduces to $T_1 = 1/\gamma_\mathrm{nr}$ as in the ordinary definition.

After having measured the relaxation time, we are able to convert the y-axis from transmitted amplitude to ground state population, as seen in most of the time-resolved measurement plots throughout the thesis. We assume that all population is in the ground state when

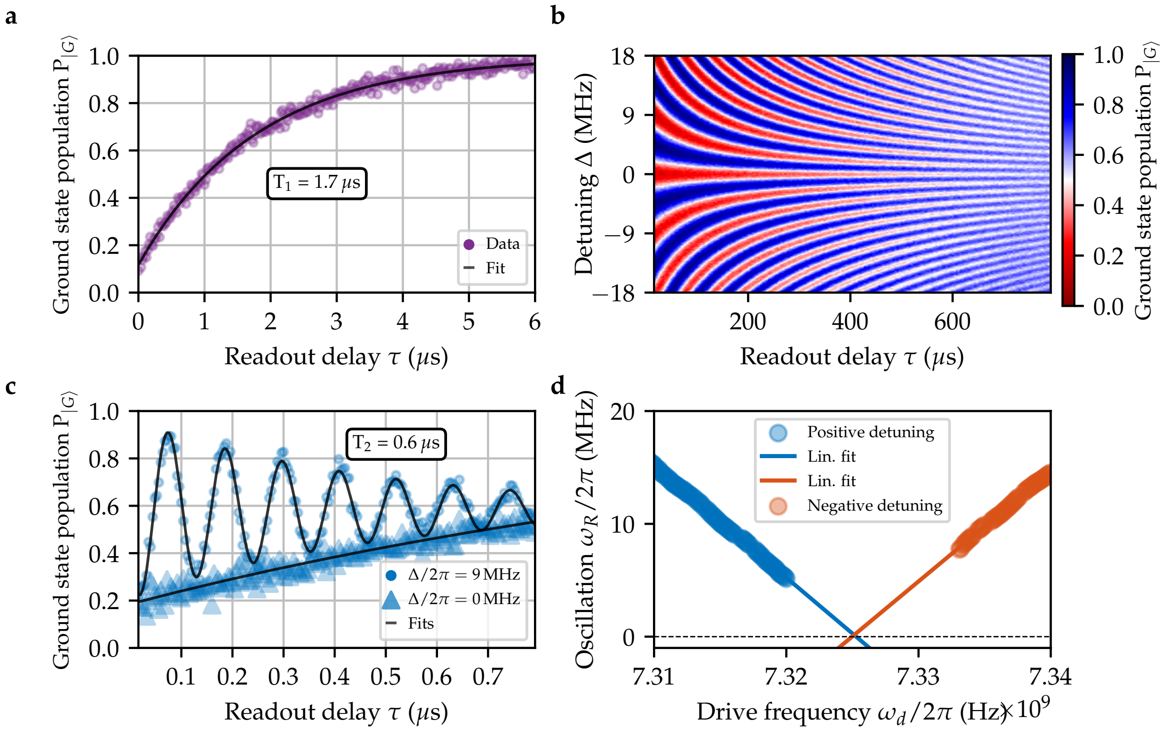

Figure 4.23: Dark state characteristic times. **a** After a π-pulse the population is in the dark state, thus an immediate readout tone measures the ground state population is at a minimum. Delaying the readout causes the dark state to relax back to the ground state due to intrinsic decoherence mechanisms. For very long delays, we recover the full ground state population. An exponential fit yields the characteristic energy relaxation time T_1. **b** After a resonant $\pi/2$-pulse the qubit Bloch vector is on the equator of the Bloch sphere, thus it is sensitive to dephasing. It rotates with the frequency of the drive for a delay time τ. The action of the second $\pi/2$-pulse is now conditioned on the relative phase between the qubit Bloch vector and the drive. The readout is performed directly afterwards. For $\tau = 0$ it brings the population into $|D_3\rangle$ just like a π-pulse but if a delay time is added the state will decohere back to the ground state. A second pulse for very long delay times is similar to only one $\pi/2$-pulse, such that we measure the population ~ 0.5. A detuned drive results in different precessions for the qubit Bloch vector and the drive vector, such that we can see the characteristic Ramsey fringes. **c** Extracted measurements from **b** for different detunings. **d** By fitting the oscillations along the delay axis in **b** for different detunings we can precisely calibrate the transition frequency of $|G\rangle$-$|D_3\rangle$. Extracted oscillation frequencies from the data in **b** is shown in circles while the lines are linear fits.

no excitation pulse is applied and record the readout pulse as the background reference for $V_{|G\rangle} = 0.31\,\mathrm{mV}$. For 3D transmons in cavities we measured a residual excited steady state population due to thermal photons of around $\rho_{11}(t \gg T_1) \sim 5\%$, corresponding to an effective qubit temperature of $\sim 100\,\mathrm{mK}$ [136]. For the waveguide setup we did not measure the effective qubit temperatures but assume $\rho_{11}(t \gg T_1) = 0$ for simplicity. For a background measurement of the readout pulse at the decoherence free frequency with all transmons tuned away we record an amplitude of $V_{\mathrm{bg}} = 6.45\,\mathrm{mV}$. During the time that the readout pulse is played the dark state already decays significantly due to its large T_1 time and $t_{\mathrm{ro}}/T_1 \sim 2.9$. Thus we can estimate the amplitude for a perfect dark state π-pulse by integrating the exponential decay over the time of the readout

$$V'_{|D_3\rangle} = \left(V_{\mathrm{bg}} - V_{|G\rangle}\right) \frac{t_{\mathrm{ro}}}{T_1} \int_0^{t_{\mathrm{ro}}/T_1} \exp\left(-x\right) dx = 1.968\,\mathrm{mV} \tag{4.6}$$

In the experiment we detect a maximal transmitted voltage $V_{|D_3\rangle} = 2.01\,\mathrm{mV}$, thus estimate that we excite depopulate the ground state by $\sim 90\%$ where we attribute the remaining 10% to the excitation of faster decaying states and the decay during the duration of the Gaussian excitation pulse with duration $t_d = 240\,\mathrm{ns}$ and standard deviation $\sigma_d = 40\,\mathrm{ns}$.

Coherence

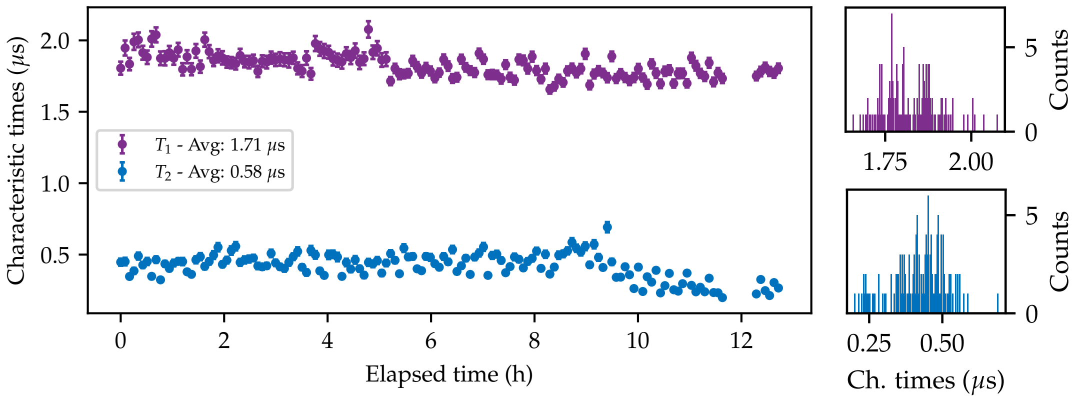

Figure 4.24: Long term characteristic times. Consecutive measurements of the characteristic dark state T_1 and T_2 times over more than 12 h show a stable dark state, which is important when trying to run longer experiments.

Even though the energy relaxation is already affected by dephasing and yields an upper bound for the dark state qubit coherence we can conduct a Ramsey measurement [137] to extract the decoherence time T_2, which was defined in Eq. (2.56):

$$T_2 = \left(\frac{\gamma_{\mathrm{nr}}}{2} + \gamma_\phi + K_\phi\right)^{-1}. \tag{4.7}$$

The Ramsey sequence consists of two $\pi/2$-pulses at the decoherence-free frequency $\Delta = f_d - f_\pi = 0$ with phase difference between the sideports $\phi = 0$ and amplitude, such that $P_{|G\rangle} = 0.5$. The excitation length is kept at $t_d = 240\,\mathrm{ns}$, similar to the power Rabi experiment and the relaxation time measurement. The first pulse takes the dark state Bloch vector to a phase sensitive point on the Bloch sphere, in the optimal case on the equator. Then the drive field is switched off, thus the state evolves freely for a variable time τ before the second $\pi/2$-pulse is applied. For a qubit with infinite coherence time the second pulse brings the qubit into the excited state, thus the readout measures $P_{|G\rangle} = 0$. Pure dephasing arises from longitudinal noise along the z-axis that changes the qubit frequency. The Bloch vector depolarization of the azimuthal phase is affected by these stochastic frequency fluctuations and gives rise to a dephasing rate γ_ϕ such that the drive phase does not match the qubit frequency and is driven less efficiently. In addition, the Bloch vector is subjected to transverse noise that causes longitudinal energy relaxation such that the Bloch vector decays. In the extreme case for a very long wait time τ the Bloch vector points to the ground state $|G\rangle$. Then, the second pulse brings the qubit back to the equator and we measure $P_{|G\rangle} = 0.5$. In Fig. 4.23b we observe Ramsey fringes when detuning the drive with respect to the $|G\rangle$-$|D_3\rangle$ transition. This is caused by the acquired phase difference of the drive and qubit during the time of the free evolution. When the drive is resonant with the qubit, the state in the rotating frame always stays on the y-axis of the Bloch sphere during the free evolution time, see Fig. 1.4. Thus, the final state will be an equal superposition of $|0\rangle$ and $|1\rangle$ or here $|G\rangle$ and $|D_3\rangle$ and does not depend on the evolution time τ. For an off-resonant drive with detuning Δ, the state precesses around z. The frequency of this precession is equal to the detuning between the transition and drive frequency and the direction (negative or positive) is given by the sign of the detuning $\pm\Delta$. Therefore, we measure a sinusoidal time-dependent oscillation of the final state for a detuned drive in Fig. 4.23b. We can see that the drive detuning scales linearly with the Ramsey oscillation frequency, thus the Ramsey detuning serves as an accurate method to determine the qubit frequency, shown in Fig. 4.23d. By extracting the linecut at $\Delta = 9\,\text{MHz}$ from Fig. 4.23b we fit a function $y = A\cos(\omega_R + \varphi_0)\exp(-\tau/T_2) + y_0$ to determine the characteristic coherence time $T_2 = (0.58 \pm 0.06)\,\mu\text{s}$, shown in Fig. 4.23c.

The measurements of the energy relaxation time T_1 and coherence time T_2 are repeated over 12 h to probe the robustness of the dark state. The result is shown in Fig. 4.24. Even though we record a slight temperature change of $\sim 3\,\text{mK}$ during the measurement cycle, the characteristic times are relatively stable, such that the dark state remains a resource of coherence.

4.3.3 Two-Excitation Manifold

The Rabi measurement in Fig. 4.20 shows a rapid saturation of the ground state population at $P_{|G\rangle} \sim 0.5$ when increasing the drive amplitude. The inability to Rabi flop between the ground state $|G\rangle$ and dark state $|D_3\rangle$ for a constant pulse length indicates that the population leaks into parasitic levels. This can either happen when the sideports phase relation is not perfectly symmetric and we drive the bright state $|B_4\rangle$ that decays more than 600 times faster than the dark state $|D_3\rangle$ or by driving two-photon and off-resonant transitions. It is necessary to understand the dynamics of the rich transition manifolds in order to improve the dark state qubit but also to design the properties of interesting many-body systems.

To study the leakage into the two-excitation manifold of the collective four-transmon system, we concatenate a spectroscopy pulse after populating the dark state $|D_3\rangle$. The pulse sequence to obtain the measurement in Fig. 4.25a consists of a π-pulse on the $|G\rangle$-$|D_3\rangle$ transition with phase $\phi = 0$ and a long Gaussian spectroscopy pulse with $\sigma = 200\,\text{ns}$ with constant amplitude and varying spectroscopy frequency ω and phase ϕ applied through the sideports, followed by a 5 µs long rectangular readout pulse through the waveguide. Fig. 4.25a shows the ground state population after the two-pulse protocol into the two-excitation manifold. The blue regions correspond to transitions that can be driven from the dark state $|D_3\rangle$ and rapidly decay, thus populate the ground state faster. The spectroscopy relative phase unveils the symmetry and energy of the states in the two-excitation manifold. When the spectroscopy pulse is resonant

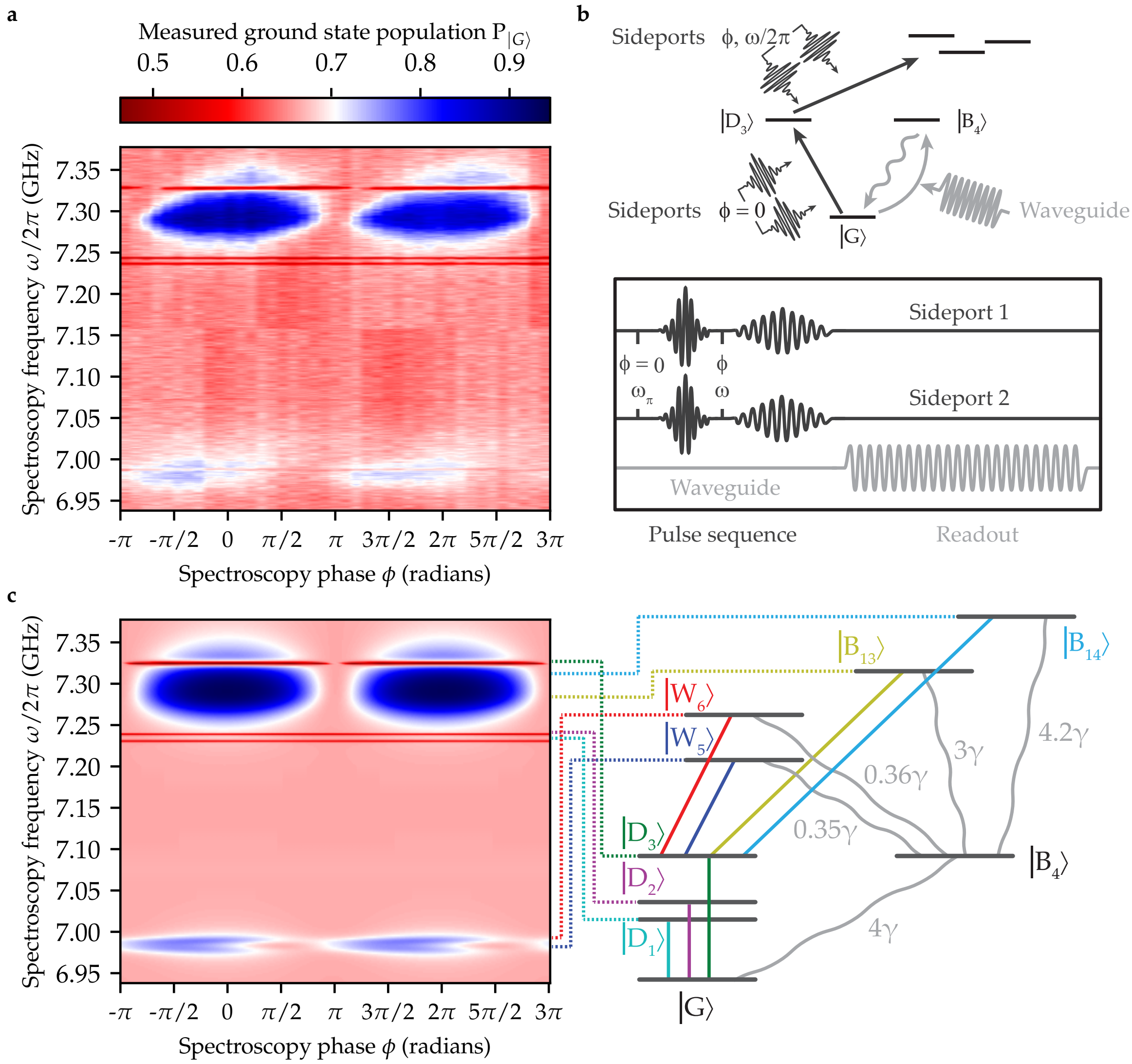

Figure 4.25: Phase-sensitive spectroscopy of the two-excitation manifold. **a** The ground state population after of the two-pulse protocol with varying spectroscopy frequency and phase shows transitions that can be driven from the dark state $|D_3\rangle$. **b** Schematic of the experiment and pulse sequence. **c** The simulation shows qualitative agreement with the measurement. To also see the local dark states we have to assume an electric field gradient of the drive within the local pairs.

with a transition, e.g. $|W_5\rangle$, $|W_6\rangle$, $|B_{13}\rangle$ or $|B_{14}\rangle$ the system is reset to the ground state due to the rapid decay of these states dominantly via the bright state $|B_4\rangle$. The notation is equivalent to the theory Section 2.6 that we repeat for convenience. We denote the collective states by $|D_i\rangle$, $|B_i\rangle$ and $|W_i\rangle$ where the letter refers to their waveguide radiation characteristics: Dark, bright or weakly radiant. The subscript is an ascending enumeration based on their energy value. The collectiveness of these states is apparent in the phase dependence of the measured ground state population. In comparison, the two lower red lines correspond to the local dark state transitions $|G\rangle$-$|D_1\rangle$ and $|G\rangle$-$|D_2\rangle$, thus show no change in phase change ϕ. The upper red line corresponds to the $|G\rangle$-$|D_3\rangle$ transition that is driven by the spectroscopy pulse, thus shows a phase dependence but no reset. These observations are consistent with the numerical simulation of the model Hamiltonian Eq. (2.31) in Fig. 4.25c. The simulation shows that indeed the states of the two-excitation manifold have to be coupled to the dark state $|D_3\rangle$ and possess a finite decay rate to the bright state $|B_4\rangle$, which then decays to the ground state $|G\rangle$. Therefore we measure a high ground state population when the spectroscopy pulse is resonant with a transition that can be driven from $|D_3\rangle$. The ability to drive collective states depends on the spectroscopy phase whereas local states can be driven with any phase, as long as the local drives also have an electric field gradient within the pairs. Comparing the measurement to the state manifold of Fig. 2.6, there are six other states in the two-excitation manifold that are not visible in the spectroscopy since they cannot be driven from the dark state $|D_3\rangle$ or do not decay to the bright state $|B_4\rangle$. During the time of the spectroscopy pulse, which is on the same order as the lifetime of $|D_3\rangle$, a part of the population decays to the ground state. As a consequence, the phase sensitive transition between states $|G\rangle$ and $|D_3\rangle$ is visible.

The only parameters that are needed for the simulation are the single transmon parameters and direct coupling strengths given in table 4.3. In order to observe the local dark states $|D_1\rangle$ and $|D_2\rangle$ in the simulation, we have included an amplitude gradient of the local drives, such that the power on transmons Q_2 and Q_4 is three quarters of that on Q_1 and Q_3. This asymmetry produces an additional driving term that is always antisymmetric with respect to the exchange of transmons within the pair. These states do not show a phase dependence as they are only coupled to one drive port.

It is essential to notice that a transmon is a bosonic multilevel system with anharmonicity α. The many-body excited state manifolds in bosonic systems are fundamentally different to those of two-level emitters. For example, in our case of four transmons, the two-excitation manifold includes 10 basis states, whereas that for two-level emitters would have only 6 states. The importance to differentiate between two-level systems and transmons increases with the total excitation number. Here, the additional states are the doubly excited states of the transmons, which make an important contribution to the collective superposition states $|W_5\rangle$, $|W_6\rangle$, $|B_{14}\rangle$ and $|B_{13}\rangle$ that we observe in Fig. 4.25. States $|W_5\rangle$ and $|W_6\rangle$ are unique to bosonic systems, as they are strongly affected by the negative transmon anharmonicites and are not reproducible by considering two-level systems [87]. Apart from the multi-excitation states, energy level and decay characteristics of two-level emitters are recovered in the hard-core boson limit $\alpha(N-1) \gg \gamma_r, J_{12}, J_{34}$, where the transmon anharmonicity α dominates over both the waveguide-mediated interactions γ and the direct capacitive coupling strengths J_{ij}. The experimental values for the data shown in this thesis are $\gamma/\alpha(N-1) \approx 0.1$ and $J_{ij}/\alpha(N-1) \approx 0.2$ resulting in an energy level structure that is clearly different from arrays of qubits and harmonic oscillators. In general, in bosonic waveguide quantum electrodynamics systems, the number of bright and dark states is higher and the bright states are brighter compared to the case of two-level emitters. The reason is a larger and more versatile many-body Hilbert space [87].

4.3.4 Optimizing the Protection of the Dark State

The spectroscopy shows that the transitions $|D_3\rangle$ to $|B_{13}\rangle$ and $|B_{14}\rangle$ not only overlap with the transition of the dark state qubit $|G\rangle$-$|D_3\rangle$ but also share the same phase condition on the drive. Consequently, we attribute the damping of the Rabi oscillations in Fig. 4.20 to the population of these states as we increase the drive amplitude. Remarkably, this leakage effect can be reduced dramatically by increasing the coupling to the waveguide so much that the unwanted excitation to this state can be adiabatically eliminated [144]. Ideally, increasing the waveguide coupling does not affect the coherence and lifetime of the dark state, only the states outside the decoherence-free subspace decay faster. In contrast to conventional solid-state qubits, a symmetry-engineered multi-qubit system makes it possible to control the decay properties of the leakage states independently of the computational states.

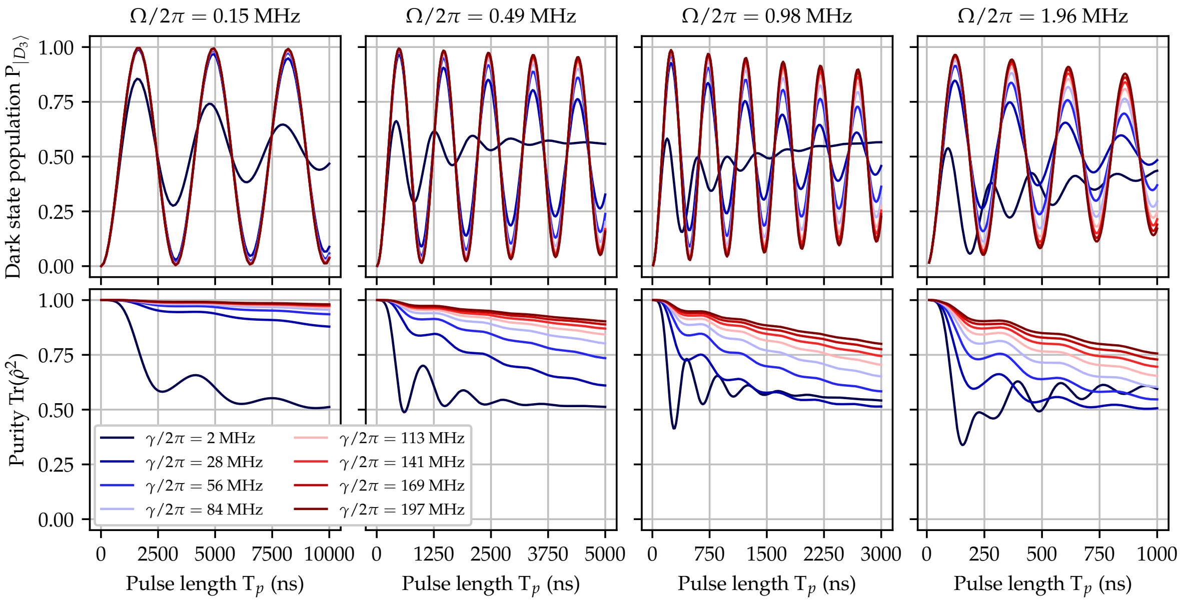

Figure 4.26: Optimizing the dark state protection. Simulated dark state populations (top row) and purities of the state of the system (bottom row) as a function of Rabi pulse length for different values of Rabi frequencies Ω and waveguide couplings γ. System parameters have been taken as average of experimental values in Tab. 4.1, corresponding to $\alpha/2\pi = 218\,\text{MHz}$ and $J_{ij}/2\pi = 45\,\text{MHz}$.

In Fig. 4.20, we observe that the Rabi drive between the ground state $|G\rangle$ and the dark state $|D_3\rangle$ excites also the states in the two-excitation manifold, mainly the states $|B_{13}\rangle$ and $|B_{14}\rangle$ that subsequently decay to the bright state $|B_4\rangle$. The effective anharmonicity of the dark state qubit $\{|G\rangle, |D_3\rangle\}$ is defined by the energy difference between the nearest transition energies $\widetilde{U}$, where we adapted the notation for the bosonic on-site interaction. Thus, with the experimental parameters the anharmonicity is $\widetilde{U}/2\pi = [(\omega_{D_3,B_{14}}) - (\omega_{G,D_3})]/2\pi \approx -15\,\text{MHz}$, where $\omega_j/2\pi$ is the corresponding transition frequency of transition j. As seen in Fig. 2.6, this is approximately $\sim 1/4$ of the waveguide-coupling rate of the state $\gamma_{B_{14}}/2\pi \approx 60\,\text{MHz}$. Additionally, the phase relation between the drive ports cannot be adjusted as the states share the same symmetry. This explains why population can leak from the state $|D_3\rangle$ to the state $|B_{14}\rangle$ when it is driven.

With single solid-state qubits such as transmons [11], the leakage can be minimized either by driving with a smaller amplitude (Rabi frequency) or by engineering larger anharmonicities between the computational state and the higher excited states. Here, we have an additional possibility: engineer the decay to the waveguide γ so large that the leakage can be adiabatically eliminated [144]. In Fig. 4.26, we demonstrate this effect in numerical simulations of the system Hamiltonian where we use the experimental parameters of table 4.1 but assume identical qubit-waveguide coupling in the range of $\gamma/2\pi = 2$ - $197\,\mathrm{MHz}$. The simulation starts from the ground state $|\psi(t=0)\rangle = |G\rangle$. For a dark state qubit that is not subjected to decoherence we would expect oscillations between $|G\rangle$ and $|D_3\rangle$ that show no damping for longer excitation pulses. Additionally, the state would remain a pure state. However, the ground state and the dark state do not form a perfect qubit because of the leakage to two-photon states $|B_{13}\rangle$ and $|B_{14}\rangle$, which are almost resonant with the driving frequency. There are two possibilities to improve the system and obtain better Rabi oscillations. First, one could use a weaker but longer Rabi pulse. This decreases the off-resonant driving, and more population remains in the dark state. However, longer pulses mean that non-radiative decay of the dark state, which has not been included in the simulations, decreases the population further. Another way is to increase the coupling to the waveguide, where $\gamma/2\pi = 15\,\mathrm{MHz}$ is the coupling in the experiment. We observe that the larger the coupling γ, the better the Rabi oscillations become. The decay of the population amplitude is also decreased. Similarly the state is more pure for larger γ. However, as is evident from the results, the improvement begins to saturate, and also approximations made in the master equation would break with too large γ. On the other hand, for weaker coupling the Rabi becomes much worse. It can clearly be seen that increasing the coupling (decay rate) to the waveguide decreases leakage effects from the decoherence-free subspace resulting in a weaker damping of the Rabi oscillations between the states $|G\rangle$ and $|D_3\rangle$ and an increased overall total purity of the driven system. The coherence time T_2 of the dark state is independent of the waveguide coupling γ, as can be seen from Eq. (2.56). The lifetime T_1 in Eq. (2.58) only depends weakly on γ when it becomes large compared to the other decoherence rates.

In the numerical simulations, we observe that the higher excitation states become only weakly excited and have negligible dynamics on the relevant timescales when the waveguide coupling is large and the Rabi frequency weak enough. In this case, the results can also be analytically explained by adiabatically eliminating the higher excitation states and reducing the dynamics only into the one-excitation manifold [144]. For simplicity we consider only the state $|B_{14}\rangle$ in the two-excitation manifold, but all the results apply also for the state $|B_{13}\rangle$. Other states in the two-excitation manifold are only very weakly coupled to the state $|D_3\rangle$ either by symmetry exclusion or energy difference. This reduces the discussion to the ground state $|G\rangle$, the bright state $|B_4\rangle$ and the dark state $|D_3\rangle$ as well as the state $|B_{14}\rangle$ from the two-excitation manifold. The driven Hamiltonian for the three states reads

$$\hat{H} = \hbar\omega_1 |B_4\rangle\langle B_4| + \hbar\omega_1 |D_3\rangle\langle D_3| + \hbar(2\omega_1 - \widetilde{U}) |B_{14}\rangle\langle B_{14}| + \hat{H}_\mathrm{d}(t), \tag{4.8}$$

where we drive the system with a Rabi drive that couples the ground state to the dark state, and the dark state to the state $|B_{14}\rangle$:

$$\hat{H}_d(t)/\hbar = 2\Omega\cos(\omega t)\left(|G\rangle\langle D_3| + |D_3\rangle\langle G|\right) + 2\widetilde{\Omega}\cos(\omega t)\left(|D_3\rangle\langle B_{14}| + |B_{14}\rangle\langle D_3|\right). \tag{4.9}$$

We choose to drive the system resonantly $\omega = \omega_1$, which yields the driven Hamiltonian in the rotating frame

$$\hat{H}'/\hbar = \Omega\left(|G\rangle\langle D_3| + |D_3\rangle\langle G|\right) + \widetilde{\Omega}\left(|D_3\rangle\langle B_{14}| + |B_{14}\rangle\langle D_3|\right) - \widetilde{U}\,|B_{14}\rangle\langle B_{14}|. \tag{4.10}$$

In addition to the drives we include the decay rates of the states $|B_4\rangle$ and $|B_{14}\rangle$ represented through the master equation

$$\dot{\hat{\rho}} = -\frac{i}{\hbar}[\hat{H}', \hat{\rho}] + \left(\hat{L}_{B_4}\hat{\rho}\hat{L}^\dagger_{B_4} - \frac{1}{2}\hat{\rho}\hat{L}^\dagger_{B_4}\hat{L}_{B_4} - \frac{1}{2}\hat{L}^\dagger_{B_4}\hat{L}_{B_4}\hat{\rho}\right) + \tag{4.11}$$

$$+\left(\hat{L}_{B_{14}}\hat{\rho}\hat{L}^\dagger_{B_{14}} - \frac{1}{2}\hat{\rho}\hat{L}^\dagger_{B_{14}}\hat{L}_{B_{14}} - \frac{1}{2}\hat{L}^\dagger_{B_{14}}\hat{L}_{B_{14}}\hat{\rho}\right), \tag{4.12}$$

where the jump operators describe the decay of the bright state $\hat{L}_{B_4} = \sqrt{\Gamma_{B_4}}\,|G\rangle\,\langle B_4|$ at rate Γ_{B_4} and the decay of the state $|B_{14}\rangle$ $\hat{L}_{B_{14}} = \sqrt{\Gamma_{B_{14}}}\,|B_3\rangle\,\langle B_{14}|$ at rate $\Gamma_{B_{14}}$.

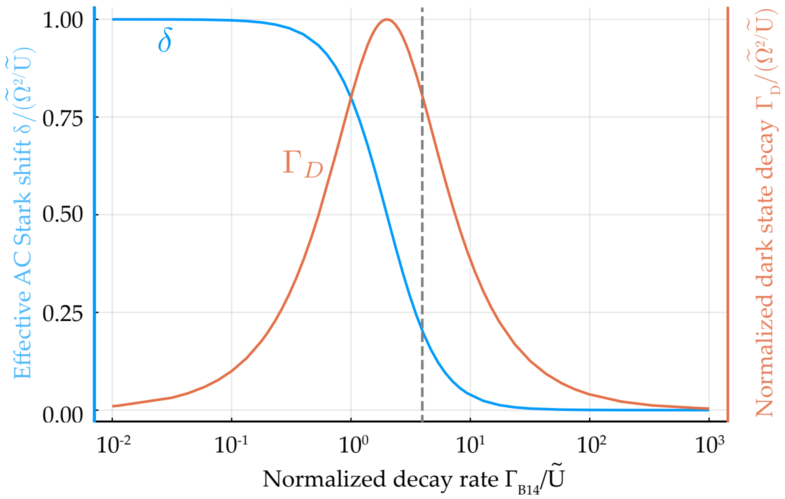

Figure 4.27: Adiabatic elimination: Effect of the two-excitation manifold on the driven dark state. Effective AC Stark shift δ and the decay rate of the dark state Γ_{D} as a function of the decay rate of the state of the two-excited state manifold $\Gamma_{B_{14}}$ in Eq. (4.16). The maximum of the decay rate Γ_{D} occurs at $\Gamma_{B_{14}}/\widetilde{U} = 2$. The experimental value corresponding to the state $|B_{14}\rangle$ is indicated by vertical dashed line $\Gamma_{B_{14}}/\widetilde{U} \approx 3.95$.

By following Reference [144] and assuming that the Rabi amplitude Ω is not too large, we can adiabatically eliminate the state $|B_{14}\rangle$ resulting in the effective Hamiltonian

$$\hat{H}_{\mathrm{eff}}/\hbar = \Omega\left(|G\rangle\,\langle D_3| + |D_3\rangle\,\langle G|\right) + \frac{4\widetilde{\Omega}^2\widetilde{U}}{4\widetilde{U}^2 + \Gamma^2_{B_{14}}}\,|D_3\rangle\,\langle D_3|\,, \tag{4.13}$$

where the energy of the dark state is AC Stark shifted by $\delta = \frac{4\widetilde{\Omega}^2\widetilde{U}}{4\widetilde{U}^2+\Gamma^2_{B_{14}}}$. This yields a dark state decay through the bright state

$$\hat{L}_D = \sqrt{\Gamma_{B_{14}}\frac{4\widetilde{\Omega}^2}{\Gamma^2_{B_{14}} + 4\widetilde{U}^2}}e^{i\theta}\,|B_4\rangle\,\langle D_3| = \sqrt{\Gamma_D}e^{i\theta}\,|B_4\rangle\,\langle D_3| \tag{4.14}$$

at the rate $\Gamma_{\mathrm{D}} = \Gamma_{B_{14}}\frac{4\widetilde{\Omega}^2}{\Gamma^2_{B_{14}}+4\widetilde{U}^2}$. Notice that if the decay rate of the excited state dominates over the detuning $\Gamma_{B_{14}} \gg \widetilde{U}$ then both the AC Stark shift and the dark state decay rate decrease as a function of the excited state decay rate $\Gamma_{B_{14}}$, depicted in Fig. 4.27, where the AC Stark shift on the dark state δ is defined as

$$\delta = \frac{4\widetilde{\Omega}^2\widetilde{U}}{4\widetilde{U}^2 + \Gamma_{B_{14}}^2} \approx \begin{cases} \widetilde{\Omega}\frac{\widetilde{\Omega}}{\widetilde{U}}, & \frac{\widetilde{U}}{\Gamma_{B_{14}}} \gg 1 \\ \widetilde{\Omega}\frac{\widetilde{\Omega}}{\widetilde{U}}\left(\frac{2\widetilde{U}}{\Gamma_{B_{14}}}\right)^2, & \frac{\widetilde{U}}{\Gamma_{B_{14}}} \ll 1 \end{cases}, \tag{4.15}$$

and the redefined dark state decay rate Γ_D as

$$\Gamma_D = \Gamma_{B_{14}}\frac{4\widetilde{\Omega}^2}{\Gamma_{B_{14}}^2 + 4\widetilde{U}^2} \approx \begin{cases} \Gamma_{B_{14}}\left(\frac{\widetilde{\Omega}}{\widetilde{U}}\right)^2, & \frac{\widetilde{U}}{\Gamma_{B_{14}}} \gg 1 \\ \Gamma_{B_{14}}\left(\frac{\widetilde{\Omega}}{\widetilde{U}}\right)^2\left(\frac{2\widetilde{U}}{\Gamma_{B_{14}}}\right)^2, & \frac{\widetilde{U}}{\Gamma_{B_{14}}} \ll 1. \end{cases} \tag{4.16}$$

This equation yields a reduction of Γ_D as a function of $\Gamma_{B_{14}}$, which itself depends on the transmon-waveguide coupling γ. Thus, the simulations in Fig. 4.26 consistently show the increased purity and amplitude of Rabi oscillations when the waveguide coupling is increased. This shows that the adiabatic elimination of the higher excited states promises the possibility to further optimize the dark state coherent control.

CHAPTER 5

Conclusions and Outlook

In the scope of the thesis, we realized an interacting multi-qubit system of four superconducting transmon qubits that are coupled to a common waveguide. The individual transmons are studied by extracting their steady-state properties in a measurement of the waveguide transmission. The waveguide gives us access to the transitions that couple to the propagating electromagnetic field and additionally mediates interactions between different qubits. Tuning two qubits into resonance with each other, we distinguish between the directly coupled pair and the distant pairs. The direct capacitive coupling strength is evident in the avoided crossing of the fundamental transmon transitions. The coupling gives rise to a non-degenerate local subradiant and superradiant state that we utilize to build a dark state qubit and a state dependent scattering readout scheme. Here, the antisymmetric drive for the dark state arises from the sideport field gradient across the transmon pair. The waveguide-mediated interaction at an effective separation of half a wavelength yields collective decay with a degenerate dark and bright state. Here, we can employ the same scheme but are now required to utilize both sideports and adjust the drive-phase with the control electronics, to switch between driving of the dark or bright state. The extracted dark state lifetimes show a maximum at a specific frequency that we identify as the optimal tuning point for maximal correlated decay. The four-transmon system has three dark states - one for each local pair and one global - and one bright state in the one-excitation manifold. In a Rabi measurement, where we change the phase-relation between the local sideports we observe the dependence of the global dark and bright states on the drive symmetry. To characterize the dark state for its usability for quantum information processing we extract its lifetime and coherence time and explore the two-excitation manifold. In the analysis it is crucial to go beyond the two-level approximation to accurately describe the higher excitation manifolds as they drastically differ from the qubit and harmonic oscillator approach [87]. We find that substantial leakage into higher lying transitions cannot be eliminated by utilizing the possibility to drive the system antisymmetrically and symmetrically but we instead outline a possible engineering approach to adiabatically eliminate fast decaying states in the two-excitation manifold.

In conclusion, the experiment demonstrates that collective dark states constitute a resource for coherent quantum information and can be controlled by local drives with an adjustable phase relation. The collective four-transmon system comprises a one-excitation state manifold with long lived dark states, as well as one rapidly decaying bright state. In particular, we achieve an effective protection from the waveguide, leading to a decrease of the relaxation rate by a factor of 160 compared to the single qubit coupling rate, or a factor of 650 compared to the collective bright state. The degenerate bright state can be used to read out the system. Whereas in conventional resonator-based architectures, the detuning between the readout cavity and the qubit plays an important role for its coherence time, the experiment shows that the protection can be engineered by taking into account the symmetry properties of the system while both transitions are resonant. Unlike in previous experiments, the observation of the weakly radiant states $|W_5\rangle$ and $|W_6\rangle$ are a direct manifestation of the transmons' bosonic nature and demonstrates the necessity to go beyond the two-level approximation when trying to engineer many-body physics with artificial atoms [87].

Looking forward, coherent control of multi-qubit dark states opens up the possibility to investigate dynamics of interacting quantum many-body systems [140, 141], to study many-body localization in disordered arrays [142, 143] or even realize a quantum computation and simulation platform within an open quantum system [25]. On the one hand, adiabatic elimination of the higher excited states promises the possibility to further optimize the coherent control of the dark state; on the other hand, the two-excitation manifold can be used to reset the dark state qubit and transfer quantum information into itinerant photons. This mechanism is a source for cluster state creation [145], while the cascaded decay can be utilized to study entanglement between photons of different frequencies. Finally, the interplay between long-lived subradiant states and weakly radiating states can give new insights into incoherent scattering properties and photon-photon correlations [146].

The experimental results presented in this thesis open the door for further investigation of the system. Overall improvements to the setup, like cold attenuators in the input lines and more isolation in the output lines of the cryostat will help to further increase the dark state coherence properties. For engineering a better isolation from the environment the qubits and qubit-photon bound states can serve as a useful tool to quantify the changes in the input and output lines. The temperature of the propagating microwaves can be investigated by primary thermometry with a transmon qubit [79]. This can potentially be extended by utilizing the (interacting) qubit-photon bound states. By placing the qubits closer to the input or output of the rectangular waveguide they are asymmetrically exposed to one of the two. By coupling the qubits weaker to the waveguide or utilizing the tunable linewidth of the dark state, the qubit transitions can be analyzed in various measurements to learn more about the contributing noise sources [80]. The transmons that were used in the experiments are from the first generation of fabricated samples in the new cleanroom and should be replaced with an advanced design. Especially the large junction areas give rise to many two-level systems that affect the dark state coherence. As can be seen in the avoided-crossing flux maps in Appendix B, there are signatures of interacting two-level systems, especially also close to the decoherence-free frequency.

The immediate follow-up experiment should verify the adiabatic elimination scheme we proposed in Sec. 4.3.4 by realizing a stronger qubit-waveguide coupling. With better control over the dark state two-qubit gates can be realized, either by creating a chain of four qubits [25] or by utilizing the auxiliary states in the current setup. Adding parametric amplifiers to the measurement apparatus enables the extraction of correlations between itinerant microwaves in a much less time consuming manner such that tomography of the emitted radiation can be used to calculate the scattering matrix of the emitter [147]. This opens up new possibilities for further developments within the quantum optics toolbox. An ongoing experiment is the utilization of the non-linear dispersion close to the waveguide cutoff frequency that enables the focusing of a chirped microwave pulse that can be used for addressing individual emitters within an array [109].

Bibliography

[1] A. S. Sheremet, M. I. Petrov, I. V. Iorsh, A. V. Poshakinskiy, and A. N. Poddubny, "Waveguide quantum electrodynamics: collective radiance and photon-photon correlations", arXiv:2103.06824 (2021).

[2] R. J. Schoelkopf and S. M. Girvin, "Wiring up quantum systems", Nature **451**, 664 (2008).

[3] A. Wallraff, D. I. Schuster, A. Blais, L. Frunzio, R.-S. Huang, J. Majer, S. Kumar, S. M. Girvin, and R. J. Schoelkopf, "Strong coupling of a single photon to a superconducting qubit using circuit quantum electrodynamics", Nature **431**, 162 (2004).

[4] A. Goban, C.-L. Hung, J. D. Hood, S.-P. Yu, J. A. Muniz, O. Painter, and H. J. Kimble, "Superradiance for Atoms Trapped along a Photonic Crystal Waveguide", Physical Review Letters **115**, 063601 (2015).

[5] P. Lodahl, S. Mahmoodian, and S. Stobbe, "Interfacing single photons and single quantum dots with photonic nanostructures", Reviews of Modern Physics **87**, 347 (2015).

[6] P. Lodahl, S. Mahmoodian, S. Stobbe, A. Rauschenbeutel, P. Schneeweiss, J. Volz, H. Pichler, and P. Zoller, "Chiral quantum optics", Nature **541**, 473 (2017).

[7] J.-H. Kim, S. Aghaeimeibodi, C. J. K. Richardson, R. P. Leavitt, and E. Waks, "Super-Radiant Emission from Quantum Dots in a Nanophotonic Waveguide", Nano Letters **18**, 4734 (2018).

[8] B. D. Josephson, "Possible new effects in superconductive tunnelling", Physics Letters **1**, 251 (1962).

[9] M. Mirhosseini, E. Kim, X. Zhang, A. Sipahigil, P. B. Dieterle, A. J. Keller, A. Asenjo-Garcia, D. E. Chang, and O. Painter, "Cavity quantum electrodynamics with atom-like mirrors", Nature **569**, 692 (2019).

[10] J. D. Brehm, A. N. Poddubny, A. Stehli, T. Wolz, H. Rotzinger, and A. V. Ustinov, "Waveguide bandgap engineering with an array of superconducting qubits", npj Quantum Materials **6**, 1 (2021).

[11] J. Koch, T. M. Yu, J. Gambetta, A. A. Houck, D. I. Schuster, J. Majer, A. Blais, M. H. Devoret, S. M. Girvin, and R. J. Schoelkopf, "Charge-insensitive qubit design derived from the Cooper pair box", Physical Review A **76**, 042319 (2007).

[12] O. Astafiev, A. M. Zagoskin, A. A. Abdumalikov, Y. A. Pashkin, T. Yamamoto, K. Inomata, Y. Nakamura, and J. S. Tsai, “Resonance Fluorescence of a Single Artificial Atom”, Science **327**, 840 (2010).

[13] M. Baur, S. Filipp, R. Bianchetti, J. M. Fink, M. Göppl, L. Steffen, P. J. Leek, A. Blais, and A. Wallraff, “Measurement of Autler-Townes and Mollow Transitions in a Strongly Driven Superconducting Qubit”, Physical Review Letters **102**, 243602 (2009).

[14] P. Forn-Díaz, J. J. García-Ripoll, B. Peropadre, J.-L. Orgiazzi, M. A. Yurtalan, R. Belyansky, C. M. Wilson, and A. Lupascu, “Ultrastrong coupling of a single artificial atom to an electromagnetic continuum in the nonperturbative regime”, Nature Physics **13**, 39 (2017).

[15] I.-C. Hoi, T. Palomaki, J. Lindkvist, G. Johansson, P. Delsing, and C. M. Wilson, “Generation of Nonclassical Microwave States Using an Artificial Atom in 1D Open Space”, Physical Review Letters **108**, 263601 (2012).

[16] B. Kannan, D. L. Campbell, F. Vasconcelos, R. Winik, D. K. Kim, M. Kjaergaard, P. Krantz, A. Melville, B. M. Niedzielski, J. L. Yoder, T. P. Orlando, S. Gustavsson, and W. D. Oliver, “Generating spatially entangled itinerant photons with waveguide quantum electrodynamics”, Science Advances **6**, eabb8780 (2020).

[17] N. M. Sundaresan, R. Lundgren, G. Zhu, A. V. Gorshkov, and A. A. Houck, “Interacting Qubit-Photon Bound States with Superconducting Circuits”, Physical Review X **9**, 011021 (2019).

[18] E. Kim, X. Zhang, V. S. Ferreira, J. Banker, J. K. Iverson, A. Sipahigil, M. Bello, A. González-Tudela, M. Mirhosseini, and O. Painter, “Quantum Electrodynamics in a Topological Waveguide”, Physical Review X **11**, 011015 (2021).

[19] A. F. van Loo, A. Fedorov, K. Lalumiere, B. C. Sanders, A. Blais, and A. Wallraff, “Photon-Mediated Interactions Between Distant Artificial Atoms”, Science **342**, 1494 (2013).

[20] K. Lalumière, B. C. Sanders, A. F. van Loo, A. Fedorov, A. Wallraff, and A. Blais, “Input-output theory for waveguide QED with an ensemble of inhomogeneous atoms”, Physical Review A **88**, 043806 (2013).

[21] N. V. Corzo, B. Gouraud, A. Chandra, A. Goban, A. S. Sheremet, D. V. Kupriyanov, and J. Laurat, “Large Bragg Reflection from One-Dimensional Chains of Trapped Atoms Near a Nanoscale Waveguide”, Physical Review Letters **117**, 133603 (2016).

[22] J. A. Mlynek, A. A. Abdumalikov, C. Eichler, and A. Wallraff, “Observation of Dicke superradiance for two artificial atoms in a cavity with high decay rate”, Nature Communications **5**, 5186 (2014).

[23] A. Rosario Hamann, C. Müller, M. Jerger, M. Zanner, J. Combes, M. Pletyukhov, M. Weides, T. M. Stace, and A. Fedorov, “Nonreciprocity Realized with Quantum Non-

linearity", Physical Review Letters **121**, 123601 (2018).

[24] D. A. Lidar, I. L. Chuang, and K. B. Whaley, "Decoherence-Free Subspaces for Quantum Computation", Physical Review Letters **81**, 2594 (1998).

[25] V. Paulisch, H. J. Kimble, and A. González-Tudela, "Universal quantum computation in waveguide QED using decoherence free subspaces", New Journal of Physics **18**, 043041 (2016).

[26] J. R. Johansson, P. D. Nation, and F. Nori, "QuTiP 2: A Python framework for the dynamics of open quantum systems", Computer Physics Communications **184**, 1234 (2013).

[27] H. Kamerlingh Onnes, "The resistance of pure mercury at helium temperatures", Commun. Phys. Lab. Univ. Leiden, b **120** (1911).

[28] P. Heidler, C. M. F. Schneider, K. Kustura, C. Gonzalez-Ballestero, O. Romero-Isart, and G. Kirchmair, "Non-Markovian Effects of Two-Level Systems in a Niobium Coaxial Resonator with a Single-Photon Lifetime of 10 milliseconds", Physical Review Applied **16**, 034024 (2021).

[29] U. Vool and M. Devoret, "Introduction to quantum electromagnetic circuits", International Journal of Circuit Theory and Applications **45**, 897 (2017).

[30] M. H. Devoret, A. Wallraff, and J. M. Martinis, "Superconducting Qubits: A Short Review", arXiv:cond-mat/0411174 (2004).

[31] A. Chatterjee, P. Stevenson, S. De Franceschi, A. Morello, N. de Leon, and F. Kuemmeth, "Semiconductor Qubits In Practice", Nature Reviews Physics **3**, 157 (2021).

[32] J. Bardeen, L. N. Cooper, and J. R. Schrieffer, "Theory of Superconductivity", Physical Review **108**, 1175 (1957).

[33] M. Tinkham, "Introduction to Superconductivity", 2nd ed. (Dover Publications Inc., New York, 2004).

[34] A. Blais, A. L. Grimsmo, S. M. Girvin, and A. Wallraff, "Circuit quantum electrodynamics", Reviews of Modern Physics **93**, 025005 (2021).

[35] P. Krantz, M. Kjaergaard, F. Yan, T. P. Orlando, S. Gustavsson, and W. D. Oliver, "A Quantum Engineer's Guide to Superconducting Qubits", Applied Physics Reviews **6**, 021318 (2019).

[36] D. A. Steck, "Quantum and Atom Optics", Vol. Revision 0.12.5, 26 January 2019 (available online at http://steck.us/teaching, 2007).

[37] M. Kjaergaard, M. E. Schwartz, J. Braumüller, P. Krantz, J. I.-J. Wang, S. Gustavsson, and W. D. Oliver, "Superconducting Qubits: Current State of Play", Annual Review of Condensed Matter Physics **11**, 369 (2020).

[38] C. E. Murray, "Material matters in superconducting qubits", Materials Science and Engineering: R: Reports **146**, 100646 (2021).

[39] S. Krinner, S. Storz, P. Kurpiers, P. Magnard, J. Heinsoo, R. Keller, J. Lütolf, C. Eichler, and A. Wallraff, "Engineering cryogenic setups for 100-qubit scale superconducting circuit systems", EPJ Quantum Technology **6**, 1 (2019).

[40] A. O. Caldeira and A. J. Leggett, "Influence of Dissipation on Quantum Tunneling in Macroscopic Systems", Physical Review Letters **46**, 211 (1981).

[41] D. Manzano, "A short introduction to the Lindblad master equation", AIP Advances **10**, 025106 (2020).

[42] R. J. Schoelkopf, A. A. Clerk, S. M. Girvin, K. W. Lehnert, and M. H. Devoret, "Qubits as Spectrometers of Quantum Noise", arXiv:cond-mat/0210247 (2002).

[43] P. A. M. Dirac and N. H. D. Bohr, "The quantum theory of the emission and absorption of radiation", Proceedings of the Royal Society of London. Series A, Containing Papers of a Mathematical and Physical Character **114**, 243 (1927).

[44] S. Tomonaga, "On a Relativistically Invariant Formulation of the Quantum Theory of Wave Fields*", Progress of Theoretical Physics **1**, 27 (1946).

[45] J. Schwinger, "On Quantum-Electrodynamics and the Magnetic Moment of the Electron", Physical Review **73**, 416 (1948).

[46] R. P. Feynman, "Space-Time Approach to Non-Relativistic Quantum Mechanics", Reviews of Modern Physics **20**, 367 (1948).

[47] S. Haroche and D. Kleppner, "Cavity Quantum Electrodynamics", Physics Today **42**, 24 (1989).

[48] E. Jaynes and F. Cummings, "Comparison of quantum and semiclassical radiation theories with application to the beam maser", Proceedings of the IEEE **51**, 89 (1963).

[49] D. F. Walls and G. J. Milburn, "Quantum optics", 2nd ed. (Springer, Berlin, 2008).

[50] Purcell, E.M., Torrey, H.C., and Pound, R.V., "Theory of Magnetic Resonance Absorption by Nuclear Moments in Solids", Physical Review **69**, 674 (1946).

[51] A. Blais, R.-S. Huang, A. Wallraff, S. M. Girvin, and R. J. Schoelkopf, "Cavity quantum electrodynamics for superconducting electrical circuits: An architecture for quantum computation", Physical Review A **69**, 062320 (2004).

[52] M. D. Reed, L. DiCarlo, B. R. Johnson, L. Sun, D. I. Schuster, L. Frunzio, and R. J. Schoelkopf, "High-Fidelity Readout in Circuit Quantum Electrodynamics Using the Jaynes-Cummings Nonlinearity", Physical Review Letters **105**, 173601 (2010).

[53] M. K. Tey, Z. Chen, S. A. Aljunid, B. Chng, F. Huber, G. Maslennikov, and C. Kurtsiefer, "Strong interaction between light and a single trapped atom without the need for a cavity", Nature Physics **4**, 924 (2008).

[54] G. Wrigge, I. Gerhardt, J. Hwang, G. Zumofen, and V. Sandoghdar, "Efficient coupling of photons to a single molecule and the observation of its resonance fluorescence", Nature Physics **4**, 60 (2008).

[55] H. J. Kimble, "The quantum internet", Nature **453**, 1023 (2008).

[56] X. Gu, A. F. Kockum, A. Miranowicz, Y.-X. Liu, and F. Nori, "Microwave photonics with superconducting quantum circuits", Physics Reports Microwave photonics with superconducting quantum circuits, **718-719**, 1 (2017).

[57] D. E. Chang, J. S. Douglas, A. González-Tudela, C.-L. Hung, and H. J. Kimble, "Colloquium: Quantum matter built from nanoscopic lattices of atoms and photons", Reviews of Modern Physics **90**, 031002 (2018).

[58] S. J. Masson and A. Asenjo-Garcia, "Atomic-waveguide quantum electrodynamics", Physical Review Research **2**, 043213 (2020).

[59] M. J. Renn, D. Montgomery, O. Vdovin, D. Z. Anderson, C. E. Wieman, and E. A. Cornell, "Laser-Guided Atoms in Hollow-Core Optical Fibers", Physical Review Letters **75**, 3253 (1995).

[60] A. V. Akimov, A. Mukherjee, C. L. Yu, D. E. Chang, A. S. Zibrov, P. R. Hemmer, H. Park, and M. D. Lukin, "Generation of single optical plasmons in metallic nanowires coupled to quantum dots", Nature **450**, 402 (2007).

[61] E. Vetsch, D. Reitz, G. Sagué, R. Schmidt, S. T. Dawkins, and A. Rauschenbeutel, "Optical Interface Created by Laser-Cooled Atoms Trapped in the Evanescent Field Surrounding an Optical Nanofiber", Physical Review Letters **104**, 203603 (2010).

[62] J. Claudon, J. Bleuse, N. S. Malik, M. Bazin, P. Jaffrennou, N. Gregersen, C. Sauvan, P. Lalanne, and J.-M. Gérard, "A highly efficient single-photon source based on a quantum dot in a photonic nanowire", Nature Photonics **4**, 174 (2010).

[63] A. Goban, C.-L. Hung, S.-P. Yu, J. Hood, J. Muniz, J. Lee, M. Martin, A. McClung, K. Choi, D. Chang, O. Painter, and H. Kimble, "Atom–light interactions in photonic crystals", Nature Communications **5**, 3808 (2014).

[64] G.-Z. Song, E. Munro, W. Nie, F.-G. Deng, G.-J. Yang, and L.-C. Kwek, "Photon scattering by an atomic ensemble coupled to a one-dimensional nanophotonic waveguide", Physical Review A **96**, 043872 (2017).

[65] J. D. Hood, A. Goban, A. Asenjo-Garcia, M. Lu, S.-P. Yu, D. E. Chang, and H. J. Kimble, “Atom–atom interactions around the band edge of a photonic crystal waveguide”, Proceedings of the National Academy of Sciences **113**, 10507 (2016).

[66] V. Krutyanskiy, M. Meraner, J. Schupp, V. Krcmarsky, H. Hainzer, and B. P. Lanyon, “Light-matter entanglement over 50 km of optical fibre”, npj Quantum Information **5**, 1 (2019).

[67] Z.-L. Xiang, M. Zhang, L. Jiang, and P. Rabl, “Intracity Quantum Communication via Thermal Microwave Networks”, Physical Review X **7**, 011035 (2017).

[68] M. W. Puckett and N. A. Krueger, “Broadband, ultrahigh efficiency fiber-to-chip coupling via multilayer nanophotonics”, Applied Optics **60**, 4340 (2021).

[69] D. Reitz, C. Sayrin, R. Mitsch, P. Schneeweiss, and A. Rauschenbeutel, “Coherence properties of nanofiber-trapped cesium atoms”, Physical Review Letters **110**, 243603 (2013).

[70] M. Arcari, I. Söllner, A. Javadi, S. Lindskov Hansen, S. Mahmoodian, J. Liu, H. Thyrrestrup, E. H. Lee, J. D. Song, S. Stobbe, and P. Lodahl, “Near-Unity Coupling Efficiency of a Quantum Emitter to a Photonic Crystal Waveguide”, Physical Review Letters **113**, 093603 (2014).

[71] A. Sipahigil, R. E. Evans, D. D. Sukachev, M. J. Burek, J. Borregaard, M. K. Bhaskar, C. T. Nguyen, J. L. Pacheco, H. A. Atikian, C. Meuwly, R. M. Camacho, F. Jelezko, E. Bielejec, H. Park, M. Lončar, and M. D. Lukin, “An integrated diamond nanophotonics platform for quantum-optical networks”, Science **354**, 847 (2016).

[72] M. K. Bhaskar, D. D. Sukachev, A. Sipahigil, R. E. Evans, M. J. Burek, C. T. Nguyen, L. J. Rogers, P. Siyushev, M. H. Metsch, H. Park, F. Jelezko, M. Lončar, and M. D. Lukin, “Quantum Nonlinear Optics with a Germanium-Vacancy Color Center in a Nanoscale Diamond Waveguide”, Physical Review Letters **118**, 223603 (2017).

[73] S. Faez, P. Türschmann, H. R. Haakh, S. Götzinger, and V. Sandoghdar, “Coherent Interaction of Light and Single Molecules in a Dielectric Nanoguide”, Physical Review Letters **113**, 213601 (2014).

[74] I.-C. Hoi, C. M. Wilson, G. Johansson, T. Palomaki, B. Peropadre, and P. Delsing, “Demonstration of a Single-Photon Router in the Microwave Regime”, Physical Review Letters **107**, 073601 (2011).

[75] A. A. Abdumalikov, O. Astafiev, A. M. Zagoskin, Y. A. Pashkin, Y. Nakamura, and J. S. Tsai, “Electromagnetically Induced Transparency on a Single Artificial Atom”, Physical Review Letters **104**, 193601 (2010).

[76] O. V. Astafiev, A. A. Abdumalikov, A. M. Zagoskin, Y. A. Pashkin, Y. Nakamura, and J. S. Tsai, “Ultimate On-Chip Quantum Amplifier”, Physical Review Letters **104**, 183603 (2010).

[77] S. H. Autler and C. H. Townes, “Stark Effect in Rapidly Varying Fields”, Physical Review **100**, 703 (1955).

[78] Y. Liu and A. A. Houck, “Quantum electrodynamics near a photonic bandgap”, Nature Physics **13**, 48 (2017).

[79] M. Scigliuzzo, A. Bengtsson, J.-C. Besse, A. Wallraff, P. Delsing, and S. Gasparinetti, “Primary Thermometry of Propagating Microwaves in the Quantum Regime”, Physical Review X **10**, 041054 (2020).

[80] Y. Lu, A. Bengtsson, J. J. Burnett, E. Wiegand, B. Suri, P. Krantz, A. F. Roudsari, A. F. Kockum, S. Gasparinetti, G. Johansson, and P. Delsing, “Characterizing decoherence rates of a superconducting qubit by direct microwave scattering”, npj Quantum Information **7**, 1 (2021).

[81] B. Kannan, M. J. Ruckriegel, D. L. Campbell, A. Frisk Kockum, J. Braumüller, D. K. Kim, M. Kjaergaard, P. Krantz, A. Melville, B. M. Niedzielski, A. Vepsäläinen, R. Winik, J. L. Yoder, F. Nori, T. P. Orlando, S. Gustavsson, and W. D. Oliver, “Waveguide quantum electrodynamics with superconducting artificial giant atoms”, Nature **583**, 775 (2020).

[82] M. Mirhosseini, E. Kim, V. S. Ferreira, M. Kalaee, A. Sipahigil, A. J. Keller, and O. Painter, “Superconducting metamaterials for waveguide quantum electrodynamics”, Nature Communications **9**, 3706 (2018).

[83] P. Magnard, S. Storz, P. Kurpiers, J. Schär, F. Marxer, J. Lütolf, T. Walter, J.-C. Besse, M. Gabureac, K. Reuer, A. Akin, B. Royer, A. Blais, and A. Wallraff, “Microwave Quantum Link between Superconducting Circuits Housed in Spatially Separated Cryogenic Systems”, Physical Review Letters **125**, 260502 (2020).

[84] M. Dalmonte, S. I. Mirzaei, P. R. Muppalla, D. Marcos, P. Zoller, and G. Kirchmair, “Realizing dipolar spin models with arrays of superconducting qubits”, Physical Review B **92**, 174507 (2015).

[85] R. N. Patel, T. Schröder, N. Wan, L. Li, S. L. Mouradian, E. H. Chen, and D. R. Englund, “Efficient photon coupling from a diamond nitrogen vacancy center by integration with silica fiber”, Light: Science & Applications **5**, e16032 (2016).

[86] B. Peropadre, J. Lindkvist, I.-C. Hoi, C. M. Wilson, J. J. Garcia-Ripoll, P. Delsing, and G. Johansson, “Scattering of coherent states on a single artificial atom”, New Journal of Physics **15**, 035009 (2013).

[87] T. Orell, M. Zanner, M. L. Juan, A. Sharafiev, R. Albert, S. Oleschko, G. Kirchmair, and M. Silveri, “Collective bosonic effects in an array of transmon devices”, arXiv:2112.08134 (2021).

[88] D. M. Pozar, “Microwave engineering”, 4th ed. (Wiley, Hoboken, NJ, 2012).

[89] G. Romero, J. J. García-Ripoll, and E. Solano, "Photodetection of propagating quantum microwaves in circuit QED", Physica Scripta **T137**, 014004 (2009).

[90] M. Devoret, B. Huard, R. Schoelkopf, and L. Cugliandolo, "Les houches notes 2011", 1st ed. (Oxford University Press, Oxford, 2011).

[91] H. Pichler, T. Ramos, A. J. Daley, and P. Zoller, "Quantum optics of chiral spin networks", Physical Review A **91**, 042116 (2015).

[92] T. Caneva, M. T. Manzoni, T. Shi, J. S. Douglas, J. I. Cirac, and D. E. Chang, "Quantum dynamics of propagating photons with strong interactions: a generalized input–output formalism", New Journal of Physics **17**, 113001 (2015).

[93] C. Eichler, C. Lang, J. M. Fink, J. Govenius, S. Filipp, and A. Wallraff, "Observation of Entanglement between Itinerant Microwave Photons and a Superconducting Qubit", Physical Review Letters **109**, 240501 (2012).

[94] M. J. Collett and C. W. Gardiner, "Squeezing of intracavity and traveling-wave light fields produced in parametric amplification", Physical Review A **30**, 1386 (1984).

[95] S. Fan, Ş. E. Kocabaş, and J.-T. Shen, "Input-output formalism for few-photon transport in one-dimensional nanophotonic waveguides coupled to a qubit", Physical Review A **82**, 063821 (2010).

[96] B. R. Mollow, "Power Spectrum of Light Scattered by Two-Level Systems", Physical Review **188**, 1969 (1969).

[97] A. vanLoo, "Interactions in waveguide quantum electrodynamics", Ph.D. thesis, ETH (2014).

[98] K. Lalumière, "Électrodynamique quantique en guide d'onde", Ph.D. thesis, Faculté des Science, Université de Sherbrooke (2015).

[99] A. Dewes, F. R. Ong, V. Schmitt, R. Lauro, N. Boulant, P. Bertet, D. Vion, and D. Esteve, "Characterization of a Two-Transmon Processor with Individual Single-Shot Qubit Readout", Physical Review Letters **108**, 057002 (2012).

[100] M. Zanner, T. Orell, C. M. F. Schneider, R. Albert, S. Oleschko, M. L. Juan, M. Silveri, and G. Kirchmair, "Coherent control of a multi-qubit dark state in waveguide quantum electrodynamics", Nature Physics , 1 (2022).

[101] S. Hacohen-Gourgy, V. V. Ramasesh, C. De Grandi, I. Siddiqi, and S. M. Girvin, "Cooling and Autonomous Feedback in a Bose-Hubbard Chain with Attractive Interactions", Physical Review Letters **115**, 240501 (2015).

[102] P. Roushan, C. Neill, J. Tangpanitanon, V. M. Bastidas, A. Megrant, R. Barends, Y. Chen, Z. Chen, B. Chiaro, A. Dunsworth, A. Fowler, B. Foxen, M. Giustina, E. Jeffrey, J. Kelly, E. Lucero, J. Mutus, M. Neeley, C. Quintana, D. Sank, A. Vainsencher,

J. Wenner, T. White, H. Neven, D. G. Angelakis, and J. Martinis, "Spectroscopic signatures of localization with interacting photons in superconducting qubits", Science **358**, 1401 (2017).

[103] R. Ma, B. Saxberg, C. Owens, N. Leung, Y. Lu, J. Simon, and D. I. Schuster, "A dissipatively stabilized Mott insulator of photons", Nature **566**, 51 (2019).

[104] G. P. Fedorov, "Photon Transport in a Bose-Hubbard Chain of Superconducting Artificial Atoms", Physical Review Letters **126**, 10.1103/PhysRevLett.126.180503 (2021).

[105] D. C. Brody, "Biorthogonal quantum mechanics", Journal of Physics A: Mathematical and Theoretical **47**, 035305 (2013).

[106] K. Packard, "The Origin of Waveguides: A Case of Multiple Rediscovery", IEEE Transactions on Microwave Theory and Techniques **32**, 961 (1984).

[107] A. Somoroff, Q. Ficheux, R. A. Mencia, H. Xiong, R. V. Kuzmin, and V. E. Manucharyan, "Millisecond coherence in a superconducting qubit", arXiv:2103.08578 (2021).

[108] K. Wu, D. Deslandes, and Y. Cassivi, in *6th International Conference on Telecommunications in Modern Satellite, Cable and Broadcasting Service*, Vol. 1 (2003) pp. P–III.

[109] S. Casulleras, C. Gonzalez-Ballestero, P. Maurer, J. J. García-Ripoll, and O. Romero-Isart, "Remote Individual Addressing of Quantum Emitters with Chirped Pulses", Physical Review Letters **126**, 103602 (2021).

[110] Y. Y. Gao, M. A. Rol, S. Touzard, and C. Wang, "Practical Guide for Building Superconducting Quantum Devices", PRX Quantum **2**, 040202 (2021).

[111] M. S. Khalil, M. J. A. Stoutimore, F. C. Wellstood, and K. D. Osborn, "An analysis method for asymmetric resonator transmission applied to superconducting devices", Journal of Applied Physics **111**, 054510 (2012).

[112] S. Probst, F. B. Song, P. A. Bushev, A. V. Ustinov, and M. Weides, "Efficient and robust analysis of complex scattering data under noise in microwave resonators", Review of Scientific Instruments **86**, 024706 (2015).

[113] R. W. Simmonds, D. A. Hite, R. McDermott, M. Steffen, K. B. Cooper, K. M. Lang, J. M. Martinis, and D. P. Pappas, in *Quantum Computing in Solid State Systems*, edited by B. Ruggiero, P. Delsing, C. Granata, Y. Pashkin, and P. Silvestrini (Springer, New York, NY, 2006) pp. 86–94.

[114] L. J. Zeng, S. Nik, T. Greibe, P. Krantz, C. M. Wilson, P. Delsing, and E. Olsson, "Direct observation of the thickness distribution of ultra thin AlOxbarriers in Al/AlOx/Al Josephson junctions", Journal of Physics D: Applied Physics **48**, 395308 (2015).

[115] C. Wang, C. Axline, Y. Y. Gao, T. Brecht, Y. Chu, L. Frunzio, M. H. Devoret, and R. J. Schoelkopf, “Surface participation and dielectric loss in superconducting qubits”, Applied Physics Letters **107**, 162601 (2015).

[116] V. Ambegaokar and A. Baratoff, “Tunneling Between Superconductors”, Physical Review Letters **10**, 486 (1963).

[117] F. Lecocq, I. M. Pop, Z. Peng, I. Matei, T. Crozes, T. Fournier, C. Naud, W. Guichard, and O. Buisson, “Junction fabrication by shadow evaporation without a suspended bridge”, Nanotechnology **22**, 315302 (2011).

[118] G. J. Dolan, “Offset masks for lift-off photoprocessing”, Applied Physics Letters **31**, 337 (1977).

[119] A. P. M. Place, L. V. H. Rodgers, P. Mundada, B. M. Smitham, M. Fitzpatrick, Z. Leng, A. Premkumar, J. Bryon, A. Vrajitoarea, S. Sussman, G. Cheng, T. Madhavan, H. K. Babla, X. H. Le, Y. Gang, B. Jäck, A. Gyenis, N. Yao, R. J. Cava, N. P. de Leon, and A. A. Houck, “New material platform for superconducting transmon qubits with coherence times exceeding 0.3 milliseconds”, Nature Communications **12**, 1779 (2021).

[120] C. Wang, X. Li, H. Xu, Z. Li, J. Wang, Z. Yang, Z. Mi, X. Liang, T. Su, C. Yang, G. Wang, W. Wang, Y. Li, M. Chen, C. Li, K. Linghu, J. Han, Y. Zhang, Y. Feng, Y. Song, T. Ma, J. Zhang, R. Wang, P. Zhao, W. Liu, G. Xue, Y. Jin, and H. Yu, “Towards practical quantum computers: transmon qubit with a lifetime approaching 0.5 milliseconds”, npj Quantum Information **8**, 3 (2022).

[121] S. Barnett and P. Radmore, “Methods in Theoretical Quantum Optics”, Oxford Series in Optical and Imaging Sciences (Oxford University Press, Oxford, New York, 2002).

[122] X. Y. Jin, A. Kamal, A. P. Sears, T. Gudmundsen, D. Hover, J. Miloxi, R. Slattery, F. Yan, J. Yoder, T. P. Orlando, S. Gustavsson, and W. D. Oliver, “Thermal and Residual Excited-State Population in a 3D Transmon Qubit”, Physical Review Letters **114**, 240501 (2015).

[123] J.-H. Yeh, J. LeFebvre, S. Premaratne, F. C. Wellstood, and B. S. Palmer, “Microwave attenuators for use with quantum devices below 100 mK”, Journal of Applied Physics **121**, 224501 (2017).

[124] Z. Wang, S. Shankar, Z. Minev, P. Campagne-Ibarcq, A. Narla, and M. Devoret, “Cavity Attenuators for Superconducting Qubits”, Physical Review Applied **11**, 014031 (2019).

[125] H. Friis, “Noise Figures of Radio Receivers”, Proceedings of the IRE **32**, 419 (1944).

[126] C. M. F. Schneider, “Magnetic coupling between superconducting circuits and a cantilever”, Ph.D. thesis, Unversität Innsbruck (2021).

[127] J. D. Brehm, “Superconducting Quantum Metamaterials” (2021).

[128] Q.-M. Chen, M. Pfeiffer, M. Partanen, F. Fesquet, K. E. Honasoge, F. Kronowetter, Y. Nojiri, M. Renger, K. G. Fedorov, A. Marx, F. Deppe, and R. Gross, "The scattering coefficients of superconducting microwave resonators: I. Transfer-matrix approach", arXiv:2109.07762 [cond-mat, physics:quant-ph] (2022).

[129] Q.-M. Chen, M. Partanen, F. Fesquet, K. E. Honasoge, F. Kronowetter, Y. Nojiri, M. Renger, K. G. Fedorov, A. Marx, F. Deppe, and R. Gross, "The scattering coefficients of superconducting microwave resonators: II. System-bath approach", arXiv:2109.07766 [cond-mat, physics:quant-ph] (2022).

[130] C. Deng, M. Otto, and A. Lupascu, "An analysis method for transmission measurements of superconducting resonators with applications to quantum-regime dielectric-loss measurements", Journal of Applied Physics **114**, 054504 (2013).

[131] F. Motzoi, J. M. Gambetta, P. Rebentrost, and F. K. Wilhelm, "Simple Pulses for Elimination of Leakage in Weakly Nonlinear Qubits", Physical Review Letters **103**, 110501 (2009).

[132] P. J. Leek, M. Baur, J. M. Fink, R. Bianchetti, L. Steffen, S. Filipp, and A. Wallraff, "Cavity Quantum Electrodynamics with Separate Photon Storage and Qubit Readout Modes", Physical Review Letters **104**, 100504 (2010).

[133] E. Sánchez-Burillo, D. Zueco, L. Martín-Moreno, and J. J. García-Ripoll, "Dynamical signatures of bound states in waveguide QED", Physical Review A **96**, 023831 (2017).

[134] A. R. Hamann, "Rectangular waveguide QED with superconducting qubits", Ph.D. thesis, University of Queensland (2019).

[135] D. Leibfried, R. Blatt, C. Monroe, and D. Wineland, "Quantum dynamics of single trapped ions", Reviews of Modern Physics **75**, 281 (2003).

[136] A. Borgognoni, "Mode temperature analysis of a readout resonator", Master's Thesis, Universität Innsbruck, Innsbruck (2020).

[137] N. F. Ramsey, "A Molecular Beam Resonance Method with Separated Oscillating Fields", Physical Review **78**, 695 (1950).

[138] E. L. Hahn, "Spin Echoes", Physical Review **80**, 580 (1950).

[139] A. Asenjo-Garcia, M. Moreno-Cardoner, A. Albrecht, H. J. Kimble, and D. E. Chang, "Exponential Improvement in Photon Storage Fidelities Using Subradiance and "Selective Radiance" in Atomic Arrays", Physical Review X **7**, 031024 (2017).

[140] A. González-Tudela, V. Paulisch, D. E. Chang, H. J. Kimble, and J. I. Cirac, "Deterministic Generation of Arbitrary Photonic States Assisted by Dissipation", Physical Review Letters **115**, 163603 (2015).

[141] A. Albrecht, L. Henriet, A. Asenjo-Garcia, P. B. Dieterle, O. Painter, and D. E. Chang, "Subradiant states of quantum bits coupled to a one-dimensional waveguide", New Journal of Physics **21**, 025003 (2019).

[142] T. Orell, A. A. Michailidis, M. Serbyn, and M. Silveri, "Probing the many-body localization phase transition with superconducting circuits", Physical Review B **100**, 134504 (2019).

[143] N. Fayard, L. Henriet, A. Asenjo-Garcia, and D. E. Chang, "Many-body localization in waveguide quantum electrodynamics", Physical Review Research **3**, 033233 (2021).

[144] F. Reiter and A. S. Sørensen, "Effective operator formalism for open quantum systems", Physical Review A **85**, 032111 (2012).

[145] J.-C. Besse, K. Reuer, M. C. Collodo, A. Wulff, L. Wernli, A. Copetudo, D. Malz, P. Magnard, A. Akin, M. Gabureac, G. J. Norris, J. I. Cirac, A. Wallraff, and C. Eichler, "Realizing a deterministic source of multipartite-entangled photonic qubits", Nature Communications **11**, 4877 (2020).

[146] Y. Ke, A. V. Poshakinskiy, C. Lee, Y. S. Kivshar, and A. N. Poddubny, "Inelastic Scattering of Photon Pairs in Qubit Arrays with Subradiant States", Physical Review Letters **123**, 253601 (2019).

[147] T. Ramos and J. J. García-Ripoll, "Multiphoton Scattering Tomography with Coherent States", Physical Review Letters **119**, 153601 (2017).

APPENDIX A

Single Qubit Circle-Fits

Here we show the results of the circle-fits [111, 112] for the individual transmons at the frequencies, effectively corresponding to $\lambda/2$. Even though it seems that the data is even lower than the fit, it is limited by noise at these low transmission amplitudes.

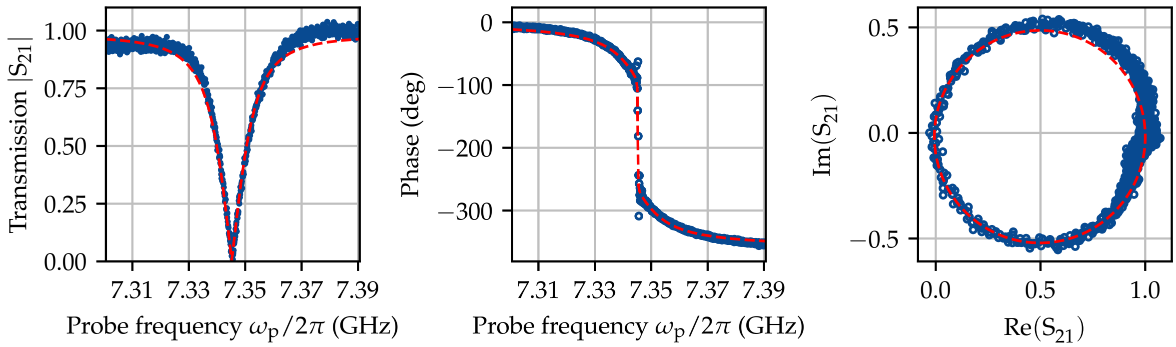

Figure A.1: Fit results. $Q_L = 430 \pm 2$, $Q_c = 440 \pm 1$, $Q_{int} = 18846 \pm 1271$, $f_r = 7.346$ GHz, $\kappa_L/2\pi = (17088 \pm 71)$ kHz, $\kappa_c/2\pi = (16698 \pm 56)$ kHz, $\kappa_{int}/2\pi = (390 \pm 26)$ kHz

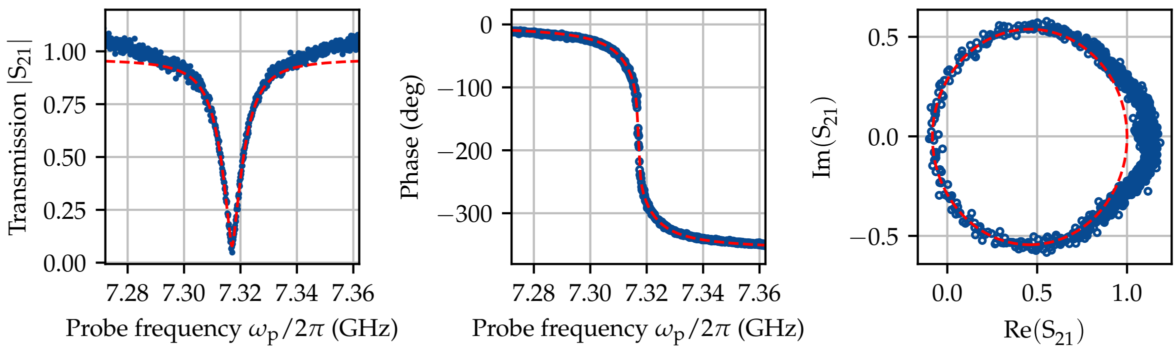

Figure A.2: Fit results. $Q_L = 504 \pm 2$, $Q_c = 520 \pm 2$, $Q_{int} = 15885 \pm 1066$, $f_r = 7.317$ GHz, $\kappa_L/2\pi = (14530 \pm 61)$ kHz, $\kappa_c/2\pi = (14069 \pm 48)$ kHz, $\kappa_{int}/2\pi = (461 \pm 31)$ kHz

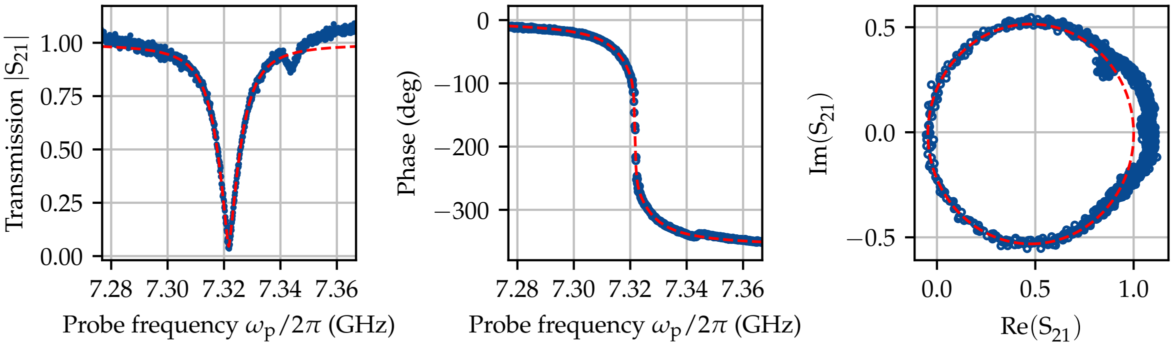

Figure A.3: Fit results. $Q_L = 506 \pm 2$, $Q_c = 527 \pm 2$, $Q_{int} = 12545 \pm 680$, $f_r = 7.322$ GHz, $\kappa_L/2\pi = (14476 \pm 59)$ kHz, $\kappa_c/2\pi = (13892 \pm 46)$ kHz, $\kappa_{int}/2\pi = (584 \pm 32)$ kHz

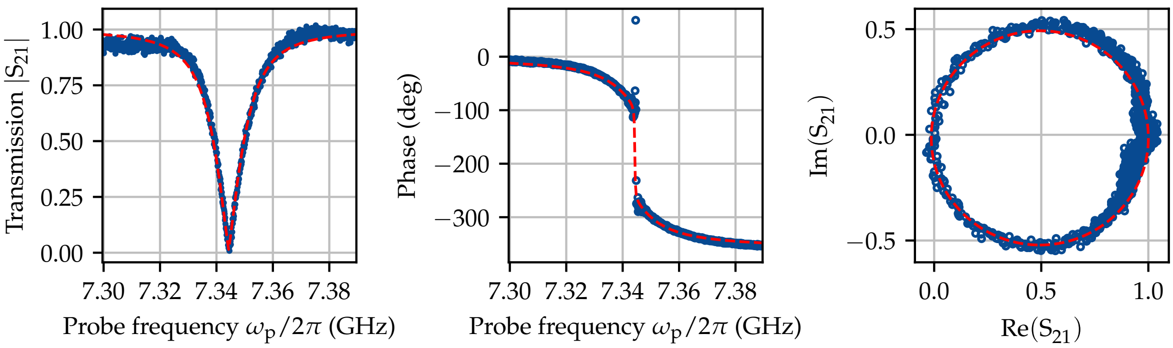

Figure A.4: Fit results. $Q_L = 420 \pm 2$, $Q_c = 431 \pm 2$, $Q_{int} = 17226 \pm 1115$, $f_r = 7.345$ GHz, $\kappa_L/2\pi = (17474 \pm 75)$ kHz, $\kappa_c/2\pi = (17048 \pm 59)$ kHz, $\kappa_{int}/2\pi = (426 \pm 28)$ kHz

APPENDIX B

Avoided Crossings

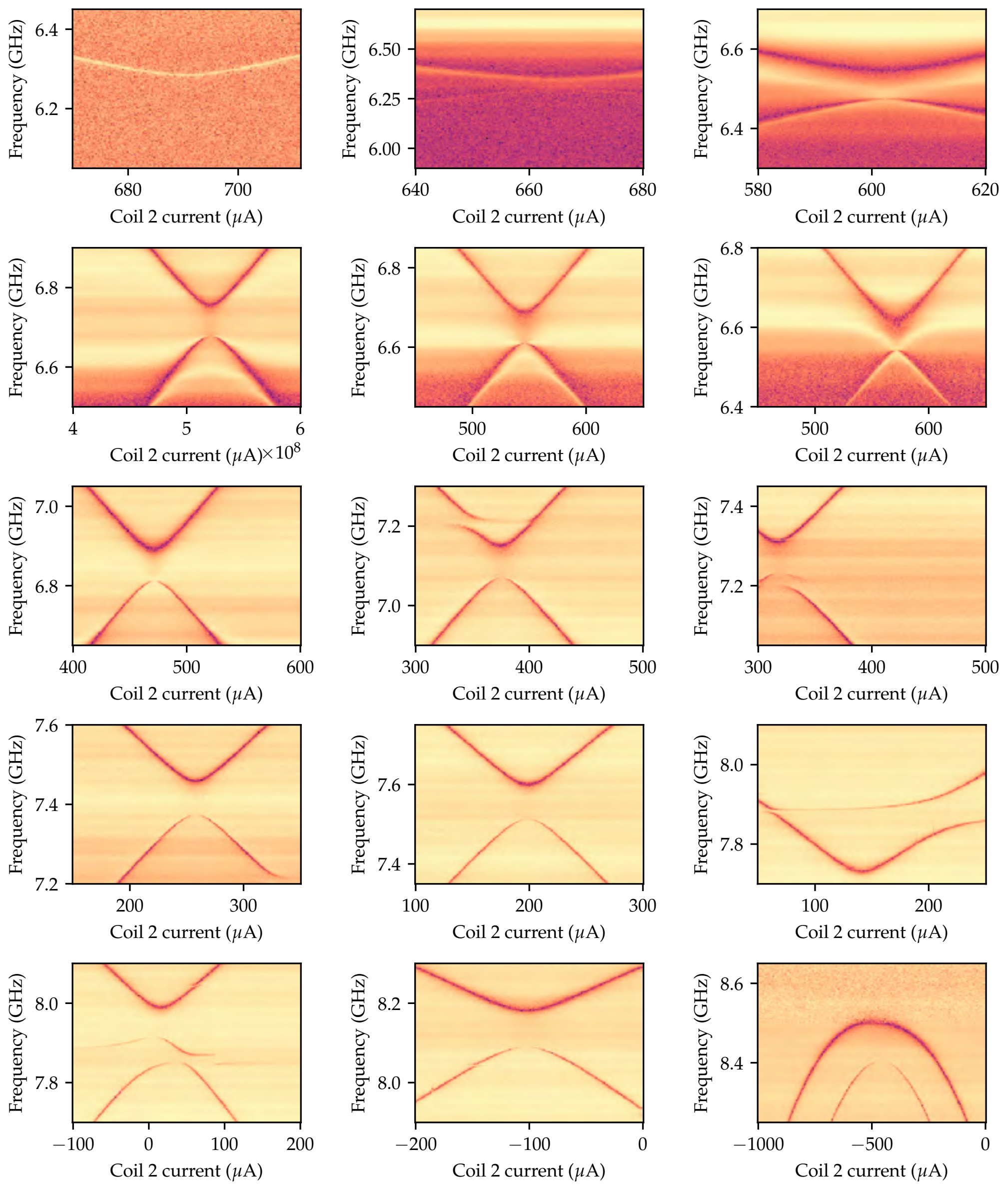

Figure B.1: Avoided crossings between qubits Q_1 and Q_2 at different frequencies. The y-axis shows the probe frequency and the x-axis the coil through the coil 3 that is used to vary the flux through the SQUID loop of the transmons.

The capacitively coupled qubits Q_1 and Q_2, as well as the other pair Q_3 and Q_4 can be tuned in resonance at different frequencies. The additional avoided crossings that appear are attributed to a coherent interaction with two-level systems. When a two-level-system was present the dark state coherence properties were deteriorated. This can also be witnessed in the missing decay times T_1 close to those frequencies in Fig. 4.14.

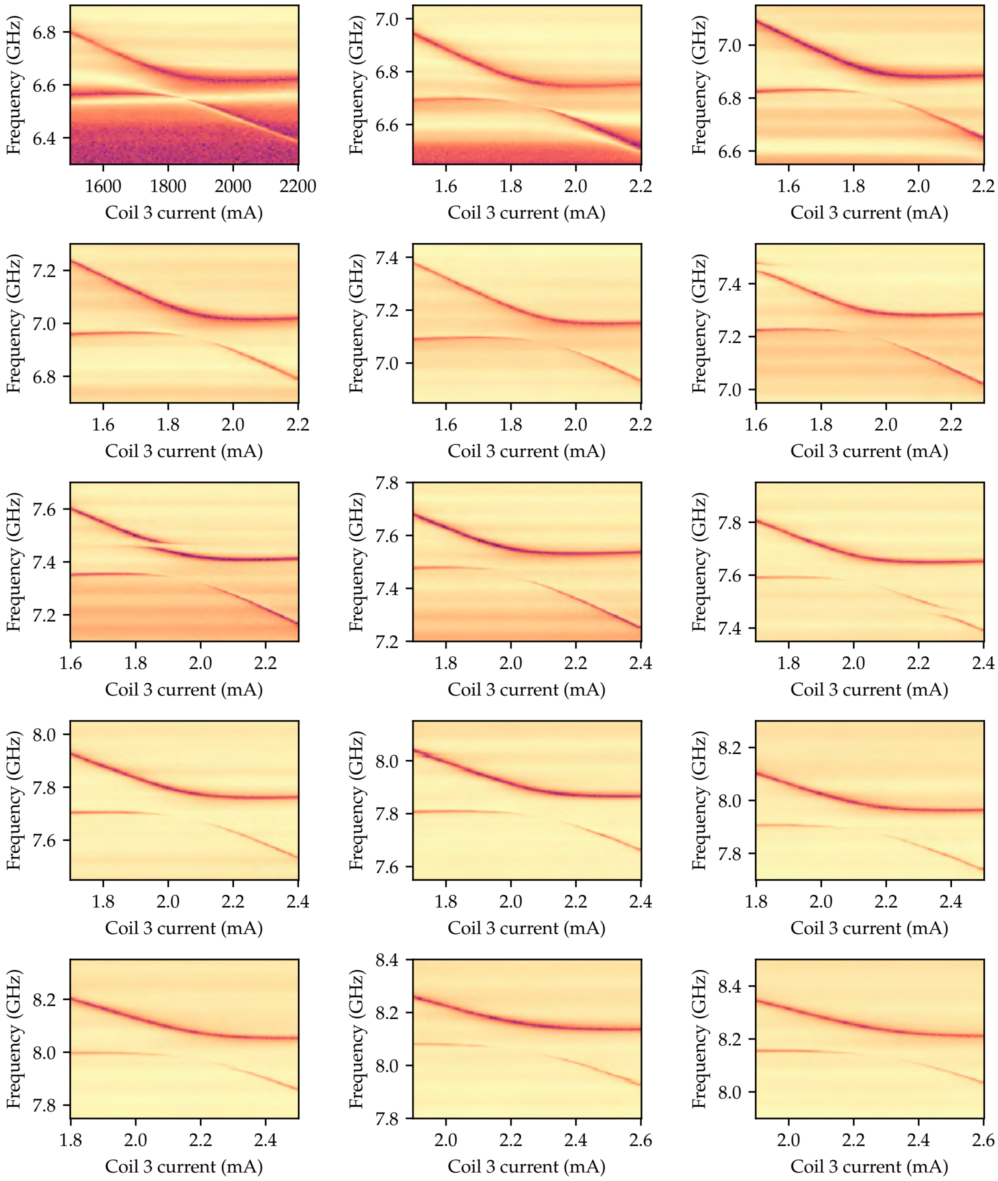

Figure B.2: Same as Fig. B.1 but for Qubits Q_3 and Q_4.

APPENDIX C

Two-Qubits Power Dependence

C.1 Measurements

Increasing the power when tuning the transmon into resonance reveals their multi-level nature.

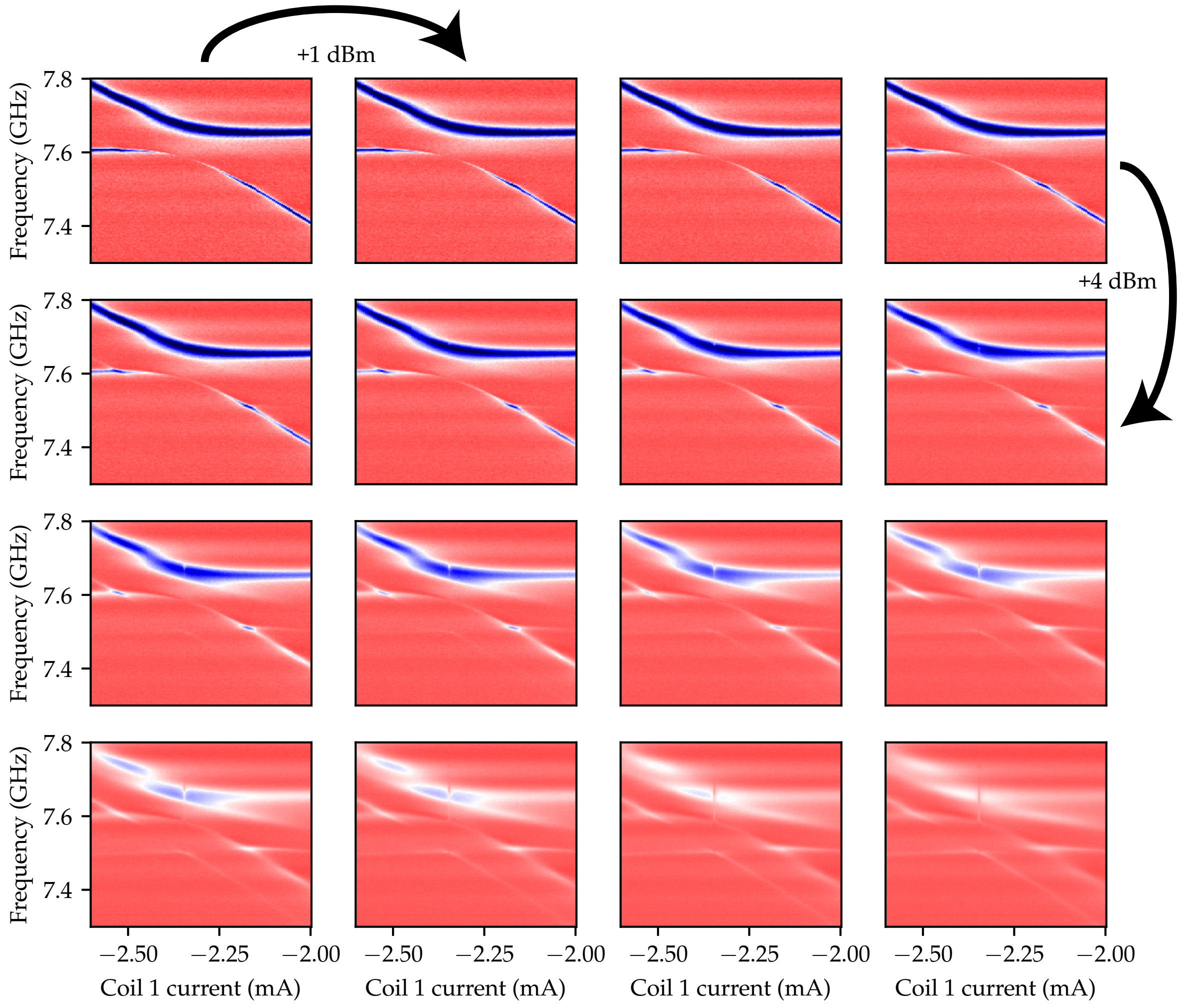

Figure C.1: Tuning the direct coupled transmons into resonance while increasing the probe power shows the two photon transition $|0\rangle$-$|2\rangle$ of the transmon and the transition $|1\rangle$-$|2\rangle$.

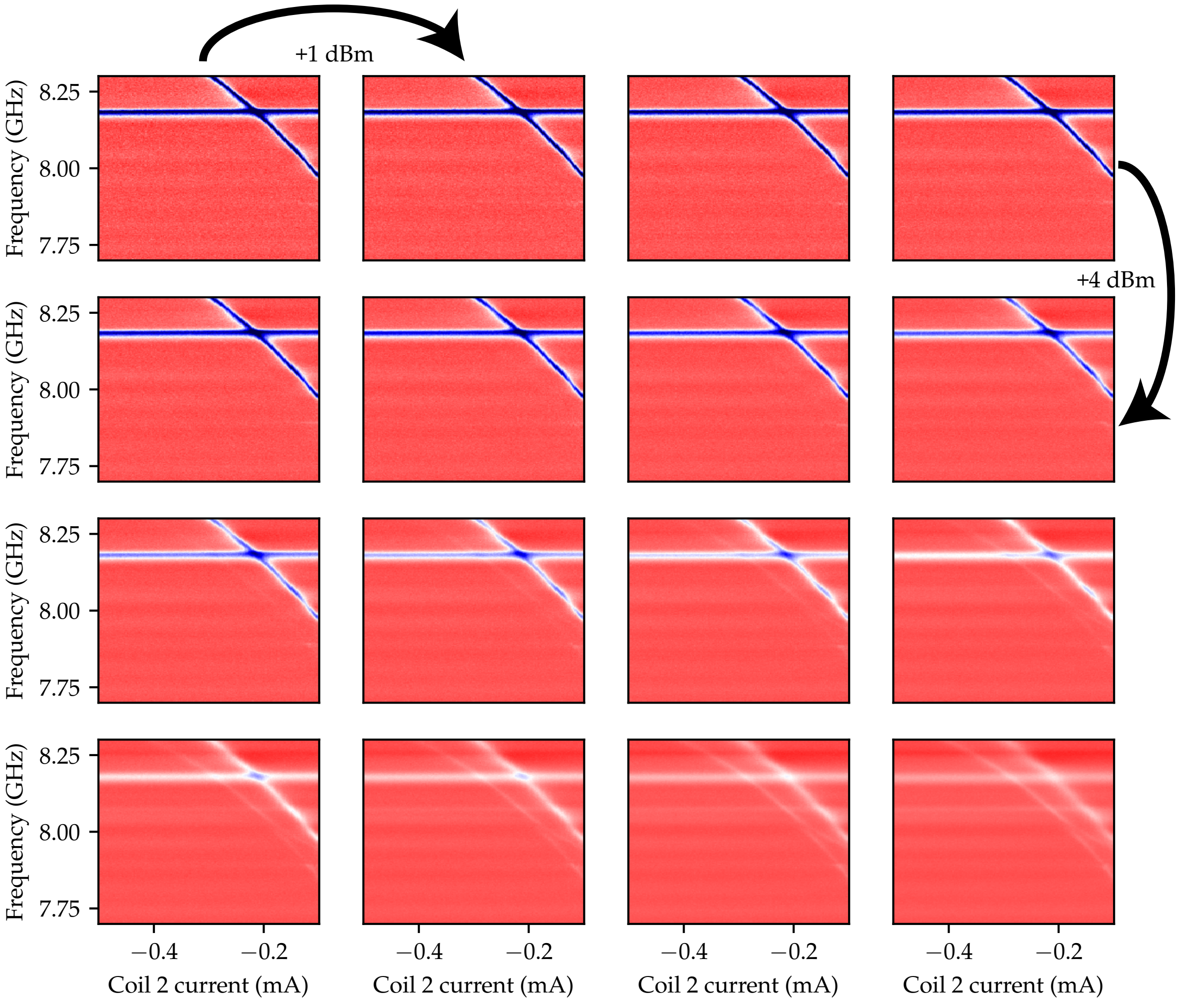

Figure C.2: Two distant transmons are tuned into resonance at a frequency corresponding to $\sim 3\lambda/4$ while increasing the probe power.

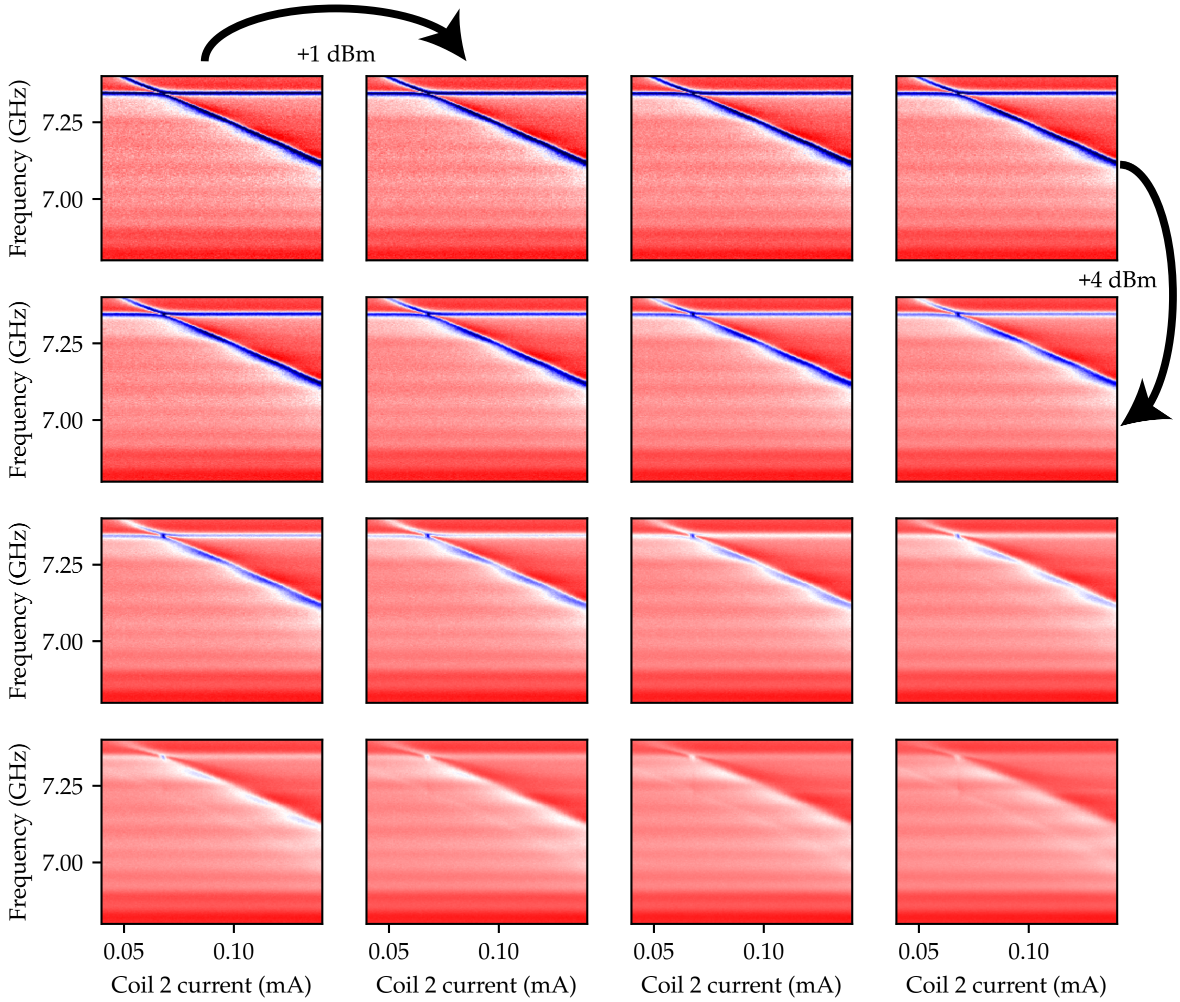

Figure C.3: Two distant transmons are tuned into resonance at a frequency corresponding to $\sim \lambda/2$ while increasing the probe power.

C.2 Simulations

The high power simulations show qualitatively consistent results with the measurements. Especially all the additional features for high power can be explained by taking into account the mulit-level nature of the transmon, driving either the two-photon transition $|0\rangle$-$|2\rangle$ and the transition $|1\rangle$-$|2\rangle$.

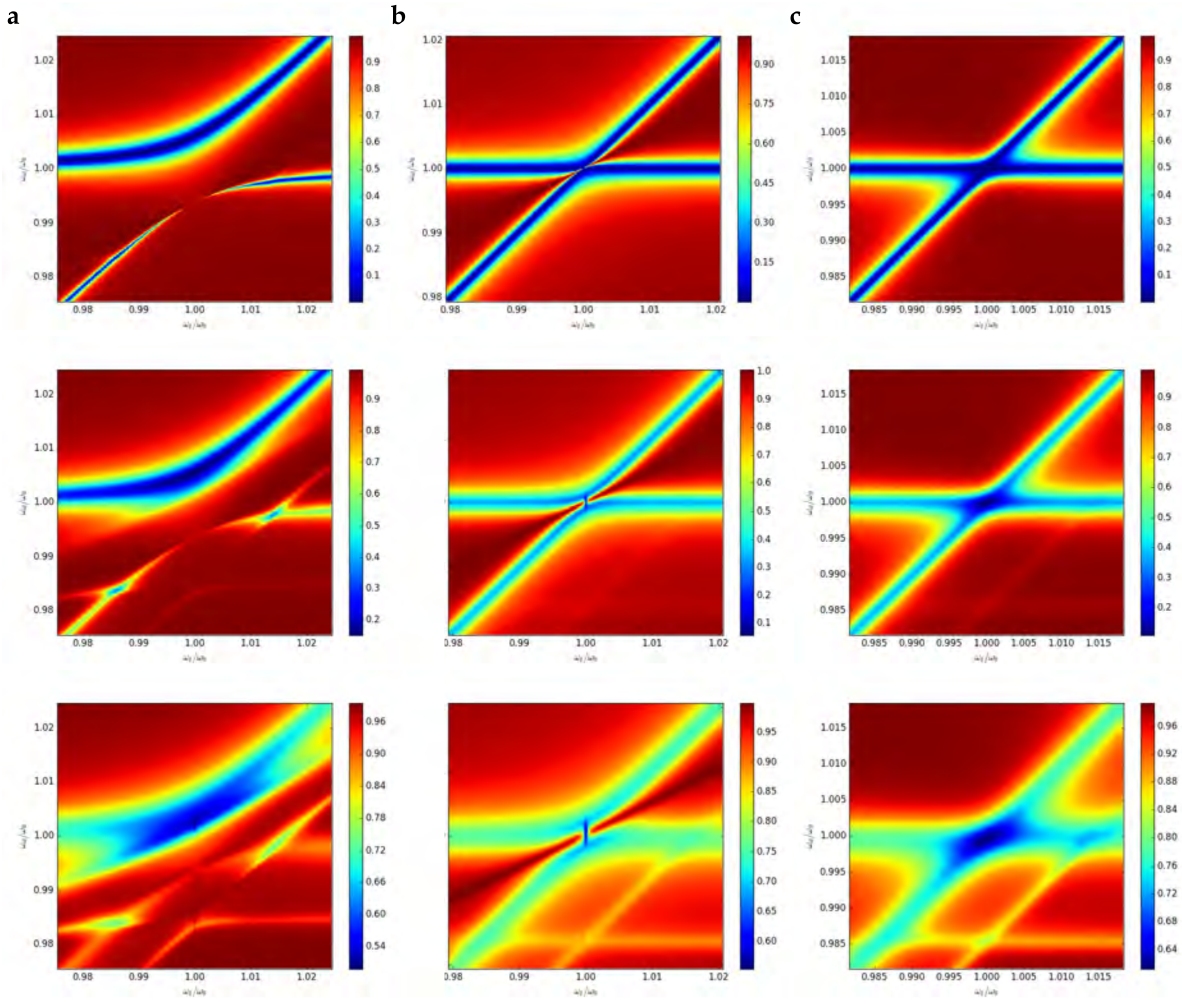

Figure C.4: Top to bottom increasing power for two transmon tuned into resonance. **a** Direct coupled transmon pair. **b** Two transmons separated by $\lambda/2$. **c** Two transmons separated by $3\lambda/4$.

APPENDIX D

Dark State Calibration

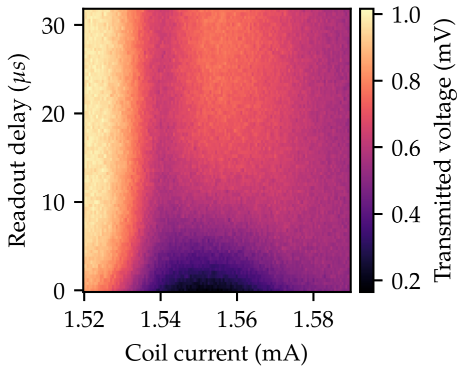

Figure D.1: Dark state decay time measurements. For a capacitively coupled transmon pair we can measure the decay time of the dark state. In order to find the perfect symmetry point we slowly tune the coil current and measure the decay time to find the longest dark state lifetime.

To calibrate the dark state lifetimes there are many flux-tuning parameters. By recording the map like depicted in Fig. D.1 we can measure the lifetime for a capacitively coupled pair for slight detunings between the individual transmon transitions. Therefore, we sweep the coil current to only detune one of the qubits while keeping the other one at a constant frequency. By measuring the decay time at every flux point we obtain the map. Then the other qubit is tuned and a similar map is recorded. This ensures that we measure the longest possible T_1 time and are not limited by a slight qubit-qubit detuning that would result in a waveguide coupling of the dark state and could potentially limit its lifetime.

Acknowledgments

In the course of my doctoral studies, I have had the privilege of meeting many different people to whom I would like to express my appreciation through these acknowledgments.

First and foremost, I would like to express my deepest gratitude to Gerhard Kirchmair. I admire your passion and positive attitude towards every aspect of scientific research. Your endless patience, constant availability, and contagious enthusiasm for physics make you an outstanding teacher and supervisor. I will always be grateful for your support, the atmosphere you created in the group, and the freedom you gave us to develop as scientists.

I owe my greatest gratitude to Christian Schneider who helped me with almost every obstacle I encountered and never got tired of discussing decay rates. Your scientific skills are only surpassed by your selflessness, camaraderie, and willingness to help anyone with anything. I couldn't have asked for a better colleague and friend during my PhD.

I would like to thank Mathieu Juan, whom I envy not only for his illustration skills (see cover image), but also for his deep knowledge of quantum optics, his work ethic, and his craftsmanship. I hope that you and your family have found a home in Sherbrooke and I wish you a successful academic career.

I would like to thank Ian Yang, who quickly became the most eager graduate student in the group and took on every task. Your work ethic was to be expected, but still impresses me every day. I am sure you will be very successful, and no matter what other people say, you are truly one in a million.

I would like to thank Romain Albert who immediately impressed me with his immense knowledge about circuits, programming and fabrication. Your willingness to share and discuss the details of all experiments improved the overall scientific level in the group. I hope we will share many more (probably too young) red wines together, while I can enjoy your diplomatic views on science politics. I look forward to see what the future holds for you.

I would like to thank Oscar Gargiulo for setting up the time domain setup and for teaching me the basics of pulsed measurements. I will be forever grateful to you for introducing me to the wonderful Brikka coffee maker, which has quickly become my most used kitchen appliance.

I would like to thank Phani Raja Muppalla for introducing me to the lab and the art of making coaxial input lines. I will never forget that despite being a year ahead, you beat my T_1 record with your first manufactured sample.

I want to thank Aleksei Sharafiev for always being at our midnight fridge closing sessions and presenting the colorful flux maps at the group meetings. I am looking forward to see the quantum computer soon.

I want to thank Stefan Oleschko for his patience and craftsmanship, especially when we were making the input lines. Taking on side-tasks, such as making fast switches, sometimes falls a little under the radar, but is still very much appreciated. I am still confused why so many people came to your birthday party.

I would like to thank Rafael Rabl and Paul Heidler, who not only showed me what culinary specialties can be prepared in the IQOQI kitchen, but also impressed me with how quickly they became a valuable part of the group during their master projects.

I would like to thank Vasilisa Usova for replacing me as the most persistent PhD student and for her contagious optimism for her project.

I would like to thank Markus Weiß for the proper management of the cleanroom facility and the maintenance of the machines.

I would like to thank David Zöpfl for his excellent scientific work mentality and great organizational skills. It feels like you have organized every group retreat. Also thanks to your last name for not leaving me last in the list of names for once.

I would like to thank Alvise Borgognoni for his great systematic noise study, which taught me a lot about how to develop a proper qubit environment. You are such a pleasant person to be around and I hope you have a great time in Paris.

I would like to thank Desislava Atanasova for her efforts in bringing parametric amplifiers to the lab. May your nightmares not be of laser writers and resist sticking problems.

I would like to thank Christian Schlager for his patience in explaining where the wire is hidden underneath the tunnel and for his great work in the cleanroom.

I would like to thank Lukas Deeg for his positive nature and enthusiasm and for helping me to supervise the visiting students. I think the mechanics experiment is in good hands.

I would like to thank Teresa Hönigl-Decrinis for enriching our group with more knowledge about waveguide QED and immediate enthusiasm for fabrication.

I would like to thank Eric Rosenthal for joining the focusing experiment and immediately driving progress with his very impressive work ethic.

I would like to thank Michael Niemack for educating me about astrophysics detectors and bridging the gap to our field, which reminded me of my time during my undergraduate project at the Karlsruhe Tritium Neutrino Experiment (KATRIN).

I would like to thank Matti Silveri and Tuure Orell for the excellent collaboration. Without your fantastic theoretical work, the publication would never have happened. I am still seriously impressed with how quickly you replicated the measurements, developed the analytical framework and calculated the numerical results.

I would like to thank the master students and summer interns I had the pleasure to work with: Stephanie Wögerer, Markus Sifft, Isabel Pietka and Michael Schmid, Adrien Moulinas, Victor Champain, Antonio d'Abbruzzo, Julian Daser and Michele Calvanese

I would like to thank Christoph R. Kaubrügger for repeatedly bringing to my attention theoretical publications that require at least a 100-qubit processor and for believing that I can build one. Also for introducing me to the world of climbing.

I would like to thank everyone in the administration and IT departments for making my life so much easier. Your work is much appreciated and highly valued, especially because it is mostly missing in the skillset of a scientist: Carina-Theresa Sassermann, Elke Wölflmaier, Heide Streicher, Alexander Kaiser, Eric Endres, Valentin Staubmann, David Jordan, Elisabeth Huck, Nikolaus Falschlunger and Markus Knabl

All of our projects profit immensely from the excellence of the IQOQI mechanical workshop. I am very happy that it is staffed with such highly qualified, motivated and uniquely nice people and I regret every minute that I spent too long thinking about problems, when 5 minutes in the workshop solved them all: Andreas Strasser, Bernhard Öttl, Stefan Haslwanter, Gerhard Hendl and David Arnold

I would like to thank Itamar Sivan, Yonatan Cohen and especially Niv Drucker for their support with the Quantum Machine and the improvised APS March Meeting 2020.

I would like to thank the PI's and all (former) members of the research group of Aleksei Ustinov, Martin Weides and Ioan Pop at the Karlsruhe Institute of Technology, especially Patrick Winkel, Lukas Grünhaupt, Andre Schneider, Marco (Markus) Pfirrmann, Hannes Rotzinger, Jürgen Lisenfeld, Sebastian Skacel, Jan Brehm, Jochen Braumüller, Nico Voss, Steffen Schlör, Alex Bilmes, Yannick Schön, Alex Stehli, etc. I admire you all for your scientific excellence. It seems like I never came home from the ski seminar. In particular, I would like to thank Ioan for sending me to Innsbruck and for advocating for me.

I would like to thank Arkady Fedorov, Markus Jerger, Clemens Müller and Andrés Rosario Hamann for the time in Brisbane and for teaching me so much during my master project.

I would like to thank all the people that accompanied me during the bachelor and master at KIT: Moritz Hackenjos, Anton Huber, Jan Bondy, Florian Heizmann, Philipp Gasch, Malte Langenhorst, Max Reimer, Simon Brose, Michael Jenne, Robert Eschbach and Rainer Kraft

Even though they might never see this, I would like to thank my non-physicist friends, Ricardo da Silva, Stefano Meloni, Davide Patel, Ashkan Khorshidpour, Thomas Puzik, Michael Gösele, Johannes Wiest, Fabian Schuck, Maximilian Pircher and Moritz Schorpp for reminding me that there is more to life than physics. Even though we do not see each other often, it always feels like nothing changed.

Thank you Frida for making sure I take breaks in the home office, and for being the happy dog that you are.

I would like to thank my girlfriend Isabel Arnst for her moral support, her love and her willingness to move to Innsbruck with me.

I would like to thank my brother Sebastian Zanner and my sister Eva Zanner for being the best siblings and putting up with me as a child (and now).

Most of all I would like to thank my parents Harald and Christa Zanner. Without your love, support and patience I would not be who I am today.
Liebe Mama, lieber Papa, ich hoffe Ihr wisst dass dies alles ohne euch nie möglich gewesen wäre und ich euch für die endlose Liebe, Freiheit und Unterstützung unendlich dankbar bin. Ich hoffe Ihr habt Spaß beim Lesen.